Modelling microstructure evolution, creep deformation and damage in Type 316H stainless steel

Markian Petkov

Hertford College, University of Oxford

Supervisor: Prof Alan Cocks



Solid Mechanics and Materials Engineering

Department of Engineering Science

University of Oxford

A thesis submitted for the degree of

Doctor of Philosophy

Hilary 2020

Abstract

The current Advanced Gas-cooled Reactors (AGR) in the UK are approaching their design life. The reactor operator, EDF Energy, is seeking to extend their life due to ecological and financial reasons. One challenge to plant life-extension is the accurate prediction of high-temperature deformation and failure of Type 316H stainless steel, used in components of the reactor boiler section. Under the operating conditions of these components (470-650°C; 10-300 MPa), creep and cyclic plasticity alter the material's microstructure and failure response. Empirical models are used in industry to predict the deformation and damage response of Type 316H. Predictions can be in poor agreement with plant-recorded/experimental deformation response under complex loading histories. Furthermore, the models are deficient in capturing the sensitivity of the creep damage process to the microstructural state of the material. The overall aim of this research is to improve the understanding of high-temperature deformation and failure response of Type 316H under common plant conditions in order to make realistic life predictions. This is achieved through development of micromechanical models for deformation and damage, employed within polycrystalline modelling frameworks.

An existing physically-based self-consistent model (SCM) for inelastic deformation, developed at Oxford University, captures accurately the global and grain-scale deformation response of Type 316H during short-term plasticity and creep. The model was found deficient in predicting cyclic deformation and stress relaxation. This study enhances the model by incorporating the fundamental physics of these processes. Predictions by the enhanced SCM provide insights into the evolution of deformation, microstructure and residual stress state of Type 316H under plant-relevant loading histories. The insights could inform assessment procedures in industry to more accurately account for the accumulation of inelastic strains and damage. Although

the enhanced SCM predicts the global response of the material, localization effects, which are of importance to creep damage processes, are not captured. To address this, a crystal plasticity finite element (CPFE) model was developed. It employs the same micromechanical model as the SCM and predictions of global material response by the two frameworks are in agreement. The CPFE scheme captures stress and strain localization near grain boundaries and it was further extended to describe the grain interface response. A combined CPFE-interface element framework was developed and initially used to study the effects of grain-boundary sliding on creep deformation. Results suggest that the effects of grain-boundary sliding on the macroscopic deformation of Type 316H are limited. Features of the local stress and strain fields at grain boundaries, which could affect intergranular damage response, are captured by the CPFE-interface element scheme.

A common creep damage mode in Type 316H under the operating range of interest is intergranular cavitation. Review of the literature confirmed that cavitation in Type 316H is controlled by cavity nucleation, which is not fully understood. In order to provide further insights into the physics of this process, existing strain-based empirical and stress-based (classical nucleation theory) nucleation models were modified in this study by considering experimentally-observed features of cavity nucleation in Type 316H. The models were employed locally within the developed CPFE-interface element framework. Modelling results suggest that the strain-based model as a function of local inelastic strain rate does not explain the physical nature of the nucleation process. By contrast, the modified classical nucleation theory captures both the macroscopic failure response and trends in distribution of cavities and failure in the microstructure. These findings outline key aspects of the nucleation process, which need to be examined experimentally. A number of missing features are identified in the mechanistic model, which need to be incorporated in future unified cavity nucleation theories.

Acknowledgements

Firstly, I would like to express my sincere gratitude and respect towards my academic supervisor, Prof Alan Cocks, for the invaluable support and guidance he provided me with during my doctoral studies. I deeply appreciate his constant encouragement and patience over the past three and a half years – these were essential for my achievements and success during my DPhil. It was truly a privilege to have worked with him and to be able to learn from his vast experience in the field.

The care, mental and financial support that my parents, Vesselina and Petko, provided me with during my doctoral studies mean the world to me. It was their trust and belief in me, which kept me working hard and thriving for success during this DPhil, even in the hardest of times. Words cannot express how much I appreciate their love and care. I would like to take this opportunity and dedicate this thesis to them. I am also thankful for the support that the rest of my family gave me. The support from my friends and their patience is greatly appreciated. I would like to thank my closest friends - Brianna, Daniel, Diana, Daire, Lyubomir, Mila, Sava, Simeon and Yordan – for always being there for me. I am thankful to my colleagues and friends at the department, in particular Dr Elsiddig Elmukashfi, Dr Jianan Hu, Dr Ed Tarleton, Dr Antonio Fernandez-Caballero and Dr Suchandrima Das, for their invaluable advice during my research.

I would like to express my gratitude to my sponsor, EDF Energy, for the opportunity to work on this project. Special thanks to my collaborators at EDF Energy - Dr David Dean, Dr Marc Chevalier and Dr Michael Spindler – for the invaluable guidance. I am also thankful to Prof Roger Reed and Prof Alexander Korsunsky (University of Oxford), Dr Tomas Martin, Prof Peter Flewitt (University of Bristol) and Prof David Knowles (Henry Royce Institute) for their assistance and collaboration on this project. Many thanks to Hertford College and the Department of Engineering Science at University of Oxford for offering me technical support.

CONTENTS

Chapter 1. Introduction 1
1.1. Motivation 1
1.2. Aims and objectives of research 3
1.3. Thesis structure 5
Chapter 2. Scientific background of research and review of literature 7
2.1. Inelastic deformation at high temperature 7
2.1.1. Creep deformation 8
2.1.2. Physical mechanisms of creep 9
2.1.3. Constitutive modelling of inelastic deformation 12
2.2. Stress relaxation 18
2.3. Cyclic deformation 22
2.4. Dynamic recovery of the dislocation structure 24
2.5. Existing multi-scale self-consistent model (SCM) 26
2.5.1. Micromechanical part of the SCM 28
2.5.2. Inclusion problem and polycrystalline modelling part 31
2.6. Creep fracture 34
2.6.1. Tertiary creep regime 35
2.6.2. Creep damage mechanisms in austenitic stainless steels 36
2.6.3. Intergranular creep failure in Type 316 stainless steel 37
2.6.4. Modelling intergranular creep failure 39
2.7. Summary 41
Chapter 3. Modelling of creep-cyclic deformation interactions under typical power plant operating histories 45
3.1. Introduction 45
3.1.1. Deformation response during creep-fatigue loading 45
3.1.2. Structural assessment industrial practice and conservatism 46
3.1.3. Model calibration and application 47
3.2. Modelling stress relaxation 48
3.2.1. Approach to modification of model 48
3.2.2. Effect of activation energy for thermal glide on creep and relaxation 49
3.3. Modelling cyclic deformation 53
3.4. Modelling creep-cyclic deformation interactions 55
3.4.1. Simple interactions between cyclic and creep deformation 56

3.4.2. Effects of cyclic loading on creep response 57
3.4.3. Cyclic-creep deformation histories with dwells at each cycle 63
3.5. Discussion 74
3.5.1. Enhanced version of SCM 74
3.5.2. Evolution of creep-cyclic response with internal state and residual stress 75
3.5.3. Predictive capabilities and limitations of SCM 77
3.6. Summary 79
Chapter 4. Development of crystal plasticity finite element model and comparison to SCM framework 81
4.1. Introduction 81
4.1.1. Deficiencies of SCM frameworks 81
4.1.2. Motivation for development of CPFE modelling frameworks 83
4.2. Implementation of micromechanical model into the CPFE framework 85
4.3. Comparison between SCM and CPFE frameworks 87
4.3.1. Monotonic elastic-plastic loading 87
4.3.2. Bauschinger effect during re-load upon pre-straining 92
4.3.3. Load-controlled creep response 94
4.4. Predictions using realistic 3D geometries 99
4.4.1. Selection of representative volume element (RVE) 100
4.4.2. Monotonic elastic-plastic response of realistic aggregate 101
4.4.3. Load-controlled creep response of realistic aggregate 102
4.5. Discussion 106
4.5.1. Comparing crystal plasticity approaches 106
4.5.2. Considerations on local response in vicinity of grain boundaries 108
4.6. Summary 109
Chapter 5. Modelling grain-boundary sliding during creep using a combined CPFE-interface element framework 111
5.1. Introduction 111
5.1.1. Main effects of grain-boundary sliding 111
5.1.2. Grain-boundary sliding in polycrystalline Type 316 stainless steel 112
5.2. Modelling approach and verification 114
5.2.1. Theoretical framework 114
5.2.2. Modelling of triple grain junctions during sliding 116
5.2.3. Framework verification for power-law creeping material 119
5.3. Modelling hexagonal arrays of grains via CPFE model 121

5.3.1. Effects of GBS on strain-rate and local stress fields 121
5.3.2. Importance of the triple line constraint 133
5.4. Modelling large polycrystalline aggregates via CPFE model 134
5.4.1. Variation of creep strain and influence by grain-boundary sliding 137
5.4.2. Inhomogeneity of stress field and influence by grain-boundary sliding 140
5.5. Accommodation process of sliding at intergranular particles 145
5.6. Discussion 147
5.7. Summary 151
Chapter 6. Intergranular creep failure in Type 316 stainless steel – Experimental observations and models 153
6.1. Motivation for better understanding of cavity nucleation and intergranular creep failure 153
6.2. Review of fracture behaviour of Type 316 stainless steel 154
6.2.1. Creep fracture response in solution-treated Type 316 stainless steel 154
6.2.2. Creep fracture in ex-service Type 316 stainless steel 155
6.3. Review of the effects of prior loading history, particle morphology and presence of impurities 157
6.3.1. Effect of prior history on creep failure in Type 316 stainless steel 157
6.3.2. Precipitate morphology and grain-boundary character 158
6.3.3. Observations on addition of impurity elements 159
6.4. Review of existing models for cavity nucleation 159
6.4.1. Informing the development of nucleation theories 159
6.4.2. Strain-based cavity nucleation theories 161
6.4.3. Mechanistic stress-based nucleation theories 164
6.5. Proposed modifications of existing nucleation models. Cavity growth models 171
6.5.1. Proposed local Dyson-type nucleation model 172
6.5.2. Proposed modification of classical nucleation theory – Distribution of particle strengths 172
6.5.3. Proposed modification of classical nucleation theory – Maximum stress at particles and residual stress due to prismatic loops 174
6.5.4. Diffusive cavity growth model and evolution of damage 179
6.6. Considerations on application of damage models in multi-scale modelling frameworks 180
6.6.1. Constrained cavity growth 180
6.6.2. Continuous nucleation and growth of cavities 181
6.6.3. Multi-scale polycrystalline modelling of intergranular creep failure 182
6.8. Summary 184
Chapter 7. Modelling intergranular creep failure in Type 316H stainless steel 188

7.1. Motivation 188
7.2. Modelling approach 189
7.2.1. Summary of proposed models for cavity nucleation and growth 189
7.2.2. Theoretical framework 191
7.2.3. Implementation of local cavity nucleation models 192
7.2.4. Triple grain junctions and inelastic opening of adjacent boundaries 196
7.2.5. Modelling approach 199
7.3. Modelling of bicrystals of Type 316 and Type 316H 200
7.3.1. Local Dyson-type nucleation model and diffusive growth 202
7.3.2. Classical nucleation theory with distribution of particle strengths and diffusive growth 205
7.3.3. Classical nucleation theory with a distribution of particle strengths and maximum stress at particles and diffusive growth 210
7.4. Intergranular creep failure in polycrystalline Type 316H 213
7.4.1. Local Dyson-type nucleation model and diffusive growth 214
7.4.2. Classical nucleation theory a distribution of particle strengths and maximum stress at particles and diffusive growth 217
7.5. Discussion 231
7.5.1. Suitability of examined cavity nucleation models 231
7.5.2. Missing features in mechanistic nucleation model and approach 235
7.6. Summary 237
Chapter 8. Conclusions and Future Work 240
8.1. Overall conclusions 240
8.2. Future work 242
8.2.1. Enhancement of micromechanical deformation models 242
8.2.2. Modelling of intergranular cavitation processes 243
8.2.3. Informing development of cavity nucleation models via experiments 244
References 246
Appendix A. 3D Crystal Plasticity Finite Element Framework 254
Appendix B. Interface element formulation 256
Appendix C. Triple line elements – shape functions 258
Appendix D. Implementation of nucleation and growth models in interface element framework – Flow Charts 260

Nomenclature

A	Constant
$\boldsymbol{A}$	Geometry of element (triple point constraints, sliding mode)
b	Burger's vector
$\boldsymbol{B}$	Shape function matrix (bulk element)
$\boldsymbol{B_c}$	Shape function matrix (interface element)
$\boldsymbol{B_n}$	Geometry of element (triple point constraints, opening mode)
c_{max}, c	Potential and already occupied nucleation sites
c_0, c_0^*	Equilibrium concentration of vacancies and number density of critical vacancy clusters
$c_h, \dot{c}_h$	Number density and nucleation rate of stable cavity nuclei
$\dot{c}_h^{f_v}$	Individual nucleation rate of critical clusters for a given population of $f_v(\psi')$
C_s, C_i	Constants
C_{ijkl}	Elastic stiffness matrix
$\boldsymbol{C^i}, \boldsymbol{C^a}$	Compliance matrices for isotropic matrix and anisotropic grain (SCM)
$\boldsymbol{C^{rot}}$	Stiffness matrix of anisotropic crystal in global co-ordinate system
$\mathbf{C_k}$	Interface element Jacobian matrix
d_p	Intergranular particle diameter
d_{sub}	Sub-grain boundary spacing
D	Grain size
$D_b, D_i, D_L, D_{vac}, D_c$	Grain boundary, interface, lattice, vacancy and core diffusion
$E, \Delta E$	Macroscopic total strain or Young's modulus; Macroscopic strain range
$E^c, E^{gbs}, E_{ij}^c, \dot{E}^p$	Macroscopic creep strain, grain-boundary sliding strain, creep strain tensor and macroscopic plastic strain rate
f_v^p	Volume fraction of intragranular particles
f_c	Ratio of minimum creep rates at fully- and non-hardened material state
f_d	Ratio of dwell creep strain (with prior deformation) and creep strain during equivalent dwell (without prior deformation)
$f_p(\psi'), f_v(\psi')$	Perimeter and volumetric shape factor of nucleated cavity/particle geometry
f_{VA}	Volume per unit area fraction (intergranular particles)

f_a^{GB}	Area fraction of intergranular particles
$f_h^0, f_h^c, f_h, \dot{f}_h$	Initial and critical area fraction of cavities; current area fraction of cavities and its rate
$\boldsymbol{F}$	Force vector
$\boldsymbol{F_t}, \boldsymbol{F_{t+\Delta t}}$	Deformation gradient at beginning and end of increment (CPFE)
ΔF_0	Total activation energy for thermally-activated glide (absence of external work done)
G, G_0	Shear modulus at temperature *T* and 0K
$\Delta G, \Delta G^*, \Delta G_{th}^*$	Total free energy change associated with cavity formation and height of energy barrier for cavity formation; Thermal activation energy for thermally-activated glide
$h(\psi')$	Geometrical factor (cavity geometry during growth)
$\boldsymbol{I}$	Identity matrix
j_s, j	Fitting parameters – hardening
J	Jacobian matrix (CPFE)
k	Boltzmann constant
K_n, K_t	Normal and tangential stiffness (interface element)
l_c	Interface element length
l_h	Half-spacing of cavities (cavitated particles)
L_d, L_p, L_s	Spacing of dislocation junctions, precipitates and solute dispersion atoms
ΔL_r	Fitting parameter – dynamic recovery
$\boldsymbol{L^i}, \boldsymbol{L^a}$	Stiffness matrices for isotropic matrix and anisotropic grain (SCM)
$\boldsymbol{L^p}$	Plastic part of velocity gradient (CPFE)
$\boldsymbol{L_k}$	Separation matrix (interface element)
$\dot{L}_\Delta^s, \dot{L}_{Line}^s, \dot{L}_{Line}^n$	Linear opening rate of triple point (2D) and triple line (3D) element (sliding-mode); Linear opening rate of triple line (3D) element (opening mode)
m	Exponent in empirical flow rule
$\boldsymbol{M_{Line}^t}$	Force-type quantity (triple point constraints, opening and sliding modes)
n	Creep exponent
$\boldsymbol{n}, n_i$	Unit vector in normal direction and component
$\boldsymbol{n^{(\alpha)}}$	Normal direction to slip plane
N, N_s	Number of cycles and cycles to saturation of hysteresis loop

N_p	Number density of intergranular particles
$N_0, N_{di}, \dot{N}_{di}$	Initial and current dislocation junction obstacle density along a slip plane; rate of change of obstacle density
$N_h^0, N_h, \dot{N}_h$	Initial, current number density of cavities (cavitated particles) and its rate
$N_{li}, \dot{N}_{li}$	Number density of prismatic loops and rate of change
$\boldsymbol{N}$	Shape function (interface element)
P	Penalty function
Q	Activation energy for creep
r_p, r_p^m, r_h	Intergranular and intragranular (lattice) particle radii; Radius of cavity
R	Universal Gas Constant
$\boldsymbol{R}$	Co-ordinate transformation matrix (interface element)
s_{ij}	Deviatoric stress tensor
$\boldsymbol{s}, s_i, \boldsymbol{s}^{(\alpha)}$	Unit vector in sliding (tangential) direction and component; slip direction
S_Δ^s, S_{Line}^s	Force-type quantities (triple point constraints, sliding mode)
$\boldsymbol{S^i}$	Eshelby matrix (inclusion)
t, t_c, t_{dwell}, t_f	Time, creep time, dwell time and failure time
$\boldsymbol{t_i}$	Unit vectors (interface element geometry)
T, T_m	Temperature, melting temperature
T_{nuc}	Stress driving vacancy condensation process for cavity nucleation
T_e	Local resultant traction at intergranular particles
T_n, T_{tk}	Normal traction and tangential (shear) tractions
$\boldsymbol{T}$	Co-ordinate transformation matrix (SCM)
$\boldsymbol{T_c}$	Interface traction vector
$\dot{u}_i^s, \dot{u}_i^n$	Sliding and normal local nodal displacement rates (triple point constraint)
$\boldsymbol{U}$	Nodal displacements vector
$v_s(x)$	Sliding velocity along boundary profile
$V, \dot{V}$	Volume; Volumetric growth rate of cavities
W_c	Fitting parameter – thermal recovery
$\boldsymbol{W}$	Continuum spin

$\boldsymbol{X^a}$	Intragranular Type II residual stress vector (SCM)
Z^*	Zeldovitch factor for dissolution of supercritical nuclei
$\alpha_0, \alpha_d, \alpha_p, \alpha_s$	Overall obstacle effectiveness; dislocation junction, precipitate, solute strength coefficients
α'	Nucleation constant (Dyson-type model)
α_n, α_t	Parameters for coupling between tangential (shear) and normal tractions
α^p, β^p	Parameter groupings – reference inelastic sliding rate
$\alpha_\Delta, \beta_\Delta, \gamma_\Delta$	Angles of triple point reference geometry
β_I	Angle of maximum principal stress direction with respect to boundary plane
β^*	Vacancy absorption rate of cavity nuclei
γ, γ_s	Resolved shear strain; Surface energy per lattice unit area
$\dot{\gamma}^{(\alpha)}, \dot{\gamma}^{max}$	Resolved shear strain rate on a slip system; Maximum resolved shear strain rate in vicinity of grain boundary
$\dot{\gamma}_0$	Reference resolved shear strain rate
Γ^*	Fraction of total deformation due to grain-boundary sliding
δ_b	Grain-boundary thickness
$\dot{\delta}_n, \dot{\delta}_n^e, \dot{\delta}_n^c$	Total, elastic and creep separation rates (normal)
$\dot{\delta}_t, \dot{\delta}_t^e, \dot{\delta}_t^c$	Total, elastic and creep separation rates (shear)
$\dot{\delta}_{0t}$	Reference inelastic sliding rate
$\boldsymbol{\delta}$	Total interface separation vector
$\varepsilon^t, \varepsilon^e, \varepsilon^p, \varepsilon^c, \varepsilon^{ine}$	Total, elastic, plastic, creep and inelastic strain
$\boldsymbol{\varepsilon^i}, \boldsymbol{\varepsilon^{ti}}$	Isotropic inclusion total and misfit strain vectors
$\boldsymbol{\varepsilon^{t*}}, \boldsymbol{\varepsilon^{ta}}$	Vectors for selected misfit strain in homogeneous inclusion and real misfit strain in anisotropic grain (SCM)
$\boldsymbol{\varepsilon^a}$	Anisotropic total strain vector (SCM)
$\dot{\varepsilon}_{ij}^c, \dot{\varepsilon}^p, \dot{\varepsilon}^c, \dot{\varepsilon}^{ss}, \dot{\varepsilon}_0$	Creep strain rate tensor, plastic, creep and minimum strain rates; reference strain rate
$\boldsymbol{\varepsilon}, \boldsymbol{\varepsilon^e}, \boldsymbol{\varepsilon^p}$	Matrices of total, elastic and plastic strain (CPFE)
$\theta_{\Delta i}, \theta_{GB}$	Angle of unit vector in global co-ordinate system (triple point constraint) and orientation of grain-boundary to load axis
κ	Angle of resultant traction orientation with respect to boundary plane
λ_p	Intergranular particle spacing

Λ	Diffusive length
μ	Mean of log-normal distribution of $f_v(\psi')$
μ_p	Angle at tip of intergranular particle
μ_0	Chemical potential
v	Poisson's ratio
ρ, ρ^*	Radius of curvature of cavity nuclei and critical nuclei
ρ_d	Dislocation density
σ_e, σ_{ij}	Von Mises stress; Stress tensor
$\sigma_H, \sigma_I, \sigma_0$	Hydrostatic stress; Local maximum principal stress; Reference stress
$\boldsymbol{\sigma^a}$	Anisotropic inclusion stress vector (SCM)
$\tilde{\sigma}$	Standard deviation of log-normal distribution of $f_v(\psi')$
$\boldsymbol{\sigma}, \boldsymbol{\sigma_{trial}}, \boldsymbol{\sigma_t}, \boldsymbol{\sigma_{t+\Delta t}}$	Matrices of stress, trial stress, stress at the beginning and at the end of the increment (CPFE)
$\Sigma, \Sigma_{ij}, \Sigma_0, \Sigma_{dwell}, \Sigma_{sat}$	Macroscopic stress and macroscopic stress tensor; Macroscopic initial stress, macroscopic dwell stress and saturated stress (hysteresis loop)
$\widetilde{\boldsymbol{\Sigma}}$	Residual stress-term (CPFE)
$\tau^{(\alpha)}, \tau_{cr}^{(\alpha)}$	Resolved shear stress; Internal resistance along slip system
τ_d, τ_p, τ_s	Internal resistance - dislocation, precipitates, solutes
$\bar{\tau}_m^r, \bar{\tau}_p^r$	Type III residual stress due to prismatic loops – lattice (m) and intragranular particles (p)
$\tau^*, \bar{\tau}_p^{GB}$	Maximum local stress at intergranular particles; Type III residual stress due to prismatic loops - intergranular particles (GB)
Φ_0	Ratio of deformation rates of the grains and grain boundaries
Φ_c	Angle at cavity/particle interface
ψ', ψ_c	Dihedral angle of nucleated cavity/particle geometry; Angle at tip of cavity
$\boldsymbol{\Psi}$	Residual stress vector
Ω	Atomic volume

CHAPTER 1

INTRODUCTION

1.1. MOTIVATION

Life estimation approaches of components, operating at high temperatures, across power-generation and aerospace applications are often based on simplistic empirical models for deformation and damage development in materials. The need to move away from curve-fitting of empirical models is widely recognised. This is for the purpose of allowing more accurate predictions of deformation and failure of structural materials across these industries. This need is amplified by the requirement for life extension of existing nuclear power plants across the world. Life extension of nuclear power-generating assets is motivated by economic factors, such as revenue generation from existing plants before the introduction of new plants, and environmental reasons - the need for sustained generation of low-CO_2 electrical power by using alternatives to fossil fuels.

At present, the electricity baseload capacity in the UK is generated from the Generation II nuclear Advanced Gas-cooled Reactors (AGR), which are approaching their design life of 40 years. The operator of these plants, EDF Energy, is currently seeking to extend the life of AGR power stations until the construction of their replacement fleet, the Generation III+ EPR nuclear plants, is complete. The operating conditions of AGR nuclear plants give rise to complex thermo-mechanical deformation histories within components. One of the prominent life-limiting issues in plant components is the time-dependent, inelastic deformation at prolonged exposures of load and elevated temperatures, known as creep. Excessive inelastic deformation and subsequent crack

formation during creep can result in unexpected component failures [1] and unplanned closure of nuclear plants.

An immediate problem that EDF Energy are facing, is associated with predicting the high-temperature deformation and damage response of austenitic Type 316H stainless steel, used mainly in the boiler section of AGR power plants (Fig. 1.1). Boiler components operate at temperatures in the range 470-650°C and stresses of the order of 10-300 MPa [2], where high-temperature creep and cyclic plasticity alter the microstructural state and failure response of the material.

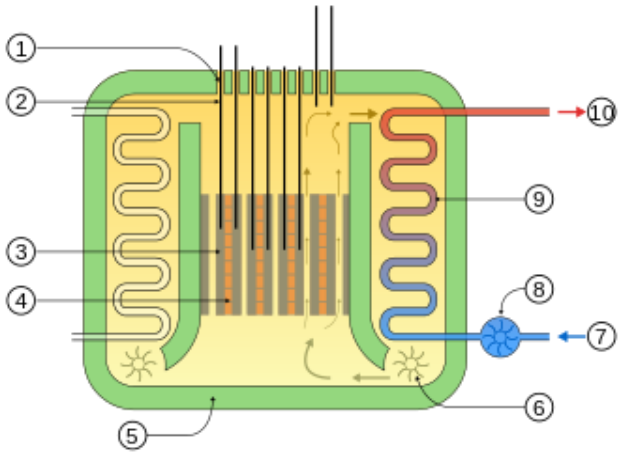


Figure 1.1. Schematic of an advanced gas-cooled nuclear reactor: 1. Charge tubes 2. Control rods 3. Graphite moderator 4. Fuel assemblies 5. Concrete pressure vessel and radiation shielding 6. Gas circulator 7. Water 8. Water circulator 9. Heat exchanger 10. Steam. Adopted from Messer Woland.

Simplistic empirical models, such as those within the R66 AGR Materials Data Handbook [3] and RCC-MR design codes (e.g. [4]) are derived from fits to uniaxial data across a range of different material casts. These models are adopted by EDF Energy to interpret and predict the deformation response of the material. Predictions via these simplistic models can be in poor agreement with experimental or plant-recorded material response under creep-cyclic deformation histories. Strain-based "ductility-exhaustion" models are employed within damage assessment procedures, such as the R5 procedure [5], employed by EDF Energy. Complications arise in

damage assessments via models based on accumulated inelastic strains. This is because such approaches are dependent on the accurate prediction of inelastic deformation response and do not capture the sensitivity of the creep damage process to changes in the microstructural state of the material. The inaccuracy of those simplistic life estimation models makes structural-assessment procedures overly-conservative.

More accurate predictions require an improved understanding of the creep deformation and failure mechanisms in Type 316H. Detailed experimental studies, replicating plant-relevant deformation histories, can be used to calibrate empirical models. However, that approach is not feasible due to the inherit cost and long duration. In order to understand better the high-temperature response of the material and provide guidelines for improvement of existing deformation models and damage assessment approaches in industry, mechanistic models are needed. Such models can capture the essential physical processes of creep deformation and damage development.

1.2. AIMS AND OBJECTIVES OF RESEARCH

A recent project was undertaken by Hu [6] at Oxford University to develop physical models of the inelastic deformation of polycrystalline 316H under the operating conditions of interest to EDF Energy. The state-variables in this multi-scale polycrystalline model are the spacings between types of obstacles to dislocation motion, such as dislocation junctions, precipitates and solute atoms. Model predictions agree well with experimental data under monotonic elastic-plastic and creep deformation of ex-service (EX) and solution treated (SA) material [7,8]. However, there is a necessity for better understanding of the mechanisms behind displacement-controlled creep (stress relaxation) and its relationship to load-controlled creep. Understanding high-temperature cyclic and combined cyclic-creep deformation is also of interest to be able to better simulate the regular shutdown and start-up of plant. The creep damage initiation process, associated with

nucleation and growth of cavities, is sensitive to the microstructural state of the material. Better understanding of this cavitation process is required for the improvement of existing damage models. None of these aspects are captured in the existing modelling framework developed in [6].

The detailed objectives of this study are summarized below:

- Review deformation mechanisms during cyclic deformation and stress relaxation. Identify approaches to enhance the existing SCM in capturing these deformation modes. Assess its ability to predict the observed experimental response during cyclic-creep interactions in Type 316H stainless steel under plant-relevant deformation histories.
- Develop a crystal plasticity finite element (CPFE) model for polycrystalline materials which captures the inelastic response of anisotropic grains using the enhanced micromechanical model. Employ the framework to verify the predictions of the SCM model.
- Enhance the CPFE model to include grain-boundary sliding by developing interface elements for the sliding process. Explore how grain-boundary sliding influences the stress distribution within polycrystalline Type 316 and the macroscopic creep response of the alloy.
- Review experimental observations of intergranular creep fracture in Type 316/316H stainless steels and existing cavitation models. Identify suitable models to describe the cavitation process. Modify the existing models to capture important features of the microstructure and local deformation processes that affect the cavity nucleation response.
- Employ the modified micromechanical damage models within the developed polycrystalline CPFE-interface element model framework. Evaluate the sensitivity of intergranular creep cavitation and failure to the assumed models and deformation response in Type 316H. Identify key aspects to be considered in the further development of cavity nucleation theories in future research.

This study aims to describe the full scope of inelastic deformation and damage development processes in Type 316H stainless steel in the operating range of interest. This will provide guidelines for i) improvement of the simplified deformation models used in industry, and ii) development of a unified mechanistic model for creep cavitation.

1.3. THESIS STRUCTURE

Chapter 2 reviews the general literature on constitutive modelling of inelastic deformation. The self-consistent modelling framework and associated micromechanical models developed by Hu [6] are summarized. The deformation mechanisms during stress relaxation and cyclic loading are reviewed and approaches to enhance the existing framework in predicting these two deformation modes are identified. A brief introduction to creep damage mechanisms in Type 316 stainless steel and the motivation for improvement of existing intergranular cavitation models are given.

Chapter 3 extends the micromechanical model, employed in the SCM, to model arbitrary combinations of cyclic deformation, creep and stress relaxation. The framework is then used to explore creep-cyclic interactions in Type 316H with a focus on the effects of i) prior cyclic deformation on subsequent creep response and ii) displacement- and load-controlled creep dwells during each cycle on saturation of the hysteresis loops. Guidelines for improvement of models, used in the existing assessment procedure, are presented and limitations of the SCM are discussed.

Chapter 4 develops a polycrystalline CPFE framework in which the enhanced micromechanical model is implemented. Comparison between predictions of monotonic elastic-plastic and creep deformation using the SCM, described in Chapter 3, and the CPFE framework are presented. Macroscopic model predictions are shown to be in agreement with each other and with experimental data, thus providing confidence in the two approaches. The CPFE framework

captures additional local features of the deformation response. The need to extend this framework to capture grain-boundary sliding and intergranular damage development is identified.

Chapter 5 extends the CPFE framework from Chapter 4 by incorporating interface elements along grain-boundary regions of the polycrystalline model, capturing the inelastic response of the boundaries. The framework is employed to study the contribution of sliding to the overall deformation and changes in stress fields as a result of sliding. Stresses along transverse boundaries are examined in terms of the crystallographic orientations of neighbouring grains. The influence of grain-boundary particles on sliding and their effectiveness in inhibiting sliding is assessed.

Chapter 6 reviews intergranular creep failure in Type 316/316H stainless steels, with focus on models for cavity nucleation. Physical modifications of the classical nucleation theory [9] are introduced to account for distributions of intergranular particles with different strengths, as well as stress concentrations and dislocation structures near particles. A local strain-based [10] nucleation model is also introduced. Models for diffusive growth and the motivation for extending the multi-scale framework from Chapter 5 to model intergranular creep failure are presented.

Chapter 7 implements the modified cavity nucleation and growth models within the CPFE-interface framework, described in Chapter 5. The framework is used to simulate bicrystal and polycrystalline geometries with the aim of probing the sensitivity of the predicted response to the details of the assumed nucleation model. Model predictions reveal important aspects of the cavitation process and help identify missing features in the mechanistic nucleation model.

Chapter 8 summarizes the major findings from this study, proposes directions for future work and provides guidelines for i) future experimental studies and ii) how these can be used to aid the development of improved models of the cavitation process.

CHAPTER 2

SCIENTIFIC BACKGROUND OF RESEARCH AND REVIEW OF LITERATURE

2.1. INELASTIC DEFORMATION AT HIGH TEMPERATURE

During operation of high-temperature power plants, complex cyclic-creep deformation histories arise during which the subsequent creep response of the material is altered. A number of damage assessment procedures used in industry, e.g. R5 procedure [11] used by EDF Energy, employ ductility-exhaustion models [12] to estimate remaining life in structures. The motivation for strain-based approaches stems from the finding that empirical strain-based model predictions lay closer to experimental data for ex-service Type 316H [13]. However, employing empirical models for deformation and damage cannot fully reproduce the response of the material across the full range of loading histories [14]. This poses the requirement for developing physically-based models for deformation and damage to better understand the creep response of the material and provide guidelines for improving the existing approaches in industry. An existing multi-scale physically-informed model for inelastic deformation of Type 316H, developed by Hu and Cocks [7,8], is reviewed in this chapter. The limitations of the existing framework to model cyclic deformation and stress relaxation are addressed and approaches to enhance the model in capturing these deformation modes are identified. A brief overview of the creep damage process in Type 316H is also given. The problem of modelling cavity nucleation during intergranular creep failure is introduced here. Note that Chapter 6 will review in detail the intergranular cavitation response of the material, and identify suitable models and assumptions, which will be employed in Chapter 7.

2.1.1. Creep deformation

Creep is a time-dependent permanent deformation that occurs in metals when subjected to constant stress at temperatures T>0.4 of their melting temperature, T_m. Similar to short-term plasticity, creep is an incompressible process, however, it can take place at stress levels below the yield strength of the material [15]. The total strain generated during creep deformation can be split into elastic, time-independent plastic and creep strain. The latter two are usually combined into an inelastic component as $\varepsilon_{ij}^{t} = \varepsilon_{ij}^{e} + \varepsilon_{ij}^{p} + \varepsilon_{ij}^{c} = \varepsilon_{ij}^{e} + \varepsilon_{ij}^{ine}$, where the elastic strain is $\varepsilon_{ij}^{e} = L_{ijkl}\sigma_{kl}$ and L_{ijkl} is the elastic compliance tensor. The creep strain rate in continuum plasticity is usually expressed in terms of the effective strain rate and stress, $\dot{\varepsilon}_e$ and σ_e, and deviatoric stresses, s_{ij} [15,16]:

$$\dot{\varepsilon}_{ij}^{c} = (3/2)\dot{\varepsilon}_e \left(s_{ij} / \sigma_e \right) \tag{2.1}$$

Eq. 2.1. is integrated to obtain the accumulated creep strain in multi-axial form. A typical creep curve for a uniaxially-loaded sample under constant stress is shown in Fig. 2.1.

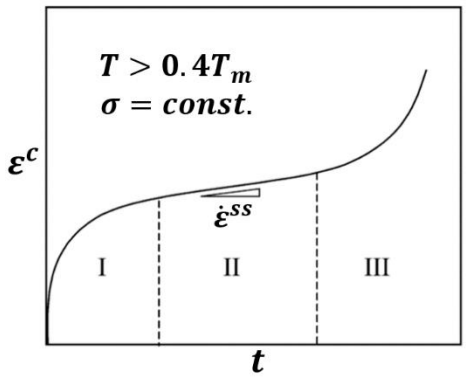


Figure 2.1. Schematic of a creep curve – primary (I), secondary (II) and tertiary (III) regimes, from [17].

Three different stages can be identified, namely primary, secondary and tertiary. During the primary regime, the strain rate gradually decreases towards the secondary regime, where a

minimum strain rate, $\dot{\varepsilon}^{ss}$, is reached. Damage eventually develops in the material and accumulates during the tertiary regime until final fracture occurs [17].

2.1.2. Physical mechanisms of creep

2.1.2.1. General phenomenology

Creep is driven by diffusional flow at lower stress and dislocation glide/climb motion at higher stress (>$10^{-3}G$) [15]. The available experimental creep data at EDF Energy are in the high stress regime [6], hence, only dislocation-controlled creep deformation is considered here. As described in Section 2.1.1, prior to damage formation in the tertiary regime, only primary and secondary regimes are associated with accumulation of creep strain. Numerous studies focus their attention on the secondary creep regime, since this stage dominates the creep response [15]. In ex-service Type 316, the secondary stage creep rate is generally found to be independent of the material state evolution and is expressed solely as a function of stress and temperature [18]. Classical approaches describe the dislocation-controlled secondary creep under the assumption that dislocations re-arrange in cell-like structures and dislocation climb occurs via either lattice or dislocation core diffusion [19]. Such a creep mechanism leads to a steady-state power-law creep rate:

$$\dot{\varepsilon}_{ij}^{ss} = A\sigma_e^n \exp\left(-Q/RT\right)\left(3s_{ij}/2\sigma_e\right) \tag{2.2}$$

where n = 3~10, A is a constant, Q is the activation energy and R is the universal gas constant. At higher stresses, a transition from dislocation climb- to glide-controlled creep is identified [20] and Eq. 2.2 is modified by a *sinh* function to capture the accelerated creep response. By contrast, the decreasing creep rate during primary creep suggests that primary creep is a function of stress, temperature and evolution of material state. The latter can be described through a set of state variables. Empirical laws, similar to Eq. 2.2, have been used in the literature to predict the primary

creep rate [21] with the state variables being either time or strain. As will be demonstrated in Chapter 3, such simplistic creep models do not fully capture the deformation response under high-temperature plant loading histories. Therefore, they lead to incorrect predictions of creep deformation when the response from laboratory conditions is extrapolated to plant-relevant scenarios [22]. This poses the requirement for the development of physically-informed state-variable models for inelastic deformation. Such approaches, which capture the evolution of internal state during inelastic deformation, e.g. competition between hardening and softening during primary creep, are described in Sections 2.1.3 and 2.5. Before discussing these, it is worth reviewing the strengthening and softening effects in ex-service Type 316H stainless steel.

2.1.2.2. Strengthening and softening effects

The strengthening and softening mechanisms, associated with dislocation-controlled inelastic deformation, in ex-service Type 316H stainless steel are briefly reviewed here. A detailed review of these and discussion on additional mechanisms in solution-treated material are found in [6].

a) Strengthening mechanisms

The strengthening mechanisms refer to the various contributions to internal resistance to dislocation motion. The most dominant strengthening mechanism in Type 316 is the refinement of the dislocation structure [23]. Lattice dislocations constitute 3D forest-like arrangements in which dislocations intersect slip planes [23,24]. Such dislocation intersections or junctions act as obstacles to mobile dislocations, see Fig. 2.2.a). Entanglement of mobile dislocations with the forest structure refines the network (i.e. hardening) and generates more dislocation obstacles.

Alloying is a strengthening approach, responsible for the presence of finely dispersed solute atoms in the lattice. Substitutional (e.g. *Cr*, *Ni*) and interstitial (e.g. *C*) solute atoms in Type 316

act as obstacles to dislocation motion (Fig. 2.2.b) [25,26]. Solute atoms generate local stress fields in the lattice, which cause either repulsion or attraction of mobile dislocations by the solutes. This contributes to the internal resistance of dislocation motion in the material. On the other hand, long exposures at high temperatures cause thermal aging. The solutes come out of solution and precipitation of second-phase particles is induced in the lattice. Discrete particles of different compositions (mainly $M_{23}C_6$ carbides) form in Type 316 [26]. The particles strengthen the material since dislocations are entrapped by and bow around them (Fig. 2.2.c). Localised dislocation structures, e.g. Orowan and prismatic loops, form in the vicinity of second-phase particles as dislocations bypass them, providing additional obstacles. The degree of strengthening in the lattice depends on the distribution of obstacles along slip planes, where closely-spaced obstacles are more effective in impeding dislocation motion [27]. Note also that at high temperatures, the thermal activation energy provided assists the glide of mobile dislocation over obstacles [28].

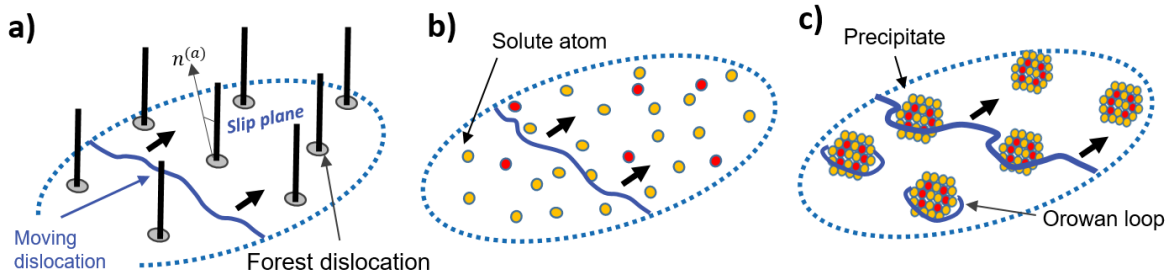


Figure. 2.2. Schematic of a) forest dislocation junction, b) solute atom and c) precipitate obstacles to dislocation motion, identified in all grades of Type 316 stainless steel in [6].

b) Softening mechanisms

The softening mechanisms in Type 316 are associated with reduction of the strengthening effects described above. In ex-service material, softening is associated with rearrangement of the dislocation structure to lower energy configurations. At high temperature, dislocation climb, for

which the rate-controlling process is the diffusional transport from one site to another via lattice or core diffusion, causes dislocation segments from Fig. 2.2.a) to move out of their slip planes. The process is termed thermal or static recovery and acts to increase the spacing between forest junctions, thereby reducing the number of obstacles to mobile dislocations [29]. On the other hand, the probability of opposite-sign dislocation annihilation along slip planes increases in refined forest networks. This process is dominant under cyclic deformation, where dislocations of opposite signs are readily generated. The annihilation process cancels out dislocation links of opposite signs, thereby increasing the spacing of dislocation junctions and attenuating their strengthening effect. This is discussed further in Section 2.4. It is worth noting that during thermal aging of solution-treated (ST) material, the formation and growth of precipitates depletes the lattice of solute atoms, reducing their contribution to internal resistance. This is not considered here since this study is limited to ex-service material, where phase transformations are slow enough to be ignored.

From a mechanistic point of view, inelastic deformation is associated with dislocation motion over distributions of obstacles. The obstacle strength is associated with the required shear stress exerted on a dislocation segment to break away from a pair of obstacles [27], taking the form of $\tau \propto \alpha_i \left(Gb / \lambda_d \right)$ where G is the shear modulus, b is the Burgers vector, λ_d is the segment length between the obstacles, and α_i is a function of the bowed dislocation configuration. This suggests that a sensible choice of a physical state variable would be the obstacle spacing [6].

2.1.3. Constitutive modelling of inelastic deformation

Theory and experiments have confirmed that the decreasing strain rate during primary stage creep is related to the i) evolution of residual stresses and ii) competition between entanglement of dislocations, resulting in hardening and static recovery of the dislocation network [8,16,30].

During secondary creep, an equilibrium between hardening and softening is reached, resulting in the nearly constant strain rate. Since changes in internal material state occur during primary creep, state variables are often introduced [31] to describe the strain rate as $\dot{\varepsilon}_{ij} = f(\sigma_{ij}, T, S_k)$ where the variable, S_k, can evolve as a function of stress, temperature, current state, time, etc. according to $\dot{S}_k = g(\sigma_{ij}, T, S_k, t, ...)$. This concept has been used in a number of continuum plasticity empirical and phenomenological models for creep, based on the evolution of internal resistance to dislocation motion and internal stress, e.g. [31]. However, under complex loading histories, such models generally require a large number of fitting parameters to produce accurate predictions. Several such models are reviewed in the following section. Models adopting state variables, which represent the evolution of internal damage during tertiary creep, are discussed in Chapter 6.

2.1.3.1. Brief overview of constitutive modelling approaches

Phenomenological models for inelastic deformation assume a yield surface, which separates the elastic and inelastic regions in stress space. One such model is the Chaboche-Lemaitre model [32], where the size and positioning of the yield surface is determined by the isotropic and kinematic contributions to hardening (see Fig. 2.3). These contributions are associated with the evolution of internal resistance and internal stress, respectively.

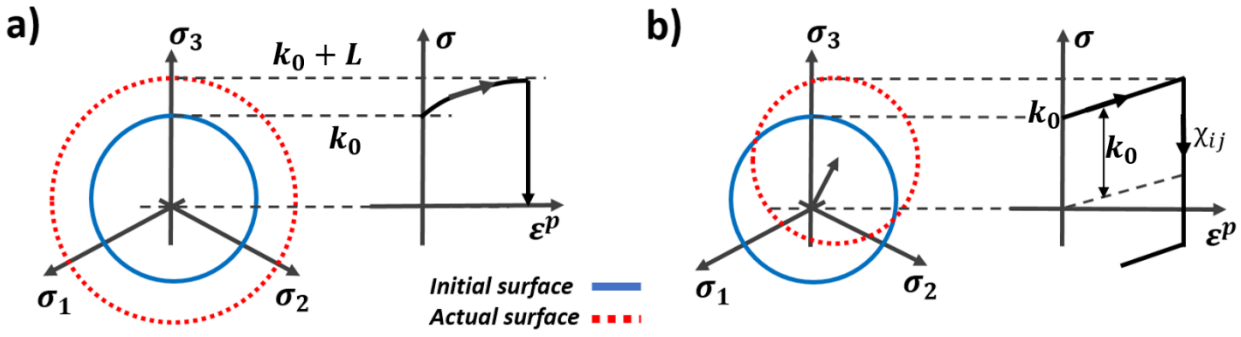


Figure 2.3. Schematic of yield surface evolution in a) isotropic and b) linear kinematic hardening, looking down the π-axis in stress space (left) and stress versus plastic strain response (right), respectively.

A yield criterion, which defines inelastic deformation for $f > 0$, is given by

$$f = \sqrt{\frac{3}{2}(s_{ij} - \chi_{ij})(s_{ij} - \chi_{ij})} - L - k_0 \tag{2.3}$$

where k_0 is the initial size of yield surface, $L+k_0$ is the current size. The evolution of the instantaneous position of the yield surface centre is defined by

$$\dot{\chi}_{ij} = \frac{2}{3} C_1 \dot{\varepsilon}_{ij}^p - C_2 \chi_{ij} \dot{p} \tag{2.4}$$

where C_i are constants determined from uniaxial tests. In this model, the inelastic strain rate is expressed by a flow-rule $\dot{\varepsilon}_{ij}^p = \dot{p}\left(\partial f / \partial \sigma_{ij}\right)$. The viscoplastic multiplier $\dot{p}$ is given by $\dot{p} = (f / D)^n$, where D is a drag stress term, $D(\varepsilon_e^p) = k_0 + wL(\varepsilon_e^p)$, scaling with the evolution of L. As an example, during cyclic deformation the increase of yield surface size is expressed in terms of hardening and dynamic recovery as $\dot{L} = b(Q - L)\dot{\varepsilon}_e^p$ [33], where w, b and Q are free parameters. The model can include a series of isotropic, kinematic and recovery terms to capture cyclic and creep deformation. However, incorporating additional variables in order to optimize fitting of experimental data does not improve the understanding of the physical processes of deformation.

A similar model by Basoalto and Dyson [34] for precipitation-hardened alloys expresses the viscoplastic multiplier function by combining an Arrhenius law with a hyperbolic sine function of the yield criterion and a drag stress:

$$\dot{p} = A \exp\left(-\frac{Q}{RT}\right) \sinh\left(\sqrt{\frac{3}{2}(s_{ij} - \chi_{ij})(s_{ij} - \chi_{ij})} / D\right)^n \tag{2.5}$$

The drag stress D consists of the contributions to internal resistance from the dislocation cell-structure (σ_d) and precipitation bypassing (σ_p) hardening mechanisms, $D = \sqrt{\sigma_d^2 + \sigma_p^2}$. The

model puts emphasis on the strengthening from precipitation hardening and has been successfully applied to nickel-based superalloys. However, the model does not accurately represent the deformation behaviour of Type 316 stainless steel [34] due to the low volume fraction of intragranular precipitates in the latter. Other phenomenological models developed by Miller and co-workers, e.g. [35], describe the viscoplastic deformation as a function of dislocation interactions with solute atmospheres in the lattice. However, their model is difficult to apply to the deformation response of alloys under complex loading histories due to the large number of fitting parameters, the complexity of equations and the lack of a generalisation to multiaxial stress states.

The empirical nature of the above-mentioned models motivated the development of viscoplastic models, in which the drag stress is associated with the evolution of material state. As described in Section 2.1.2, the dislocation density ρ_d evolves during inelastic deformation, associated with both hardening and softening of the microstructure. The internal resistance can be expressed as $\sigma_d(\rho_d)$, where ρ_d is the state-variable. Physically-informed models have been developed in the literature, such as that introduced by Kocks and co-workers [36–38] and extended by Balke and Estrin [39]. This model captures the hardening and dynamic recovery of the dislocation structure during inelastic deformation based on the evolution of ρ_d. The model assumes that an increment in effective plastic strain $d\varepsilon_e^p$ produces a change in ρ_d:

$$d\rho_d / d\varepsilon_e^p = C_1 \rho_d^{1/2} - C_2 \rho_d \tag{2.6}$$

where C_i are free parameters. The model was enhanced by Lagneborg [30] to describe the decrease of dislocation density due to thermal recovery by considering the thermal mobility, M, and line tension, T_d, of dislocations:

$$d\rho_d / dt = -2MT_d \rho_d^2 \tag{2.7}$$

By accounting for the mean over all grain orientations in the polycrystal through a Taylor factor [36], $\bar{K}$, the on-average internal resistance from dislocation junctions, σ_d, is obtained as:

$$\sigma_d = \alpha_d \bar{K} G b \sqrt{\rho_d} \tag{2.8}$$

where α_d is a dimensionless parameter describing the average strength of dislocation, after Foreman and Makin [40]. The evolution of internal resistance in Eq. 2.8 is described by Eqs. 2.6-2.7. Different forms of the viscoplastic function $\dot{p}$ can then be assumed to define the inelastic strain rate as a function of the internal resistance σ_d and the applied stress [36,41]. But the continuum plasticity models, described in this section, are simplified functions predicting general trends in response. Such models do not capture the detailed physics behind the deformation behaviour of real polycrystalline materials. Furthermore, continuum plasticity does not take into account the local interactions between anisotropic crystals which has been observed to affect the macroscopic response [42]. A crystal plasticity framework, the theory behind which is briefly reviewed in the following section, is required to do this [43].

2.1.3.2. Crystal plasticity

Deformation of polycrystals is dependent on interactions between the individual grains, comprising the aggregate. Crystal plasticity allows for the determination of inelastic strain rate in each crystal by considering the slip rate on individual slip systems. In face-centred cubic (FCC) materials, such as Type 316 stainless steel, 12 systems are formed from the four slip planes $\mathbf{n}^{(\alpha)}(n_1^{(\alpha)}, n_2^{(\alpha)}, n_3^{(\alpha)})$ and three slip directions $\mathbf{s}^{(\alpha)}(s_1^{(\alpha)}, s_2^{(\alpha)}, s_3^{(\alpha)})$ [27]. The plastic strain rate in every grain can be obtained by summing the contributions from each slip system, α [44,45]:

$$\dot{\boldsymbol{\varepsilon}}^{\mathbf{p}} = \sum_{\alpha}^{12} sym\left(\mathbf{n}^{(\alpha)} \otimes \mathbf{s}^{(\alpha)}\right)\dot{\gamma}^{(\alpha)} \tag{2.9}$$

where the bolded terms signify a tensor. The term $\mathrm{sym}\left(\mathbf{n}^{(\alpha)} \otimes \mathbf{s}^{(\alpha)}\right)$ represents the Schmid factor – the symmetric part of the direct vector product of the slip plane normal and slip direction of the system (see Fig. 2.4) [46]. Physical models for the flow rule describing the evolution of shear strain rate generally take the form [28]:

$$\dot{\gamma}^{(\alpha)} = \dot{\gamma}_0 . g\left(\Delta G_{th}^{*}, T, \tau^{(\alpha)}, \tau_{cr}^{(\alpha)}\right) \tag{2.10}$$

Eq. 2.10 describes the shear strain rate $\dot{\gamma}$ as a function of ΔG_{th}^{*} - the required thermal activation energy to allow the system to plastically deform - and $\tau^{(\alpha)}$ and $\tau_{cr}^{(\alpha)}$ being the resolved and critical resolved shear stress on a slip system [47]. The resolved shear stress on a system is obtained through the Schmid factor as a function of the grain stress according to

$$\tau^{(\alpha)} = \left[sym\left(\mathbf{n}^{(\alpha)} \otimes \mathbf{s}^{(\alpha)}\right)\right]^{T} \boldsymbol{\sigma}^{\mathbf{a}} \tag{2.11}$$

where $\boldsymbol{\sigma}^{\mathbf{a}}$ is the stress vector in an anisotropic grain in its local coordinate system. It should be noted that use of rate-dependent flow rule models allows for automatic selection of active slip systems [44] - a type of selection difficult to achieve with rate-independent models [48,49].

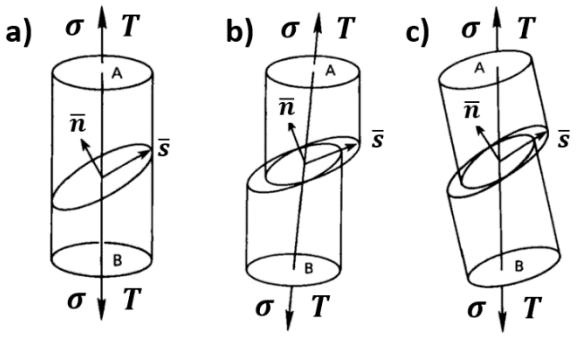


Figure 2.4. Schematic of a) undeformed crystal undergoing b) slip. Rigid rotation is caused in c) [45].

Note that mechanistic deformation models can be applied at the grain scale within a multi-scale crystal plasticity framework allowing the physical effects of microscopic deformation

processes on the global response to be assessed. These observations demonstrate that mechanistic physical models of dislocation-obstacle interactions within multi-scale crystal plasticity models could provide a more detailed description of deformation behaviour. This can offer the potential of accurate predictions of the material behaviour under complex thermo-mechanical loading histories. The dislocation density-based mechanistic models, described in the previous section, have provided the physical basis and motivation for development of the multi-scale crystal plasticity self-consistent model (SCM) developed by Hu and Cocks [7,8] and its further development as part of this project. This SCM is summarised in Section 2.5. Previous studies [7,8,50] have shown that the SCM accurately predicts mesoscopic lattice strains and macroscopic deformation under monotonic elastic-plastic deformation and creep of ex-service (EX) and solution-treated (ST) 316H stainless steel. However, as identified in [6], the model in its current form is unable to i) simulate cyclic deformation and ii) correctly predict stress relaxation during a displacement-controlled dwell using parameters calibrated to load-control creep data. The following sections review these deformation modes. This helps identify methods for modelling stress relaxation and cyclic deformation, as well as approaches to enhance the SCM in capturing these deformation modes. The treatment of crystal plasticity here is consistent with small-deformation theory, since the SCM is built within a framework where lattice rotations are ignored. Chapter 4 will demonstrate that predictions via the small-deformation SCM are consistent with those from a large-deformation crystal plasticity finite element (CPFE) model for levels of strain experienced in plant components, within which the same micromechanical model is incorporated.

2.2. STRESS RELAXATION

Many components in power-generating plants are subjected to displacement-controlled creep deformation, essentially resulting in creep at constant strain rather than stress [18]. At constant

total strain, i.e. $\dot{\varepsilon}^t = 0$, relaxation of stress occurs due to accumulation of creep strain and a concomitant reduction of elastic strain, illustrated in Fig. 2.5.a-b). A major focus in recent years has been the prediction of relaxation behaviour from forward creep (creep at constant stress) models. Expressions for minimum creep strain rate are usually integrated [51–53] to express stress as a function of time. However, such simplistic approaches usually underestimate the extent of stress relaxation. Accurate predictions are often achieved by using creep models with a large number of fitting parameters [42,54] or "back stress" terms (e.g. $(\sigma - \sigma_{back})^n$), whose physical origin is not yet fully understood [52,55,56]. Predicting relaxation of Type 316H stainless steel from forward creep has mainly been carried out through the RCC-MR equations by the power generation industry [52]. Accurate predictions using such empirical models for creep are possible (Fig. 2.5.c), but this normally requires fitting the model to relaxation rather than creep data, and does not aid the physical understanding of the relationship between forward creep and relaxation.

Models often assume an internal stress term, which attempts to describe the internal friction in the lattice during deformation. One such phenomenological model used in [4] combines a model proposed by Feltham [53] with a "back-stress" term. The predictions agree well with experimental data for Type 316H at 550°C. The selected value of the back-stress term, however, is arbitrary. Other more successful attempts approach the problem by splitting the initial rapid decrease of stress, relating it to short-term high-temperature plasticity, from the long-term steady-state stress drop [57]. The observations of a two-stage relaxation process agree with the description of initial transient relaxation behaviour given by Hart and Solomon [58]. Larger amounts of relaxed stress at a higher constant strain were recorded during the transient period of a relaxation test [18]. Similar observations were made during low cycle fatigue (LCF) tests on Type 316 stainless steel between 500°C and 650°C [59]. In those tests, it was observed that the higher the amplitude of the

initial strain at the start of a dwell, the larger the amount of stress relaxation during the transient period. These observations propose that the initial stages of relaxation during creep in Type 316 over the temperature range of interest are controlled by thermally-activated glide of mobile dislocations. This further suggests that the physical description of dislocation glide and the evolution of the microstructure should be considered separately. By contrast, the long-term creep part of stress relaxation has been associated with thermal recovery of the dislocation structure [56] at high temperature with the rate-controlling mechanism being dislocation climb [29,60]. These observations lead to the conclusion that micromechanical models, which capture the effects of both thermally-activated glide and climb-controlled recovery should be considered in modelling stress relaxation in the material of interest. It is important to note that, in Type 316 stainless steel, the creep-controlling mechanisms in the temperature range between 500-650°C can change significantly [6,8,52,56] across this range. An example of such behaviour is the strong effect of solute drag [8] at temperatures below 550°C and strain rates below 10^{-6} s^{-1}. As described in the Section 2.1.2, this study is limited to ex-service material where the phase transformation processes are slow and solute drag effects are minimal [6]; both can be ignored for any practical purposes.

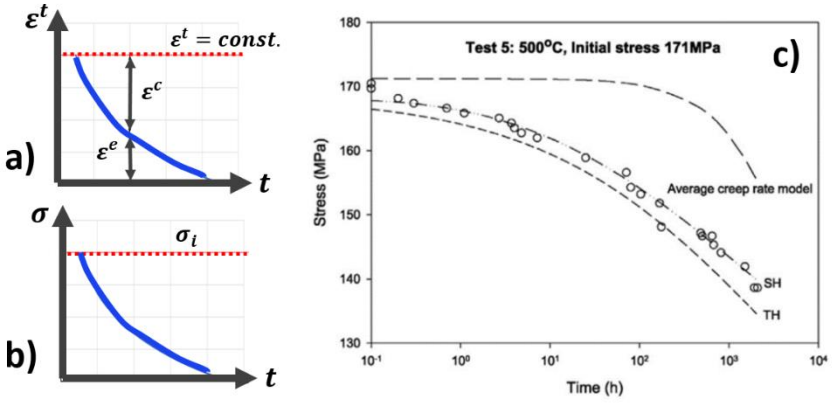


Figure 2.5. Schematic of a) accumulation of creep strain and b) stress relaxation behaviour during creep. c) Example of stress relaxation modelling in 316H stainless steel at 500°C and initial stress 171 MPa via RCC-MR models [52]. Note: SH and TH refer to strain- and time-hardening forms of the assumed primary creep relation, $\varepsilon_{pc} = C_1 t^{C_2} \sigma^{n_1}$. The average creep rate refers to $\dot{\varepsilon}_{ave} = \left(\varepsilon_{pc} + \varepsilon_{ss}\right) / \left(t_p + t_{ss}\right)$.

The relaxation behaviour has also been found to depend on prior deformation history [22]. In [24], the macroscopic stress relaxation response of Type 316H during displacement-controlled dwells, introduced at different cycles during cyclic deformation, was found to depend strongly on the stress redistribution between different families of grain orientations. The findings from [24] illustrate that the intragranular residual stress field is changing during the relaxation process. This supports the hypothesis that assuming a constant "back-stress" term in constitutive models for both forward creep and relaxation is unrealistic. Furthermore, those findings suggest that successful relaxation modelling approaches should capture the evolution of the internal stress field.

These findings suggest that the initial and long-term regimes of stress relaxation depend on the evolution of internal state and residual stress field, similar to primary stage during constant-stress creep [61,62]. It can be reasoned that within the stress and temperature range of interest, the mechanisms controlling constant-load and constant-displacement creep deformation are the i) thermally-activated glide process, ii) hardening and thermal recovery of the dislocation microstructure and iii) intragranular stress redistribution process. As discussed in Section 2.1, self-consistent models (SCM) similar to that presented in Section 2.5, allow microstructural evolution models to be applied at the grain scale, with the mechanics framework providing information about the grain-to-grain interactions and their effects on the global response. Self-consistent modelling of stress relaxation in stainless steels carried out by Wang et al. [42] confirms the importance of the evolution of internal material state and residual stress in determining the stress relaxation response. However, the micromechanical model considered in [42] is empirical and does not provide a physical description of the processes of thermal recovery and thermally-activated glide.

The SCM framework from Section 2.5 successfully describes these micromechanical processes during load-control creep in Type 316H stainless steel. This suggests that the existing

model should be able to capture the stress relaxation process in the material. Its ability to predict macroscopic stress relaxation after calibration to constant-load creep data will be examined in Chapter 3. It will be demonstrated that predictions are in good agreement with experimental data when appropriate physically-informed considerations are made on the overall effectiveness of obstacles to dislocation motion for which the parameter α_0 (Eq. 2.17) is the controlling parameter.

2.3. CYCLIC DEFORMATION

Understanding cyclic deformation of structural materials in power-generating plants is important, where the major loading cycle is due to periodic shutdowns for scheduled maintenance. During such cycles, the material experiences complex deformation histories. This results in hardening, and dynamic and static recovery [41] of the dislocation structure with accumulation of cycles until saturation of the stress-strain response is reached after a number of cycles [63]. A widely-used model to describe cyclic behaviour is the Chaboche-Lemaitre viscoplasticity model [32,64] described earlier. The model has been used to predict strain- and stress-controlled cyclic deformation of Type 316 stainless steel, e.g. [65]. Although predictions of the saturated hysteresis loop can be in agreement with experimental data (Fig. 2.6), the model is unable to capture the deformation response during complex loading scenarios without the addition of more state variables. In fact, model predictions via Chaboche-type models in [66] indicate that interactions between cyclic plasticity and creep are minimal. This finding is erroneous since cyclic plasticity is known to affect the subsequent creep, relaxation and failure response, particularly in Type 316 [14,67]. This suggests that physically-based modelling of cyclic deformation and more complex cyclic-creep deformation histories is required to accurately predict the deformation response.

Physically, the deformation behaviour during cyclic deformation in Type 316 is a result of the change in internal resistance to dislocation motion (hardening and dynamic recovery of the dislocation network) and the evolution of residual stress fields within the polycrystal [24,68,69]. The evolution of dislocation microstructure and changes in the residual stress field at the grain scale have been studied within polycrystalline crystal plasticity frameworks by Roters et al. [43] and Turkmen et al. [70] under strain- and stress-controlled loading histories, respectively. Both studies identified the importance of elastic anisotropy and redistribution of stress between different grain orientation families on the macroscopic stress-strain response during cyclic loading. The coupling between the elastic anisotropy of the crystal and its plastic anisotropy, associated with the micromechanical deformation mechanisms at the slip system level, was observed to drive the evolution of the local and global mean stress field. Furthermore, in both the empirical Chaboche-type models and multi-scale crystal plasticity models, it is recognised that saturation of the stress-strain response occurs when there is a balance between the rates of hardening and dynamic recovery of the dislocation structure. Any physically-based model must contain these elements if it is to successfully capture the cyclic material response.

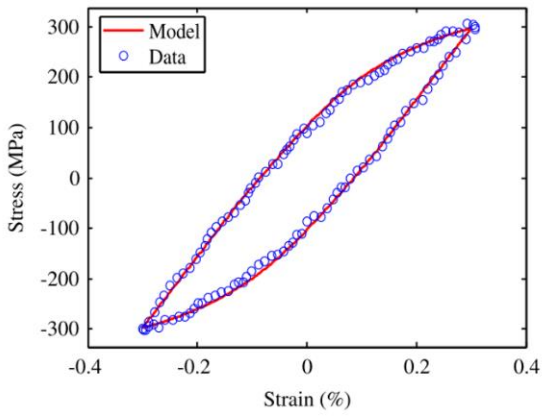


Figure 2.6. Experimental data and model prediction of saturated stress-strain curve, AISI 316 at 550°C [63].

One of the main objectives of this study is to capture the deformation response during cyclic loading by considering the physical processes, which control the macroscopic cyclic behaviour. The existing SCM framework from Section 2.5 captures the stress redistribution process and the hardening as a result of the interactions between gliding dislocations and dislocation obstacles. The following section considers the incorporation of the softening mechanism of dynamic recovery of the dislocation structure during cyclic deformation within the framework. The aim is to allow for modelling the microstructural evolution during cyclic and cyclic-creep deformation.

2.4. DYNAMIC RECOVERY OF THE DISLOCATION STRUCTURE

As identified in the previous section, including this feature of the material response is particularly important under cyclic loading [41]. The phenomenon is not yet captured in the multi-scale SCM from Section 2.5, and its incorporation as part of this study enhances the existing framework. Nes et al. [71] suggest that dynamic recovery is a function of dislocation annihilation frequency (v_g), strain rate and dislocation density. Their model is based on dislocation cell formation within the lattice due to dipole annihilation, for which climb is the rate-controlling process. Assuming that dislocation jogs climb in the direction of mutual annihilation and representing their annihilation frequency as a function of climb rate and spacing of jog segments, an expression for reduction in dislocation density, $d\rho_d = -v_g \rho_d d\gamma / \dot{\gamma}$, was derived. Model predictions of the decrease in internal resistance were in agreement with experimental data for pure FCC materials (e.g. Cu, Ni) [71]. However, cell formation is observed in Type 316H at temperatures >625°C [6,72], higher than the temperature range of interest to the present study. Below 625°C, TEM studies of Type 316 and 316H stainless steels demonstrate that formation of distinctive dislocation cells or subgrains during both cyclic and creep deformation histories is not pronounced [24,72–76]. This

is due to the presence of uniformly-dispersed intragranular precipitates of $M_{23}C_6$ type, which are not present in the pure metals examined in [71]. Hence, for simplicity, the present framework does not incorporate any features of the cell formation model by Nes et al. [71]. Kocks [36] suggests a simpler model of dynamic recovery based on the probability that a dislocation segment length (ΔL_r) is annihilated through statistical dipole interactions along individual slip planes. It is assumed that the reduction in dislocation density in a volume, *V*, is a function of ΔL_r and the possible annihilation sites $\rho_d da$ along a slip plane area, *da*, and is given by $d\rho_d = -\Delta L_r \rho_d da / V$ (Fig. 2.7). The probability of a recovery event scales with the probability of contact between mobile dislocations and segments, expressed by the shear strain increment $d\gamma = bda / V$. The change in dislocation density due to dynamic recovery is given by

$$d\rho_d = -(\Delta L_r \rho_d / b) C_i d\varepsilon^p \tag{2.12}$$

where all quantities are as defined previously. The model of Eq. 2.12 does not consider the formation process of distinct cells and is more relevant to the evolution of microstructural state in Type 316H stainless steel in the temperature regime <600°C, as compared to the model in [71]. Note that, although based on the concept of slip at the microscale, Eq. 2.12 has been applied in the literature within the context of continuum plasticity deformation response, e.g. [36,37].

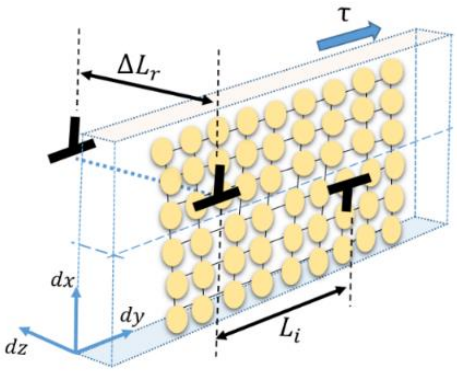


Figure 2.7. Schematic of annihilated dislocation dipole segment length ΔL_r.

It is worth pointing out that Eq. 2.12 is compatible with the state-variable approach in the SCM and can be incorporated directly within the existing SCM framework from Section 2.5. This will be demonstrated in detail in Chapter 3.

2.5. EXISTING MULTI-SCALE SELF-CONSISTENT MODEL (SCM)

The three-dimensional SCM framework developed by Hu and Cocks [7,50] captures the anisotropic elastic-plastic deformation of individual crystals in a polycrystalline aggregate. This is achieved by treating the grains as spherical anisotropic inclusions, embedded in an elastic matrix (Fig. 2.8). This does not only allow the macroscopic deformation of the aggregate to be captured, but also allows both the evolution of i) the microstructure within individual grains and ii) the residual intragranular stresses due to incompatible deformation of the neighbouring grains to be described. This SCM homogenisation approach follows the work of Kroner [77] and Budiansky and Wu [78] (KBW), where the constraint on the grain inclusions is imposed by the homogeneous elastic matrix. Hill [79] and Hutchinson [80] challenge the assumption that the matrix properties will remain elastic during macroscopic inelastic deformation. They reason that the KBW approach is expected to produce inaccuracies over large macroscopic inelastic strains, as it predicts a stiffer response. Instead, they proposed that the instantaneous tangent modulus of the matrix, surrounding the grains, will exert a more realistic constraint on the inclusions. This assumption has been adopted in recent developments of self-consistent averaging schemes, describing monotonic inelastic deformation histories, e.g. EPSC and EVPSC from [81,82]. However, the tangent modulus may vary during different types of loading due to the real anisotropy of the material. Nemat-Nasser and Obata [83] find that the selection of the matrix tangent modulus is difficult during non-proportional loading histories, since its determination is informed by the inelastic constitutive response of individual grains. Furthermore, Weng [84,85] employed the KBW

approach with a physically-rich rate-dependent constitutive formulation at the slip system level to simulate various elasto-plastic-creep deformation histories. The author found good agreement with experimental data over the inelastic strains of interest to the present study. Following the approach from [84,85], here we simply adopt the KBW averaging scheme. This is to overcome the issue of non-uniqueness of the tangent modulus during the complex deformation histories, of interest here, and to allow for easier implementation of the wide range of constitutive micromechanical models from Section 2.5.1, describing inelastic deformation in Type 316 stainless steel at the microscale. Note that the employed SCM will also be validated against full-field FE solutions in Chapter 4.

The employed SCM framework is based on the consideration of deformation at three different scales – microscopic, mesoscopic and macroscopic. The mean spacing between individual types of obstacles to dislocation motion is employed as the state variable. The SCM is written in MATLAB as a series of individual routines describing simple loading histories, e.g. load-controlled creep, monotonic elastic-plastic deformation, etc. These routines are then coupled to describe any desired loading history (examples in Chapter 3). An explicit numerical integration method is used to compute the plastic strain and intragranular residual stress increments for a given increment of macroscopic stress. Only a brief introduction to the constitutive models and the averaging scheme is given here; a full description can be found in the following studies [6–8,86].

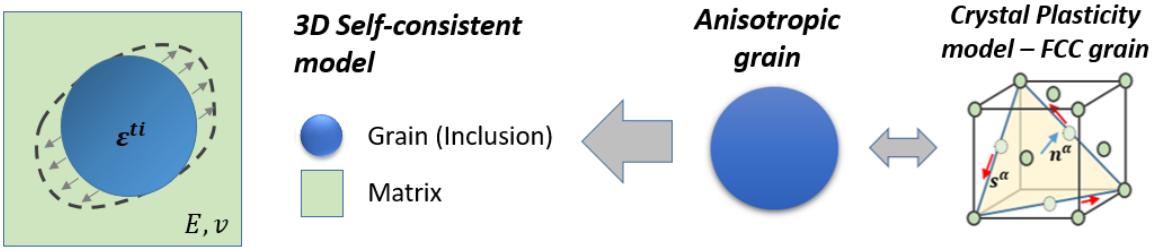


Figure. 2.8. Schematic of the multi-scale self-consistent modelling framework developed in [6].

As discussed at the beginning of this chapter, a major objective of this study is to enhance the existing SCM in order to predict cyclic deformation and stress relaxation. This will be presented in Chapter 3, where the enhanced version of the SCM framework is employed to study the interactions between creep and cyclic plasticity under deformation histories representative of those experienced in high-temperature power generation plants.

2.5.1. Micromechanical part of the SCM

The micromechanical model captures the contributions to internal resistance $\tau_{cr}^{(\alpha)}$, assumed the same for every three slip systems on a given slip plane, of the dominant obstacles to dislocation motion, i.e. dislocation junctions (τ_d) with spacing L_{di} along the *i*-th plane, intragranular precipitates (τ_p) with spacing L_p, and discrete solute atoms in the matrix (τ_s) with spacing L_s:

$$\tau_{cr}^{(\alpha)} = \sqrt{\tau_d^2 + \tau_p^2} + \tau_s = \left(\sqrt{\left(\frac{\alpha_d G b}{L_{di}} \right)^2 + \left(\frac{\alpha_p G b}{L_p} \right)^2} \right) + \frac{\alpha_s G b}{L_s} \tag{2.13}$$

where G is the shear modulus, b - the Burgers vector, and α_p, α_d and α_s are dimensionless obstacle strength parameters [47]. Superscript $\alpha = 1 \sim 12$ is associated with a slip system, whereas subscript i = 1~4 is associated with a slip plane. Note that the spacing of dislocation junctions on a given slip plane is shared between the three corresponding slip systems, e.g. $L_d^{(1\sim3)} = L_{d1}$. The evolution of L_{di} is a function of the dislocation junction obstacle density, N_{di}, as $\dot{L}_{di} = -N_{di}^{3/2} \dot{N}_{di} / 2$. The rate of change of obstacle density on the *i*-th slip plane evolves due to self- and latent-hardening as a result of dislocation multiplication as

$$\dot{N}_{di}^{self} = j_s \dot{\gamma}_i \tag{2.14}$$

$$\dot{N}_{di}^{latent} = j/(m-1)\sum_{k\neq i}\dot{\gamma}_k \tag{2.15}$$

where $\dot{\gamma}_i$ is the sum of resolved shear strain rates on all three slip systems along the *i*-th slip plane; j_s and j are the self- and latent hardening parameters, respectively [7]. The thermal recovery of the dislocation network is modelled by assuming that, at elevated temperature, long dislocation links grow at the expense of shorter ones, as described by Hu and Cocks [50]. As a result, the decrease in dislocation-junction number density on the *i*-th plane due to static recovery can be expressed as

$$\dot{N}_{di} = -\frac{2W_c D_c G b^5}{kT} N_{di}^3 \tag{2.16}$$

where D_c is the core diffusivity and W_c is the parameter controlling thermal recovery [6]. The deformation of the anisotropic grains is modelled using crystal plasticity (CP) theory from Section 2.1.3.2 [7], where the plastic strain rate in each crystal is determined by summing the slip rate, $\dot{\gamma}$, on each individual slip system, α. The assumed flow rule for Eq. 2.10 describes the thermally-activated dislocation glide process at a temperature *T* and is given by [28] as

$$\dot{\gamma}^{(\alpha)} = \dot{\gamma}_0 \exp\left(-\frac{\Delta F_0}{kT}\left(1-\left|\frac{\tau^{(\alpha)}+\bar{\tau}_m^r}{\tau_{cr}^{(\alpha)}}\right|^{3/4}\right)^{4/3}\right)\mathrm{sgn}(\tau^{(\alpha)}+\bar{\tau}_m^r) \tag{2.17}$$

where ΔF_0 ($\alpha_0 G_0 b^3$, G_0: shear modulus at 0 K) is the required free activation energy, k is Boltzmann constant, $\bar{\tau}_m^r$ is the microscopic residual stress in the matrix, caused by the presence of prismatic loops punched out at the precipitates as they are bypassed by the gliding dislocations [87], and $\dot{\gamma}_0$ is the reference shear strain rate. The resolved shear stress along a slip system is determined from Eq. 2.11 as $\tau^{(\alpha)} = \left[sym\left(\mathbf{n}^{(\alpha)}\otimes\mathbf{s}^{(\alpha)}\right)\right]^T \boldsymbol{\sigma}^{\mathbf{a}}$. The generation and annihilation of prismatic loops on the *i*-th slip plane during creep are determined as a function of the resolved

shear strain rates ($\dot{\gamma}_i$) and dislocation obstacle density (N_{di}) on that plane. The production rate of loops $\dot{N}_{li}$, which adds a contribution to the overall dislocation obstacle density on the *i*-th plane, is

$$\dot{N}_{li} = \frac{3 f_v^p}{2\pi \left(r_p^m\right)^2} \dot{\gamma}_i - \frac{N_{li}}{N_{di}} \dot{N}_{di} \tag{2.18}$$

where f_v^p and r_p^m are the volume fraction and radius of intragranular precipitates, respectively. The residual stress in the lattice due to prismatic loops is also considered in the model. Based on the works by Kroupa [88] and Ashby [89], it is assumed that the stress field exerted by a prismatic loop on a straight dislocation will resemble the stress field exerted by the same loop on a spherical particle. By considering the equilibrium in the unloaded state between the microscopic stress at the intragranular particles ($\bar{\tau}_p^r$) and the residual stress in the lattice ($\bar{\tau}_m^r$) due to the presence of prismatic loops, the evolution of $\bar{\tau}_m^r$ is approximated in [6] by

$$\dot{\bar{\tau}}_m^r = -0.7\alpha_d G \left(2\pi \left(r_p^m\right)^2 \dot{N}_{li} \left(3 f_v^p\right)^{-1}\right) \left(f_v^p\right)^{3/2} \tag{2.19}$$

Note that the parameter α_0 in Eq. 2.17 controls the overall effectiveness of obstacles to dislocation motion. It will be demonstrated in Chapter 3 that α_0 is important in predicting creep deformation during both displacement- and load-controlled histories and is treated as a free parameter within the physical range, described in [90], for different obstacle types. The evolution of precipitate and solute atom concentrations and spacing due to long-term aging is also incorporated into the framework [6,8]. However, the focus of the present study is on ex-service material. In this case, the evolution of such microconstituents is negligible and $\dot{L}_p, \dot{L}_s$ are set equal to zero in all simulations in this study. The microstructural features, which play a role during monotonic high-temperature deformation of ex-service material, considered in the original form of the model, are shown in Fig. 2.9.

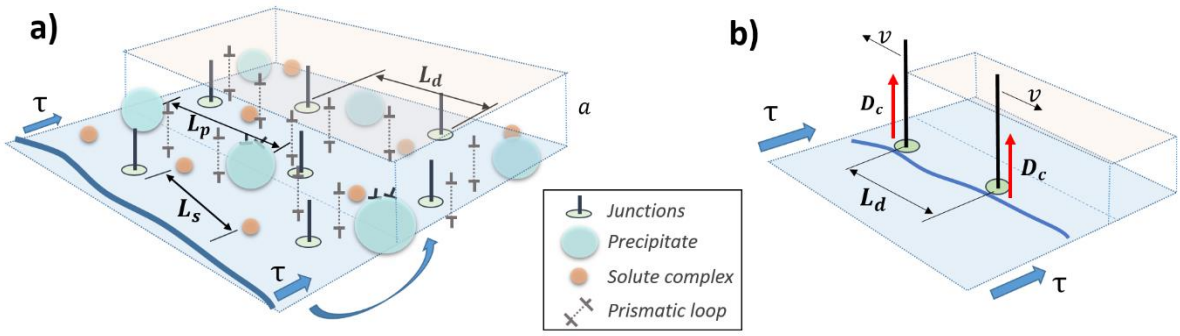


Figure 2.9. a) Schematic of the three dominant types of obstacles to dislocation motion. The resolved shear stress, τ, is acting upon the dislocation represented by the thick solid line. Prismatic loops are also shown. b) The static recovery mechanism, considered in [8]. Core diffusion transports material along dislocation cores allowing climb of segments resulting in an increase of dislocation junction spacing.

2.5.2. Inclusion problem and polycrystalline modelling part

The polycrystalline aggregate is modelled using a self-consistent (SC) scheme [7] by treating grains as anisotropic inclusions in an elastic matrix. This was done for reasons highlighted in the beginning of this section. The relationship between the total ($\boldsymbol{\varepsilon}^{\mathbf{i}}$) and misfit strain ($\boldsymbol{\varepsilon}^{\mathbf{ti}}$) in an isotropic inclusion (superscript i) is given by $\boldsymbol{\varepsilon}^{\mathbf{i}} = \mathbf{S}^{\mathbf{i}}\boldsymbol{\varepsilon}^{\mathbf{ti}}$, where the bolded term represents a tensor (see Fig. 2.8). N.B. Non-bolded terms are scalars unless written in tensor notation, e.g. ε_{ij}. The stress and strain in the isotropic inclusion for an applied stress $\boldsymbol{\sigma}$ are then expressed as

$$\boldsymbol{\sigma}^{\mathbf{i}} = \mathbf{L}^{\mathbf{i}}\left(\mathbf{S}^{\mathbf{i}} - \mathbf{I}\right)\boldsymbol{\varepsilon}^{\mathbf{ti}} + \mathbf{T}\boldsymbol{\sigma} \tag{2.20}$$

$$\boldsymbol{\varepsilon}^{\mathbf{i}} = \mathbf{C}^{\mathbf{i}}\mathbf{T}\boldsymbol{\sigma} + \mathbf{S}^{\mathbf{i}}\boldsymbol{\varepsilon}^{\mathbf{ti}} \tag{2.21}$$

where $\mathbf{S}^{\mathbf{i}}$ is the Eshelby tensor [6], $\mathbf{I}$ is the identity matrix, $\mathbf{T}$ is the coordinate transformation matrix, and $\mathbf{L}^{\mathbf{i}}$ and $\mathbf{C}^{\mathbf{i}}$ are the elastic stiffness and compliance matrices of the material. The Eshelby isotropic inclusion cannot be used directly for an anisotropic inclusion (superscript a). In [6], an equivalent inclusion method is adopted to determine the total strain ($\boldsymbol{\varepsilon}^{\mathbf{a}}$) and stress ($\boldsymbol{\sigma}^{\mathbf{a}}$) in an anisotropic inclusion by selecting an appropriate misfit strain in the homogeneous inclusion, $\boldsymbol{\varepsilon}^{\mathbf{t}*}$,

[91] to give $\boldsymbol{\sigma}^{\mathbf{i}} = \boldsymbol{\sigma}^{\mathbf{a}}; \boldsymbol{\varepsilon}^{\mathbf{i}} = \boldsymbol{\varepsilon}^{\mathbf{a}}$. Then, the anisotropic inclusion stress and strain are expressed in terms of the misfit strain in the equivalent isotropic inclusion and the real misfit strain ($\boldsymbol{\varepsilon}^{\mathbf{ta}}$) as

$$\boldsymbol{\sigma}^{\mathbf{a}} = \mathbf{L}^{\mathbf{i}}(\mathbf{S}^{\mathbf{i}} - \mathbf{I})\boldsymbol{\varepsilon}^{\mathbf{t*}} + \mathbf{T}\boldsymbol{\sigma} \tag{2.22}$$

$$\boldsymbol{\varepsilon}^{\mathbf{a}} = \mathbf{C}^{\mathbf{a}}\mathbf{L}^{\mathbf{i}}(\mathbf{S}^{\mathbf{i}} - \mathbf{I})\boldsymbol{\varepsilon}^{\mathbf{t*}} + \mathbf{C}^{\mathbf{a}}\mathbf{T}\boldsymbol{\sigma} + \boldsymbol{\varepsilon}^{\mathbf{ta}} = \mathbf{C}^{\mathbf{i}}\mathbf{T}\boldsymbol{\sigma} + \mathbf{S}^{\mathbf{i}}\boldsymbol{\varepsilon}^{\mathbf{t*}} \tag{2.23}$$

where $\mathbf{L}^{\mathbf{a}}$ and $\mathbf{C}^{\mathbf{a}}$ are the elastic stiffness and compliance matrices of the anisotropic grain. During elastic deformation, $\boldsymbol{\varepsilon}^{\mathbf{ta}} = 0$ and the stress and strain in the elastically-deforming inclusion are

$$\boldsymbol{\sigma}^{\mathbf{a}} = \left(\left(\left(\mathbf{I} - \left(\mathbf{S}^{\mathbf{i}} \right)^{-1} \right)^{-1} \mathbf{C}^{\mathbf{i}} - \mathbf{C}^{\mathbf{a}} \right)^{-1} \left(\mathbf{C}^{\mathbf{a}} - \mathbf{C}^{\mathbf{i}} \right) + \mathbf{I} \right) \mathbf{T}\boldsymbol{\sigma} = \mathbf{H}^{\mathbf{a}}\mathbf{T}\boldsymbol{\sigma} \tag{2.24}$$

$$\boldsymbol{\varepsilon}^{\mathbf{a}} = \left(\mathbf{C}^{\mathbf{i}} + \left(\left(\mathbf{C}^{\mathbf{a}} - \mathbf{C}^{\mathbf{i}} \right)^{-1} \mathbf{C}^{\mathbf{a}}\mathbf{L}^{\mathbf{i}} \left(\mathbf{S}^{\mathbf{i}} \right)^{-1} - \mathbf{L}^{\mathbf{i}} \right)^{-1} \right) \mathbf{T}\boldsymbol{\sigma} = \mathbf{K}^{\mathbf{a}}\mathbf{T}\boldsymbol{\sigma} \tag{2.25}$$

During inelastic deformation, plastic strain accumulates in the inclusions. Kroner [77] and Budiansky and Wu [78] expressed in incremental form the real misfit strain in an inclusion as

$$\Delta\boldsymbol{\varepsilon}^{\mathbf{ta}} = \Delta\boldsymbol{\varepsilon}^{\mathbf{p}} - \mathbf{T}^{-\mathbf{T}}\Delta\mathbf{E}^{\mathbf{p}} \tag{2.26}$$

where $\Delta\boldsymbol{\varepsilon}^{\mathbf{p}} = \sum sym\left(\mathbf{n}^{(\alpha)} \otimes \mathbf{s}^{(\alpha)} \right) \dot{\gamma}^{(\alpha)} \Delta t$ is the plastic strain increment in the inclusion and $\Delta\mathbf{E}^{\mathbf{p}}$ is the macroscopic plastic strain increment in the aggregate, obtained by the Principle of Virtual Work. Eq. 2.23 is then solved for the increment in the misfit strain $\boldsymbol{\varepsilon}^{\mathbf{t}*}$ in the unloaded state:

$$\Delta\boldsymbol{\varepsilon}^{\mathbf{t*}} = \left[\mathbf{C}^{\mathbf{a}}\mathbf{L}^{\mathbf{i}} \left(\mathbf{I} - \mathbf{S}^{\mathbf{i}} \right) + \mathbf{S}^{\mathbf{i}} \right]^{-1} \Delta\boldsymbol{\varepsilon}^{\mathbf{ta}} \tag{2.27}$$

The intragranular residual stress in a grain, $\Delta\mathbf{X}^{\mathbf{a}}$, is obtained from Eqs. 2.22 and 2.27:

$$\Delta\mathbf{X}^{\mathbf{a}} = \mathbf{L}^{\mathbf{i}} \left(\mathbf{S}^{\mathbf{i}} - \mathbf{I} \right) \left[\mathbf{C}^{\mathbf{a}}\mathbf{L}^{\mathbf{i}}(\mathbf{I} - \mathbf{S}^{\mathbf{i}}) + \mathbf{S}^{\mathbf{i}} \right]^{-1} \Delta\boldsymbol{\varepsilon}^{\mathbf{ta}} \tag{2.28}$$

The total stress exerted within the grain during plastic deformation of the aggregate is updated by the combined contribution from the changes in the applied stress $\Delta\boldsymbol{\sigma}$ and the

intragranular (Type II) residual stress $\Delta\mathbf{X}^{\mathbf{a}}$, according to $\Delta\boldsymbol{\sigma}^{\mathbf{a}} = \mathbf{H}^{\mathbf{a}}\mathbf{T}\Delta\boldsymbol{\sigma} + \Delta\mathbf{X}^{\mathbf{a}}$. The polycrystalline aggregate behaviour is determined by an averaging method using the Principle of Virtual Work [92]. According to this principle, the work done by the virtual applied stress ($\boldsymbol{\Sigma}^*$) on the aggregate equals the volume average of the work done by all of the individual grains

$$\boldsymbol{\Sigma}^* \Delta\mathbf{E} = \frac{1}{V}\int_V \boldsymbol{\sigma}^* \Delta\boldsymbol{\varepsilon} dV \tag{2.29}$$

where V is the volume of the aggregate, $\boldsymbol{\sigma}^*$ and $\Delta\boldsymbol{\varepsilon}$ are the stress and strain increment in the grain which are in equilibrium and compatible with the external stress $\boldsymbol{\Sigma}^*$ and strain increment $\Delta\mathbf{E}$, respectively. During elastic deformation, the total strain in the aggregate is purely elastic:

$$\Delta\mathbf{E} = \frac{1}{V}\int_V \mathbf{K}^{\mathbf{a}}\mathbf{T} dV \Delta\boldsymbol{\sigma} \tag{2.30}$$

During plastic deformation, in the case of no externally-applied stress, only the macroscopic plastic strain exists with contributions from both misfit strain and inelastic slip activity. According to the Principle of Virtual Work, the macroscopic behaviour is expressed as

$$\boldsymbol{\Sigma}^* \Delta\mathbf{E}^{\mathbf{p}} = \frac{1}{V}\int_V \boldsymbol{\sigma}^* \mathbf{C}^{\mathbf{a}} \Delta\mathbf{X}^{\mathbf{a}} dV + \frac{1}{V}\int_V \boldsymbol{\sigma}^* \Delta\boldsymbol{\varepsilon}^{\mathbf{p}} dV \tag{2.31}$$

Since the residual stress $\Delta\mathbf{X}^{\mathbf{a}}$ is in equilibrium with zero externally-applied stress, and the grain stress is determined from the elastic problem, the volume average of $\Delta\mathbf{X}^{\mathbf{a}}$ is zero. The macroscopic plastic strain is obtained from the second part of the integral in Eq. 2.31 as

$$\boldsymbol{\Sigma}^* \Delta\mathbf{E}^{\mathbf{p}} = \frac{1}{V}\int_V \mathbf{H}^{\mathbf{a}}\mathbf{T}\boldsymbol{\Sigma}^* \Delta\boldsymbol{\varepsilon}^{\mathbf{p}} dV \tag{2.32}$$

By incorporating the mechanism of dynamic recovery (Section 2.4), and considering the ability of the micromechanical model to describe simultaneously thermally-activated glide and

thermal recovery of the dislocation structure, the full scope of micromechanical processes considered in the framework is summarised in Fig. 2.10. The existing SCM is enhanced in Chapter 3, where its ability to predict stress relaxation and cyclic deformation will be examined. Once verified against experimental data for simple loading scenarios, the enhanced framework will be employed to simulate complex deformation histories, common to high-temperature plant components. The overall aim is to provide better understanding of creep-cyclic interactions in Type 316H and inform the improvement of practical assessment models.

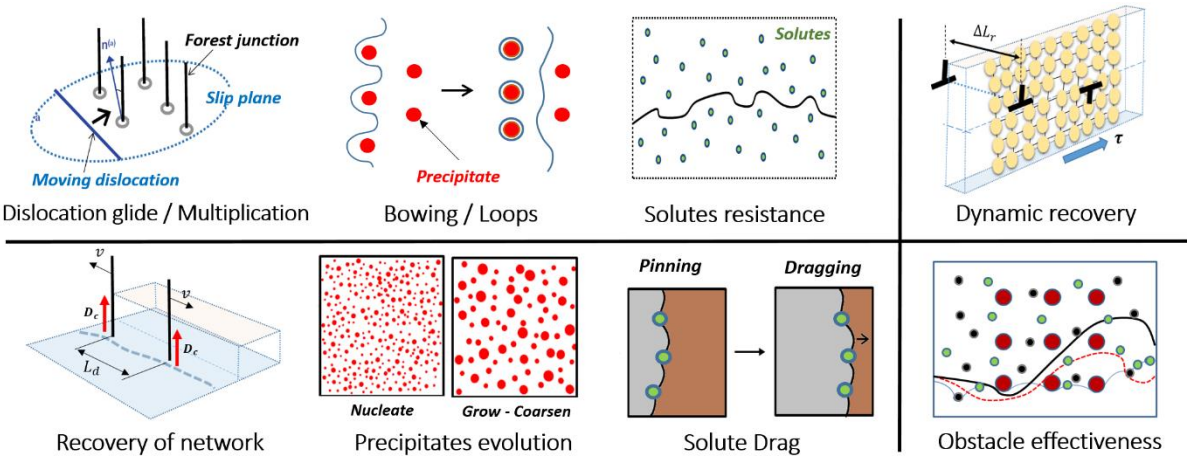


Figure 2.10. The micromechanical deformation mechanisms considered - evolution of dislocation structures (hardening, static and dynamic recovery) and precipitates and solutes, and overall effectiveness of dislocation obstacles. Note: Evolution of precipitates and solutes is not considered in the present study.

2.6. CREEP FRACTURE

Following inelastic deformation during the primary and secondary creep regimes, creep damage develops during the tertiary creep stage. A better understanding of the creep damaging process in Type 316H stainless steel is of importance, since creep strength and ductility of the material vary significantly under different thermo-mechanical loading scenarios and the associated damage mechanisms. The following sections only give a short overview of the most common creep failure mode in Type 316H under the temperature-stress range of interest here, namely, intergranular

creep failure. Note that detailed evaluation of intergranular creep failure and the sensitivity of the process to different microstructural features, as well as appropriate modelling approaches and assumptions, will be made in Chapter 6.

2.6.1. Tertiary creep regime

Continuous degradation of the load-carrying capacity of the material develops during the tertiary stage of creep, eventually leading to failure. Ashby and Dyson [93] describe the damage development through an additional state variable, ω, and relate it to different phenomena – loss of cross-sectional area, void formation and growth, microstructural or environmental degradation. Dyson and McLean [94] also suggest that the initial stages of tertiary creep are related to increased thermal recovery of the dislocation network near grain boundaries. Experimental observations demonstrate that austenitic stainless steels typically experience void nucleation and growth along the grain boundaries [95–97] and within the grains [25,98] during creep (see Fig. 2.11). The following sections and Chapter 6 will demonstrate that intergranular creep failure by nucleation and growth of cavities occurs in ex-service austenitic Type 316H stainless steel under common high-temperature power plant operating conditions.

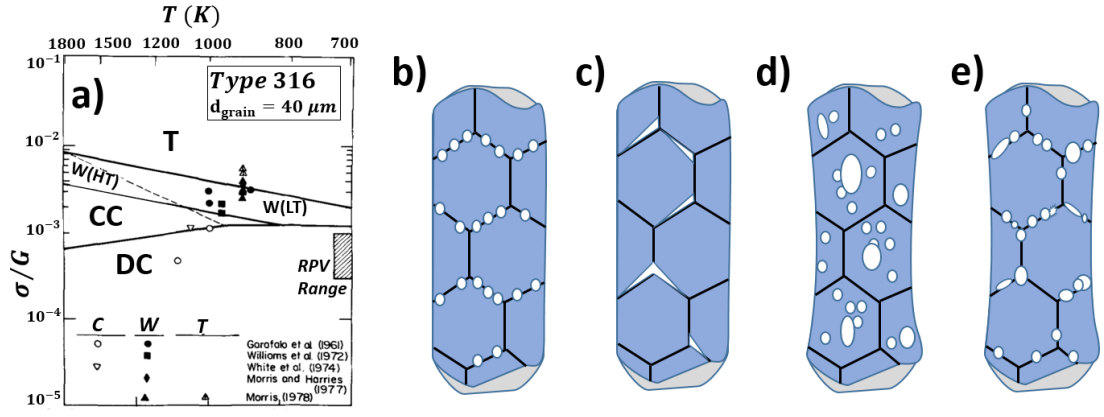


Figure 2.11. a) Fracture mechanism map for Type 316 [99]. Schematic of microstructural damage – b) diffusive GB cavitation (DC), c) wedge cracking (W), d) transgranular creep fracture (T) and e) dislocation creep controlled GB cavitation (CC). Reactor pressure vessel (RPV) operating ranges shown in a).

2.6.2. Creep damage mechanisms in austenitic stainless steels

2.6.2.1. Intergranular cavitation

Cavities nucleate, grow and coalesce along grain boundaries (see Fig. 2.12.a) of austenitic stainless steels during creep leading to brittle fracture. The growth of lenticular cavities, assisted by diffusion (Fig. 2.11.b) [100], dislocation creep (Fig. 2.11.e) [101] or a combination of both [102], is well understood. However, no clear understanding of the physical mechanism of void nucleation exists and nucleation is often represented via empirical models [103] (see Section 2.6.4). It should be noted that nucleation is a continuous process with time, which affects growth and complicates the physical explanation of damage formation, as discussed by Dyson [10] and Cho et al. [104].

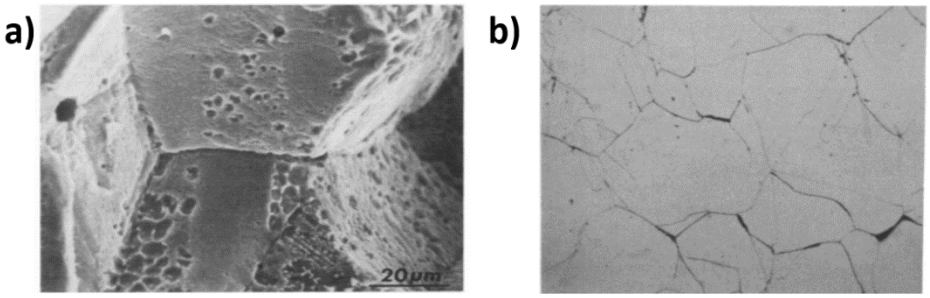


Figure 2.12. a) Cavitation along grain boundaries in AISI 304 [96] and b) wedge cracking in AISI 316 [105].

Cavitating grain boundaries are usually widely-spaced and global failure of the material is controlled by the deformation of the surrounding material and the process of facet interlinkage [106]. Brittle wedge cracking often develops along boundaries near the triple grain junctions at high stresses [96] (Fig. 2.12.b) and intermediate temperatures (e.g. for Type 316, wedge cracks were found <650°C [98,105]). The formation and growth of wedge cracks near triple grain junctions is understood as a result of grain-boundary sliding along adjacent interfaces (Section 2.6.2.2) [16]. Evidently, brittle intergranular creep damage is of importance under high-temperature power plant conditions. Hence, detailed evaluation of this failure process in Type 316

stainless steel and the associated modelling approaches is carried out in Chapters 6 and 7, with only a brief overview given in Sections 2.6.3-2.6.4. Transgranular creep fracture [99] is not considered here, since the focus of this study is on the dominant failure mechanism in Type 316 stainless steels over the temperature-stress range of interest, i.e. intergranular creep failure.

2.6.2.2. Grain-boundary sliding

At high temperatures, grain boundaries slide relative to one another as the grains deform. The effect diminishes with increase in grain size [105]. Grain-boundary sliding is understood as an accommodation process for damage and deformation [107] and should not be interpreted as a separate damaging process, as discussed in [108]. The mechanism is of importance to the intergranular damage process, as it is believed to increase the stress exerted on facets, normal to the applied load. This enhances the strain rate and influences the failure propagation pattern in polycrystals [109]. Therefore, the effect of grain-boundary sliding should be considered in models describing intergranular creep failure in polycrystals. This is discussed in Section 2.6.4.

2.6.3. Intergranular creep failure in Type 316 stainless steel

2.6.3.1. Cavity nucleation and growth at second-phase particles

Intergranular precipitates and slip band ledges along grain boundaries are identified as the most common creep cavity nucleation sites in Type 316/316H under plant-relevant thermo-mechanical conditions [110]. Cavities mainly form at $M_{23}C_6$ intergranular carbide particles [111] (Fig. 2.13).

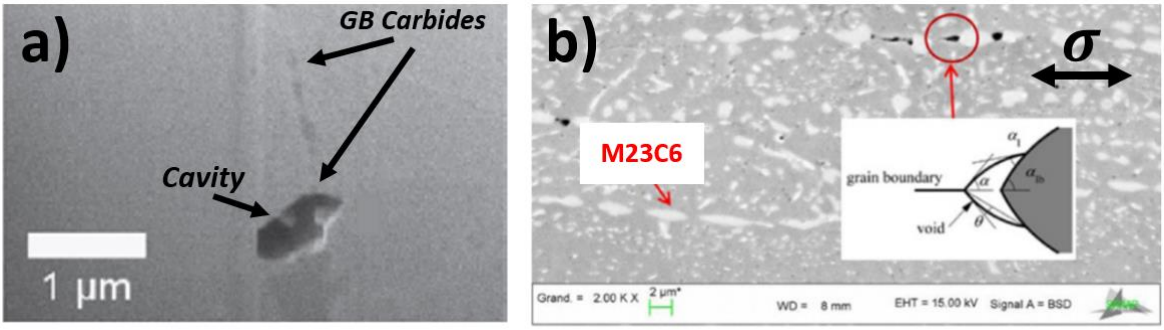


Figure 2.13. Cavities at $M_{23}C_6$ carbides in EX 316H after service at a) 525°C [111] and b) 700°C [112].

Spherical cavities in ex-service Type 316H (65000 h at 490-530°C) examined by Chen et al. [111] and Jazaeri et al. [97] of size 50-400 nm were recorded, with similar observations in ex-service material at 700°C [112]. The studies suggest that cavities form due to accumulation of high stress at intergranular particles as a result of grain-boundary sliding or localised slip near such particles. However, experimental observations of cavities usually examine voids that have already undergone substantial growth, which does not aid the understanding of their formation process (i.e. nucleation of cavities). None of these studies successfully identifies the mechanism of cavity nucleation, posing challenges to the development of physical models for the process.

2.6.3.2. Impurity segregation at intergranular interfaces

Cavity formation in Type 316 is also associated with the presence of impurities, which can segregate to the grain boundaries. Erhart and Grabke [113] found that addition of Cr, Mo and V in Fe-C systems reduces carbon activity, thus allowing phosphorus to diffuse to the energetically-favourable grain boundaries. Martinez-Ubeda et al. [114] noted that one ex-service Type 316H sample had cavitated more along the grain boundaries than the rest of the examined samples. The reason was attributed to phosphorus segregation to the interphase and grain boundaries. This aspect will be discussed further in Chapter 6.

2.6.3.3. Inelastic deformation and microstructural features

Observations of the fracture behaviour of Type 316H (Cast AaD) in [98] show that relations between creep ductility, strain rate, stress and different fracture modes are difficult to establish via existing empirical damage models, employed in industry. The study concluded that the intergranular creep failure response of the material is sensitive to the deformation response of the grains, and the evolution of second-phase particles along grain boundaries and within the lattice. It is also found that intergranular creep failure of Type 316 stainless steel is strongly influenced by prior inelastic deformation [115]. Observations from this and the preceding sections suggest that intergranular creep damage is closely linked to the local microstructural features along grain boundaries, as well as the lattice stress and strain fields in the vicinity of grain boundaries. An evaluation of microstructural features and local deformation processes, which influence cavity nucleation and growth behaviour in the material, is provided in Chapter 6.

2.6.4. Modelling intergranular creep failure

2.6.4.1. Intergranular cavity nucleation and growth

Approaches to creep damage modelling usually represent either global loss of load-bearing section through continuum damage mechanics [116] or the micromechanical processes of cavity formation and growth explicitly [100]. The present study focuses on mechanistic modelling of intergranular cavitation with the aim to provide a better understanding of this micromechanical process and identify important features to be considered within improved nucleation and growth models.

Under common high-temperature plant operating conditions, intergranular cavity growth is driven by grain-boundary diffusion [95]. Mechanistic growth models have been developed and applied in the literature [100,117,118], capturing well the evolution of cavity size along boundaries.

Life estimation models usually couple such diffusive growth models with cavity nucleation models. Damage along a cavitating facet then occurs when the cavities have grown and coalesce [112]. However, Dyson [106] reasoned that in polycrystalline materials, where damaging facets are usually widely-spaced, failure along a single facet does not mean global failure of the material. As will be discussed in Chapter 6, this poses a limitation on damage models within continuum plasticity formalisms, which do not capture such local aspects of the failure process.

Empirical nucleation models, in which the cavity nucleation rate is linearly proportional to the inelastic strain rate of the material [10], are commonly employed to represent the intergranular cavity nucleation process in polycrystalline materials. Successful application of such models to predict the cavitation response in austenitic stainless steels can be found in the literature, e.g. [119,120]. Empirical nucleation models capture the general trend in failure response and support the strong link between lattice deformation and grain-boundary damage. However, such models do not provide any understanding of damage initiation and its sensitivity to local microstructural features, e.g. composition, particle morphology, dislocation structures, etc.

By contrast, mechanistic models for cavity nucleation assume that the process is driven by condensation of vacancies as a result of the applied stress. The condensation process causes formation of stable cavity nuclei [9]. The vacancy condensation theory for nucleation considers a number of microstructural features, such as cavity/particle shape, diffusion and interfacial energy, to which the cavity nucleation process can be sensitive [121]. This theory, however, effectively predicts a threshold stress above which rapid nucleation of cavities at all available sites occurs. Below this threshold, the rate of nucleation is so slow that it can be ignored for practical purposes. This disagrees with experimental results, according to which the nucleation rate varies linearly with inelastic strain rate [122]. Furthermore, the threshold nucleation stress predicted by this model

can be several orders of magnitude higher than experimentally-recorded values (10-40 MPa) [121] at which nucleation is readily observed. As will be demonstrated in Chapter 6, suggestions are made in the literature that potential stress concentrations at intergranular particles should be considered to allow for better estimation of the nucleation threshold stress. Such stress concentrations are believed to be a result of diffusive accommodation [123] or local dislocation structures in the vicinity of the grain boundary [10]. This suggests that models for cavity nucleation need to consider the detailed microstructure of the grain boundary, as well as the deformation behaviour of the lattice in the vicinity of the boundary, in order to provide further understanding of the intergranular cavitation process. This is discussed in detail in Chapters 6 and 7.

2.6.4.2. Modelling of grain-boundary sliding

The increase in creep rate due to grain-boundary sliding in polycrystalline solids has been modelled in an extrinsic way by adding a stress enhancement factor, f, to the continuum plasticity creep relations in an attempt to capture the accelerated deformation rate [124–126]. Another approach is modelling the micromechanics of the grain boundaries [127] within polycrystalline modelling frameworks, e.g. [109,128]. The increase in stress along the boundaries in power-law creeping aggregates as a result of grain-boundary sliding [109] is of importance to intergranular damage. Chapter 5 will develop a modelling approach to capture the variation of local stress fields in polycrystalline aggregates, comprised of realistic anisotropic grains, as a result of sliding.

2.7. SUMMARY

Approaches to life estimation of components in the power-generation industry are usually based on accumulated inelastic strain. Simplistic empirical strain-based models, however, are overly conservative and inaccurate as far as long-term life predictions are concerned. Physically-based

models for deformation of polycrystalline materials are needed to better predict the inelastic response of structural materials, such as Type 316H stainless steel, and improve the understanding of the deformation process in order to inform industrial assessment approaches. To address this, a multi-scale physically-based self-consistent model (SCM) was developed by Hu et al. [7,8,50,87]. The SCM captures well the global and micro-scale deformation response of the material under monotonic elastic-plastic and creep loading. Nevertheless, a major limitation of the original form of the model is the inability to predict cyclic deformation and stress relaxation (from a fit to constant-stress creep data). Experimental observations and modelling studies suggest ways to improve the model by taking into consideration the overall effectiveness of obstacles to dislocation motion and by incorporating a model for the dynamic recovery of the dislocation microstructure. The enhanced version of the SCM is employed in Chapter 3. Its ability to predict stress relaxation and cyclic deformation, as well as predict the deformation response during complex plant-relevant histories and explain the associated creep-cyclic interactions, are assessed.

There is a need to study creep fracture within a framework, which could explicitly capture the micromechanical processes of intergranular damage, as well as the elastic-plastic-creep deformation of the surrounding anisotropic grains. The effects of grain-boundary sliding on the deformation rate and local stress fields in the vicinity of boundaries should also be evaluated. Existing phenomenological models for creep damage, employed in current assessments, do not fully represent the creep damage processes and the sensitivity of failure to microstructural features in the material. The discrepancy between phenomenological and mechanistic cavity nucleation theories indicates the need to revisit the existing models. Suitable physically-informed models would need to be identified for intergranular cavity nucleation and growth, which in particular take into consideration the effect of microstructural features on the nucleation process. Their

application within a multi-scale crystal plasticity modelling framework could provide a better understanding of intergranular failure in Type 316 stainless steel.

The key expressions employed in the SCM framework in subsequent chapters are summarized below:

a) Plastic strain rate in individual grains (SCM)

$$\dot{\boldsymbol{\varepsilon}}^{\mathbf{p}} = \sum_{\alpha}^{12} sym\left(\mathbf{n}^{(\alpha)} \otimes \mathbf{s}^{(\alpha)}\right)\dot{\gamma}^{(\alpha)}$$

b) Inelastic shear strain rate on individual slip system

$$\dot{\gamma}^{(\alpha)} = \dot{\gamma}_0 \exp\left(-\frac{\alpha_0 G_0 b^3}{kT}\left(1-\left|\frac{\tau^{(\alpha)}+\overline{\tau}_m^r}{\tau_{cr}^{(\alpha)}}\right|^{3/4}\right)^{4/3}\right)\mathrm{sgn}(\tau^{(\alpha)}+\overline{\tau}_m^r)$$

c) Internal resistance on a slip system from dislocation junction, precipitates and solutes

$$\tau_{cr}^{(\alpha)} = \left(\sqrt{\left(\frac{\alpha_d Gb}{L_{di}}\right)^2+\left(\frac{\alpha_p Gb}{L_p}\right)^2}\right)+\frac{\alpha_s Gb}{L_s}$$

d) Self- and latent-hardening due to increase in dislocation junction obstacle density

$$\dot{N}_{di}^{self} = j_s\dot{\gamma}_i; \quad \dot{N}_{di}^{latent} = j/(m-1)\sum_{k\neq i}\dot{\gamma}_k; \quad i=1\sim 4$$

e) Softening due to thermal recovery of the dislocation network via core diffusion

$$\dot{N}_{di} = -\frac{2W_c D_c Gb^5}{kT}N_{di}^3$$

f) Evolution of Type III microscopic residual stress due to the presence of prismatic loops

$$\dot{\overline{\tau}}_m^r = -0.7\alpha_d G\left(\frac{2\pi\left(r_p^m\right)^2}{3f_v^p}\dot{N}_{li}\right)\left(f_v^p\right)^{3/2}$$

g) Evolution of density of prismatic loops on the *i*-th slip plane

$$\dot{N}_{li} = \left(3 f_v^{\,p} \Big/ 2\pi \left(r_p^m\right)^2\right)\dot{\gamma} - \left(N_{li}/N_{di}\right)\dot{N}_{di}$$

h) Resolved shear stress on individual slip system as a function of grain stress

$$\tau^{(\alpha)} = \left[\, sym\left(\mathbf{n}^{(\alpha)} \otimes \mathbf{s}^{(\alpha)}\right)\right]^T \boldsymbol{\sigma}^{\mathbf{a}}$$

i) Total elastic response of individual grain, elastic deformation (SCM)

$$\boldsymbol{\sigma}^{\mathbf{a}} = \left(\left(\left(\mathbf{I} - \left(\mathbf{S}^{\mathbf{i}}\right)^{-1}\right)^{-1}\mathbf{C}^{\mathbf{i}} - \mathbf{C}^{\mathbf{a}}\right)^{-1}\left(\mathbf{C}^{\mathbf{a}} - \mathbf{C}^{\mathbf{i}}\right) + \mathbf{I}\right)\mathbf{T}\boldsymbol{\sigma} = \mathbf{H}^{\mathbf{a}}\mathbf{T}\boldsymbol{\sigma}$$

$$\boldsymbol{\varepsilon}^{\mathbf{a}} = \left(\mathbf{C}^{\mathbf{i}} + \left(\left(\mathbf{C}^{\mathbf{a}} - \mathbf{C}^{\mathbf{i}}\right)^{-1}\mathbf{C}^{\mathbf{a}}\mathbf{L}^{\mathbf{i}}\left(\mathbf{S}^{\mathbf{i}}\right)^{-1} - \mathbf{L}^{\mathbf{i}}\right)^{-1}\right)\mathbf{T}\boldsymbol{\sigma} = \mathbf{K}^{\mathbf{a}}\mathbf{T}\boldsymbol{\sigma}$$

j) Type II residual intragranular stress and total stress in grains during plasticity (SCM)

$$\Delta\mathbf{X}^{\mathbf{a}} = \mathbf{L}^{\mathbf{i}}\left(\mathbf{S}^{\mathbf{i}} - \mathbf{I}\right)\left[\mathbf{C}^{\mathbf{a}}\mathbf{L}^{\mathbf{i}}(\mathbf{I} - \mathbf{S}^{\mathbf{i}}) + \mathbf{S}^{\mathbf{i}}\right]^{-1}\left(\Delta\boldsymbol{\varepsilon}^{\mathbf{p}} - \mathbf{T}^{-\mathbf{T}}\Delta\mathbf{E}^{\mathbf{p}}\right)$$

$$\Delta\boldsymbol{\sigma}^{\mathbf{a}} = \mathbf{H}^{\mathbf{a}}\mathbf{T}\Delta\boldsymbol{\sigma} + \Delta\mathbf{X}^{\mathbf{a}}$$

k) Global elastic and inelastic deformation of the polycrystalline aggregate (SCM)

$$\Delta\mathbf{E} = \frac{1}{V}\int_V \Delta\boldsymbol{\varepsilon}^{\mathbf{a}} dV = \mathbf{C}^{\mathbf{i}}\Delta\boldsymbol{\sigma}$$

$$\boldsymbol{\Sigma}^{*}\Delta\mathbf{E}^{\mathbf{p}} = \frac{1}{V}\int_V \boldsymbol{\sigma}^{*}\Delta\boldsymbol{\varepsilon}^{\mathbf{p}} dV$$

CHAPTER 3

MODELLING OF CREEP-CYCLIC DEFORMATION INTERACTIONS UNDER TYPICAL POWER PLANT OPERATING HISTORIES

3.1. INTRODUCTION

3.1.1. Deformation response during creep-fatigue loading

Creep-fatigue deformation histories arise during operation of high-temperature power-generating plants. Such histories alter the creep and cyclic response of the material, which could affect damage formation in the microstructure. The focus here is on the behavior of Type 316H stainless steel [1]. Experimental studies demonstrate a reduction in primary creep strain following cyclic loading, found to be as a result of hardening of the microstructure [67,129]. In [130,131], prior plasticity showed a subtle influence on minimum creep rate at high dwell stresses. However, at lower stresses the decrease in minimum creep rate was pronounced [24]. The presence of stress relaxation dwells during cyclic deformation gives rise to a higher inelastic strain accumulated in the loading cycle [14]. Furthermore, when cycles are interrupted by such dwells, the saturated stress amplitude of the hysteresis loop decreases [14]. The positioning of such dwells with respect to strain is also of interest to plant operation. It has been suggested that the extent of hysteresis loop softening is lower when dwells are not positioned at the maximum tensile strain position, typically considered in experiments [14]. In addition to the observed reduction in creep strain accumulation with prior cyclic loading, Mamun [24] found a difference in the creep response during a tensile creep dwell upon re-load from either a compressive or tensile stress state in the cycle.

3.1.2. Structural assessment industrial practice and conservatism

The simplified models used in structural assessment procedures are unable to fully capture the complex evolution of creep and cyclic deformation described above. This poses difficulties, since the R5 [11] damage assessment procedure, employed by EDF Energy, is based on a ductility exhaustion approach, which requires an accurate assessment of inelastic strain. Typically, a range of assumptions are made by the industrial user of the procedure in order to ensure a conservative prediction of component lifetime. Often these assumptions lead to excessive conservatism since they do not account for some of the deformation behaviour reviewed in the previous section.

The R5 procedure [11] uses the peak-hardened deformation response of Type 316H, with the stabilized cyclic stress-range/strain-range response captured by a Ramberg-Osgood model, calibrated by the R66 AGR Materials Handbook [3]. The R66 advice recognizes the decrease in saturated stress amplitude of hysteresis loops due to the presence of creep dwells. Modification of the cyclic curve, following [3], is conservative in estimation of the saturated stress and potentially results in underestimation of inelastic strain range. The R5 procedure provides limited advice on the effect of prior plasticity on subsequent creep response, where the conservative approach is to assume full re-initiation of the primary creep stage ("re-priming") at the start of each dwell. For deformation histories where creep-fatigue failure is dominated by creep, the above assumptions are overly-conservative. In addition, the simplified models used in assessment procedures are typically informed by experimental studies, where the macroscopic strain range (normally $\Delta E >$ 0.6%) and creep dwell duration (t_{dwell}<100 hours) are different to actual dwell durations and strain ranges, experienced during plant operation (t_{dwell}~1000 hours and ΔE < 0.4%). Employing the assessment procedure models to quantify creep strain accumulation in service histories with longer dwells introduces further conservatism and uncertainty in lifetime predictions.

The SCM, presented in Chapter 2, offers the potential to capture complex deformation patterns. In order to examine the creep-cyclic deformation interactions described above, the existing version of the model is enhanced in this chapter to capture stress relaxation and cyclic deformation. In Section 3.2, the interpretation of physical terms within the SCM is modified, which allows both relaxation and load-controlled creep to be represented by the same model. In Section 3.3, the SCM is enhanced to take into account the effect of dynamic recovery on the constitutive response in order to capture macroscopic behaviour under cyclic loading. A variety of combined creep-relaxation-cyclic deformation histories are examined in Section 3.4 using the enhanced model. The objective of this chapter is to interpret and quantify the creep-cyclic interactions during plant-relevant deformation histories through predictions by the physically-based SCM. This aims to provide insights into potential improvements of the assessment procedures, employed in industry.

3.1.3. Model calibration and application

The micromechanical model, employed in the SCM framework, contains a number of parameters that need to be fit to experimental data (see Chapter 2). Only monotonic elastic-plastic and creep deformation were considered in the original model [6]. Under these conditions, dynamic recovery does not play a significant role and was ignored. The solute concentration and spacing of precipitates were determined from the alloy composition, and from micrographs and EDX studies, respectively. The model captures the phase transformation processes in Type 316H [8], but focus of this thesis is on ex-service (EX) material for which the evolution of solutes and precipitates at elevated temperatures is ignored. The degree of latent hardening, represented by $j/3j_s$, was set to 1.4 based on the results of DDD simulations [87]. The initial internal resistance (Eq. 2.13) along a slip plane is determined by the initial value of dislocation junction density N_0, while evolution of internal resistance due to hardening is determined by j_s in Eqs. 2.14-15. These parameters are

chosen to provide a fit to stress-strain experimental data. The creep response is determined by the parameters α_0 (Eq. 2.17) and W_c (Eq. 2.16), controlling thermally-activated glide and static recovery, respectively. The original model assumed the value of $\alpha_0 = 1$ [6], which is a numerical average of values of α_0 for the different types of obstacles [90]. The value of W_c is determined by fitting the experimental creep data, once the hardening response is calibrated to stress-strain data. In this chapter, modelling both creep and relaxation behaviour is of importance, both of which are controlled by α_0 and W_c. In Section 3.2, the assumption that $\alpha_0 = 1$ is re-evaluated. It will be demonstrated that both α_0 and W_c need to be treated as independent fitting parameters, with the constraint that α_0 must be in the physical range $0.02 < \alpha_0 < 2$ [132]. In Section 3.3, model calibration to cyclic response through adjusting the parameter ΔL_r, controlling dynamic recovery (see Eq. 3.1), is discussed. The research presented in this chapter can be found in [132–134].

3.2. MODELLING STRESS RELAXATION

3.2.1. Approach to modification of model

The rate-dependent processes of thermally-activated glide and thermal recovery control the response during creep [50]. However, as identified in Section 2.2, the initial stages of the stress relaxation process appear to be dependent on the thermally-activated glide process, whereas thermal recovery is dominant during long-term relaxation response. In order to provide initial insight into the relative importance of thermally-activated glide and static recovery, we use the SCM to examine the creep and relaxation behaviour of pure copper. The understanding gained from evaluating this microstructurally simpler FCC material provides insights into modelling stress relaxation via the SCM of ex-service (~65×10^3 hours, Cast 69431) Type 316H stainless steel, whose chemical composition is shown in Table 3.1. The experimental data for monotonic

elastic-plastic deformation, forward creep and stress relaxation on Type 316H have been provided by EDF Energy. The texture in the material employed in previous studies, e.g. [7,135], was weak (Fig. 3.1), hence the material is treated as a globally-isotropic body. The aggregate comprises 100 grains, allowing sufficient efficiency of the simulation without loss of accuracy, agreeing with [6].

Table 3.1. Chemical composition (wt%) of Type 316H.

C	Si	Mn	P	S	Cr	Mo	Ni	Co	Fe
0.07	0.41	0.98	0.024	0.017	17.1	2.3	11.6	0.07	Bal.

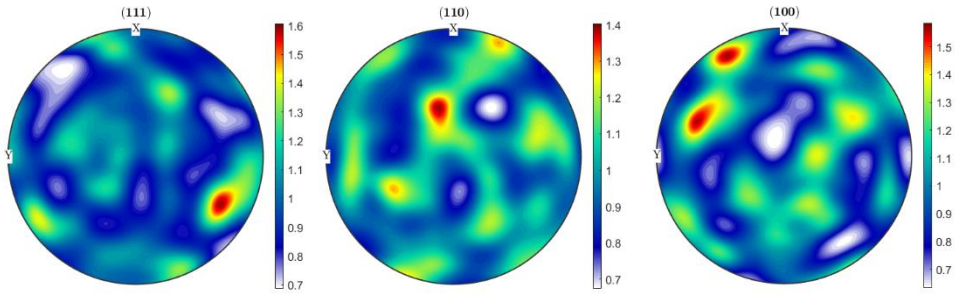


Figure 3.1. Pole figures of initial texture - ex-service 316H material considered (100 grains). Pole figures are generated using MTEX [136]. The same grain orientations are used to examine the behaviour of Cu.

3.2.2. Effect of activation energy for thermal glide on creep and relaxation

As reasoned in Section 2.2, the micromechanical deformation process during load- and displacement-controlled creep deformation in the temperature and stress range of interest should be the same. Therefore, a physical creep model should predict both forward creep and relaxation using the same physical parameters. Firstly, the SCM is calibrated to both the monotonic stress-strain and creep deformation response of Type 316H stainless steel at 550°C for $\alpha_0 = 1$. The contribution from precipitates to τ_{cr} was calculated by considering the experimentally-measured distribution of intragranular $M_{23}C_6$ particles in EX 316H [7]. The solute resistance was estimated by selecting a value of 0.000457 for α_s and considering the concentration of alloying elements in the material [6]. The free parameters used are those employed in [6] for $\alpha_0 = 1$: $N_0 = 2 \times$

$10^{13}\ m^{-2}$, $j_s = 5 \times 10^{14}\ m^{-2}$ and $W_c = 80$. The calibrated response is not presented here for the sake of brevity. Preliminary studies of stress relaxation at 550°C using these parameters with $\alpha_0 = 1$ indicate that the SCM underestimates the relaxed stress with not enough inelastic strain being generated (see Fig. 3.3). Findings from Section 2.2 suggest that thermally-activated glide is dominant during the initial stages of relaxation. Hence, to capture better the relaxation response, the role of the activation energy for thermally-activated glide, represented by the parameter α_0 (Eq. 2.17), needs to be investigated in more detail. When α_0 is large, i.e. the overall effectiveness of obstacles to dislocation motion is large [28], thermally-activated glide is difficult. Decreasing the value of α_0 makes thermally-activated glide easier. Thus, during the transient relaxation stage, inelastic deformation would occur without significant recovery of the dislocation structure. To investigate the effect of α_0, forward creep and relaxation modelling of commercially pure copper at 250°C was conducted. Pure Cu (FCC) was selected since only dislocation junctions contribute to the internal resistance, allowing for a clearer understanding of the role of the activation energy.

The calibration procedure consists of selecting a value for α_0 (Eq. 2.17). The parameters N_0, j_s and W_c are calibrated to provide a fit to stress-strain and constant-stress creep response of Cu. Consequently, the set of α_0, N_0, j_s and W_c is used to predict stress relaxation after monotonic load-up to different start-of-dwell stresses at the same temperature. Studies on copper show that the extent of stress relaxation over a given period increases with decreasing value of α_0. A good agreement with both creep and relaxation data is obtained for $\alpha_0 = 0.18$ (Fig. 3.2) – a value within the physical range $\alpha_0 = 0.02{\sim}2$ from [90]. All other physical properties and parameters for Cu are summarised in Table 3.2. The observations on copper suggest that the parameters α_0 and W_c should be determined by simultaneously fitting both creep and relaxation data.

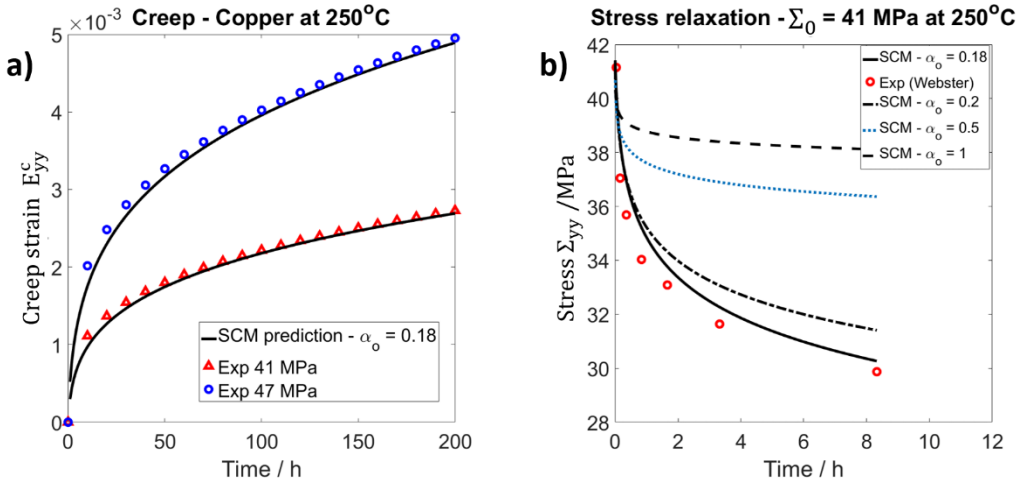


Figure 3.2. Creep and relaxation model predictions with α_0 for Cu at 250°C. Data after [51,137].

The procedure is repeated for EX Type 316H at 550°C for start-of-dwell stress in the range 230-280 MPa. The same trend of increasing amount of relaxed stress with lower α_0 is found with a good fit to relaxation data obtained for $\alpha_0 = 0.18$ (Fig. 3.3). All model parameters and physical values for Type 316H with $\alpha_0 = 0.18$ are summarised in Table 3.2. It is interesting to note that this value of α_0 matches that obtained for copper. The value found is consistent with the lower end of the α_0 range in [90], identified with thermal activation over dislocation junctions and solutes.

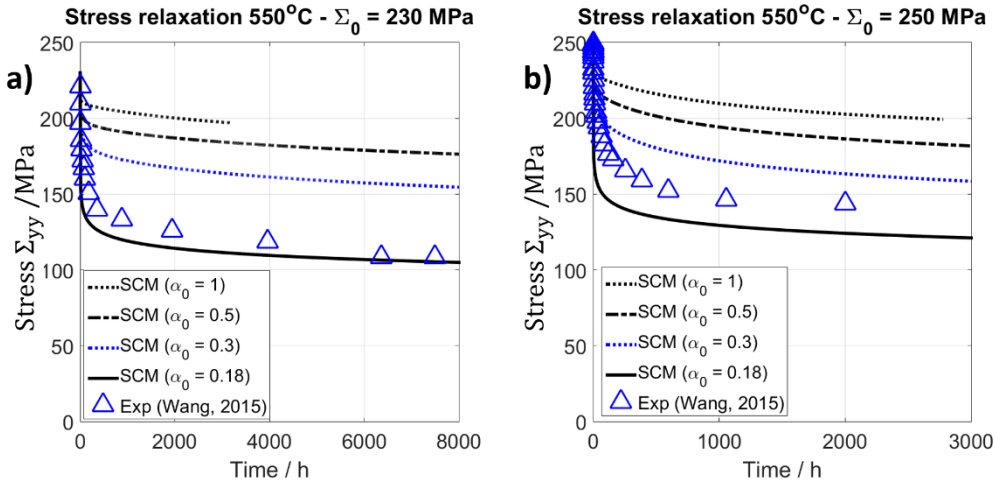


Figure 3.3. Stress relaxation model predictions with α_0 and experimental data, EX 316H at 550°C with start-of-dwell (initial) macroscopic stress Σ_0 of a) 230 and b) 250 MPa.

This is consistent with the observation that the major contribution to τ_{cr} in Type 316H is from dislocation junctions and solute complexes, if present, and not precipitates [87]. This would suggest that the value of α_0 for Cu and Type 316H should be approximately equal to each other, which they are. This physical modification of the model allows both relaxation and forward creep to be captured. This modified model will be employed in Section 3.4 to evaluate the creep response of the alloy during load- or displacement-controlled dwells under cyclic loading histories.

Table 3.2. Parameters for SCM, Type 316H (T_m = 1810 K) and commercially pure Cu (T_m = 1356 K).

Parameter	Value (316H)	Value (Cu)	Parameter	Value (316H)	Value (Cu)
C_{11}	198 GPa*	138 GPa§	N_0 / m^{-2}	1.5 x 10^{14}	8.0 x 10^{12}
C_{12}	125 GPa*	76 GPa§	j_s / m^{-2}	2.0 x 10^{15}	7.0 x 10^{15}
C_{44}	122 GPa*	75 GPa§	j / m^{-2}	1.0 x 10^{16}	3.5 x 10^{16}
E	101.3 GPa	84.3 GPa	W_C	0.015	1.0
v	0.39	0.355§	D_C	6.47 x 10^{-15} m^2/s	1.57 x 10^{-17} m^2/s **
G_0	139 GPa	79.8 GPa**	ΔL_r	8b	38b
b	2.5 x 10^{-10} m	2.58 x 10^{-10} m**	τ_p	21 MPa	-
$\dot{\gamma}_0$	1.0 1/s		τ_s	37 MPa	-
α_0	0.18		α_d	0.35	

* Data taken from Kamaya [138]. § Data from [139]. ** Parameters from [90].

Examples of constant-stress creep curves for Type 316H, obtained via the SCM at 550°C and stress levels of 250 and 280 MPa with $\alpha_0 = 0.18$, are illustrated in Fig. 3.4 for completeness. For brevity, other predictions are omitted. Note the significant variation of creep response between batches from the same cast of Type 316H stainless steel, illustrated in Fig. 3.4. It is important to note that such a variation in Type 316/316H is well-known [114,140] and differences between predictions and data within a factor of two are acceptable. Hence, the focus of this study is not to produce an exact fit to a set of experimental data, but to predict the general trend in response through physical considerations in the models adopted. In the following section, the deformation response of the material during cyclic loading is examined.

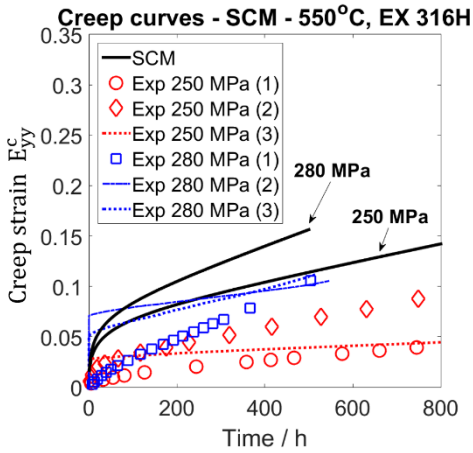


Figure 3.4. Examples predicted macroscopic creep strain with time for EX 316H at 550°C, $\alpha_0 = 0.18$. Experimental data on different batches (1-3) of Cast 69431 after EDF Energy.

3.3. MODELLING CYCLIC DEFORMATION

Cyclic deformation of the same cast of Type 316H at 550°C under strain-controlled loading is investigated in this section via the SCM considering the combined mechanisms of hardening and dynamic recovery. As already discussed in Section 2.4, the dynamic recovery model by Kocks [36] (Eq. 2.12) is suitable for Type 316H stainless steel in the temperature range of interest. In the following approach, a similar form of this model is employed at the scale of original modelling in the SCM. Applied at the slip plane level, Eq. 2.12 is compatible with the state variable in the SCM (number density of dislocation obstacles, N_{di}, on the *i*-th slip plane) and takes the form

$$\dot{N}_{di} = -\frac{\Delta L_r}{b} N_{di} \dot{\gamma}_i \tag{3.1}$$

where $\dot{\gamma}_i$ is the sum of resolved shear strain rates along the three slip systems on the *i*-th slip plane. Incorporation of this dynamic recovery model represents an additional term for the evolution of N_{di} (Eqs. 2.14-2.16) arising from dislocation motion, which acts to increase the spacing between junctions with an increment of resolved shear strain. The full evolution law for the number density of dislocation junctions, including the hardening, static and dynamic recovery terms, is:

$$\dot{N}_{di} = j_s\dot{\gamma}_i + j/(m-1)\sum_{k\neq i}\dot{\gamma}_k - \frac{2W_cD_cGb^5}{kT}N_{di}^3 - \frac{\Delta L_r}{b}N_{di}\dot{\gamma}_i; \quad i=1,4; m=3 \tag{3.2}$$

Note that the initial obstacle density and hardening parameters, N_0 and j_s, are already calibrated in the preceding section to the monotonic stress-strain curve of Type 316H at 550°C for $\alpha_0 = 0.18$. Then, the calibration procedure of the model with dynamic recovery consists of finding a suitable value of ΔL_r which fits the saturated cyclic hysteresis loop after a given number of cycles. Asymmetric strain range of 0.6% was selected to calibrate and probe the ability of the model to predict cyclic deformation. The dynamic recovery model was tuned to predict saturation of the hysteresis loop (assumed when the change in stress amplitude between cycles is less than 1 MPa), which occurs after about 80 cycles for Type 316H [22]. This requires a value of $\Delta L_r = 8b$ in Eq. 3.1. The model also captures the cycle-to-cycle response up to saturation (Fig. 3.5.a) which gives confidence in the micromechanical model of dynamic recovery employed. Preliminary studies of cyclic deformation of EX 316H at 550°C were also carried without the incorporation of dynamic recovery using only the hardening models from Section 2.5 and the fitted value of j_s from Table 3.2. The comparison in Fig. 3.5.b) demonstrates the significance of the softening mechanism with accumulation of cycles. In the absence of dynamic recovery, the material continually hardens.

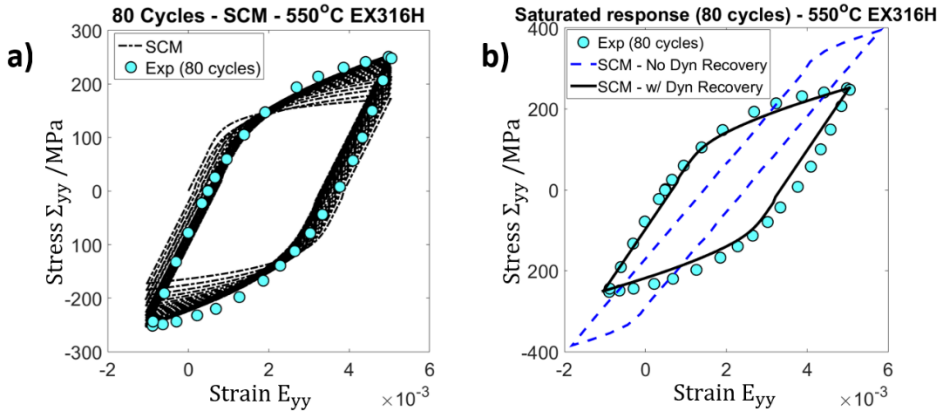


Figure 3.5. a) Stress-strain curve for 80 cycles – SCM and data for 80th cycle, ex-service 316H at 550°C. b) Saturated response after 80 cycles – SCM prediction with and without the model of dynamic recovery.

The competition between hardening and dynamic recovery gives rise to a steady state distribution of dislocation link lengths after a number of cycles. This, together with the changing residual stress state in the aggregate during a cycle [50,87] determines the saturated stress-strain curve. Furthermore, predictions for both symmetric and asymmetric strain-controlled histories by the enhanced SCM are found to agree with experimental data on Type 316H, with the use of just one parameter controlling dynamic recovery. Other examples are not shown here. Note that the experiments from Section 3.2 were re-examined by considering dynamic recovery during creep. The results were not altered. Hence, Eq. 3.1 could be neglected during creep exposures over the strains examined here. In the following section, the parameters determined here for cyclic deformation are combined with those from Section 3.2 for creep and relaxation to simulate the material response under plant-relevant cyclic-creep deformation histories. Although the predicted distributions of dislocation obstacle density (N_d) and intragranular residual stress (X^a) are discussed in the following sections in order to explain the material response, they are not compared to experimental data. This is because the focus here is on how the predicted global deformation response informs industrial assessment procedures. Nevertheless, predictions of N_d via the SCM in [132] were in agreement with experimental data from [24] during cyclic-creep loading histories.

3.4. MODELLING CREEP-CYCLIC DEFORMATION INTERACTIONS

The enhanced SCM is now employed to systematically simulate a range of cyclic-creep loading histories in ex-service Type 316H stainless steel at 550°C between the strain ranges of 0.2% and 0.8%, and creep dwell times >24 hours. The framework is calibrated in the preceding sections meaning that all predictions are independent of free parameters. This aims to provide better understanding of material state evolution during cyclic-creep interactions. The objective in Section 3.4.2 is to isolate the effect of prior cyclic hardening on creep deformation, as well as explain the

difference in creep response upon re-load from different stress states. Histories with load-controlled and displacement-controlled dwells at each cycle are examined in Section 3.4.3 with the objective to provide guidelines for improvement of models, used in assessment procedures.

3.4.1. Simple interactions between cyclic and creep deformation

Firstly, simple loading histories comprised of prior cyclic loading to saturation and subsequent cyclic loading with strain-controlled dwells at each cycle are simulated here. Several histories of this type, motivated by the experiments by Fookes et al. [22], were investigated by Petkov et al. [132]. These serve as an initial verification of the enhanced SCM against an existing material database. For the sake of brevity, only one of the scenarios from [132] is presented here. The deformation history consists of prior strain-controlled cycling to saturation with $E_{min} = -0.1\%$ and $E_{max} = 0.5\%$ at 0.025%/s. Following saturation of the hysteresis loop, another 28 cycles were carried out with 50-hour strain-controlled dwells at $E = 0.4\%$. An example of the predicted response for the 101st-105th cycles is shown in Fig. 3.6. Predictions are in general agreement with stress relaxation data during selected strain-controlled dwells (Fig. 3.6.b) from [22]. This provides confidence in the micromechanical model adopted, which is used to simulate more complex deformation histories in the following sections.

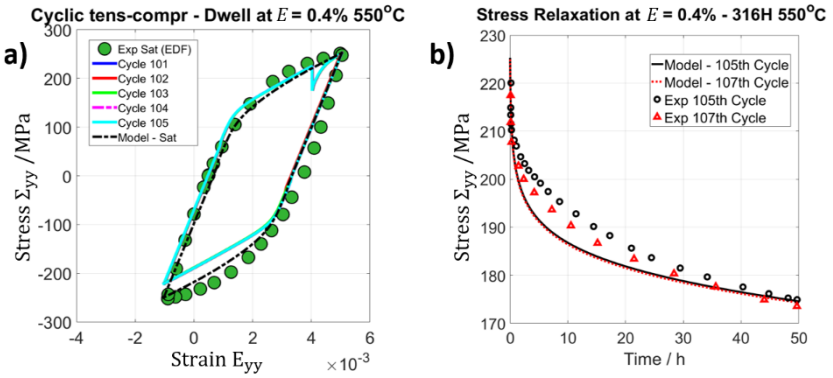


Figure 3.6. Predicted stress-strain response after saturation during cycles 101-105 with relaxation dwells at ΔE = 0.4%. Model prediction and experimental data of stress relaxation during 105th and 107th cycles [132].

3.4.2. Effects of cyclic loading on creep response

3.4.2.1. Evolution of creep strain accumulation with prior cyclic deformation

The creep-fatigue loading history simulated in this section is illustrated in Fig. 3.7. A strain range for the cyclic loading test is assumed between 0.3% and 0.8%. The sample is initially loaded in tension to a prescribed strain level, equal to the assumed strain range amplitude, following which a load-controlled creep dwell is introduced at Position 1 in Fig. 3.7.a. The start-of-dwell stress at Position 1 is recorded. A new sample is then cyclically-deformed to a prescribed number of cycles, e.g. 3rd cycle in Fig. 3.7, with the cycle ending at macroscopic compressive state of stress at Position 2. Then, the sample is re-loaded from Position 2 to Position 3, where a tensile load-controlled dwell at the same stress as in Position 1 is introduced. In Fig. 3.7.b), a similar loading history is illustrated with the cyclic loading ending in macroscopic tensile stress state at Position 4. The sample is then elastically-unloaded to Position 5 and re-loaded in tension to Position 6 where a tensile creep dwell at the same start-of-dwell stress is introduced.

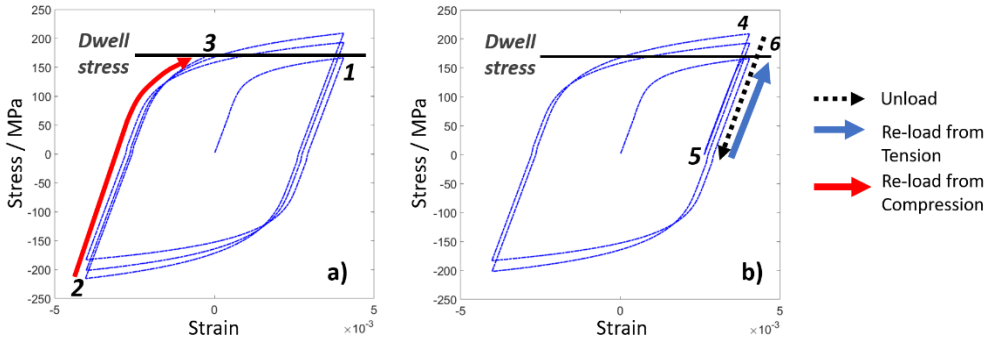


Figure 3.7. a) Schematic of the deformation history examined. A sample is loaded to a prescribed strain (1) where a tensile load-controlled creep dwell is introduced. Another sample is cyclically-deformed and re-loaded from compressive stress state at (2) to (3) where a tensile dwell is carried out (same stress as (1)). In b), the cyclically-deformed sample is unloaded from (4) to (5) with a tensile dwell introduced at (6).

The deformation history of Fig. 3.7.a), comprising tensile creep dwells upon re-load from a macroscopic compressive stress state, is examined first. An example of the predicted

macroscopic creep response during dwells, following prior cyclic loading to different numbers of cycles at ΔE = 0.8% and macroscopic dwell stress Σ_{dwell} =167 MPa, is shown in Fig. 3.8.a). The model predicts a decrease in the extent of primary creep strain and minimum creep rate with cycles (here, minimum creep rate is arbitrarily selected as the difference in creep strain over the final 20% of creep time). The same trend is observed for ΔE = 0.3, 0.4 and 0.8%. The evolution of minimum creep rate with N / N_s - the ratio between number of cycles prior to the dwell and cycles to saturation of the hysteresis loop - for these three strain ranges is examined in Fig. 3.8.b). Based on this, the ratio between the minimum creep rate after cyclic loading to a fully-hardened state and the minimum creep rate after the initial load-up at the same dwell stress (Cycle 1), $f_c = \dot{E}^{ss}_{N_s} \big/ \dot{E}^{ss}_{Cycle1}$, is extracted. The obtained values of f_c are 0.6, 0.39 and 0.32 for ΔE = 0.3% ($N_s = 200$ cycles, $\Sigma_{dwell} = 140$ MPa), 0.4% (150 cycles, 150 MPa) and 0.8% (80 cycles, 167 MPa), respectively. The model predictions for ΔE = 0.8% are in agreement with the experimental data by Joseph et al. [67], where a value of $f_c \approx 0.4$ was recorded for fully-hardened ex-service Type 316H. At ΔE = 0.3%, which is more relevant to plant operating condition, the model predicts $f_c \approx 0.6$. This illustrates the diminishing effects of prior cyclic hardening on the subsequent creep response with decreasing strain range, in agreement with Joseph et al. [67] and Mehmanparast et al. [141]. The hardening effect is expected to be even less pronounced for shorter strain ranges towards the elastic regime. Nevertheless, simple models used in industrial assessments should consider the diminishing creep rate as a result of prior inelastic deformation. Otherwise, the accumulated inelastic strain could be significantly overestimated in assessments. This is considered for plant-relevant scenarios in Section 3.4.3.2. The dependence of the observed behaviour on evolution of the microstructure is discussed in the following section.

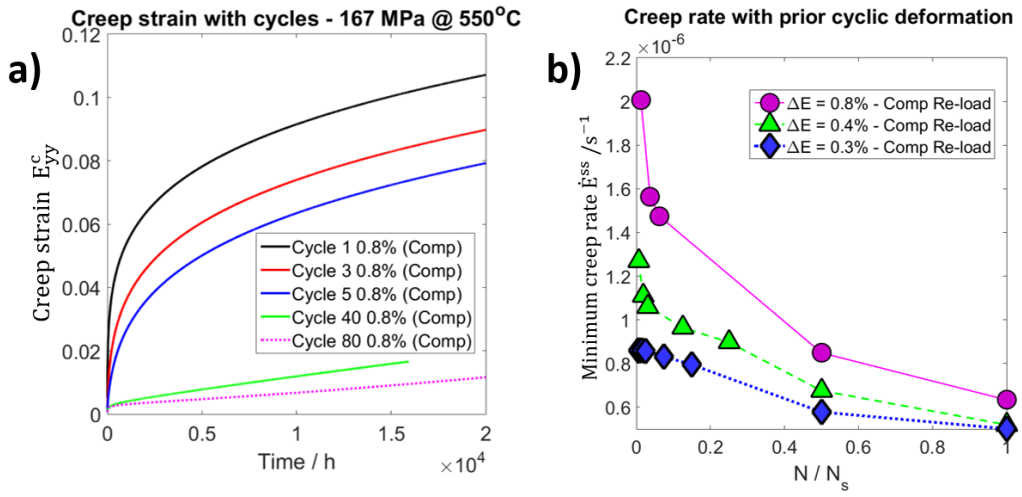


Figure 3.8. a) Model predictions of creep strain accumulation with different number of prior cycles at ΔE = 0.8%. b) Predicted variation of minimum strain rate with N / N_s for the three strain ranges examined.

3.4.2.2. Creep strain accumulation upon re-load from different macroscopic stress states

In the present section, the difference in creep strain accumulation during tensile dwells upon re-load from either a compressive (Fig. 3.7.a) or tensile (Fig. 3.7.b) stress state after cyclic plasticity is evaluated. In Fig. 3.9, the predicted accumulation of creep strain during tensile load-controlled dwells after prior cyclic loading to the 40th and 80th cycle at ΔE = 0.8% upon re-load from different macroscopic stress states is examined. The predictions in Fig. 3.9 illustrate that a lower amount of primary creep strain has accumulated during the tensile dwell upon re-load from a tensile macroscopic stress state, compared to re-load from a compressive stress state. The effect is more pronounced in fully-hardened samples deformed to the 80th cycle. Model predictions from Fig. 3.9 demonstrate a qualitative agreement with experimental results from Mamun [24] on solution treated (ST) Type 316H stainless steel at 650°C. In addition, Petkov et al. [132] simulated the deformation histories from [24] using the present SCM and established agreement with experimental data for the creep response during tensile dwells following re-load from different

stress states. As discussed in [132], employing the multi-scale SCM framework allows for a physical explanation of some of the observed trends discussed above.

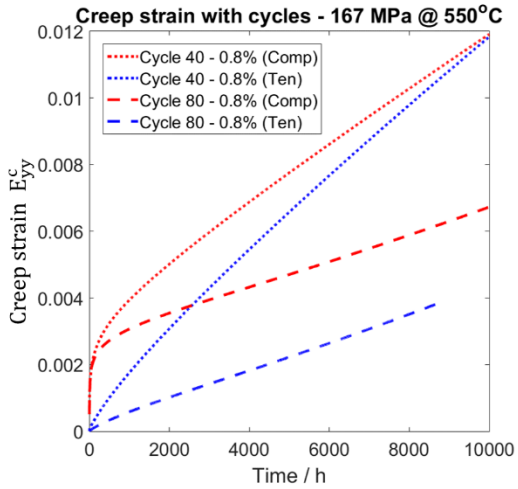


Figure 3.9. Differences in creep strain accumulation during tensile dwell at 167 MPa (ΔE = 0.8%) after prior cyclic loading to 40 and 80 cycles upon re-load from either tensile or compressive stress state.

The characteristic decrease in accumulated inelastic strain during primary creep with prior cyclic deformation, noted in Fig. 3.8.a), is also evident in Fig. 3.9. The phenomenon is associated with evolution of the dislocation microstructure. During cyclic deformation, the spacing between dislocation junctions in the material is reduced as part of the continuous interaction between hardening and dynamic recovery [24]. This refined dislocation network allows the balance between hardening and thermal recovery during subsequent creep to be reached quicker, since the rate of thermal recovery is greater for the higher dislocation densities [29]. Both of these phenomena are captured within the micromechanical model. On the other hand, the elimination of primary creep during tensile dwells upon re-load from a macroscopic tensile stress state is associated with the intragranular Type II residual stress. During inelastic deformation of the aggregate, micro-yielding in some grain families redistributes load to elastically-deforming grains. The induced mismatch strains between the grains and the surrounding matrix results in the

development of intragranular residual stresses, which in turn assist the subsequent generation of inelastic strain within the grains. The mismatch is eventually attenuated when the majority of grains deform inelastically, compatibly within the aggregate, and the residual stress state reaches a steady-state. This evolution of residual stress state has been observed to control the deformation response, e.g. giving rise to a Bauschinger effect during monotonic load-reversals in Type 316H by Hu et al. [87] and Hu and Cocks [50]. The evolution of the Type II residual stress state in the crept, peak-hardened samples reloaded from both tensile and compressive macroscopic stress states from Fig. 3.9 are compared. Comparison between the residual stress states at i) the end of the 80^{th} cycle, ii) the start of the creep dwell and iii) the secondary creep regime, revealed that the same process from [50,87] controls the difference in creep response in Fig. 3.9. The Type II residual stress state at Position 4 (macroscopic tension) in Fig. 3.7.b) was found to resemble closely the residual stress state predicted during the secondary creep stage in the tensile dwell. Hence, a suitable intragranular stress state already exists at maximum tensile strain (Position 4) allowing compatible plastic deformation during the creep dwell. At Positions 2 (macroscopic compression) and 3 (prior to tensile dwell), however, the Type II residual stress state is different to the steady-state residual stress state during the tensile dwell. As noted in [6], the distribution and magnitude of Type II residual stress in the grains at Position 2 is the same as that at Position 4, but has opposite sign. Hence, the residual stress state redistributes during the initial stages of the tensile creep dwell following re-load from a compressive stress state until the steady-state compatible residual stress state is achieved. As already mentioned, the stress redistribution process is associated with incompatible plastic deformation, i.e. accumulation of inelastic strain during the primary creep stage following the change of load. Note that the detailed evolution of residual stress is not presented here, since the focus of this chapter is on the macroscopic response of the material. The

observations, however, demonstrate that the primary creep regime in the material is controlled by the evolution of the dislocation microstructure, as well as the evolution of the intragranular residual stress state. This is further discussed in Section 3.5.

Another aspect of the difference in creep strain accumulation with prior cyclic deformation is the effect of stress level. Ajaja and Ardell [130] suggest that the effect of prior cyclic hardening on the minimum creep rate during a subsequent dwell is weaker at higher stress. To examine this effect, another deformation history is studied using the SCM. A sample is cyclically-loaded at a given strain range; again, the cycle ends in either a compressive or tensile macroscopic stress state. At peak hardening, the sample is unloaded and a tensile creep dwell is carried out at a dwell stress $\Sigma_{dwell} < \Sigma_{sat}$. The ratio between the minimum creep rate for non- and fully-hardened samples from Section 3.4.2.1, f_c, is evaluated in Table 3.3. The trend in f_c with strain range at higher stresses similar to that from Section 3.4.2.1 for creep dwells at lower stresses (140-167 MPa). This disagreement between model predictions and findings from [130] suggests the need for further experimental evaluation of the considered histories. Such experiments could either confirm the predicted response or identify missing features in the SCM. Further discussion is outside the scope of this thesis. Of interest, however, is the deformation behaviour for the plant-relevant strain range ΔE = 0.3% and dwell stress $\Sigma_{dwell} = 170$ MPa (Σ_{sat} = 196 MPa), given in Table 3.3. The predicted creep response suggests that, for shorter strain ranges relevant to plant operation, the creep response during a tensile dwell, following re-load from a compressive state of stress, resembles closely the creep response during a tensile dwell, following elastic unloading and re-load from a tensile state of stress. Hence, no modifications of the existing models in assessment procedures are required to address the difference in creep strain accumulation during dwells upon re-load from different stress states, if they are to be applied at strain ranges <0.3%.

Table 3.3. Trend in f_c for fully-hardened samples at $\Sigma_{dwell} < \Sigma_{sat}$; re-load from opposite stress state and ΔE.

ΔE ; Σ_{dwell}	Σ_{sat}	Sat. cycles	$f_{c,com.re-load}$	$f_{c,ten.re-load}$
0.3%; 170 MPa	196 MPa	200	0.75	0.75
0.8%; 240 MPa	275 MPa	80	0.32	0.36

3.4.3. Cyclic-creep deformation histories with dwells at each cycle

3.4.3.1. Modelling cyclic deformation histories with displacement-controlled dwells

In the present section, the SCM is employed to evaluate the cyclic response of Type 316H under cyclic deformation histories with displacement-controlled dwells (no elastic follow-up), introduced at the maximum tensile strain position $E^{max,tens}$ of every cycle. An experimental data set on the deformation response during this cyclic-creep history for dwell durations of 1-100 hours at strain ranges ΔE = 0.6-1.2% is provided by EDF Energy [14]. Based on the available experimental data and plant-relevant strain ranges of ΔE < 0.4%, the SCM is employed here to examine strain ranges which capture both experimental- and operation-relevant histories (i.e. ΔE = 0.2%~0.8% and dwell times varying from 1 to 1000 hours). This systematic study allows direct comparison between SCM predictions, experimental data and hysteresis-loop modification advice, provided in the R66 data handbook. Once an agreement is established with experimental results for dwells <100 hours, the physically-informed model is used to assess the effect of longer plant-relevant dwells.

Examples of the predicted hysteresis loop at strain ranges of 0.3% and 0.8% for relaxation dwells of 24 and 1000 hours are shown in Fig. 3.10, and compared to the hysteresis loops in the absence of dwells. The model captures the progressive softening of saturated stress amplitude with increasing dwell duration. In addition, the predictions illustrate a decrease in number of cycles to saturation of the hysteresis loop for longer dwells, qualitatively agreeing with [14].

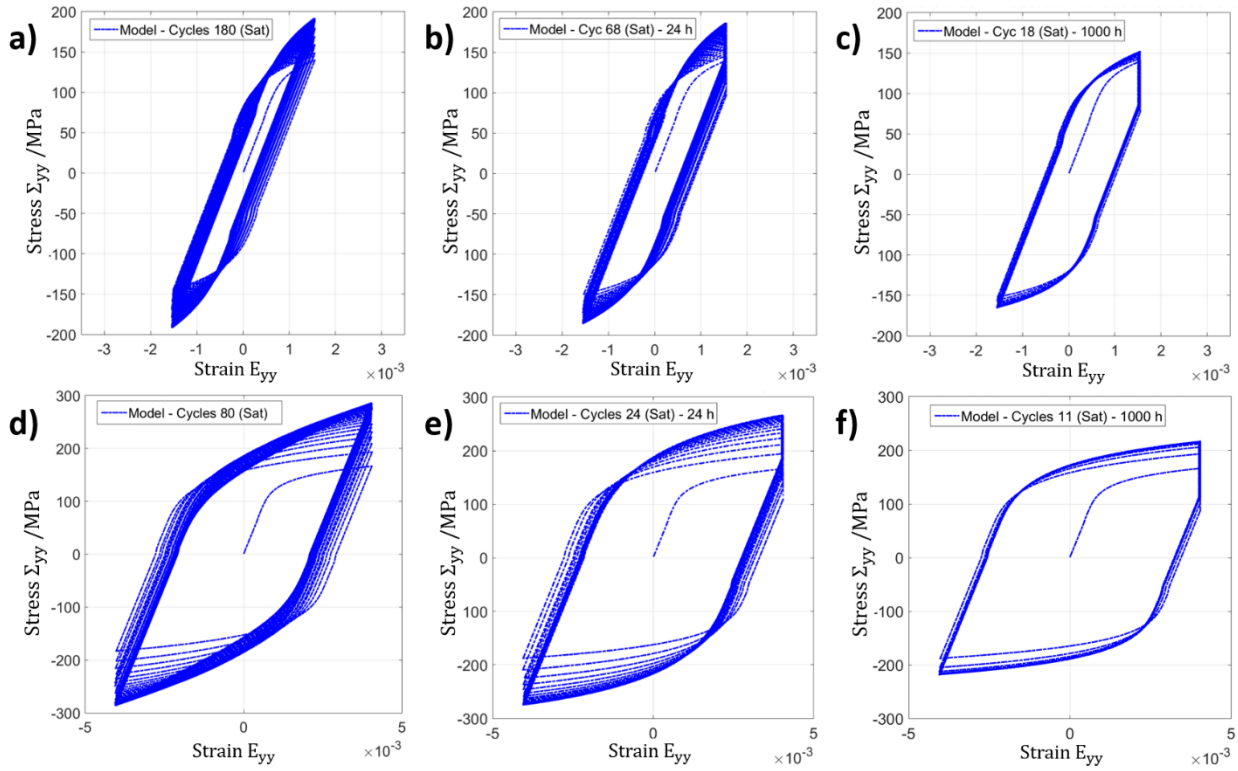


Figure 3.10. Predicted hysteresis loops at ΔE = 0.3% for a) pure fatigue and relaxation dwells at maximum tensile strain position of b) 24h and c) 1000h. The equivalent predictions at ΔE = 0.8% are shown in d)-f).

Examination of the microstructural evolution during the dwell demonstrated an increase in the spacing of dislocation junctions as a result of thermal recovery, in agreement with observations in [132]. This results in fewer obstacles to dislocation motion during the tensile-compressive cycle upon re-load after the dwell, manifesting itself in the observed softening of the hysteresis loop. Predictions across different strain ranges for the saturated stress amplitude and how this varies with inelastic strain, i.e. the sum of creep strain during the dwell and the plastic strain accumulated during the cyclic loading part of the history, are compared in Fig. 3.11.a) with experimental results at ΔE = 0.6% from [14]. The model correctly predicts the relation between inelastic strain, dwell time and saturated stress amplitude. Greater amounts of creep strain are accumulated at longer dwells resulting in a more pronounced decrease in the saturated stress amplitude. The trends of higher saturated stress with increasing strain range and inelastic strain accumulation with

increasing duration are also captured. Due to the physical nature of the model and the agreement with experimental data over dwell times <100 hours, model predictions could provide insights into the response during histories with dwell periods ~1000 hours (i.e. beyond experimental data).

Comparison between SCM predictions and R66 advice (which provides a multi-cast experimental data fit) on the modification of saturated stress amplitude with inelastic strain and dwell time is made in Fig. 3.11.b). In cases where the assessment is focused on fatigue, the SCM modelling predictions suggest that the R66 advice could be non-conservative in terms of the accumulation of inelastic strain. Both the experimental data and SCM predictions confirm the lack of conservatism in the R66 advice on the prediction of inelastic strain accumulation for such histories. In high-temperature power-plants, the deformation histories are dominated by the creep response (i.e. longer dwells) and prediction of the softening of the hysteresis loop due to creep is essential. No experimental data for 1000-hour dwells are available at present. Based on the general agreement of the SCM with experimental data for dwells of 1-100 hours, modelling predictions suggest that the R66 advice on reduction of Σ_{sat} will remain conservative for dwell durations <1000 hours. Nevertheless, the R66 advice significantly underestimates the softening of saturated stress amplitude. At 0.3% strain range, the predicted decrease in Σ_{sat} from that at pure fatigue to a history with a 1000-hour dwell is ~25 MPa compared to ~75 MPa, predicted by the SCM. An overestimation of the dwell stress could result in a conservative underestimation of the creep strength of Type 316H stainless steel when using stress-modified ductility exhaustion damage assessment approaches [142]. Experimental data on the creep strength of ex-service material at 550°C, provided by EDF Energy, indicate that failure time increases by a factor ~10 with a decrease in applied stress of 50 MPa (see Chapter 7). Hence, creep strength could be under-estimated by a factor of ~10, when following the R66 data handbook approach.

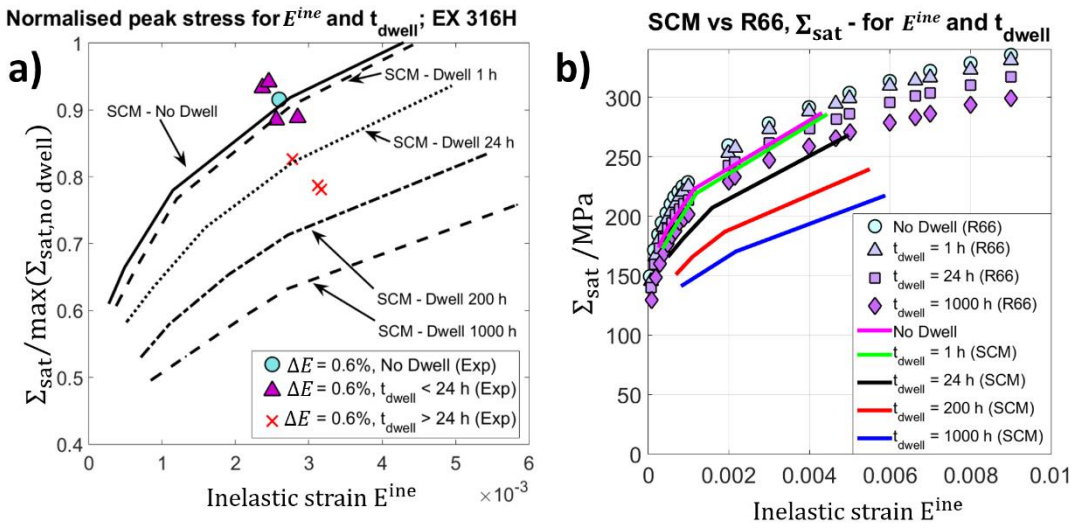


Figure 3.11. a) Comparison between experimental results (Cast 69431) on Σ_{sat} with E^{ine} at ΔE = 0.6% and SCM predictions. b) Comparison - R66 and SCM predictions on Σ_{sat} with E^{ine} and dwell time.

The effect of varying the relaxation dwell position in the cycle on the saturated stress amplitude Σ_{sat} of the hysteresis loop is also examined. This cyclic-creep history is highly-relevant to plant operating conditions where dwells may not always be at the maximum tensile strain position. However, models in assessment procedures do not provide any advice on modification of the hysteresis loop with dwell positioning. The SCM framework is employed here in the same manner demonstrated in Fig. 3.10 to examine the response when the dwell is positioned at E = 0.0%, for strain ranges between 0.2% and 0.8% and dwell times of 1-1000 hours. The predicted cyclic hysteresis loops of the material at strain ranges of 0.3% and 0.8% for relaxation dwells of 24, 200 and 1000 hours are shown as examples in Fig. 3.12. Faster saturation of the hysteresis loop with longer dwell times is again predicted. However, for dwells at the E = 0.0% position, the saturation of the cyclic response is reached after a greater number of cycles to saturation, as compared to when the dwells are at the maximum strain level. This is shown in Fig. 3.13.a).

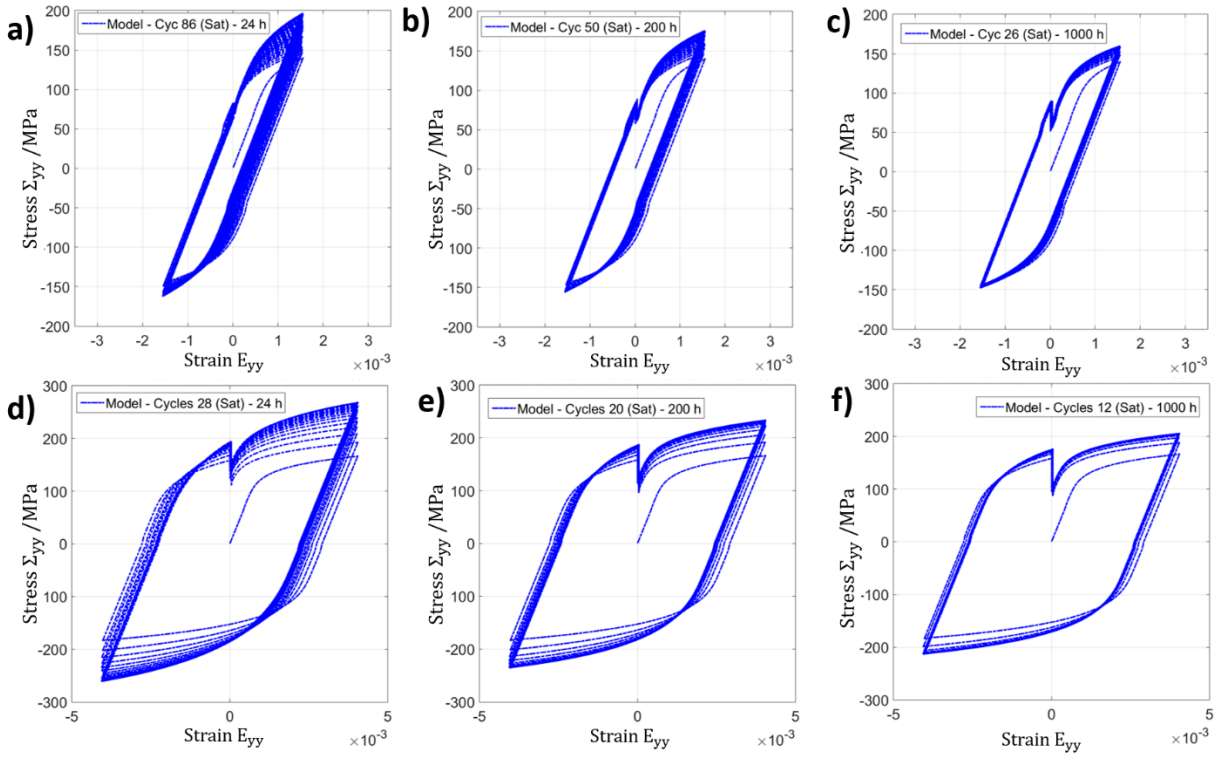


Figure 3.12. Predicted hysteresis loops at ΔE = 0.3% for a) 24-hour, b) 200-hour and c) 1000-hour relaxation dwells at 0.0% strain position. The equivalent predictions at ΔE = 0.8% are shown in d)-f).

Comparison of the predicted variation in saturated stress with inelastic strain and experimental data on the same ex-service cast of 316H stainless steel at ΔE = 0.6% for 24-hour dwells at E = 0.0% and $E^{\max,tens}$ [14] is made in Fig. 3.13.b). The agreement between SCM predictions and experimental data demonstrates that the softening effect on saturated stress is weaker for mid-strain dwells, which is expected due to the lower start-of-dwell stress, confirming the hypothesis from [14]. The softening effect of thermal recovery scales with the spacing of the dislocation junctions (Eq. 2.16), whose value upon the start of the dwell is determined by the start-of-dwell stress. Although not presented, it is found that the initial dislocation junction density is higher for dwells at the $E^{\max,tens}$ position or peak stress, due to the greater degree of hardening induced, as compared to intermediate dwells. The subsequent rate of thermal recovery during the dwell is lower for intermediate dwells. Hence, the softening effect of intermediate dwells (or rate

of stress relaxation) on continuing cyclic deformation will be lower, as compared to dwells positioned at peak stress.

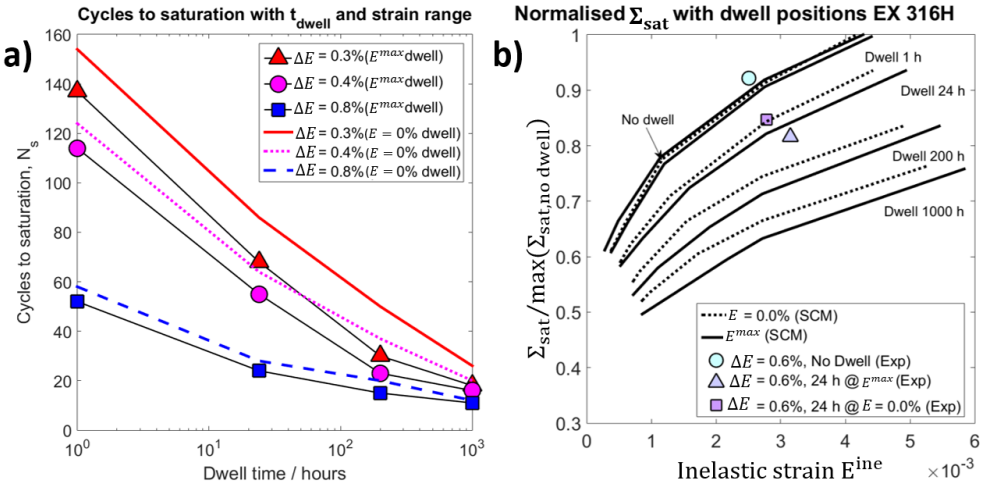


Figure 3.13. a) SCM predictions of cycles to saturation with different cyclic-dwell histories and strain ranges. b) Experimental data on Σ_{sat} at ΔE = 0.6% and SCM predictions for different dwell positions.

Several aspects of existing assessment approaches can be improved from the model predictions. The R66 advice is informed by short-term creep dwell experimental data. As discussed above, the degree of softening is underestimated to ensure that the practical advice remains conservative. The findings from Figs. 3.11.b) and 3.13.b) illustrate that the SCM could be used systematically to construct an empirical extrapolation framework for the decrease in saturated stress amplitude with dwell time and dwell position with respect to strain for different ΔE. The pure fatigue response could be used as reference. This framework could be implemented within the R66 advice and lead to a decrease in the degree of conservatism in estimation of the start-of-dwell stress. Direct improvements using the SCM could be made in another aspect of the practical advice. Constitutive models in assessment procedures are incapable of predicting the evolution of accumulated inelastic strain during dwells at each cycle, i.e. creep response during a dwell at a given stress and duration is assumed the same as that during an equivalent dwell without prior cyclic history. SCM predictions of creep strain accumulation during a dwell in a cyclic history at

a given stress and duration from Fig. 3.10 in the range ΔE = 0.3-0.8% and 24-1000 hours ($E^{c,dwell(\sigma_0,t)}$) are compared to additional predictions of accumulated creep strain during equivalent relaxation dwells with the same duration and start-of-dwell stress, but without any prior plasticity ($E^{c,monoton(\sigma_0,t)}$). Based on this, a factor $f_d = E^{c,dwell(\sigma_0,t)} / E^{c,monoton(\sigma_0,t)}$ is introduced and quantified as a function of N / N_s in Fig. 3.14. Significant differences are expected between the accumulated creep strain during actual dwells to saturation and the creep strain accumulated during the equivalent creep dwells without prior history. This is illustrated for lower strain ranges and shorter dwell times by the predicted variation of the numerical factor f_d in Fig. 3.14. The practical approach of using an equivalent dwell without considering the effect of prior history appears to be conservative for short strain ranges by overestimating the creep strain during the dwell. The difference diminishes for longer dwells and larger strain ranges.

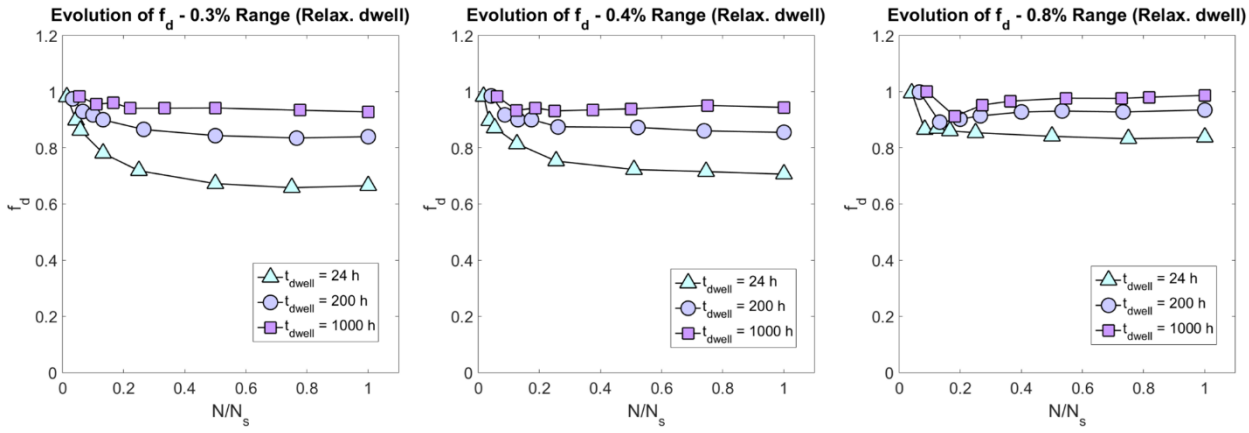


Figure 3.14. Evolution of f_d with ΔE, N/N_s and t_{dwell} for relaxation dwells at maximum tensile strain.

The decreasing difference between the actual response and the practical approach is believed to be due to the greater tendency for re-initiation of the primary creep stage ("re-priming") at larger strain ranges [132]. Fig. 3.14 illustrates that at full saturation for ΔE = 0.3% and dwell durations of 1000 hours, estimation of the dwell creep strain obtained via the practical approach

could be overestimated by ~10%. At shorter dwell times this difference increases, e.g. for a 24-hour dwell at ΔE = 0.3% and N / N_s = 1.0 the creep strain could be overestimated by approx. 35%. These findings demonstrate that the ratio f_d could be employed in assessment procedures. Its value could be used as a multiplier on the creep strain for equivalent dwells with the aim to reduce the conservatism in creep strain estimation during dwells. This approach and the tendency for primary creep re-initiation during subsequent dwells is further examined in Section 3.4.3.2.

3.4.3.2. Modelling cyclic deformation histories with load-controlled dwells

In this section, the interaction between cyclic and creep deformation during a loading history similar to that experienced by components, such as thin-walled pipes and pressure vessels, is examined [1]. The history comprises of cyclic loading to a particular stress level, followed by a load-controlled creep dwell with a constant ΔE load reversal after the end of the dwell (N.B. Σ_{dwell} is the same at each cycle). During such histories, large amounts of inelastic strain could be accumulated in the material. The R5 procedure for damage assessment advises the user to consider two practical approaches for estimation of accumulated creep strain during dwells:

a) Assuming that cyclic deformation causes complete removal of primary creep during dwells (e.g. a 9000-hour dwell equivalent to 9 dwells of 1000 hours, no "re-priming");

b) Assuming that primary creep stage is fully re-initiated during each dwell (e.g. E^c during nine 1000-hour dwells equal to $9 \times E^c$ during the first 1000-hour dwell).

The SCM is employed here to examine which of the two practical assessment approaches a) and b) provides the most reasonable prediction of the accumulated creep strain during the actual cyclic-creep history across different strain ranges and dwell durations. Strain ranges between 0.3% and 0.8% and dwells of duration between 24 and 1000 hours are examined. Two examples of the

predicted stabilised cyclic response for ΔE = 0.3% with different dwell durations are shown in Fig. 3.15. The corresponding creep strain accumulation during selected dwells shown in Fig. 3.16.

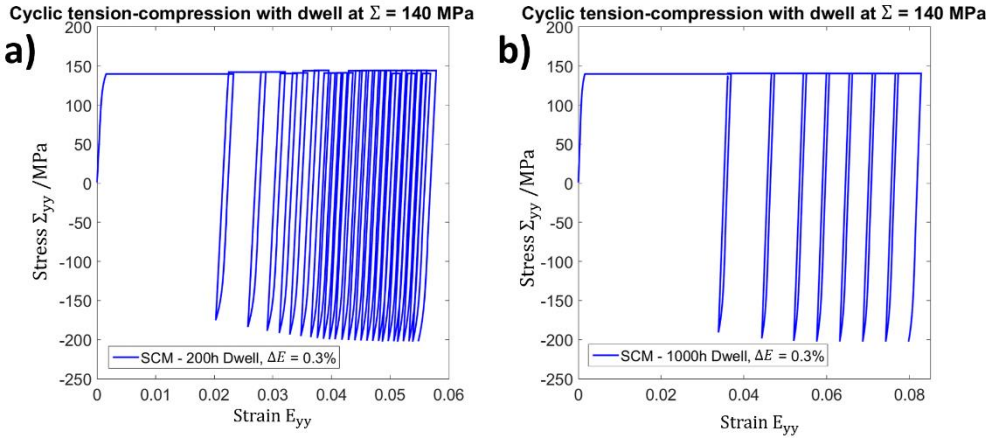


Figure 3.15. Predicted creep-cyclic response; ΔE = 0.3%, load-controlled dwells of a) 200 h and b) 1000 h.

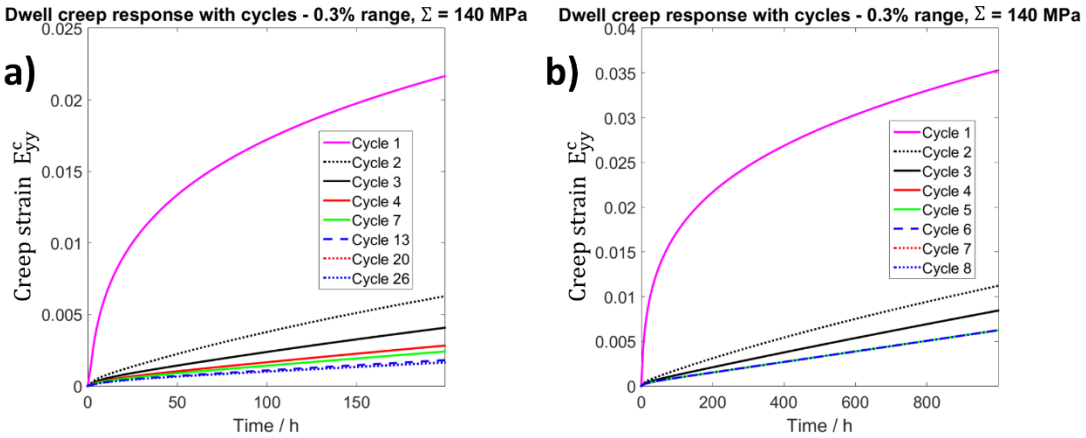


Figure 3.16. Predicted creep strain accumulation during load-controlled dwells at different cycles (ΔE = 0.3%) for a) 200 h and c) 1000 h.

The normalized parameter f_d is evaluated for the load-controlled dwell history examined in this section. Load-controlled dwells result in the accumulation of greater inelastic strains during the cycle since Σ_{dwell} is constant. By contrast, during the displacement-controlled dwells from Section 3.4.3.1, stress relaxation during the dwell causes a continuous decrease in stress and, respectively, a decrease in creep strain rate during the dwell. Accumulation of greater inelastic strains leads to more pronounced hardening induced in the microstructure during load-controlled dwells. This causes a substantial decrease in the primary creep rate during subsequent cycles, as

compared to the reference primary creep rate during the first cycle. This is illustrated in Fig. 3.17. The value of f_d for load-controlled dwells at $N / N_s \approx 0.5$ is of the order of 0.1-0.3. This is lower than that estimated for the displacement-controlled dwells in Fig. 3.14 by a factor of ~3. In effect, the simulation results suggest that the estimated extent of creep damage during dwells would be overestimated by a factor of 3-10 when assessment approach b) is adopted to assess the histories from Fig. 3.15. This observation highlights the conservatism of approach b) in estimation of accumulated creep strain when the assessment procedure assumes full "re-priming".

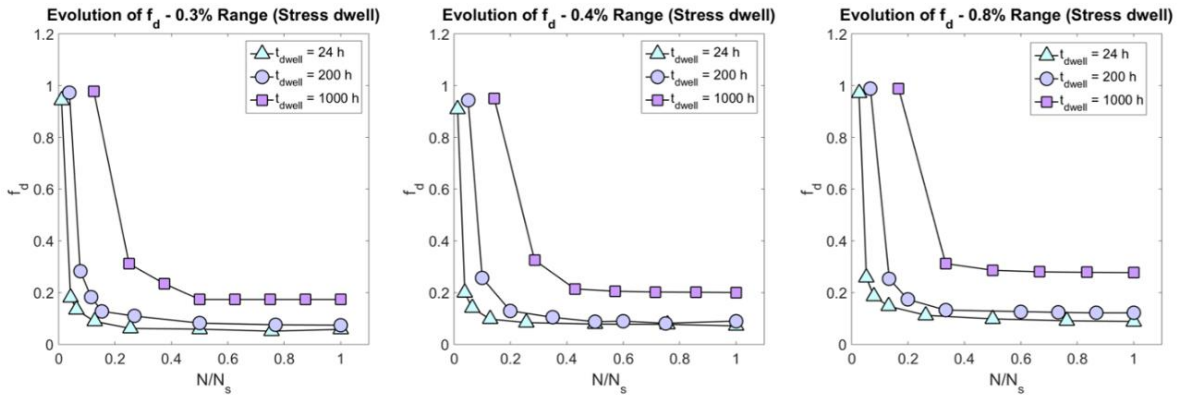


Figure 3.17. Evolution of f_d with ΔE, N/N_s and t_{dwell} for constant-stress dwells at maximum tensile strain and constant strain range load reversal.

In order to assess the suitability of approaches a) and b), a particular deformation history with a cumulative dwell duration of 9000 hours is examined. Note that three different cases are considered: 9 cycles×1000-hour, 45 cycles×200-hour and 375 cycles×24-hour dwells. Based on the simulated creep response of the three histories during each dwell, the total creep strain obtained via the practical approaches a) and b) is computed and compared in Table 3.4 to the accumulated creep strain during the actual histories, predicted by the SCM. The comparison in Table 3.4 illustrates that the difference between the predicted creep strain using the practical approaches and the actual simulated history is strongly dependent on dwell duration and strain range. In all cases examined, approach a) underestimates the accumulated creep strain and remains non-conservative,

whereas approach b) is overly-conservative. The actual-dwell history simulated response falls in between the two extremes. For dwells of 24-200h the modelling results demonstrate that approach a) becomes increasingly non-conservative with differences of ~35% for 200-hour dwells at ΔE = 0.8%, and ~65% and 80% for 24-hour dwells at ΔE = 0.3% and 0.8%, respectively. Approach a) estimates the accumulated creep strain for 1000-hour dwells with a reasonable degree of accuracy across all strain ranges with a difference ~10% since the extent of primary creep diminishes significantly with plastic loading (see Section 3.4.2). On the other hand, approach b) overestimates the accumulated creep strain by a factor of 3 for the history of 9×1000-hour dwells across all strain ranges considered. For shorter dwells, the accumulated creep strain is overestimated by approach b) by factors of 10 and 7 for the 45×200h history, and 14 and 11 for the 375×24h history at ΔE = 0.3% and 0.8%, respectively. The results in Table 3.4 illustrate that the discrepancies between the approaches and actual simulated response increase for shorter dwell periods (<1000 hours). This is associated with the balance between hardening and thermal recovery of the dislocation structure during the primary creep stage in each dwell. For shorter dwells, e.g. 24 hours, the effect of thermal recovery is limited. The hardening during initial stages of the dwell is more pronounced over a given time period. This causes a further decrease in the creep rate during subsequent dwells, in addition to the hardening induced from cyclic hardening outside the dwell. Hence, the accumulated creep strain during primary creep in the actual dwell response will progressively decrease as compared to the primary creep response during the reference first-cycle dwell, considered in approach b). By contrast, the accumulated creep strain during such shorter dwells is still greater than that assumed during a single dwell in approach a). Nevertheless, model predictions from this section indicate that approach a) results in reasonable predictions of the accumulated creep strain during load-controlled dwells. Modification of approach b) by incorporating the parameter f_d from

Fig. 3.17, as a multiplier on the accumulated creep strain with cycles, could improve the assessment accuracy of accumulated creep strain.

Table 3.4. Creep strain accumulation for ΔE = 0.3-0.8% after 9×1000-hour, 45×200-hour and 375×24-hour stress dwells and comparison with approaches a) and b) for the three different 9000h histories.

ΔE / Σ_{dwell}	Accumulated macroscopic creep strain						
	9000-hr dwell (a)	9×1000-hr		45×200-hr		375×24-hr	
		Approach (b)	Actual (SCM)	Approach (b)	Actual (SCM)	Approach (b)	Actual (SCM)
$0.8\%, 167\ MPa$	0.157	0.456	0.172	1.61	0.24	7.19	0.69
$0.4\%, 150\ MPa$	0.109	0.370	0.116	1.16	0.14	4.74	0.41
$0.3\%, 140\ MPa$	0.087	0.317	0.092	0.97	0.10	3.68	0.25

3.5. DISCUSSION

3.5.1. Enhanced version of SCM

The five fitting parameters in the enhanced version of the multi-scale SCM can be determined from four different loading conditions, namely elastic-plastic monotonic, forward creep, cyclic and relaxation deformation, as described in Section 3.1.3. These parameters are motivated from the essential physics of the different processes considered. As shown in Section 3.4, employing such a micromechanically-based model allows a clearer understating of the physical phenomena, responsible for the deformation response in Type 316, to be gained.

Predictions of relaxation behaviour using parameters obtained from fitting the model to forward creep data suggest that the micromechanical deformation process is the same under load- and displacement-controlled high-temperature loading at prolonged periods. The parameter α_0 (Eq. 2.17) which controls the activation energy for dislocation bypassing sets of obstacles, hence the overall effectiveness of obstacles, is found to control the deformation response. Frost and Ashby [90] provide guidelines for selecting α_0 through mechanistic considerations: $2 > \alpha_0 > 1$ for strong obstacles (precipitates), $\alpha_0 < 1$ for medium obstacles (dislocation junctions) and $\alpha_0 <$

< 0.1 for weak obstacles (solute atoms). The parameter α_0 should be treated as a physical constant, which can be tuned depending on the material examined. It was demonstrated in this chapter that accurate predictions of both forward creep and relaxation behaviour are obtained when α_0 is at the mid-to-lower end of the physical range identified in [90]. This indicates that the major contribution to obstacles to dislocation motion in Type 316H are dislocation junctions, together with a moderate contribution of solute atoms. Initial relaxation transients, associated with thermally-activated glide, and the subsequent steady-state relaxation regime, controlled by thermal recovery of the dislocation structure, are captured better with the thermal activation parameter employed here.

Cyclic deformation is captured by the SCM through the incorporation of the simplistic physical dynamic recovery model. The enhanced SCM describes the change in microstructural state during hardening and dynamic recovery, as well as the evolution of internal residual stress state, both of which influence the macroscopic response of the aggregate. The extent of dynamic recovery increases with accumulation of inelastic strain, which affects the local stress state and global response. It is important to note that in this study no dislocation cell formation within the grains was assumed, since at the temperature range of interest no distinct cell structures have been observed experimentally [72]. Cell formation at higher temperatures (>625°C) will alter the dynamic recovery process. At these temperatures, the dynamic recovery model employed in this study may not produce accurate predictions.

3.5.2. Evolution of creep-cyclic response with internal state and residual stress

The simulation results from Section 3.4 confirm the effect of prior cyclic deformation on reducing the extent of primary creep and the minimum creep rate in austenitic Type 316H stainless steel, agreeing with [67]. The phenomena were associated with refinement of the dislocation structure due to prior cyclic deformation, agreeing with [67,68]. In addition to the microstructural evolution,

it is demonstrated that the extent of the primary creep stage is dependent on the redistribution of Type II intragranular residual stresses. Model predictions from Section 3.4.2.2 and Petkov et al. [132] demonstrate the disappearance of primary creep in dwells for which the prior deformation history has already established a suitable residual stress field for compatible plastic deformation of the aggregate, agreeing with [50,87]. Model predictions suggest that the phenomenon is more significant under larger strain ranges and negligible under plant-relevant strain ranges (0.3%). In theory, simplistic models employed in assessment procedures could capture the phenomenon in an empirical fashion by considering the contribution to internal resistance by isotropic and kinematic hardening terms (Section 2.1.3.1). However, in the SCM, the internal resistance and intragranular residual stress field, which the isotropic and kinematic hardening contributions resemble in an empirical way [50], are determined from the detailed physics of the deformation process and interactions between elastic-plastic anisotropic grains. Employing isotropic and kinematic hardening terms requires fitting these to particular deformation histories. This does not ensure the accurate capture of the response during different loading scenarios, particularly if these lie outside the range of experimental data used to fit parameters in the model.

The extent of decrease in Σ_{sat} during cyclic histories, interrupted by creep dwells, increases with dwell time due to thermal recovery of the dislocation network. Longer dwells result in a greater extent of softening of the hysteresis loop. During shorter dwells hardening dominates over thermal recovery and the post-dwell response during re-load is harder (e.g. the 24-hour mid-strain dwell at ΔE = 0.3%, Fig. 3.12.a.). Thermal recovery is also responsible for the faster saturation of the hysteresis loop in the presence of dwells. This is because it acts to increase dislocation junction spacing, allowing for a faster balance between hardening and dynamic

recovery to be achieved during cyclic loading. This aspect needs to be implemented in simplistic models in assessment procedures, if they are to capture the observed response during such histories.

Practical assessment approaches to quantify accumulated creep strain during cyclic-creep histories were examined in Section 3.4.3.2. Approach a), which does not consider any re-initiation of primary creep, provides a more sensible prediction for load-controlled dwells. Approach b), which assumes full "re-priming" for each cycle, is overly-conservative in predicting creep strain during load-controlled histories, the degree of which decreases for larger ΔE and longer t_{dwell}. Results from Fig. 3.14 demonstrate that, at ΔE > 0.3% and t_{dwell}=1000h, each displacement-controlled dwell resembles the relaxation response during a dwell with the same duration and start-of-dwell stress without prior deformation history. This is due to the persistency of rapid stress-drop during relaxation. This suggests that approach b) would result in a more sensible estimation of the accumulated creep strain during displacement-controlled dwells than approach a), especially at larger ΔE (e.g. the value f_d is over 0.85 for all dwell durations at ΔE = 0.8%). The applicability of the practical approaches is quantified in greater detail in Petkov et al. [134] and is omitted here for brevity.

3.5.3. Predictive capabilities and limitations of SCM

The chapter demonstrates various ways in which SCM predictions can inform the existing assessment procedures used in industry, particularly providing more insights into creep-fatigue interactions in Type 316H stainless steel under plant-relevant deformation histories. The model can be employed by industry in a systematic way to develop empirical extrapolation frameworks beyond the experimental data range. Such frameworks can serve to evaluate: i) changing creep properties due to prior cyclic hardening (parameter f_c in Section 3.4.2), ii) evolution of inelastic

strain accumulation during creep or relaxation dwells with cycles (parameter f_d in Section 3.4.3) and iii) softening of the hysteresis loop due to the presence of such dwells (Σ_{sat} with t_{dwell}, ΔE and relative position of dwells with respect to strain). Such extrapolation frameworks and parameters could be incorporated directly into the existing R5 procedure and R66 data handbook. This could ensure that simplified models, used in assessments, remain within reasonable extrapolation bounds while estimating component lifetimes.

A potential limitation of the SCM model is associated with the micromechanical models embedded within the framework. At the very long-term and low-stress regime (<100 MPa at 500-600°C), thermally-activated glide can become inhibited, but dislocation climb over intragranular second-phase particles could result in the accumulation of inelastic strain [143]. The coupling between dislocation glide and climb over obstacles is not considered in the present model, but could potentially control the deformation during low-stress creep exposures in plant conditions.

As described in [144], the developed SCM offers similar capabilities for predicting global inelastic deformation at lower computational cost than FE approaches, typically employed in industry to assess inelastic deformation under multi-axial loads. One of the major objectives of this thesis, however, is to study creep damage processes in polycrystalline Type 316H. Local damage development in the microstructure is an important pre-cursor to failure [111,145,146]. The SCM employed in this chapter does not capture strain localisation or stress concentrations in constrained regions between grains. To address this deficiency and to capture important local features of the deformation process, a higher-fidelity crystal plasticity FE framework, which incorporates the same micromechanical model from Section 2.5, is developed in Chapter 4.

3.6. SUMMARY

In this chapter, the SCM developed by Hu et al. [7,8,50,87] is enhanced to capture cyclic deformation and stress relaxation in addition to monotonic elastic-plastic deformation and forward creep. Once calibrated to elastic-plastic, forward creep, cyclic and relaxation deformation experimental data on Type 316H at 550°C, the model is employed to simulate plant-relevant creep-fatigue deformation histories. Better understanding of the physics behind cyclic-creep interactions in the material is provided within the strain ranges of 0.2% and 0.8% and creep dwell times >24 hours. The effect of prior cyclic deformation on subsequent creep response is evaluated and an explanation of the difference in creep response upon re-load from different stress states is given. The degree of softening of the hysteresis loop due to the presence of displacement-controlled dwells is quantified for different dwell durations, strain ranges and dwell positions. The suitability of practical approaches to quantify accumulated creep strain during histories with displacement – and load-controlled dwells is evaluated. The main findings in this chapter are:

1. The activation energy for thermally-activated glide has a significant effect on stress relaxation and forward creep. A value of $\alpha_0 = 0.18$ in Eq. 2.17, which controls the overall effectiveness of obstacles, was found to capture well the stress relaxation response in Type 316H from a fit to forward creep data. This value is consistent with the major contribution to internal resistance of this material being from dislocation junctions and solute content.
2. Incorporation of dynamic recovery in the model allows accurate prediction of the stress-strain response during cyclic loading. This is achieved through fitting the model to the saturated hysteresis loop after a number of cycles by adjusting the value of ΔL_r in Eq. 3.1.
3. The extent of primary and secondary creep stages decreases following prior cycling due to the induced hardening in the microstructure. Prior cycling, during which a suitable residual stress

field for compatible plastic deformation is established, results in a near-complete removal of primary creep during subsequent load-controlled dwells.

4. Primary creep is controlled by the evolution of both dislocation microstructure and residual stress state. Modelling results suggest that for plant-relevant strain ranges (~0.3%, 550°C) the creep response during a dwell will not be dependent on the stress state upon re-load.
5. The extent of softening of the hysteresis loop due to the presence of relaxation dwells is captured by the SCM. It is significantly underestimated by the R66 advice, where for dwell of 1000 hours at ΔE = 0.3%, Σ_{sat} is overestimated by ~50 MPa. This could underestimate the creep strength by a factor of ~10 using stress-modified ductility exhaustion damage models.
6. The weaker softening effect on the hysteresis loop for dwells away from the maximum tensile position is confirmed by SCM predictions. Systematic modelling of histories with dwells at different positions in the cycle can yield an extrapolation framework for the change in softening behaviour. This could be incorporated in the R66 advice to reduce conservatism.
7. The parameter f_d captures the ratio between the predicted creep strain accumulation during dwells i) in a cyclic history at given stress and duration and ii) at the same stress and duration without any prior history. The parameter can be computed by the SCM and employed directly in assessments, allowing for more accurate estimation of creep strain, generated during dwells.
8. Model predictions suggest that practical approach a) of Section 3.4.3.2 for estimation of accumulated creep strain during dwells (no "re-priming") results in sensible predictions for load-controlled dwells. The accuracy of this approach increases when the assumed 1st-cycle dwell resembles closely the actual duration of the dwells examined. Practical approach b) of Section 3.4.3.2 could produce sensible predictions for displacement-controlled dwells.

CHAPTER 4

DEVELOPMENT OF CRYSTAL PLASTICITY FINITE ELEMENT MODEL AND COMPARISON TO SCM FRAMEWORK

4.1. INTRODUCTION

4.1.1. Deficiencies of SCM frameworks

The first-order multi-scale SCM framework of Budiansky and Wu [78] employing a crystal plasticity model, developed by Hu and Cocks [7,50], was improved as part of this study. It was then used in Chapter 3 to study the deformation response of Type 316H stainless steel under typical power plant thermo-mechanical loading histories. The SCM captures the evolution of intragranular residual stress and internal resistance with contributions from the dislocation microstructure, precipitates and solute distributions. This allowed for accurate predictions of macroscopic deformation and a physical explanation of the complex cyclic-creep interactions during such histories. Predictions of this SCM also agree with experiments on mesoscopic lattice strains and the global response under monotonic plasticity and creep of ex-service (EX) and solution treated (ST) material, as demonstrated in [7,8,50].

The employed SCM in this study is an averaging scheme treating the grains as anisotropic elastic-plastic inclusions in an isotropic elastic matrix (KBW SCM framework). This methodology is different to the approach by Hill [79] and Hutchinson [80], where the inclusions are embedded in an elastic-plastic homogeneous matrix. As discussed in Chapter 2, by bypassing the need to define the instantaneous tangent modulus of the matrix, the assumption of an elastic homogeneous matrix adopted here allows a more straight-forward implementation of micromechanical plasticity

models within the inclusions. It was demonstrated in Chapter 3 that predictions via this KBW averaging scheme are in agreement with experimental results during complex thermo-mechanical loading histories, giving rise to moderate plastic strains. Although predictions of the macroscopic response and lattice strains in grain families using this first-order (FO) SCM agree with experimental results, local grain-to-grain interactions and strain incompatibilities are not explicitly captured. This is due to the assumption of uniform grain stress and strain fields [135], and that each grain is surrounded by a material with the average properties of the polycrystalline material. To capture intragranular field variations in polycrystalline SCM schemes, novel second-order (SO) homogenization schemes have been developed recently in [147–154]. A SO homogenisation model by Ponte Castañeda [150] was employed in [147,148] to describe the deformation behaviour of viscoplastic FCC and HCP single crystals with the predictions of statistical variations in stress and strain fields agreeing well with full-field FE results. Note that the second-order homogenization schemes, developed in [147–154], are based on the existence of a potential for the constitutive response. These schemes have been successfully applied to model monotonic, proportional loading histories, e.g. in [147]. Dohgri et al. [155] demonstrated a limitation of one such higher-order homogenization scheme in capturing the Bauschinger effect in a two-phase steel. The scheme employed in [155] otherwise yielded agreement with full-field solutions and experiments under monotonic loading. This demonstrates that further work is required in this field to generalize such higher-order homogenization approaches to general loading scenarios of interest to this study.

The focus in Chapter 3 was to simulate the response of Type 316H stainless steel under cyclic loading histories with creep dwells during which the material creeps or the stress relaxes. In these situations, capturing the detailed evolution of microstructure and intragranular residual stress

state is essential for determining the overall material response. The FO SCM in Chapter 3, which adopts a physical micromechanical model, captures the main features of these processes and is more feasible than SO schemes to represent the macroscopic response during such loading histories. The remainder of this thesis focuses on investigation of the combined creep deformation and damage response of the material. Localised grain deformation and damage development are essential for understanding the processes leading to failure in polycrystals [43]. These are strongly influenced by short-range grain-to-grain interactions and irregularity in grain shapes. This is not captured by polycrystalline averaging schemes and poses the requirement for development of higher-fidelity modelling approaches.

4.1.2. Motivation for development of CPFE modelling frameworks

With advances in computational power, crystal plasticity finite element (CPFE) methods are being used increasingly. They provide extensive insight into the effects of grain morphology and relative crystallographic orientations on localized behaviour at grain boundaries, intragranular stress fields, etc. [43]. Pierce et al. [156] and Asaro and Needleman [44] investigated the deformation of anisotropic single crystals and polycrystalline aggregates via CPFE approaches, establishing robust numerical techniques as the basis and guidelines for future studies, e.g. [157,158]. CPFE approaches subsequently gained popularity in describing grain-to-grain interactions and effects of the redistribution of mesoscale residual stress fields on global behaviour of polycrystalline aggregates. These approaches demonstrate that local field variations and stress redistribution between anisotropic grains have a significant effect on global deformation and failure response, e.g. [135,159,160]. Understanding localized damage formation and evolution in polycrystalline materials has been a long-standing problem, and crystal plasticity methods provide a feasible approach to gain better understanding of the factors controlling microscopic and global failure

processes. Dunne et al. [160] investigated cold-dwells in Ti-alloys through a physically-based CPFE model noting the importance of local residual stress evolution in determining the macroscopic response during strain-controlled dwells. Findings from [160] on the stress redistribution process between "hard-soft" grain configurations and slip localization indicate that locations associated with stress concentrations in the vicinity of certain grain boundaries or within grains are possible crack formation sites, agreeing with [161]. Studies by Srivastava and Needleman [162], Liu et al. [163], Wei and Anand [164] and Simonovski and Cizelj [165] used CPFE modelling to demonstrate the importance of stress triaxiality, slip localization, and grain morphology on the development of trans- and intergranular damage during monotonic plasticity in polycrystalline aggregates. Such modelling approaches have the potential to provide further understanding into intergranular creep damage in Type 316, as briefly discussed in Section 2.6. However, no unified, physically-informed polycrystalline CPFE framework exists, which captures the detailed deformation processes of both individual grains and grain boundaries during creep in Type 316. In the remainder of this thesis, a suitable framework will be developed and employed to model and assess the development of creep damage in this polycrystalline material.

The initial step in the development of such CPFE framework is presented in the remainder of this chapter. The detailed physical micromechanical model for Type 316 stainless steel, described in Chapter 2, is implemented within a large-deformation CPFE framework in Section 4.2. The predictive capabilities, level of information provided and practicality of the SCM and the CPFE framework in describing polycrystalline material deformation under monotonic elastic-plastic and short-term creep loading are assessed in Section 4.3. Another major objective of this chapter is to verify further the validity of the first order self-consistent model from Chapter 3. This will be achieved by comparing model predictions using the SCM with those from the CPFE

method and with experimental data. The effect of different grain morphologies on the predicted response is assessed in Section 4.4. In subsequent chapters, other features of the material behaviour, such as grain-boundary sliding and grain-boundary cavitation, are incorporated into the model.

4.2. IMPLEMENTATION OF MICROMECHANICAL MODEL INTO THE CPFE FRAMEWORK

In this section the setup of the CPFE modelling framework and examined polycrystalline geometries are introduced. The micromechanical model for Type 316, employed in Chapter 3 within the SCM, is incorporated at the slip system level within a large-deformation CPFE model. The numerical implementation of the constitutive model within a user-defined material (UMAT) routine in the FE software ABAQUS is given in Appendix A and in [144]. Note that the objective of this study is to compare the capabilities of a CPFE model with a first-order SCM approach, which does not contain information about strain gradient effects [166] (e.g. geometrically-necessary dislocations, GND, employed in [160]). Hence, such aspects of the constitutive response are not considered in the conventional CPFE model employed here. Note, however, that the concept of GNDs has been used in the prismatic dislocation loop model from Section 2.5. The characteristic length scales in the prismatic loop model are particle size and spacing, determining the size of loops and distance over which the loops are punched out, respectively.

In this chapter, comparison between the developed CPFE model and SCM scheme is carried out during monotonic short-term plasticity (Section 4.3.1) and forward creep (Section 4.3.3) of ex-service (EX) Type 316H at 550°C. At this temperature, dislocation motion along slip systems is described by the thermally-activated glide flow rule of Eq. 2.17, as described in Chapters 2 and 3. In Section 4.3.2, the room-temperature deformation response of the material

upon re-load from high-temperature pre-straining is assessed. The same cast of ex-service material from Chapter 3 is considered with experimental data provided by EDF Energy. The evolution of precipitate populations and solute distributions in EX Type 316H is ignored ($\dot{L}_p, \dot{L}_s = 0$). Three geometries are investigated using the CPFE approach: 1) a 3D aggregate of 216 cubic grains to provide an "on-average" macroscopic response; 2) a realistic grain-shape, quasi-3D thin polycrystal of 39 grains, developed to assess localized deformation across grain boundaries; and 3) another aggregate of 216 grains, generated as a tessellation in 3D and developed to provide an accurate description of grain shapes and arrangement in 3D space. The three configurations together with the employed boundary conditions are shown in Fig. 4.1. The geometric size of the models, number of elements and average grain size are summarized in Table 4.1. The average grain size selected for the geometries follows the experimental observations from [114]. For consistency in comparison, simulations by the SCM here employ 216 grains with the same set of crystallographic orientations considered in the CPFE model. The polycrystalline models are treated as an isotropic material with a weak texture (similar to Fig. 3.1), with the orientations of the grains represented by sets of three Euler angles [6]. Investigation of the size of representative volume element (RVE) used in the CPFE model predictions is presented briefly in Section 4.4 in the context of geometries, generated through 3D tessellations. Similar investigations of the RVE size were carried for the cubic grain polycrystalline aggregate (Fig. 4.1.a), but are not shown here. Sections 4.3.1 to 4.3.3 review the CPFE model predictions using the 3D approximate cubic grain and thin quasi-3D geometries. Predictions using the more realistic grain aggregates in a full-3D formulation, developed through tessellations, are presented in Section 4.4. Note that a more detailed evaluation of the results presented in this chapter is given in Petkov et al. [144].

Table 4.1. Model size, number of elements and grain size for the three types of geometries considered.

Geometry	Size – X x Y x Z (μm)	No. Elements	Average grain dia (μm)
216 cubic grains	300 x 450 x 200	5832 (C3D20R)	50
39 grain thin slice	200 x 360 x 2	44296 (C3D8)	55
216 grains tessellation	300 x 450 x 200	60081 (C3D10)	60

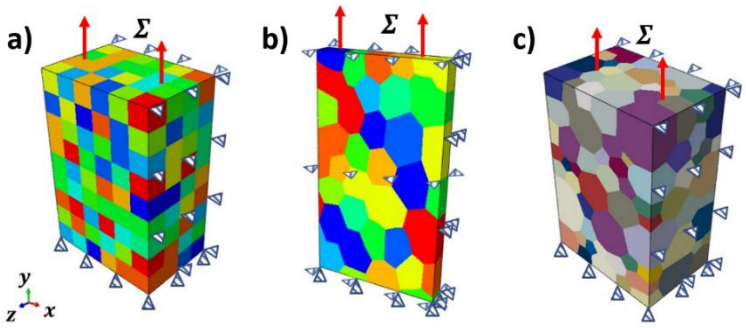


Figure 4.1. a) Polycrystalline aggregates approximated by cubic grains and b) realistic grain-shape geometry. c) 3D tessellation of 216 grains of realistic shapes, generated using Neper Generation software [167]. N.B. Images not presented to the same scale.

4.3. COMPARISON BETWEEN SCM AND CPFE FRAMEWORKS

4.3.1. Monotonic elastic-plastic loading

The short-term elastic-plastic behaviour of EX Type 316H at 550°C is examined in this section using the CPFE model. Predictions are compared to those given by the SCM. The parameters for initial density of dislocation junctions on each slip plane N_0, hardening coefficient j_s and physical properties of Type 316H are the same for the SCM and CPFE models (see Table 4.2). Note that in this chapter only the material response during short-term plasticity and forward creep is examined. Hence, for simplicity a value of $\alpha_0 = 1$ is assumed here, i.e. adopting the value from [6].

Table 4.2. Material parameters for SCM and CPFE, EX Type 316H. Parameters C_{ij}, E, v, G_0, b and $\dot{\gamma}_0$ are those of Table 3.2 for EX Type 316H. Values in brackets used in Section 4.3.2.

Parameter	Value	Parameter	Value
α_0	1	N_0	2.5 x 10^{13} (3 x 10^{13}) m^{-2}
α_d	0.35	j_s	1.75 x 10^{15} (7 x 10^{14}) m^{-2}
τ_s	37 MPa	j	8.75 x 10^{15} (3.5 x 10^{15}) m^{-2}
τ_p	21 MPa	W_c	80
ΔL_r	15b	D_c	6.47 x 10^{-15} m^2/s

The geometry of 216 cubic grains was loaded in simple tension with the bottom (y_0), right (x_{max}) and back (z_0) sides of the aggregate prevented from moving in the direction normal to the boundary (Fig. 4.1). A multi-point constraint was imposed on the forward (z_{max}), left (x_0) and top (y_{max}) sides of the body such that their faces remain planar. Periodic boundary conditions (PBC) are not imposed here due to the selected aggregate and its mesh, which does not have symmetrical discrete nodal arrangements on opposite sides to allow for PBC. The macroscopic stress (Σ_{yy}) in the loading direction (y-axis) is obtained by $\Sigma_{yy} = \left(1/A_{top}\right)\int_0^A \sigma_{yy}^i dA_i$, where σ_{yy} is the stress along the top surface of element *i* in the loading direction; *A* is the area of the top surface (y_{max}) given in terms of deformed dimensions of the aggregate. The macroscopic strain rate in the y-direction is

$$\dot{E}_{yy} = \dot{Y}/Y \tag{4.1}$$

where *Y* is the deformed dimension of a side of the aggregate in the y-direction, respectively.

The predictions of macroscopic deformation from the CPFE and SCM agree with one another, with both results replicating the experimental data in Fig. 4.2.a). However, it is observed that the CPFE prediction lies below the SCM prediction (N.B. In these simulations, the SCM and CPFE have used exactly the same constitutive laws, formulations of the flow rule and material constants). This behaviour is consistent with the general observation in mechanics that increasing the number of degrees of freedom (i.e. increasing the number of different ways that a body can deform) gives a more compliant and softer predicted macroscopic response. In the CPFE model, the strain is inhomogeneous within the grains. Stress and strain concentrations develop in the vicinity of grain junctions, while in the SCM a uniform state of stress and strain is assumed within each grain, which is surrounded by a homogeneous material [7]. The local inelastic deformation distribution is shown in Fig. 4.2.b-c) – the fields of accumulated effective inelastic strain and

average dislocation junction density are given at E_{yy} = 5.0%. The distributions of these quantities resemble each other, as expected due to the relationship between dislocation junction density and local shear strain (Eq. 3.2). Note that the order of magnitude of the dislocation obstacle density is in general agreement with values recorded experimentally, e.g. [60].

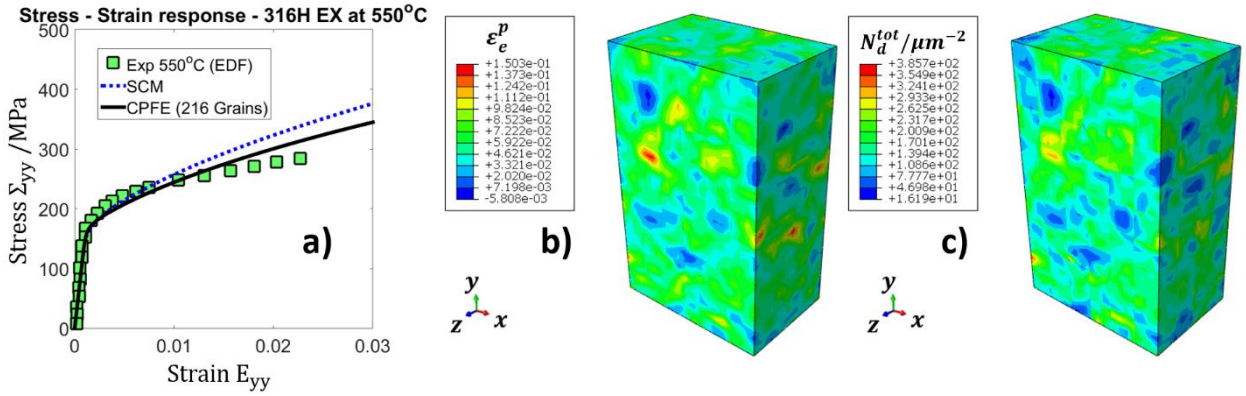


Figure 4.2. a) Stress-strain response of Type 316H, 550°C. SCM and CPFE (cubic grains) results are compared to experimental data. Contour plots of b) ε_e^p and c) average N_d^{tot} (in 1/μm^2) at E_{yy} = 5%.

The distribution of axial stress σ_{yy}, the von Mises effective stress σ_e and N_d^{tot} for 10 selected grains predicted by the CPFE scheme with cubic grains is compared to the SCM predictions in Fig. 4.3. A statistical approach is employed that has been used to assess higher-order homogenisation scheme [168]. The plot presents the grain average stress ($\bar{\sigma}_{yy}{}^{(gr)}$ and $\bar{\sigma}_e{}^{(gr)}$) and obstacle density ($\bar{N}_d{}^{(gr)}$) with bounds of the standard deviation, e.g. $SD^{(gr)}(\sigma_{yy}) = \sqrt{\langle \sigma_{yy}^2 - \bar{\sigma}_{yy}^2 \rangle^{(gr)}}$, for the CPFE model. The averaged values of dislocation obstacle density and axial stress predicted by the CPFE model differ by 11.5% and 8.0% from the SCM predictions. The standard deviation of these field quantities is examined within the whole aggregate, e.g. $\overline{SD^{(poly)}(\sigma_{yy})} = \sqrt{\langle \sigma_{yy}^2 - \bar{\sigma}_{yy}^{2\,(gr)} \rangle}$. The standard deviation is then normalised with respect to the average polycrystal values according to $\overline{SD(\sigma_{yy})}^* = \overline{SD^{(poly)}(\sigma_{yy})}/\Sigma_{yy}$, $\overline{SD(\sigma_e)^*} =$

$\overline{SD^{poly}(\sigma_e)}/\overline{\sigma_e^{(poly)}}$ and $\overline{SD(N_d)^*} = \overline{SD^{(poly)}(N_d)}/\overline{N_d^{(poly)}}$. After monotonic deformation to 5% true strain, the latter quantities take values of 0.27, 0.14 and 0.186, respectively. Note that the standard deviation for σ_e is nearly 4 times lower than that obtained in [168] (for the particular constitutive model in [168]). This indicates that the von Mises stress variation within grains predicted here is lower than that for the model employed in [168], suggesting that second-order effects are less important under the conditions examined here. However, these variations in local fields for the CPFE model are responsible for the difference in predicted monotonic response from Fig. 4.2.a. The difference stems from local field variations arising from geometric constraints, as well as local variation in crystallographic grain orientations. In Sections 4.3.3 and 4.4.3, the same method is employed to assess and explain the link between localised variations and changes in macroscopic response under forward creep loading.

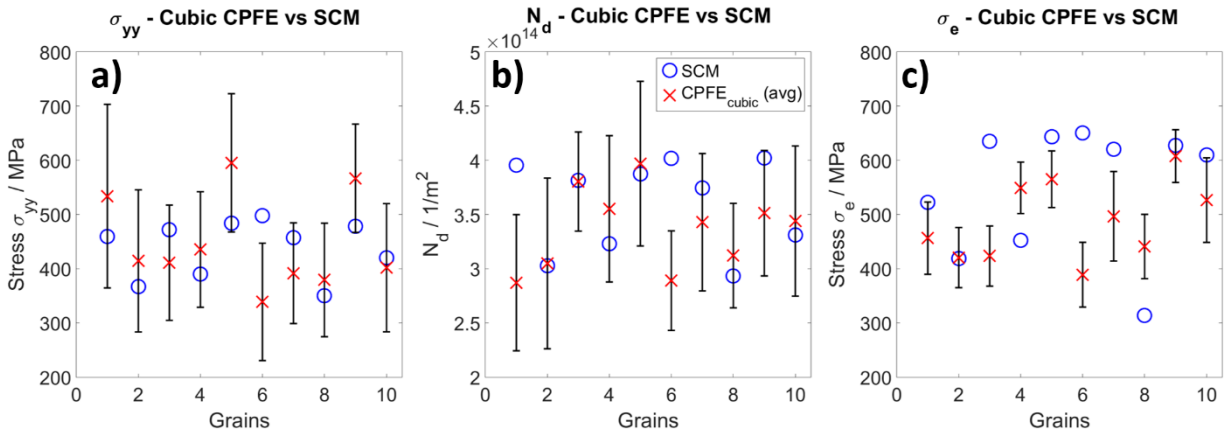


Figure 4.3. The average values and variation within grains, represented via the standard deviation of quantities within a given grain $SD^{(gr)}(\sigma_{yy})$ and $SD^{(gr)}(N_d)$, of σ_{yy} (a), N_d^{tot} (b) and σ_e (c) for 10 selected grains within the CPFE model (with cubic grains), compared to the SCM results, at E_{yy} = 5%.

In addition to the cubic grain geometry, the thin-slice aggregate of tessellated grain shapes from Fig. 4.1.b) using the same fitting parameters was also investigated. The geometrical grain shapes are based on the work by Gill and Cocks [169] who reason that more realistic grain shapes

are obtained by redistribution of quadruple into triple junctions according to out-of-balance grain-boundary tensions, until they are in equilibrium. This results in thin-slice geometries where there are only triple grain junctions and grain boundaries meet at ~120° to one another [169]. Note that using this approach, some of the boundaries in the 39-grain geometry, shown in Fig. 4.1.b), have curvatures. This is closer to a realistic grain structure, contrary to the common idealisation by generic Voronoi approaches [167]. The sample was loaded in tension under quasi-3D plane-strain with the left-hand side constrained by an MPC. Generalized plane strain BC was imposed along the z-direction. Predictions of macroscopic deformation for this geometry agree with experimental data (Fig. 4.4.a). General agreement is also established with the larger 3D cubic-grain geometry. A mesh sensitivity study using the 39-grain geometry consisting of 5424 and 44296 elements was also conducted, only to find no significant variation in the result. The field variations of accumulated effective plastic strain and dislocation junction density at E_{yy} = 1.2% are shown in Figs. 4.4.b) and c). Note that concentrations in the distribution are found near grain boundaries. In turn, the variation of σ_{yy} across grains of different crystallographic orientations is extracted from the contour plots of σ_{yy} in Fig. 4.5.a) along Paths 1 and 2 and given by the line plots in Figs. 4.5.b) and c). Concentrations of axial stress are localized in the vicinity of grain boundaries.

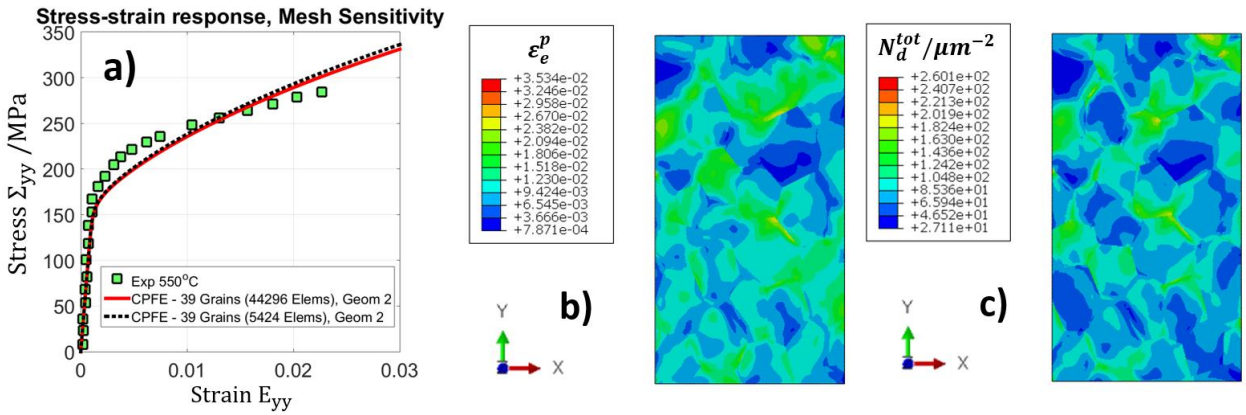


Figure 4.4. a) Stress-strain response of 316H at 550°C for 39-grain geometry. Contour plots of b) ε_e^p and c) average N_d^{tot} at E_{yy} = 1.2%.

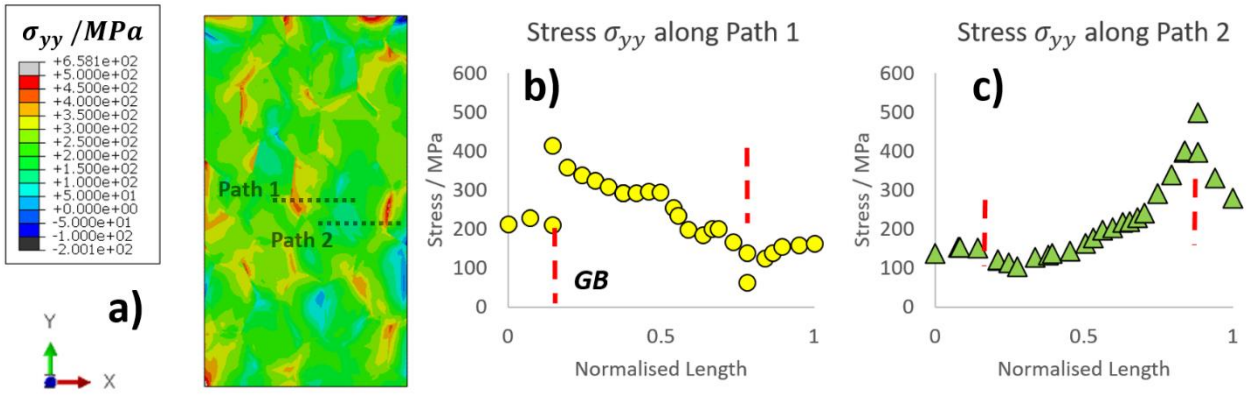


Figure 4.5. a) Contour plots of axial stress σ_{yy} at E_{yy} = 1.2%. Line plots of σ_{yy} along b) Path 1 and c) Path 2 crossing grains of different crystallographic orientations.

These observations show that the effects of elastic and plastic anisotropy are significant at the grain scale, which agrees with observations made by Dunne et al. [160]. The variation in stress fields across grains will be further examined in Section 4.3.3. In the next section, the Bauschinger effect in Type 316H during monotonic deformation under load-reversal is investigated.

4.3.2. Bauschinger effect during re-load upon pre-straining

In this section, the Bauschinger effect in the material is simulated using the CPFE model and predictions are compared to a set of results by the SCM, obtained by Hu et al. [87]. The simulated loading scenario comprises of high-temperature (HT) pre-straining in tension at 550°C, followed by unloading. The sample is then cooled and re-loaded in either tension or compression at room temperature (RT). The fitting parameters of the constitutive model were fit to capture only the HT pre-straining stress-strain response. The subsequent response during RT deformation is independent of free parameters. The 216-grain aggregate is used under the same boundary conditions from Section 4.3.1. During HT pre-straining, dislocation slip rate is represented by the thermally-activated glide flow rule of Eq. 2.17. A simple power-law empirical flow rule of the

form $\dot{\gamma}^{(\alpha)} = \dot{\gamma}_0 \left| \left(\tau^{(\alpha)} + \bar{\tau}_m^r \right) / \tau_{cr}^{(\alpha)} \right|^m \operatorname{sgn}\left(\tau^{(\alpha)} \right)$ is used at RT with m = 600 and $\dot{\gamma}_0 = 1 \times 10^{-6} s^{-1}$ [87] in order to replicate the rate-insensitive response of the material at this low temperature.

The Bauschinger effect, manifested in the sharp change in global stress-strain response at RT tensile re-loading, contrary to the smooth evolution of response during RT compressive re-loading, is captured by both models (Fig. 4.6). Predictions by both models show that this complex response is a result of the evolution in the internal microstructural state and intragranular residual stress field. A detailed examination by Petkov et al. [144] of the variation in residual stress in the aggregate revealed that at the end of the compressive re-load cycle the stress state is a "mirror image" of that after the tensile cycle. This agrees qualitatively with observations on the variation of intragranular stress in selected families of grain orientations in Hu et al. [87]. The differences in deformation response upon re-load depend on the stress redistribution process, and the presence or absence of a suitable residual stress field, established during pre-straining, which allows compatible plastic deformation (see Section 3.4.2.2).

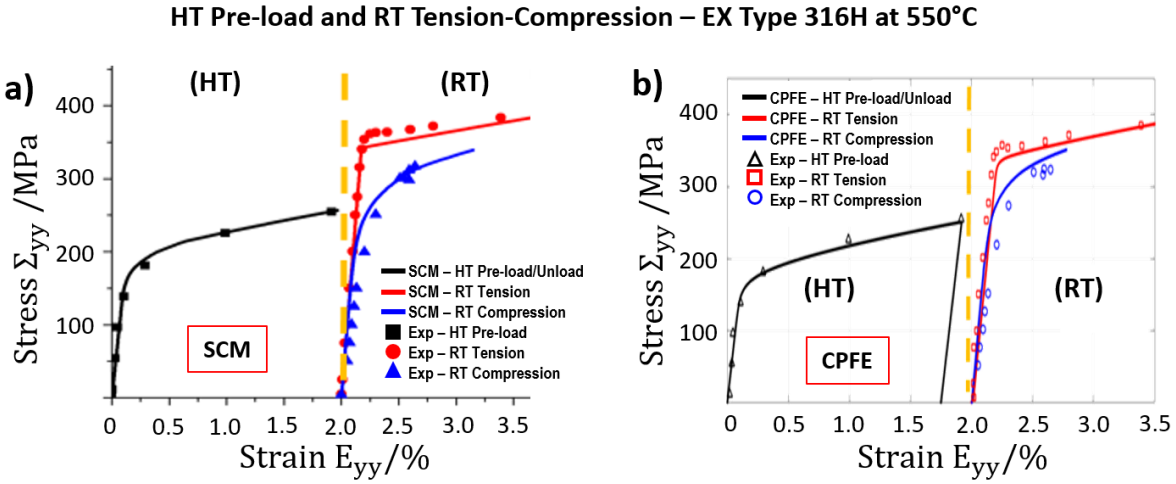


Figure 4.6. Stress-strain response of high-temperature (HT) pre-loading and room-temperature (RT) re-loading – a) SCM [87] and b) CPFE. N.B. Compression response shown in absolute stress values.

Note that the CPFE model predicts a more gradual change in the deformation response upon yielding during the tensile re-load, compared to the SCM prediction. This is potentially as a result of localized residual stress relaxation during HT unloading, captured by the 3D CPFE framework but not by the SCM, causing localized plastic deformation earlier upon subsequent re-loading.

4.3.3. Load-controlled creep response

The short-term creep response of ex-service material was also simulated using the CPFE model and compared to SCM predictions. The simulated conditions were pre-loading at 550°C up to stresses of 250, 280 or 320 MPa, which was then kept constant over the experiment/simulation. The additional free parameter W_c, defining the extent of the static recovery of the dislocation network (Eq. 2.16), was calibrated through fitting the SCM to experimental data. The predicted macroscopic creep curves are shown in Fig. 4.7. It is found that the CPFE over-predicts the inelastic strain compared with the SCM, suggesting that the extent of static recovery is greater in the former framework for the same value of W_c. This is consistent with the general finding that a softer, more creep-compliant response is obtained for a greater number of degrees of freedom and relaxation of internal constraint. A better match between the CPFE predictions and experimental data is achieved by recalibrating the fitting parameter W_c with a reduced value ($W_c = 19$), compared to that employed in the SCM. The variations of axial stress, effective stress and dislocation junction density predicted using the two frameworks are illustrated in Fig. 4.8. A large difference between the average obstacle densities in the polycrystalline array, predicted by the two frameworks, is found with mean differences of 33% and 29% for W_c = 19 and 80 in the CPFE model, respectively. Note that the average axial stress for each grain shows a mean difference of 3% between the two schemes. The overall normalised standard deviations are assessed within the whole polycrystalline aggregate after creep for 555 hours at 550°C using the approach described

in Section 4.3.1. These are found to be different to those for time-independent monotonic loading. For the cubic grain geometry and $W_c = 19$, it is found that $\overline{SD(\sigma_{yy})^*}$ increases from 0.242 to 0.288, while $\overline{SD(\sigma_e)^*}$ and $\overline{SD(N_d)^*}$ decrease from 0.135 to 0.114 and from 0.14 to 0.069, respectively, compared to the time-independent CPFE results at the same stress. For $W_c = 80$, the difference in axial stress is more pronounced with $\overline{SD(\sigma_{yy})^*}$ = 0.349; $\overline{SD(\sigma_e)^*}$ and $\overline{SD(N_d)^*}$ decrease from 0.135 to 0.109 and from 0.14 to 0.0643, respectively. These findings illustrate an important point. As described in Chapter 3, creep is a balance between two highly non-linear processes – thermally-activated glide and climb-controlled thermal recovery of the dislocation structure. Small variations of deviatoric stress, for which σ_e can provide a simple measure here, and obstacle density can have a significant effect on the creep rate. During creep, the stress and microstructural state in the aggregate evolve towards a more uniform state. Increasing the characteristic rate of thermal recovery would promote a more uniform state in effective stress and critically resolved shear stress, which depends on N_d. The variation of axial stress was found to increase during creep as a result of the stress redistribution process between grains. This results in a more significant variation of hydrostatic stress σ_H within the polycrystalline body, compared to the hydrostatic stress variation after monotonic short-term plasticity loading to the same stress, as illustrated in Fig. 4.9. Note that the hydrostatic stress predicted by the SCM in Fig. 4.9 is the same for each grain, whereas σ_e varies for each grain in Fig. 4.8. According to Chapter 2, the stress in each grain is determined from $\boldsymbol{\sigma}^{\mathbf{a}} = \mathbf{H}^{\mathbf{a}}\mathbf{T}\boldsymbol{\sigma} + \mathbf{X}^{\mathbf{a}}$, where $\mathbf{H}^{\mathbf{a}}$ is the same for each grain. Here, $\boldsymbol{\sigma}$ is the macroscopic stress and $\mathbf{X}^{\mathbf{a}}$ is the intragranular residual stress, determined from the difference in local and global plastic strain (Eqs. 2.26-2.28). The hydrostatic stress is determined as $3\sigma_H = Tr\left(\boldsymbol{\sigma}^{\mathbf{a}}\right)$. The value of $\mathbf{X}^{\mathbf{a}}$ is different in each grain due to its plastic anisotropy. However,

$\mathbf{X}^{\mathbf{a}}$ is purely deviatoric and $Tr\left(\mathbf{X}^{\mathbf{a}}\right)=0$, from which it follows that $3\sigma_H = Tr\left(\mathbf{H}^{\mathbf{a}}\mathbf{T}\boldsymbol{\sigma}\right)$, i.e. the same for each grain. By contrast, σ_e varies for each grain since the second invariant of stress of $\mathbf{X}^{\mathbf{a}}$ is non-zero and different for each grain.

The results demonstrate that local variations of stress and dislocation obstacle density in the CPFE framework, compared to the SCM, result in faster rates of thermal recovery. This assists the accumulation of larger amounts of inelastic strain, as observed in the predicted macroscopic response between the two frameworks with the same set of parameters. Hence, parameters employed in any modelling scheme need to take into account the fidelity of the model and how the average macroscopic response is determined, as well as the details of the physical processes that control the macroscopic response. This is further discussed in Section 4.5.

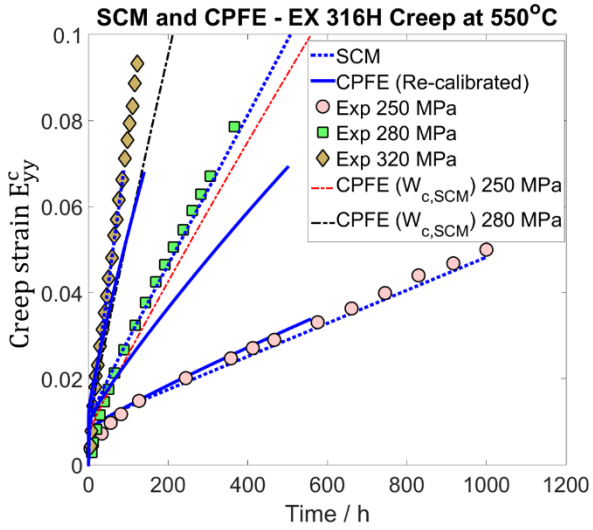


Figure 4.7. Creep response of EX 316H at 550°C – SCM and CPFE predictions. Initial CPFE predictions before calibration using the same parameters as SCM, at 250 MPa and 280 MPa are also shown.

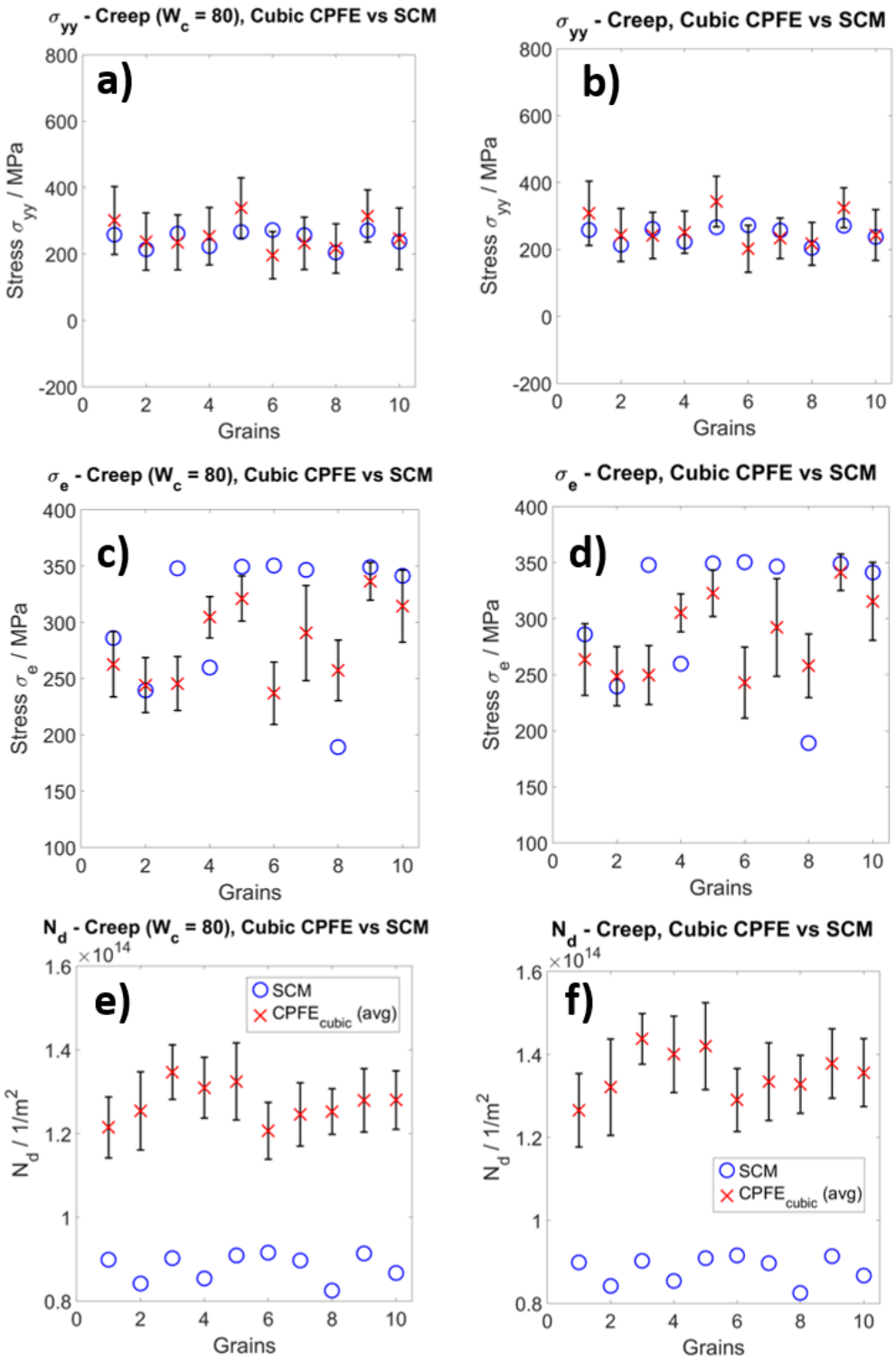


Figure 4.8. Variation of σ_{yy} within 10 selected grains within the CPFE model, represented via the standard deviation within a given grain, is shown for a) $W_c = 80$ and b) $W_c = 19$ and compared to SCM results after creep for 555 hours at 250 MPa. In c) and d) the respective variation of σ_e is presented. The variation of N_d^{tot} for e) $W_c = 80$ and f) $W_c = 19$ shows the increase in dislocation obstacle density with reduction in W_c by a factor of 4, responsible for the lower values in accumulated creep strain.

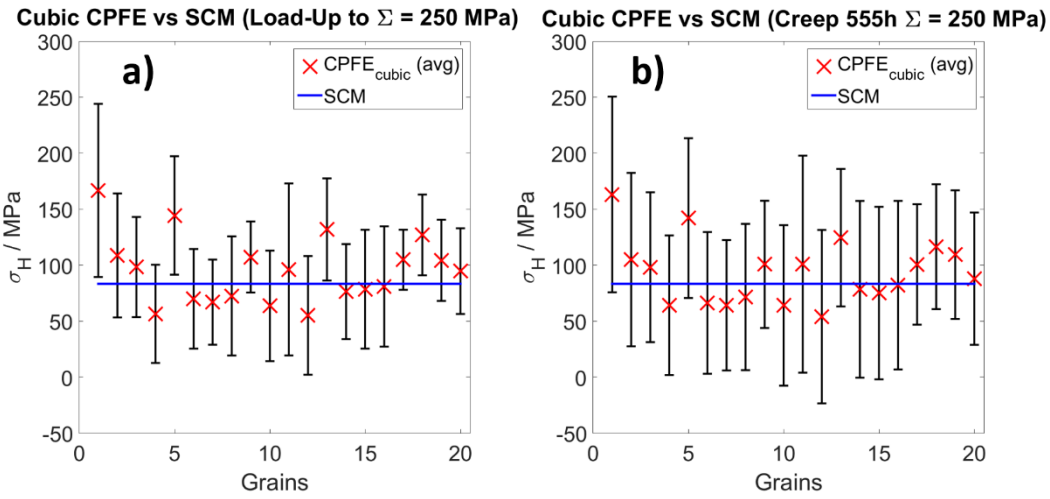


Figure 4.9. Variation of the hydrostatic stress σ_H within 20 selected grains predicted via the CPFE model, shown in a) after short-term plasticity loading to 250 MPa prior to creep and b) after 555 hours of creep at 250 MPa. Comparison is also made with the SCM results. The variation of σ_H within grains is greater in b) due to the increase in variation of axial stress as a result of the stress redistribution process.

The short-term creep response of ex-service Type 316H was also simulated using the realistic geometry of Fig. 4.1.b) under generalized plane strain at 550°C and 250 MPa. Although not shown here, creep curves predicted for the geometry for $W_c = 19$ are in general agreement with the experimental data. The stress redistribution between grains during creep, arising due to compatibility and equilibrium requirements, is shown at different creep times t_c in Fig. 4.10. The axial stress field evolves during primary creep but stabilises within the secondary creep regime. This agrees with modelling and experimental results from [170]. Similar to observations made from Figs. 4.4 and 4.5, stress concentrations are localized in grain-boundary regions during creep loading – more specifically near the triple grain junctions (see Fig. 4.11). This observation provides an initial insight into the potential locations of damage development during creep. This is simply flagged up here. Consideration of damage development during creep will be made in Chapter 7. In the context of crystal plasticity, grains of "hard" crystallographic orientations from Fig. 4.11 are those in which plastic deformation is difficult due to the orientation of their slip systems in three-dimensional space. Note that intergranular creep damage is dependent on the local tractions

along grain boundaries [100]. More detailed evaluation of the stress distributions within grains and along grain boundaries in relation to the crystallographic orientations will be made in Chapter 5. Modelling the creep response using this quasi-3D geometry here serves as an introduction to studies using 3D tessellation geometries of Fig. 4.1.c), presented in the following section.

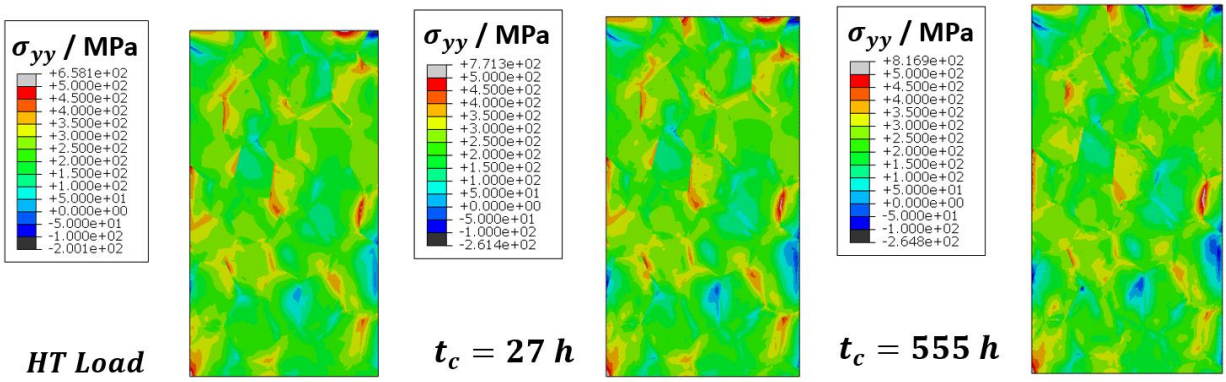


Figure 4.10. Contour plots of σ_{yy} during creep, 39 grains thin-slice geometry. The stress fields shown at $t_c = 27\ h$ is within the primary creep regime and that at $t_c = 555\ h$ is within the secondary creep regime.

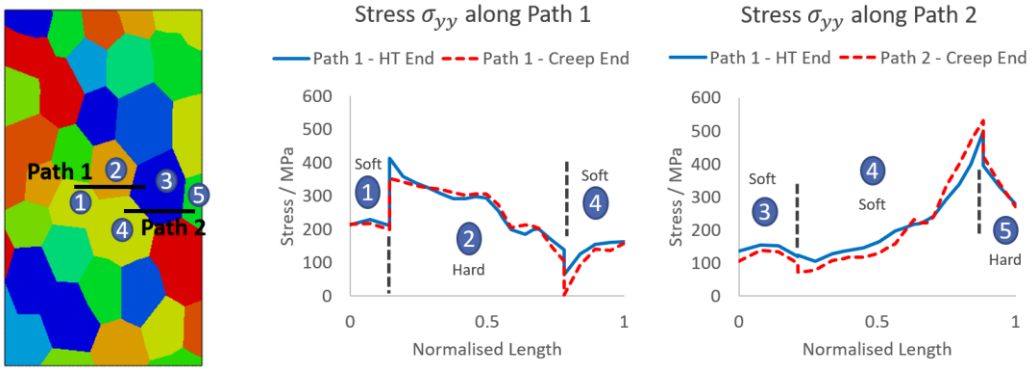


Figure 4.11. Line plots of σ_{yy} along paths crossing grains of softer and harder orientations showing the redistribution of stress fields, generated during the initial elastic-plastic loading step, during stress-controlled long-term creep after 555 h at 250 MPa. Identified are relatively "harder" and "softer" grains.

4.4. PREDICTIONS USING REALISTIC 3D GEOMETRIES

Predictions using more realistic tessellated grain aggregates in 3D are presented in this section. The geometries are constructed using the Neper Generation software [167]. The 3D tessellation

geometry is more realistic than the quasi-3D geometry, due to the fact that grain boundaries are also at an angle through the thickness of the geometry, similar to real microstructures. This idealisation is more representative of the material. It allows us to gain a deeper understanding of the localised deformation fields in polycrystalline materials and how these influence the macroscopic response. A polycrystal, consisting of 216 grains, was generated allowing for direct comparison with the original 216-cubic grain aggregate. The size of the model is given in Table 4.1 and Fig. 4.12. To construct the grain cells, a procedure similar to that proposed by Gill and Cocks [169] (see Section 4.3.1) was employed by implementing a standard option in Neper, allowing modification of the sphericity and centroid position of cells to replicate experimentally-observed grain growth morphologies ("morpho –gg"). The mesh is comprised of quadratic tetrahedral elements (C3D10) with a characteristic length of approx. 12 μm. For the tessellated geometry, tetrahedral rather than brick elements are used allowing realistic geometries to be meshed without the need for highly distorted elements, as shown in Fig. 4.12.

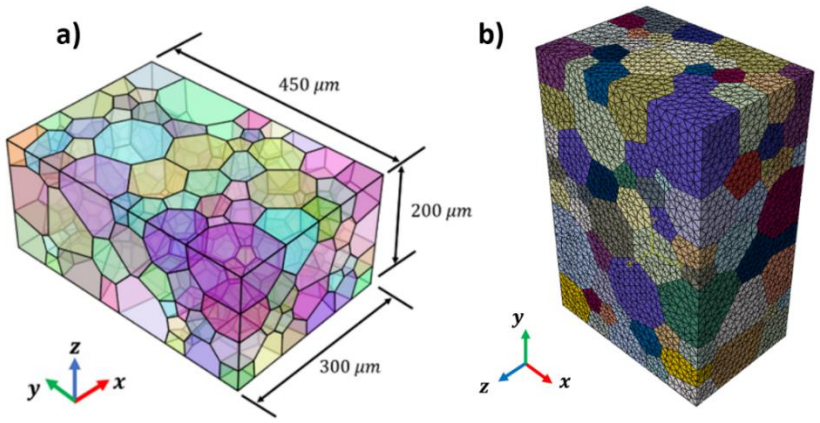


Figure 4.12. a) The 3D tessellation with 216 grains and b) the generated mesh.

4.4.1. Selection of representative volume element (RVE)

In this study an approach for determination of RVE, employed in [171], is adopted and modified by assessing the standard deviation of predicted macroscopic creep strain for geometries with

increasing numbers of grains, proposed by Mirkhalaf et al. [172]. In order to determine the size and number of grains of the RVE, five tessellation geometries with 50, 100, 200, 216 and 300 grains were analysed. The set of crystallographic orientations were selected to give a random texture. The detailed determination of RVE sizes and mesh convergence studies of the tessellation and cubic grain geometries are given in Petkov et al. [144]. They are not presented here for the sake of brevity. The analysis indicated that adding more grains to the tessellation realisation of 200 grains does not result in significant changes in macroscopic response, agreeing with Cailletaud et al. [173]. Hence, the geometry with 216 grains was selected, which provides a good balance between the accuracy in the resulting predictions and reasonable computational efficiency.

4.4.2. Monotonic elastic-plastic response of realistic aggregate

Monotonic elastic-plastic behaviour of the material at 550°C is examined in this section for the polycrystalline tessellated aggregate. The simulation setup is the same as that employed for the cubic grain geometry of Section 4.3.1, except the grain shape. This allows the effects of the realistic geometry on macroscopic response to be isolated. Predictions of the stress-strain behaviour for the cubic- and tessellated-grain full-3D geometries are in agreement (Fig. 4.13.a). This suggests that using cubic-shaped grain aggregates is appropriate to capture the monotonic elastic-plastic deformation response. The effective inelastic strain field during monotonic loading within the realistic grain aggregate is shown in Figs. 4.13.b-c), initially accumulating near grain boundaries as a result of localised slip activity within favourably orientated grains for activation of multiple slip systems. Note that the distribution of ε_e^p within the polycrystal of Figs. 4.13.b-c) appears more realistic than that for the cubic grain geometry in Fig. 4.2, but the macroscopic monotonic elastic-plastic deformation response of the two aggregates is identical.

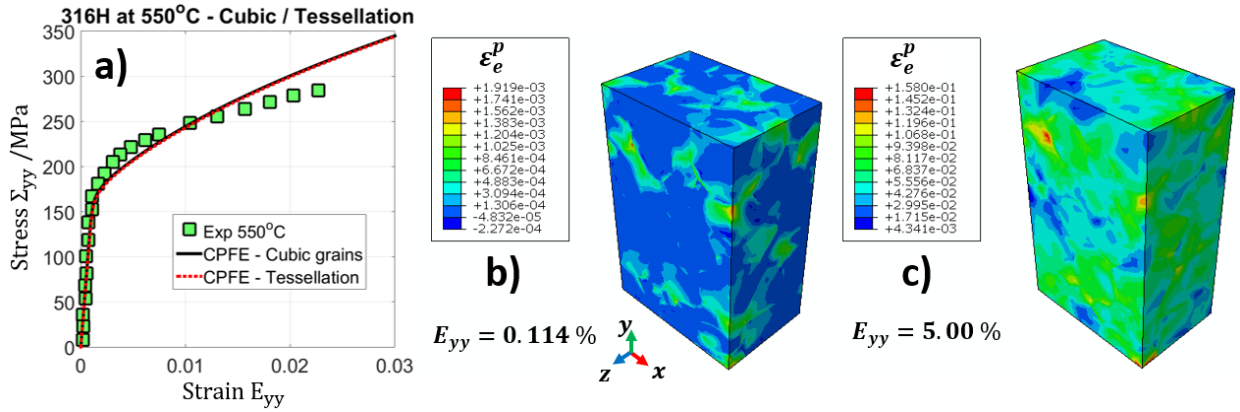


Figure 4.13. a) Macroscopic stress-strain response of Type 316H at 550°C. Predictions via the CPFE model using cubic and realistic tessellation grain shapes compared to experimental data. Contour plot of the evolution of effective plastic strain, ε_e^p, with macroscopic strain at b) E_{yy} = 0.114% and c) E_{yy} = 5%.

4.4.3. Load-controlled creep response of realistic aggregate

Predictions of short-term creep of Type 316H at 550°C through the tessellation geometry are compared to those from Section 4.3.3 in Fig. 4.14 using the same value of W_c = 19, determined for a fit of the cubic-grain geometry. The trend of creep strain accumulation with time for increasing values of applied stress is captured by both geometries. Note that the negligible difference in monotonic loading in Fig. 4.13.a) (< 1%) between the two geometries does not become pronounced during load-controlled creep loading. The creep predictions for both geometries agree well with experimental data. At larger strains, discrepancies are again observed between the SCM and CPFE predictions. Such differences are amplified by the finite lattice rotations, captured by the CPFE framework, which affects the axial creep rate of crystals. The employed micromechanical models are highly-nonlinear, capturing the interactions between the thermal glide activity of dislocations, as well as thermal recovery and hardening. However, the predictions from this and Section 4.3.3 demonstrate that sufficiently refined meshes with an appropriate selection of element types allow the macroscopic response of the RVE to be simulated, independent of grain shapes.

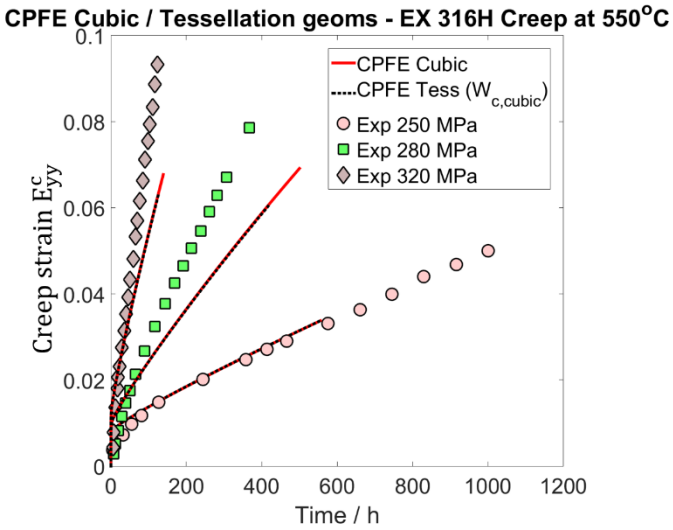


Figure 4.14. Creep response of EX 316H at 550°C at different stress levels – CPFE predictions through cubic grain and realistic tessellation geometries.

Minor differences are observed between the predicted macroscopic creep and elastic-plastic deformation responses for the cubic grain and tessellation geometries. This supports the use of simplistic crystal cubic shapes for modelling polycrystalline material deformation, where the prime interest is the macroscopic response. Although not shown here, contour plots of the effective plastic strain and the accumulated dislocation-junction obstacle density in the two geometries after creep into the primary and secondary stages were also compared only to find minor differences, thus supporting this argument. However, the deformation of individual grains will be affected by both their shapes and neighbouring crystals. The predictions for the cubic- and tessellated grain realisations are assessed further using statistical analyses of the local fields. Variations of axial stress, effective stress and dislocation obstacle density under creep at 250 MPa, predicted by the SCM and the two CPFE geometries, are illustrated in Fig. 4.15. The results illustrate differences between the average obstacle densities predicted for the cubic-shaped grain and tessellation geometries, as compared to the SCM results, of 33% (cubic) and 33.9% (tessellated) for the polycrystalline array. Furthermore, the variation of dislocation junction density in Fig. 4.15

indicates minor differences across the two grain realisations, supporting the findings in Fig. 4.14. The polycrystalline averages of axial stress within the grains between the tessellation geometry and SCM modelling results show a mean difference of 4.7%, which is consistent with the result for the cubic grain geometry (Section 4.3.3). However, greater variation in axial stress is found in Fig. 4.15.f) for the tessellation geometry with $\overline{SD(\sigma_{yy})}^{*} = 0.538$. This is as a result of the higher geometric constraint in the tessellated geometry as compared to the cubic-grain geometry.

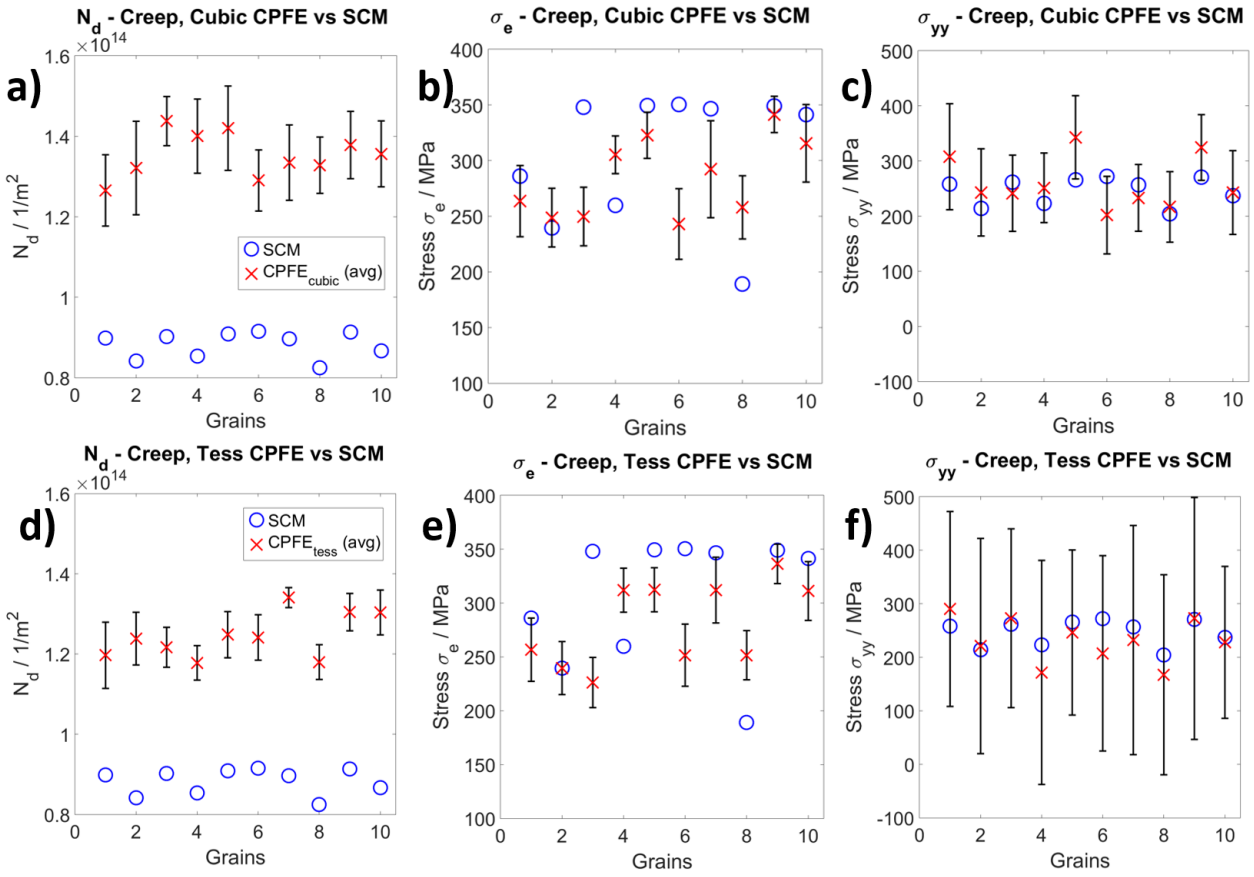


Figure 4.15. Variation of N_d^{tot} within 10 selected grains within the CPFE model for $W_c = 19$ for a) cubic and d) realistic grains, compared to SCM results after creep for 555 hours, 250 MPa. The variation of σ_e is shown for cubic (b) and realistic grains (e). Variation of σ_{yy} is shown for cubic (c) and realistic grains (f).

The variation of the hydrostatic stress σ_H in the two geometries after 555 hours is demonstrated in Fig. 4.16.a-b). The variation in σ_H is greater for the tessellated geometry with

$\overline{SD(\sigma_H)^*} = 1.63$, which is associated with the larger axial stress variation, noted in Fig. 4.15.f). A major origin of the difference is the effect of grain shape. The predictions suggest that greater local constraint on the deformation of the individual grains is present in the tessellated geometry, leading to larger variations in the axial stress. This observation further supports the hypothesis behind the increase in axial stress variation within the grains during creep as a result of the stress redistribution process. Note that the values of $\overline{SD(\sigma_e)^*}$ and $\overline{SD(N_d)^*}$ for the tessellation geometry take values of 0.1167 and 0.0528, respectively, and are similar to those obtained for the cubic grain geometry.

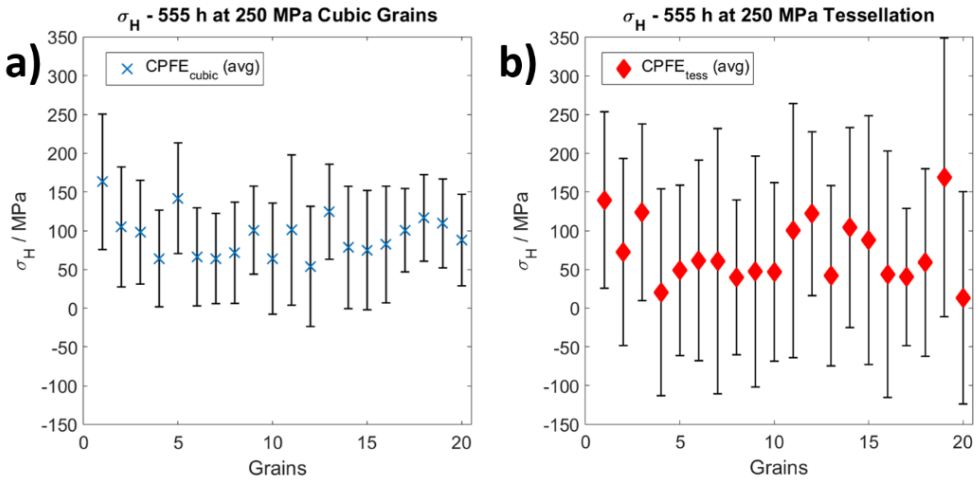


Figure 4.16. The variation of σ_H is shown within 20 grains for cubic (a) and realistic grains (b); 555 hours. Variation is greater in b) as a result of local constraint and arrangement of stress concentration features.

Although both polycrystalline geometries are suitable RVEs, local stress fields or microstructural state may evolve differently. Findings from this chapter suggest that field variations are less likely to affect the macroscopic deformation response, but could have pronounced effects in damage development (e.g. nucleation and growth of cavities) where the detailed distribution of local stress can play a significant role. The significance of using realistic grain shapes with regard to evolution of material state is further discussed in Section 4.5.

4.5. DISCUSSION

4.5.1. Comparing crystal plasticity approaches

The same physically-based micromechanical model, which captures the interaction between gliding dislocations and obstacles to their motion along slip systems, together with evolution of microstructural state, was employed within the SCM of Chapter 3 and the CPFE framework, developed in this chapter. The different level of internal constraint in the two polycrystalline frameworks gives rise to minor differences in the predicted macroscopic response for the same set of model parameters. The difference is more pronounced during load-controlled creep deformation, as compared to monotonic elastic-plastic response, which stems from the variation of internal state in the CPFE framework and non-linearity of the thermal recovery model (Eq. 2.16). The weaker internal constraint in the CPFE framework leads to a more compliant creep response. A lower value of the static recovery parameter (W_c) by a factor of 4, compared to the value calibrated for the SCM, is obtained for the CPFE model. Hence, the constitutive models within an assumed framework and geometry need to be calibrated independently against a given set of experimental data. Nevertheless, the aim of employing multi-scale modelling frameworks in this study is to capture the macroscopic response of the material and to evaluate local processes associated with evolution of internal material state. It is demonstrated that both frameworks describe the global response, evolution of internal residual stress and microstructural state during monotonic short-term plastic (Section 4.3.1-4.3.2) and creep loading histories (Section 4.3.3 and 4.4.3). The observed response is in agreement with findings from Chapter 3. Hence, the developed SCM has been validated with the higher-fidelity CPFE model developed as part of this chapter.

The agreement between the two frameworks with experimental data provides confidence in the adopted methodologies to describe the macroscopic deformation of polycrystalline materials. However, the difference between SCM and CPFE predictions of monotonic plasticity and creep responses, as well as between CPFE model geometries of different grain shapes, highlights the importance of local features of the deformation process in determining the macroscopic response. The first aspect of localisation processes, captured within the finite strain CPFE model and not the averaging SCM, is the evolution of lattice rotations within the grains. Lattice rotations can lead to evolution of texture and alter the deformation response at larger strains. Although not strongly pronounced, lattice rotations were responsible for minor changes of creep rate predicted by the CPFE model at macroscopic inelastic strains >5% in Section 4.3.3. The second aspect is the development of local stress concentrations within the grains. This leads to accumulation of higher dislocation obstacle densities locally, which in turn alters the hardening process and evolution of residual stress fields (e.g. smoother transition upon re-load, Section 4.3.2), or increases in the rate of thermal recovery (e.g. accumulation of higher creep strain, Section 4.3.3). The variation of axial stress, effective stress and dislocation obstacle density within the CPFE frameworks were analysed in this chapter. The statistical analyses revealed that small variations in the effective stress and the dislocation obstacle density can influence the deformation rate of the material during creep, with both stress and material state evolving towards a more uniform distribution. An important finding is the larger variation of axial and hydrostatic stress within grains after creep, as compared to the variation after short-term plasticity to the same stress. This illustrates that the axial and hydrostatic stress fields developed during creep are highly heterogeneous. Note that this can have implications on the local damage formation process. Although the predicted macroscopic responses for the cubic-grain and tessellated geometries are comparable, the statistical analyses of local stress fields

revealed more significant variation of local quantities within the tessellation geometry. This suggests employing the CPFE model for aggregates comprised of grains of irregular, realistic shapes when local features of the deformation process play an important role, e.g. damage development. From a practical point of view, the SCM captures the global response, and evolution of microstructure and residual stress fields with sufficient accuracy to evaluate the material response under complex loading histories (Chapter 3). However, when detailed understanding of global and localised deformation is required, e.g. initiation and evolution of damage, using the CPFE framework with irregular grain geometries would be the suitable choice.

4.5.2. Considerations on local response in vicinity of grain boundaries

Since damage development in localised regions within a material is an important pre-cursor to failure [43,121], the CPFE approach is the most appropriate framework out of those examined in this study to assess the evolution of creep damage, despite its computational complexity. The effects of local variation, redistribution of intragranular stress fields and strain localization within confined regions are captured by the CPFE model. Note that although the framework provides insights into the development of intragranular stress, of importance to intergranular creep damage is the variation and distribution of local stress and deformation fields along grain boundaries. Furthermore, observations from [174,175] suggest that the presence of grain-boundary sliding during creep can alter the local and global deformation response of polycrystalline aggregates, predicted in this chapter. This poses the requirement to combine the developed CPFE framework from this chapter with modelling approaches that describe the deformation response of grain boundaries. This can allow for a complete description of the response during intergranular creep damage. Therefore, the modelling framework from this chapter is extended in Chapter 5 to assess the response of polycrystalline aggregates of Type 316 in the presence of sliding. Note that only a

limited amount of sliding in this material is observed in practice. Hence, the predicted trends in global deformation from this and the preceding chapter will not drastically change. However, some changes in local response will be pronounced. The framework of Chapter 5 will then be extended in Chapters 6 and 7 to describe intergranular creep damage in Type 316 stainless steel.

4.6. SUMMARY

The SCM, described in Chapter 3, does not account for local field variations, which can influence damage formation. A crystal plasticity finite element (CPFE) framework is developed in this chapter to address this deficiency. The micromechanical model from Chapter 2 is applied within a CPFE polycrystalline framework using simplistic cubic grains. Predictions of short-term plasticity and load-controlled creep deformation are compared. A general agreement between predictions via the frameworks validates the existing SCM. A discrepancy between predictions of macroscopic creep is found using the two frameworks for the same set of parameters. This stems from the sensitivity of the constitutive models to local variations in stress, evolution of dislocation microstructure and lattice rotations, which are captured by the CPFE model. Furthermore, the CPFE framework predicts a greater variation in stress during creep as compared to short-term plasticity. This could have potential implications on localised damage formation in the vicinity of grain boundaries. Observations from this chapter demonstrate that such variations in stress are more severe when realistic grain shapes are employed within the CPFE framework, due to the higher geometrical constraint. It is worth emphasising that the presence of grain-boundary sliding and/or intergranular failure can alter the predictions from this chapter. The CPFE framework can be extended in capturing the response of grain boundaries during creep in polycrystals with irregular grain shapes to assess the response during grain-boundary sliding and intergranular creep damage. This is the focus of Chapters 5 and 7, respectively. The conclusions from this chapter are:

1. The SCM and mechanistic constitutive models, developed by Hu et al. [7,176] and extended in Chapter 3 as applied to austenitic Type 316H stainless steel, have been verified. This was achieved through comparison of predictions using a full-field CPFE model, which considers lattice rotations, local field variation and realistic grain shapes.
2. The main limitation of the employed SCM is the inability to capture the local stress and internal state (e.g. dislocation obstacle density) variation within the grains. Such variations affect the predicted macroscopic response, which is demonstrated by the CPFE scheme.
3. The variation of stress within the grains obtained from the CPFE simulations is less than that reported for other models in the literature (e.g. [168]). This supports the use of the first order SCM scheme for the current crystal plasticity constitutive model. The SCM is particularly efficient in determining the global response under complex deformation histories.
4. The developed CPFE framework is more suitable in applications where the local axial and hydrostatic stresses are of importance, e.g. damage development, since it captures large variations in local stress fields.
5. The nature of the CPFE framework could result in changes to the physical parameters, calibrated for the SCM. Localised processes and variation in grain shapes affect the local constraint, stress and microstructural state in the aggregate. Differences in predictions of the macroscopic creep response are found between the SCM and CPFE approaches, stemming from the greater sensitivity of the static recovery model to the local stress and strain fields.
6. The CPFE-predicted macroscopic response for the tessellated and cubic-grain geometries are in agreement. However, employing geometries of realistic grains, results in a greater variation of axial and hydrostatic stresses within the grains. Hence, realistic, irregular grain-shapes should be used where local effects become important, e.g. damage development.

CHAPTER 5

MODELLING GRAIN-BOUNDARY SLIDING DURING CREEP USING A COMBINED CPFE-INTERFACE ELEMENT FRAMEWORK

5.1. INTRODUCTION

5.1.1. Main effects of grain-boundary sliding

Experimental observations of grain-boundary sliding during creep of polycrystalline metallic materials show that, although the creep deformation of the aggregate is controlled by deformation of the grains, grain-boundary sliding provides an additional contribution to the accumulated inelastic strain [105,177]. Sliding in pure metals is determined by diffusion over grain-boundary ledges, which provides the intrinsic viscosity of the boundary. Raj and Ashby [178] and Gates [179] found that grain-boundary sliding in engineering alloys is controlled by the accommodation processes around intergranular particles, which could inhibit sliding. Relative sliding relaxes the shear stress along sliding boundaries, leading to a redistribution of stress within the grains and an increase in strain rate [180]. Most studies of grain-boundary sliding assume that grains deform by an isotropic power-law creep model and the effect of sliding is quantified through the use of a stress enhancement factor, f [124,175,180]. These studies demonstrate that in the freely sliding limit the normal stress on boundaries, transverse to the direction of the maximum principal stress, is greater than that experienced in the case of no sliding. This could alter the rate of intergranular creep damage, as noted in [181]. These observations suggests that the predicted local deformation response of Type 316 from Chapter 4 could be modified in the presence of sliding. The next section reviews experimental observations of the phenomenon in this material.

5.1.2. Grain-boundary sliding in polycrystalline Type 316 stainless steel

Garofalo et al. [182] examined the effects of grain-boundary sliding on the creep deformation of solution-treated (ST) Type 316 of grain size 90 μm at 704 and 830°C. The contribution to the total creep strain E^c from sliding was quantified in terms of the grain-boundary sliding strain, E^{gbs}, as $\Gamma^* = E^{gbs}/E^c$, which increases with decreasing applied stress, e.g. 6% at 100 MPa and 47% at 41 MPa. The trend in Γ^* does not appear to change with temperature [105,182]. Gates [179,183] and Gates and Horton [184] examined the dependence of grain-boundary sliding on stress, creep strain and grain size in solution treated (ST) and laboratory-aged (LA) Type 316. This was in order to assess the sensitivity of sliding to the presence of intergranular particles. Larger values of Γ^*were recorded for ST (~ 25%) as compared to LA samples (~ 10%) at 40 MPa and 800°C [179]. This indicated that intergranular $M_{23}C_6$ precipitates in the latter samples inhibit sliding. Furthermore, detailed experimental examination of the formation of wedge cracking (Section 2.6.2) in Type 316 by Morris and Harries [105] provides a general insight into the relationship between fracture and interface sliding. The formation of wedge cracks was suggested in [105] to be the result of athermal decohesion near triple junctions. However, another study [96] suggests that accelerated cavity interlinkage due to local stress concentration on transverse boundaries, resulting from sliding on adjacent boundaries, leads to wedge crack formation. Although these studies suggest that stress concentrations near triple junctions result from relative sliding and cause local cracking, the studies do not provide details of the characteristics and redistribution of local stresses.

These observations reveal that the deformation and damage response in complex alloys is sensitive to the evolution of local strain and stress fields in the presence of sliding. This chapter aims to develop a general numerical approach for modelling grain-boundary sliding (GBS) in polycrystalline materials. The objective is to provide further insights into how sliding affects the

behaviour of polycrystalline Type 316 stainless steel. Examination of the problem in the context of continuum creep models [174,180] does not consider the effect of crystallographic orientation and localisation effects in realistic materials. Advanced multi-scale models for grain-boundary sliding during creep in polycrystals exist in the literature, e.g. [128]. However, none of the studies in the literature examines the evolution of local stress profile along boundaries with different amounts of sliding, nor do they describe grain deformation by physically-based models for creep. This poses the requirement for extending the developed CPFE framework from Chapter 4 by combining physical creep models for deformation of anisotropic grains and grain boundaries. Linear-viscous sliding models are implemented within interface elements in the FE framework in Section 5.2.1. When implementing models for sliding, it is important to satisfy the compatibility at grain-boundary intersections, such as at triple points (2D) or triple lines (3D). This is to prevent the boundaries from separating at these locations to create artificial pores, which is implemented by imposing a constraint at triple junctions to prevent dilation as described in Section 5.2.2. A schematic of the framework is shown in Fig. 5.1. The developed framework was verified for idealised arrays of power-law creeping hexagonal grains by comparing the predictions with results from the literature [109,175] via different numerical approaches (Section 5.2.3). In this chapter, the grain deformation is captured via the micromechanical CPFE model, verified for this material in Chapter 4. In Section 5.3, regular hexagonal arrays of grains with different crystallographic orientations are analysed. The effect of grain neighbours and grain-boundary sliding on local stress state within the grains and across the boundaries is analysed, paying close attention to the vicinity of the triple lines. This serves to provide initial insight into the analysis of the creep response of realistic irregular grain structures in the presence of sliding, which is studied in Section 5.4. The role of intergranular $M_{23}C_6$ precipitates on the sliding response is also briefly examined via a

micromechanical model for the sliding velocity in Section 5.6. The research, presented in this chapter, can be found in Petkov et al. [185].

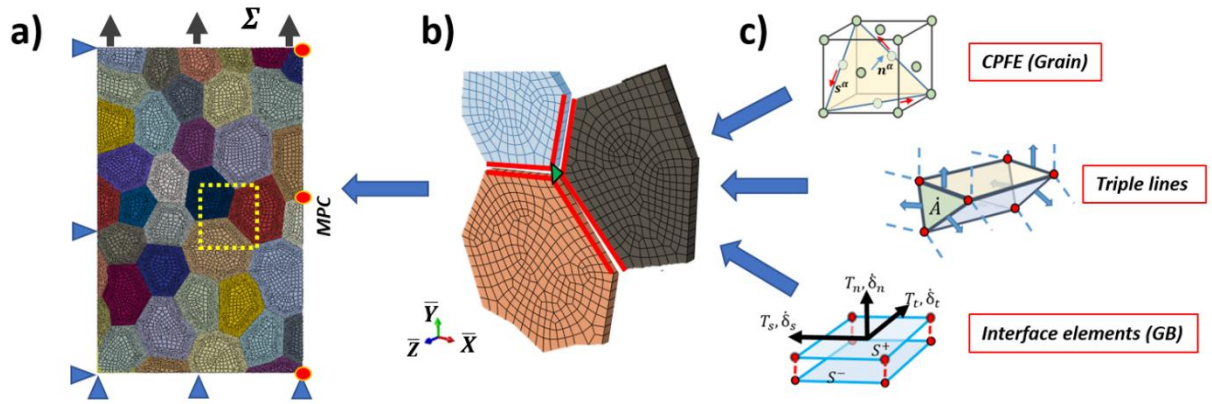


Figure 5.1. a) The meshed quasi-3D, irregular grain shape aggregate. Regions of the grains, triple grain junctions and boundaries are illustrated in b) with computational models for each structural entity in c).

5.2. MODELLING APPROACH AND VERIFICATION

5.2.1. Theoretical framework

Consider a body of volume V and surface S, which contains interfaces/grain boundaries of area Γ_c. The solution of a boundary value problem in which the body is discretized into a number of finite continuum and interface elements with nodal displacements **U**, a vector containing all the degrees of freedom, is given by the system of equations [186]

$$\mathbf{\Psi} = \int_V \mathbf{B}^T \boldsymbol{\sigma} dV + \int_{\Gamma_c} \mathbf{B}_\mathbf{c}^T \mathbf{T}_\mathbf{c} d\Gamma - \mathbf{F} = 0 \tag{5.1}$$

where **B** and $\mathbf{B_c}$ are matrices that relate the local strain and separation ($\boldsymbol{\delta}$) across an interface to the nodal displacements, respectively; $\boldsymbol{\sigma}$ is the local stress, $\mathbf{T_c}$ are the interface tractions and **F** is a vector of nodal forces. Employing creep models for the bulk response and interface models for sliding in Eq. 5.1 gives rise to a set of non-linear equations to solve. An iterative procedure for the

solution at the end of each time increment via a Newton-Raphson method is used, such that if $\mathbf{U}^i$ is the solution after iteration *i*, more accurate solution is given as $\mathbf{U}^{i+1} = \mathbf{U}^i - \left[\partial\boldsymbol{\Psi}^i/\partial\mathbf{U}^i\right]^{-1}\boldsymbol{\Psi}^i$, where

$$\frac{\partial\boldsymbol{\Psi}}{\partial\mathbf{U}} = \int_V \mathbf{B}^T \frac{\partial\boldsymbol{\sigma}}{\partial\boldsymbol{\varepsilon}}\mathbf{B}dV + \int_{\Gamma_c} \mathbf{B}_\mathbf{c}^T \frac{\partial\mathbf{T}_\mathbf{c}}{\partial\boldsymbol{\delta}}\mathbf{B}_\mathbf{c}d\Gamma \tag{5.2}$$

As in Chapter 4, the commercial software ABAQUS is used to obtain solutions to Eq. 5.1, providing standard shape functions **B** for a range of continuum elements. The continuum constitutive response and determination of $\boldsymbol{\sigma}$ and $\partial\boldsymbol{\sigma}/\partial\boldsymbol{\varepsilon}$ in this chapter is described by the CPFE model used in Chapter 4 and described in Appendix A. Note that for the verification of this modelling framework, presented in Section 5.2.3, the bulk response is modelled using a standard power-law creep model. The interface element is implemented as a User Element (UEL) in ABAQUS, following the approach by Elmukashfi and Cocks [186]. This approach adopts a surface-type formulation of the interface from [187]. Full description of the interface element approach for 2D and large-deformation 3D problems is given in [186] and [185], respectively. A summary of the interface element formulation for 3D problems is given here for reference in Appendix B. For the constitutive grain-boundary response, a traction-separation rate law is assumed which decomposes into individual normal ($\dot{\delta}_n$) and tangential ($\dot{\delta}_{tk}$) separation rates

$$\dot{\delta}_n = \dot{\delta}_n^e = \frac{\dot{T}_n}{K_n} \tag{5.3}$$

$$\dot{\delta}_{tk} = \dot{\delta}_{tk}^e + \dot{\delta}_{tk}^{cr} = \frac{\dot{T}_{tk}}{K_t} + \dot{\delta}_{0t}\frac{T_{tk}}{\sigma_0} \tag{5.4}$$

where $\dot{\delta}_i^e$ and $\dot{\delta}_i^{cr}$ are the elastic and viscous components, respectively, and and k = 1,2. N.B. The total separation and traction vectors are $\boldsymbol{\delta} = [\delta_{t1} \quad \delta_{t2} \quad \delta_n]$ and $\mathbf{T}_\mathbf{c} = \left[T_{t1} \quad T_{t2} \quad T_n\right]$ (Appendix B). K_n and K_t are the normal and tangential stiffnesses and $\dot{\delta}_{0t}$ is the rate of sliding at a tangential

traction $T_{tk} = \sigma_0$. The elastic response is chosen to be sufficiently stiff so that it has a negligible effect on the material response. Implementation of the framework from Appendix B does not automatically satisfy compatibility where a number of interface elements meet, i.e. triple lines in 3D. In the following section, a constraint at the triple lines is introduced in order to ensure that the compatibility condition is met. This is implemented through a penalty function.

5.2.2. Modelling of triple grain junctions during sliding

In the remainder of this thesis, thin-slice aggregates of one element through the thickness with irregular grain shapes under quasi-3D plane strain boundary conditions are considered. This is in an attempt to reduce simulation times, while providing sufficient information on stress and strain field variation, and how this depends on crystallographic orientation configurations. The employed triple junction constraint here is similar to that used in the 2D polycrystalline model framework by Bower and Wininger [128]. However, due to the different nature of the problem and interface elements considered in this study, implementation of this constraint requires care. The constraint at triple junctions in this thesis is implemented through the introduction of a triple point element.

Consider an interface element of thickness *h*. Where interface elements meet at triple points as illustrated in Fig. 5.2.a), an arbitrary triangular region *N* of sides h_{12}, h_{13}, h_{23}, shown in Fig. 5.2.b), is created. The rate of change of area of any triangular region *N* can be determined by integrating over its perimeter:

$$\dot{A}^s_\Delta = \oint \dot{u}^s_i n_i ds \tag{5.5}$$

where n_i is the outward unit vector to a side of the element and $\dot{u}^s_i$ is the respective displacement rate in the sliding direction of the adjacent interface element. Linear variation of $\dot{u}^s_i$ is assumed

between nodal values. Applying Eq. 5.5 to a general triple point element in 2D with an arbitrary orientation and diving through by h_{13} gives a rate quantity, independent of the boundary thickness:

$$\dot{L}^s_\Delta = \frac{\dot{A}^s_\Delta}{h_{13}} = \frac{1}{2}\left[\left(\dot{u}_i^{s1} + \dot{u}_i^{s3}\right) n_i^{13} + \left(\dot{u}_i^{s1} + \dot{u}_i^{s2}\right) n_i^{12} \frac{\sin\alpha_\Delta}{\sin\gamma_\Delta} + \left(\dot{u}_i^{s2} + \dot{u}_i^{s3}\right) n_i^{23} \frac{\sin\beta_\Delta}{\sin\gamma_\Delta}\right] \tag{5.6}$$

where angles are given by geometry (Fig. 5.2). When the triple point is in equilibrium, region *N* is an equilateral triangle as is the case for hexagonal grains (e.g. Fig. 5.2.a). Then, Eq. 5.6 becomes

$$\dot{L}^s_\Delta = \frac{1}{2}\left[\left(\dot{u}_i^{s1} + \dot{u}_i^{s3}\right) n_i^{13} + \left(\dot{u}_i^{s1} + \dot{u}_i^{s2}\right) n_i^{12} + \left(\dot{u}_i^{s2} + \dot{u}_i^{s3}\right) n_i^{23}\right] \tag{5.7}$$

The constraint requires $\dot{L}^s_\Delta = 0$ (i.e. $\dot{A}^s_\Delta \to 0$ normalised with respect to an arbitrary element side) which is implemented through the use of penalty functions. Eq. 5.6 can be re-written as $\dot{L}^s_\Delta = \mathbf{A}\dot{\mathbf{U}} = 0$. The matrix **A**, describing the general triple point element in Fig. 5.2.b), is given in Appendix C. A prescribed penalty function, *P*, is imposed on $\dot{L}^s_\Delta$ according to

$$\sum_\Delta \delta\dot{L}^s_\Delta P\dot{L}^s_\Delta = \delta\mathbf{U}^T \sum_\Delta \mathbf{A}^T P\dot{L}^s_\Delta = \delta\mathbf{U}^T \sum_\Delta \mathbf{A}^T S^s_\Delta = 0 \tag{5.8}$$

The quantity $S^s_\Delta = P\dot{L}^s_\Delta$ has the dimensions of force; summation is over all triple points within the body. In a quasi-3D thin-slice geometry, the triple points become triple lines (Fig. 5.2.c). The prism can change in length, but the constraint requires its cross-sectional area to remain constant along its length. This is achieved by imposing the constraint from Eq. 5.8 at the triangles formed of nodes (1-3) and (4-6) in Fig. 5.2.c). Linear variation of displacement rates is assumed along the axis of the prismatic element. For this element, the rate quantity $\dot{L}^s_\Delta$ from Eq. 5.6 becomes

$$\dot{L}^s_{Line} = \frac{1}{2}\frac{\dot{A}^s_\Delta}{h_{13}} + \frac{1}{2}\frac{\dot{A}^s_\Delta{}'}{h'_{13}} = \frac{1}{4}\begin{bmatrix} \left(\dot{u}_i^{s1} + \dot{u}_i^{s3}\right)n_i^{13} + \left(\dot{u}_i^{s4} + \dot{u}_i^{s6}\right)n_i^{13} + \\ +\left(\dot{u}_i^{s1} + \dot{u}_i^{s2}\right)n_i^{12}\frac{\sin\alpha_\Delta}{\sin\gamma_\Delta} + \left(\dot{u}_i^{s4} + \dot{u}_i^{s5}\right)n_i^{12}\frac{\sin\alpha_\Delta{}'}{\sin\gamma_\Delta{}'} + \\ +\left(\dot{u}_i^{s2} + \dot{u}_i^{s3}\right)n_i^{23}\frac{\sin\beta_\Delta}{\sin\gamma_\Delta} + \left(\dot{u}_i^{s5} + \dot{u}_i^{s6}\right)n_i^{23}\frac{\sin\beta_\Delta{}'}{\sin\gamma_\Delta{}'} \end{bmatrix} \tag{5.9}$$

where the primed quantities are associated with the rear face of the prismatic triple line element.

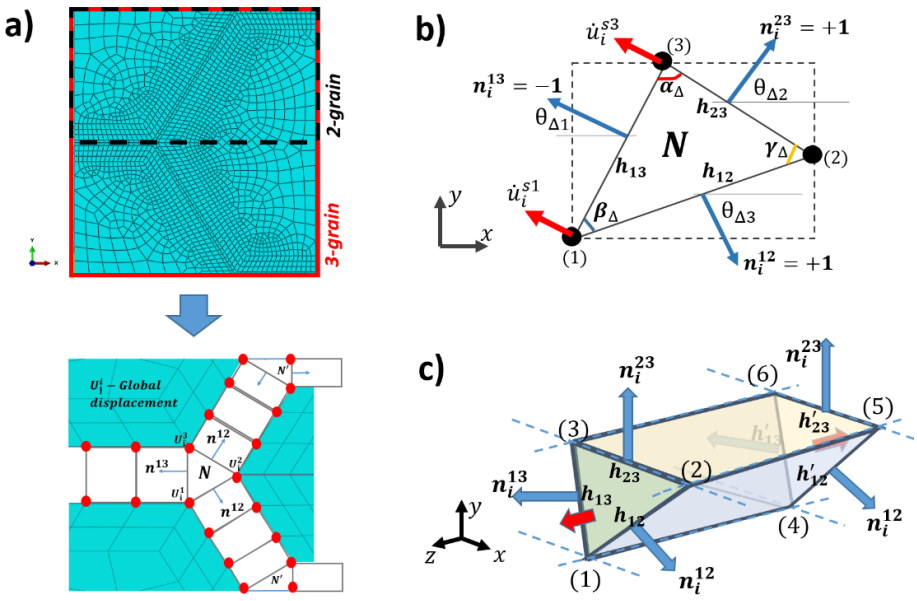


Figure 5.2. a) Illustration of 2- and 3-grain hexagonal arrays, and formation of triple point at interface element intersections. Schematic of an arbitrary b) triple point (2D) and c) triple line (3D) element.

For the triple line element, Eq. 5.8 assumes the same form and the constraint requires

$$\sum_\Delta \mathbf{A}^T S^s_{Line} = 0 \tag{5.10}$$

where $S^s_{Line} = P\dot{L}^s_{Line}$ with matrix $\mathbf{A}$ for the triple line element given in Appendix C. For the triple line, the quantity from Eq. 5.10 is then added to Eq. 5.1 and a solution to the set of equations

$$\bar{\boldsymbol{\Psi}} = \boldsymbol{\Psi} + \sum_\Delta \mathbf{A}^T S^s_{Line} = \int_V \mathbf{B}^T \boldsymbol{\sigma} dV + \int_{\Gamma_c} \mathbf{B}_\mathbf{c}^T \mathbf{T}_\mathbf{c} d\Gamma + \sum_\Delta \mathbf{A}^T S^s_{Line} - \mathbf{F} = 0 \tag{5.11}$$

needs to be determined. The Newton-Raphson scheme for the iterative solution of Eq. 5.11 is

$$\frac{\partial \bar{\Psi}}{\partial \mathbf{U}} = \frac{\partial \Psi}{\partial \mathbf{U}} + \sum_{\Delta} \frac{\partial \mathbf{A}^T S^s_{Line}}{\partial \mathbf{U}} = \int_V \mathbf{B}^T \frac{\partial \boldsymbol{\sigma}}{\partial \boldsymbol{\varepsilon}} \mathbf{B} dV + \int_{\Gamma_c} \mathbf{B}_{\mathbf{c}}^T \frac{\partial \mathbf{T}_{\mathbf{c}}}{\partial \boldsymbol{\delta}} \mathbf{B}_{\mathbf{c}} d\Gamma + \sum_{\Delta} \mathbf{A}^T \frac{\partial S^s_{Line}}{\partial L^s_{Line}} \mathbf{A} \qquad (5.12)$$

For triple points, Eqs. 5.11 and 5.12 assume the same form with $S^s_{Line} = S^s_{\Delta}$. Parametric studies in which the penalty function is systematically increased have been carried out to ensure that the linear growth rates ($\dot{L}^s_{\Delta}$, $\dot{L}^s_{Line}$) are constrained. In Section 5.3.2, it will be demonstrated that artificial voids form at triple grain junctions in the absence of the constraint. Note that in the calculations presented here interface elements of zero thickness are employed. The constraint at the triple junction is treated in this study as a method to allow for the consistent computational implementation of the approach. It is worth pointing out that the constraint can also be interpreted in terms of the micromechanisms at the vicinity of the triple junction. This is further discussed in Section 5.3.3.

5.2.3. Framework verification for power-law creeping material

Validation of the developed framework within both small and large deformation analyses has been carried out by Petkov et al. [185] for power-law creep ($\dot{\varepsilon}_e = \dot{\varepsilon}_0 \left(\sigma_e / \sigma_0\right)^n$) of the hexagonal grain aggregates of Fig. 5.2.a). By progressively increasing the relative sliding rate, $\dot{\delta}_{0t}$, differences in macroscopic creep rates and steady-state stress fields were recorded for creep exponents $n = 1 - 9$. The parameter $\phi_0 = \dot{\varepsilon}_0 D / \dot{\delta}_{0t}$, describing the ease with which the interface deforms as compared to the creep rate of the grains with diameter *D*, is introduced. This allows for comparison across configurations and different reference creep rates, $\dot{\varepsilon}_0$. The increase in strain rate was quantified by the stress enhancement factor $f = \left(\dot{E}_e(\Phi_0) / \dot{E}_e(\infty)\right)^{1/n}$, where $\dot{E}_e\left(\Phi_0\right)$ is the macroscopic effective strain rate for a given value of ϕ_0 and $\dot{E}_e\left(\infty\right)$ is that in the absence of sliding [175]. The variation of f with n and ϕ_0 is shown in Figs. 5.3.a-b). The predictions agree with

results for the same configuration from [109,175]. The limit of free sliding is approached for $\phi_0 \ll 1$. It is important to note that values of f in this section are higher due to the use of a finer mesh here, compared to mesh reference 'Fine' used by Ghahremani [175]. Examples of steady-state σ_{yy} fields are illustrated in Figs. 5.3.c) and d). A heterogeneous stress field is predicted in the presence of sliding, with discontinuity of stress in tension or compressive on either side of the triple junctions, while the stress is uniform in the absence of sliding, agreeing with findings from [180].

The results summarised in this section and [185] provide confidence in the developed methodology to capture the response of creeping polycrystals in the presence of sliding. In the following sections, the framework is employed to study the effects of grain-boundary sliding in polycrystalline aggregates, where grains deform by the CPFE model, described in Chapter 4.

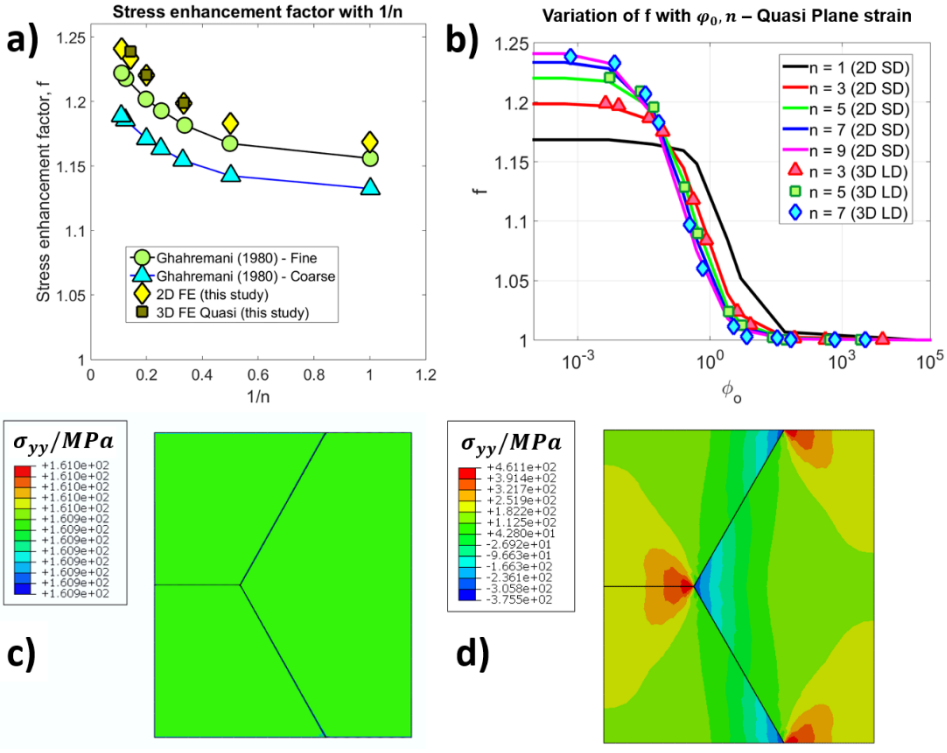


Figure 5.3. Stress enhancement factor with a) n and b) ϕ_0 – 2-grain hexagonal grain array, power-law creep. Contour plots of steady-state σ_{yy} in 3-grain array, n = 7 for a) no sliding and b) free sliding, $\phi_0 = 10^{-3}$.

5.3. MODELLING HEXAGONAL ARRAYS OF GRAINS VIA CPFE MODEL

In this section, the developed modelling framework is employed to analyse the effects of grain-boundary sliding on the behaviour of regular, hexagonal grain arrays of different crystallographic orientations. Simulations for regular 2- and 3-grain arrays were used in Section 5.2 to validate the framework for power-law creep models. Symmetric boundary conditions were imposed on the aggregate when these isotropic plasticity models were used. For the crystal plasticity model, equivalent symmetry conditions cannot be employed directly due to the grain anisotropy. Generally, larger elemental units and different boundary conditions are required to determine the material response. This section begins by analysing the 3-grain aggregate (Fig. 5.2.a) and employing the symmetry boundary conditions from Section 5.2, as shown in Fig. 5.4.a). This geometry provides preliminary results by identifying some general trends in material behaviour in the presence of sliding. The larger aggregates from Figs. 5.4.b-c) contain 4 half grains, and 6 half and one full grain, respectively. They are analysed to assess the sensitivity of the deformation response to the imposed boundary conditions in more realistic aggregates in the absence and presence of sliding. These simulations provide insights into the effects of grain-boundary sliding on local stress fields within different grain configurations. This serves as a precursor to analysing the response of a larger 39-grain aggregate in Section 5.4.

5.3.1. Effects of GBS on strain-rate and local stress fields

The interface sliding models from Section 5.2.1 and CPFE model from Chapter 4 are implemented as UEL and UMAT routines in ABAQUS. C3D8 and C3D6 continuum elements are used for the grains; the 8-noded linear interface element (Appendix B) is incorporated along boundaries. A computational scheme for updating the interface element configuration within a large deformation analysis is developed in this study and employed throughout. This is in order to allow for applying

the shape functions of the reference interface-element configuration to its deformed configuration. For brevity, this updating framework is not presented here. However, a description of the approach can be found in Petkov et al. [185]. A sensitivity study of the interface stiffnesses, K_t and K_n, revealed that a value of 10^6 MPa/mm restricts the elastic opening and tangential separations to magnitudes lower than their creep counterparts. The value of the penalty function, P, for enforcing the constraint on the triple line was selected to be 8 x 10^{10} N/mm. This constrains the opening of the triple line, as demonstrated in Section 5.3.2, without introducing numerical difficulties. In this section, the arrays of Figs. 5.4.a)-c) are analysed with different combinations of crystallographic orientations (Fig. 5.4.d), where S and S2 are plastically softer orientations than H.

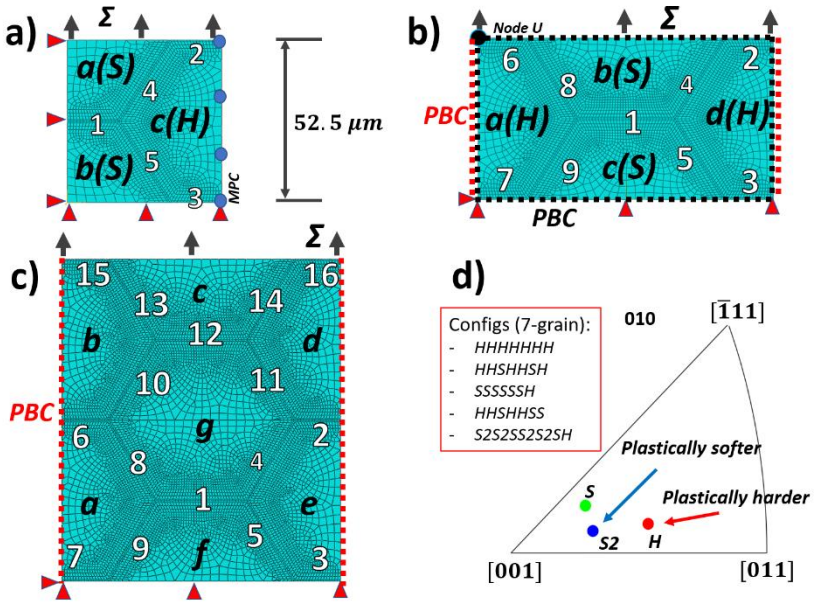


Figure 5.4. a) 3-grain hexagonal array under uniaxial loading (div4) with straight edges. b) The 4-grain array with periodic boundary conditions imposed on either vertical faces only, or on both vertical and horizontal faces under displacement-controlled loading. c) The 7-grain array with a "floating" grain in its centre and PBC imposed on vertical faces. Grain boundaries are numbered in a-c). d) IPF (010-direction) showing crystallographic orientations used in the analysis of idealised grain cells - S and S2 are plastically softer than H. Five crystallographic orientations sets are examined for the 7-grain aggregate with crystallographic orientations for grains 'a'-'g': HHHHHHH (Set i), HHSHHSH (Set ii), HHSHHSS (Set iii), SSSSSSH (Set iv) and S2S2SS2S2SH (Set v). Note: Effective grain size of thin-sliced cells is 52.5 μm.

The CPFE model is calibrated to experimental short-term plasticity and creep data of Type 316 stainless steel at 625°C. This particular condition is examined, since experimental data for grain-boundary sliding in the material under this particular temperature is available in the literature (see Section 5.4). The model parameters, calibrated following the procedure from Chapter 3, are given in Table 5.1. These are obtained from simulating the response of the larger 39-grain aggregate. In this section, the constitutive grain response is simulated to provide initial insight into local grain-to-grain interactions and not to predict the global deformation response of the alloy.

5.3.1.1. Variation of strain-rate in the presence of sliding

Initially the 3-grain aggregate from Fig. 5.4.a) is considered and loaded in uniaxial tension under quasi-3D plane strain. The grain configuration resulting in a crystallographic set SSH is examined. To examine the variation of macroscopic creep strain accumulation in the presence of grain-boundary sliding, the reference sliding rate ($\dot{\delta}_{0t}$) is progressively increased until there is limited change of the predicted creep response, considered as the free-sliding limit. The characteristic S-shaped curve from Fig. 5.3.b) for the minimum creep rate $\dot{E}_e$ with decreasing $\phi_0 = \dot{\varepsilon}_0 D/\dot{\delta}_{0t}$ (where the reference value $\dot{\varepsilon}_0 = \dot{E}_{e,locked}$ in the absence of sliding) is predicted in Fig. 5.5. Values of $\dot{E}_e/\dot{\varepsilon}_0$ are equal to 1.7, 2.85 and 3.6 at ϕ_0 = 0.4, 0.1 and 0.04, respectively. A mesh convergence study of the variation of macroscopic minimum creep rate with ϕ_0 is also shown in Fig. 5.5. The meshes examined consisted of 1896 bulk and 112 interface elements (div4), 2971 bulk and 336 interface elements (div3), and 8097 bulk and 672 interface elements (div2). No significant change in $\dot{E}_e/\dot{\varepsilon}_0$ with mesh refinement is observed. In an attempt to increase computational efficiency, mesh reference "div4" was selected for further simulations of aggregates from Fig. 5.4. Note that examples of predicted creep curves are shown in Fig. 5.7.a) for the 3-grain SSH configuration, where a transition from "locked" to freely-sliding grain boundaries is observed at $\phi_0 \ll 1$. As

crystallographic lattice rotations are continuous during inelastic deformation, creep strain rate will continually evolve and a steady-state will not be achieved. The minimum creep rate is arbitrarily defined here as the difference in macroscopic creep strain over the final 10% of creep time.

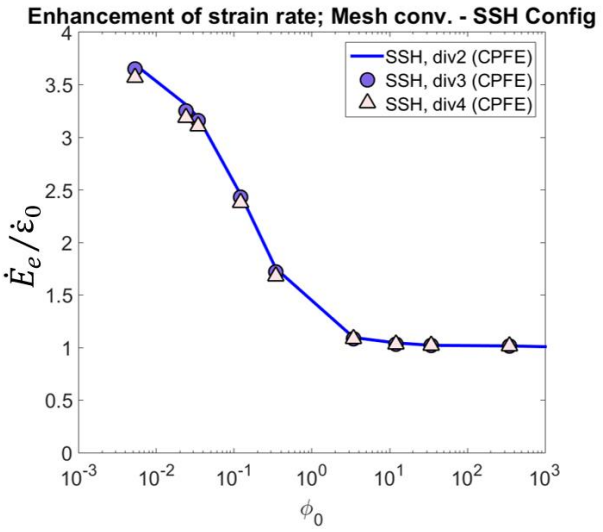


Figure 5.5. Variation of macroscopic creep strain for different values of ϕ_0 for configuration SSH (3-grain cell) and mesh sensitivity of $\dot{E}_e/\dot{\varepsilon}_0$ against ϕ_0 – div2 is the finest mesh with 192 interface elements along an inclined boundary and div4 - the coarsest with 32 interface elements, respectively.

The 3-grain aggregate provides an initial indication of the effect of sliding on creep rate, but the symmetry boundary conditions are not appropriate for the CP models considered [188]. The 3-grain SSH geometry can be stacked side-by-side forming the 4-grain HSSH cell of Fig. 5.4.b). Grains adjacent to the vertical boundaries have the same crystallographic orientations and periodic boundary conditions (PBC) can be used for the vertical boundaries. Here, PBC need to be imposed on these aggregates with limited number of grains in order to reproduce their response as if they were embedded in a real polycrystal. Contrary to the case in Chapter 4, the mesh of the aggregates from Fig. 5.4. is symmetric (nodes on opposite boundaries match) which allows the consistent implementation of PBC. If the orientations of grains ‘b’ and ‘c’ of Fig. 5.4.b) are the same, PBCs can be used on horizontal boundaries. The pattern can be repeated by stacking two

mirror-images of 4-grain cells on top of each other when grains "b" and "c" are of different orientations. This forms the 7-grain array (Fig. 5.4.c). If orientations are the same for grains, adjacent to the two vertical boundaries of the 7-grain array, PBCs can be employed for these boundaries. The central grain in the 7-grain aggregate can have any orientation. Its response is less sensitive to the global BCs employed. This grain is referred to as a "floating grain" below, because it is not tied to the boundaries. The 4- and 7-grain geometries from Figs. 5.4.b) and c) are examined under uniaxial stress-controlled loading. PBCs are employed on the vertical cell faces, with the nodal displacements along the right face linked to those along the left face, following the approach from [189]. The periodicity conditions take the form $u_i = \tilde{\varepsilon}_{ik} x_k + u_i^*$, where $\tilde{\varepsilon}_{ik}$ are the average strains and u_i^* is the periodic part of the nodal displacements. The implementation of the PBC is described in Petkov et al. [185] and is omitted here. By imposing PBCs to the left- and right-hand sides of the aggregates, their deformation response is closer to the behaviour when they are embedded in a polycrystal. Note that no PBCs are applied to the top and bottom surfaces of the aggregates. Stress is applied along these surfaces as the aim here is to explore the change in stress-controlled creep rate in the presence of grain-boundary sliding.

Five different crystallographic orientation sets, allowing the application of PBCs to the vertical faces of the aggregates, are examined with combinations of plastically "harder" and "softer" crystallographic orientations (Fig. 5.4.d). The material response under an applied uniaxial stress of 220 MPa at 625°C is simulated. In Fig. 5.6, the macroscopic creep response of the five 7-grain orientation sets from Fig. 5.4.d) are presented for no sliding ($\phi_0 \to \infty$) and for $\phi_0 = 4.8 \times 10^{-2}$, which results in a response towards the freely-sliding limit. In both of these situations, more inelastic strain is accumulated for plastically "softer" configurations, agreeing with arguments in [190]. The extent of primary creep is greater when the boundaries slide freely. According to

Chapter 3, primary creep is controlled by the evolution of microstructural state (i.e. dislocation structure) and the redistribution of stress from an initial state to a steady state distribution. The initial state is determined by the relative elastic anisotropy of the grains, whereas the steady state distribution is determined by the creep response of the grains. In the case of Fig 5.6.b), grain-boundary sliding also controls the primary creep response. When boundaries slide freely, the stress redistribution process is more pronounced as the shear stresses supported by the grain-boundaries initially relax giving rise to the more extensive primary creep response observed in this limit.

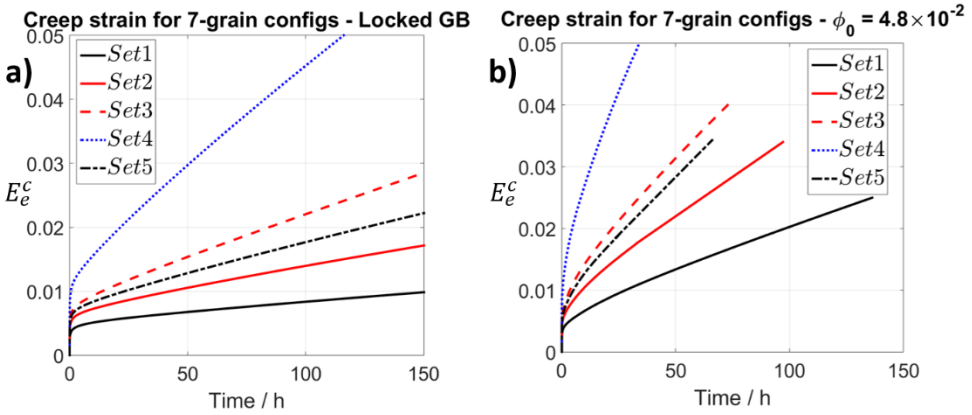


Figure 5.6. Macroscopic creep strain curves for the five 7-grain cell configurations of crystallographic orientations – a) no sliding ($\phi_0 \rightarrow \infty$) and b) free sliding ($\phi_0 = 4.8 \times 10^{-2}$).

Similar findings were made on the predicted creep response of the 4-grain aggregate under these conditions. The response under uniaxial load of 220 MPa at 625°C of the 3-, 4- and 7-grain aggregates with crystallographic orientation configurations SSH, HSSH and HHSHHSS, respectively, is now compared for the same set of parameters. The creep responses are compared in Fig. 5.7.a) for values of ϕ_0 = +∞, 0.2 and 0.04. When sliding along the boundaries is restricted, the creep responses are virtually the same. However, in the presence of sliding, a weaker increase in creep strain rate with decreasing value of ϕ_0 is observed for the 7-grain cell compared to the 3-grain cell, with the 4-grain cell lying in-between the two. This observation suggests that a weaker

constraining effect on the grains results in a weaker increase in creep rate in the presence of sliding. This difference is illustrated in Fig. 5.7.b) by the variation of normalised strain rate $\dot{E}_e/\dot{\varepsilon}_0$ with ϕ_0 for the three arrays. The following sections examine in detail the origin of the differences. Note that this reduced effect of grain-boundary sliding on the creep rate for the 7-grain cell is similar to the trend predicted for the larger grain array in Section 5.4.

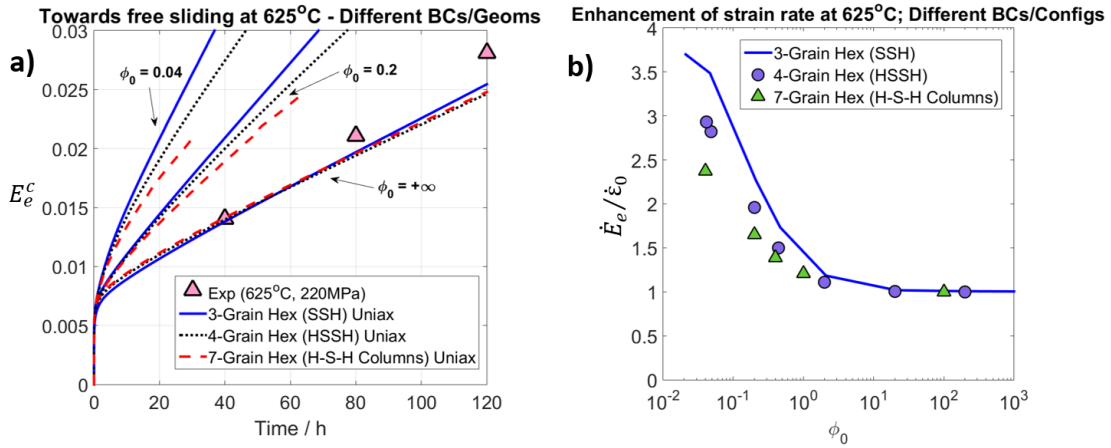


Figure 5.7. a) Macroscopic creep strain for different values of ϕ_0 for 3-grain SSH, 4-grain HSSH and 7-grain columnar H-S-H (Set iii) configurations at 625°C under uniaxial loading. b) Comparison between variation of $\dot{E}_e/\dot{\varepsilon}_0$ with ϕ_0 for creep responses of the three hexagonal geometries from a).

5.3.1.2.Contribution of grain-boundary sliding to overall deformation rate

As discussed in Section 5.1.2, the enhancement of macroscopic strain rate when grain boundaries slide is due to i) the non-uniform intragranular stress field and ii) the contribution to global strain from relative sliding along boundaries. A procedure for estimating only contribution ii) is developed in this study. Here, the approach is applied to quasi plane strain problems, but can be extended to 3D problems. Consider a polycrystal of volume V that contains grain boundaries of total area Γ_c. It deforms with a macroscopic strain rate $\dot{E}_{ij}$ as a result of straining of the grains $(\dot{\varepsilon}_{ij})$ and grain boundaries, sliding at a rate v_s. The Principle of Virtual Power can then be written as

$$\dot{E}_{ij}\Sigma^*_{ij} = \frac{1}{V}\left[\int_V \dot{\varepsilon}_{ij}\sigma^*_{ij}dV + \int_{\Gamma_c} v_s\sigma^*_{ij}n_i s_j d\Gamma\right] \tag{5.13}$$

where Σ^*_{ij} is an arbitrary applied stress and σ^*_{ij} is the grain stress field in equilibrium with Σ^*_{ij}; n_i is the normal to the sliding boundary and s_i is a unit vector in the direction of sliding. For a uniform stress σ^*_{ij}, such that $\sigma^*_{ij} = \Sigma^*_{ij}$, the components of strain rate can be expressed from Eq. 5.13 as

$$\dot{E}_{ij} = \frac{1}{V}\left[\int_V \dot{\varepsilon}_{ij}dV + \int_{\Gamma_c} v_s n_i s_j d\Gamma\right] \tag{5.14}$$

The macroscopic components of strain rate and the contributions from sliding can be measured experimentally (see [105]) and can be determined from the FE analyses in this chapter, allowing direct comparison. Then, consider a body subjected to a stress Σ_{yy}, resulting in a strain rate $\dot{E}_{yy}$. The fraction of the total macroscopic strain rate in the y-direction due to sliding, Γ^*_{yy}, is

$$\Gamma^*_{yy} = \frac{\dot{E}^{gbs}_{yy}}{\dot{E}_{yy}} = \frac{1}{V\dot{E}_{yy}}\int_{\Gamma_c} v_s n_2 s_2 dS \tag{5.15}$$

To obtain Γ^*_{yy} for the 3-, 4- and 7-grain aggregates, the predicted sliding velocity profiles $v_s(x)$ were numerically integrated along all grain boundaries and summed. As an example, the steady-state sliding velocities along grain boundaries of the 4-grain aggregate at 625°C are given in Fig. 5.8.a). The computed values of Γ^*_{yy} for the 3-grain SSH, 4-grain HSSH and 7-grain H-S-H (Set iii) configurations under uniaxial loading and $\phi_0 = 0.04$ are 20.1%, 20.9% and 21.1%, respectively. At this particular value of ϕ_0, the contributions from grain-boundary sliding to the total deformation rate are virtually the same for the three idealisations. The increase in creep rate due to sliding stems from: i) the heterogeneous stress field resulting from relaxation of shear stress along boundaries due to sliding; and ii) the additional contribution from sliding itself. Therefore,

the weaker increase in creep rate from Fig. 5.7 is likely to be as a result of differences in the intragranular stress state across the three geometries. This is investigated in the following section. Furthermore, by computing the values of Γ^*_{yy} for each of the five 7-grain configurations examined, larger contributions to the overall deformation from sliding are found in the "softer" configurations (Fig. 5.8.b). Note that parameter Γ^*_{yy} is of great importance. Section 5.4 demonstrates how experimental data for Γ^*_{yy} can inform the calibration of the interface-element deformation response.

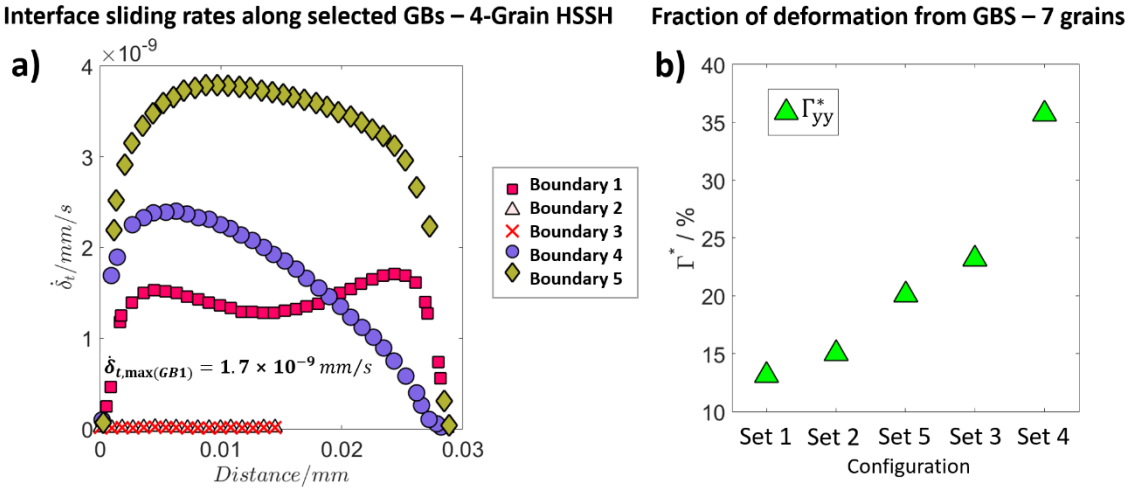


Figure 5.8. a) Example, steady-state sliding rate along selected boundaries of the 4-grain HSSH aggregate during creep at 625°C at $\phi_0 = 4 \times 10^{-2}$. In b), the fractions of total deformation due to GBS with respect to the y-direction (Γ^*_{yy}) are shown for the five different 7-grain crystallographic configurations.

Another important conclusion from the predictions is that boundaries, normal to one of the principal loading axes, can also slide (see Boundary 1 in Fig. 5.8.a). However, the steady-state sliding rates along these boundaries are approximately 1-3 orders of magnitude lower than those along inclined boundaries. This phenomenon arises from the elastic-plastic anisotropy mismatch between the grains either side of the boundary. Because of this mismatch, the structural problem is not symmetric about the interface. Thus, contrary to the commonly held view [121], sliding can occur on boundaries normal to the loading axis. This is discussed in more detail in Section 5.6.

5.3.1.3.Variation of stress state due to sliding and imposed boundary conditions

The major contribution to the increased deformation rate due to sliding arises from the non-uniform intragranular stress field as a result of the relaxation of shear stresses along sliding interfaces. The predicted heterogeneous σ_{yy} stress fields within the 4-grain HSSH and 7-grain H-S-H configurations under uniaxial load of 220 MPa at 625°C are compared for the cases of no sliding and $\phi_0 = 4.0 \times 10^{-2}$ in Fig. 5.9. The distinct pattern in the plots from Fig. 5.9 at the free sliding limit is similar to that for the power-law creeping material from Section 5.2. The stress profile shows a discontinuity of stress in tension or compression across the transverse interfaces with a concentration of stress near the triple junctions. It is important to note that the additional heterogeneity due to anisotropy of each individual grain in the CPFE model enhances this effect. For the anisotropic crystals, the symmetry of the stress field, present in the isotropic power-law creeping aggregates from Fig. 5.3, is lost. This is illustrated in the line plot in Fig. 5.10.a) of predicted steady-state σ_{yy} profile after 50 hours at 625°C along transverse boundaries 1, 2 and 6 of the 4-grain HSSH configuration. Inconsistencies in the stress profiles for boundaries 2 and 6 are found, with concentrations of stress at locations along the boundaries near the end of the cell.

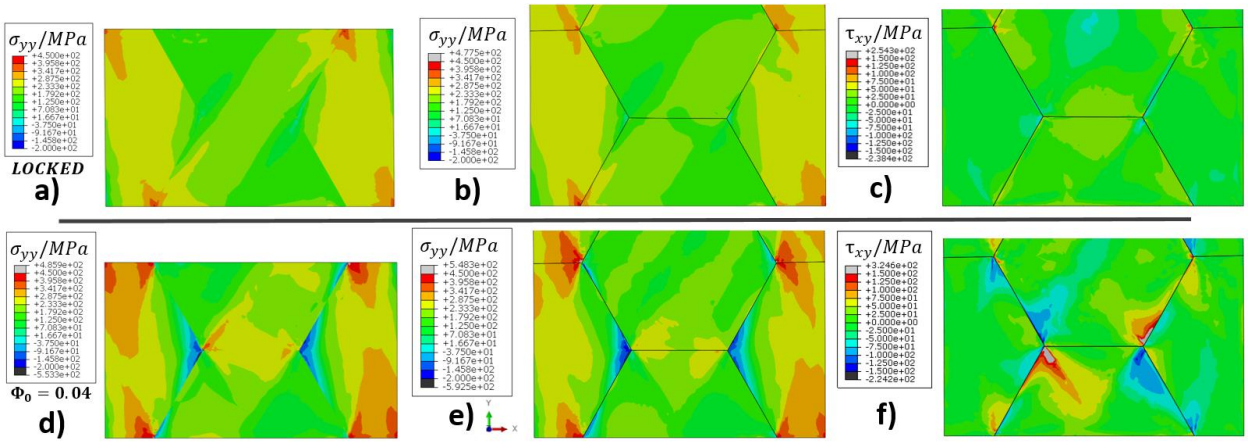


Figure 5.9. Contour plots of σ_{yy} after 50 hours at 625°C in the absence of sliding in a) the 4-grain and b) 7-grain aggregates; and at $\phi_0 = 4 \times 10^{-2}$ in d) and e), respectively. Contour plots of τ_{xy} in the 7-grain cell without sliding and at $\phi_0 = 4 \times 10^{-2}$ in c) and f), respectively. Portion of the 7-grain cell is shown.

This is a direct result of the constraint arising from the imposed boundary condition at the top and bottom surfaces and it is not representative of real polycrystalline material response. Attention is now focused on evaluating the effect of the imposed BCs on redistribution of stress in the presence of grain-boundary sliding by comparing the resultant stress fields for the 4- and 7-grain cells. The objective is to identify the nature of the weaker increase in creep rate due to sliding in the 7-grain aggregate (Fig. 5.7). In Fig. 5.10, direct comparison is made between the predicted normal stress along the transverse grain boundaries of the 4- and 7-grain cells after 50 hours of creep at 625°C and applied macroscopic stress of 220 MPa. Results are compared in the absence of sliding and at $\phi_0 = 4 \times 10^{-2}$. Two important observations are made from the comparison in Fig. 5.10. Firstly, the stress distributions along the transverse boundaries 2 and 6 in the 7-grain aggregate are similar to each other. But the inconsistent stress profile in the 4-grain aggregate is illustrated by increase of stress at the left-hand end of boundary 6 and decrease at the right-hand end of boundary 2. Such variations are not found along these boundaries in the 7-grain cell. This is expected since, in the 7-grain geometry, the grains either side of these boundaries and the periodic boundary conditions of the aggregate exert natural constraints on them. Secondly, the relative increase in normal traction along boundaries 1, 2 and 6 as a result of sliding is greater for the 4-grain aggregate. For the 4-grain cell, the average steady-state σ_{yy} stress after 50 hours along boundaries 1, 2 and 6 increases from 185, 238 and 304 MPa (no sliding) to 258, 308 and 353 MPa ($\phi_0 = 4 \times 10^{-2}$), respectively. For the 7-grain cell, the average σ_{yy} increases from 178, 273 and 275 MPa in the absence of sliding to 238, 313 and 317 MPa at $\phi_0 = 4 \times 10^{-2}$ for the same boundaries. Note also that boundary 1, enclosed by grains of plastically "softer" orientations, carries lower stresses than boundaries 2 and 6, which are enclosed by "harder" grains, agreeing with [160,191,192].

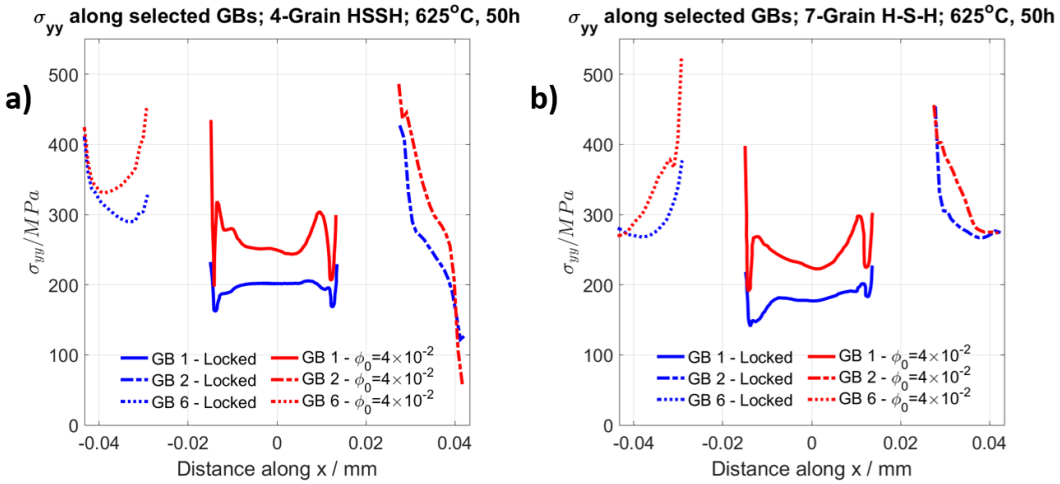


Figure 5.10. Line plots of σ_{yy} under uniaxial loading after 50 hours with distance along x-coordinate for grain boundaries (GBs) 1,2 and 6 within the a) 4-grain HSSH aggregate and b) 7-grain H-S-H columnar configuration (Set iii) at 625°C. Scenarios in the absence of sliding and $\phi_0 = 4 \times 10^{-2}$ are illustrated.

This examination of the predicted stress fields within the two cells reveals that the difference in creep response between the 4- and 7-grain geometries at $\phi_0 < 1$ (Fig. 5.7) stems from partial relaxation of stresses in the less-constrained 7-grain geometry. The additional degrees of freedom in this aggregate allow for the accommodation of inhomogeneous deformation between grains with natural boundary conditions (i.e. the "floating" grain). This leads to attenuation of the heterogeneous stress field, naturally arising due to the relaxation of shear stresses along sliding interfaces. A similar trend as a result of sliding is observed in Section 5.4 for the more realistic grain array. The findings from this section provide useful insight in explaining the predictions in Section 5.4. Furthermore, grain-boundary sliding is known to accelerate intergranular damage in polycrystals [193,194]. The observations from this section further suggest that intergranular cavitation will depend on the crystallographic orientations of the grains either side of the boundary, whether cavitation is stress- or inelastic-strain-controlled (Section 2.5.4). Hence, the stress variation along boundaries in realistic geometries is examined for different combinations of crystal

orientations in Section 5.4. Chapter 7 then discusses the effects of stress and inelastic strain variation for different crystallographic orientations on intergranular failure.

5.3.2. Importance of the triple line constraint

The simulations, presented in Section 5.2 for power-law creeping material, were conducted with and without implementation of the triple junction constraint of Eqs. 5.8-5.10. Equivalent solutions were obtained using these approaches. This is due to the strong symmetry of the configuration and the isotropic nature of the material model adopted. However, the constraint plays an important role in the CPFE-interface element framework. As an example, contour plots of σ_{yy} stress fields are shown in Fig. 5.11 for a) no-sliding, b) freely-sliding boundaries with the constraint of Eq. 5.10 and c) freely-sliding boundaries without the constraint. When sliding is absent, the constraint is redundant (Fig. 5.11.a). In the presence of sliding, the triple junction in Fig. 5.11.b) rotates due to the anisotropic deformation of each grain and the imposed constraint at the triple line. This is not the case in Fig. 5.11.c) where a "void" forms in the absence of the constraint, violating the compatibility requirement. Similar observations are made across geometries from this and the following section. More importantly, Figs. 5.11.b-c) indicate that absence of the constraint modifies the local stress concentration at the triple junction when sliding occurs. This is supported by the argument from [195] on the potential inaccuracies in local stress where interface elements intersect. This could have an impact on predicting intergranular damage when grain-boundary sliding is considered. As mentioned in Section 5.2.2, the constraint can be interpreted in terms of local micromechanical processes near the triple junction. In cases where diffusive transport along boundaries is considered, the stress concentration at the triple junction could be alleviated. Such approach to model the triple junctions was adopted by Bower and Wininger [128], who considered the volume flux, grain-boundary tension equilibrium and grain-boundary migration at the triple

junction. The present study does not explicitly model the diffusive transport along grain boundaries, hence the assumed constraint is purely computational. Nevertheless, other local diffusive processes can modify this local constraint and these are discussed in Chapter 7. Extension of the constraint formulation to full-3D, where triple lines intersect to form apices, is outside the scope of this thesis.

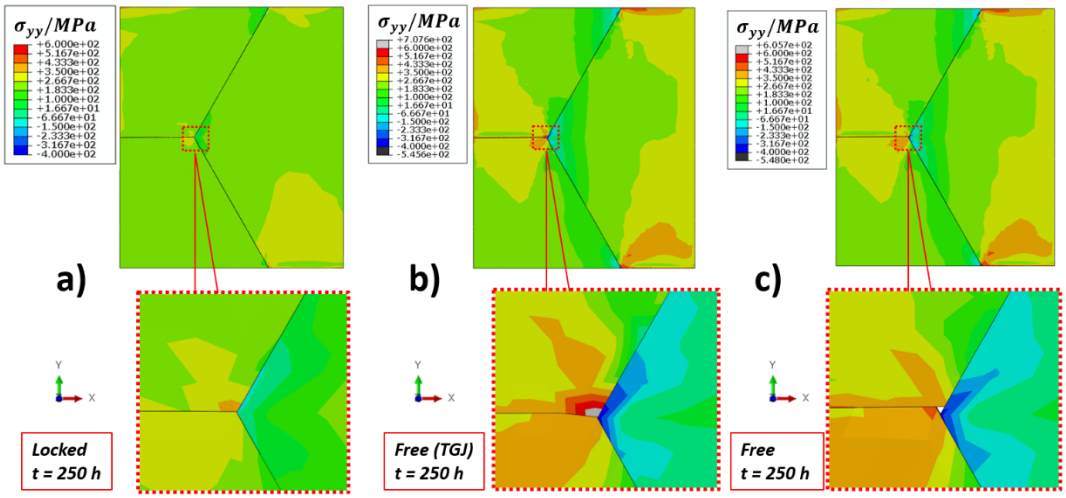


Figure 5.11. Example of contour plots of σ_{yy} in configuration HSH after creep under uniaxial loading – a) no sliding, b) freely-sliding boundaries with the constraint, and c) freely-sliding boundaries without the constraint. Close-up images of the triple junctions in each case are shown at the bottom row.

5.4. MODELLING LARGE POLYCRYSTALLINE AGGREGATES VIA CPFE MODEL

In this section, the CPFE-interface element framework is employed to study the effects of grain-boundary sliding in larger polycrystalline aggregates for Type 316 stainless steel at 220 MPa and 625°C. For this material, Morris and Harries [105] measured experimentally the fraction of deformation due to sliding $\Gamma^*_{yy} \approx 6\%$ under these conditions. The creep response of the CPFE model and interface elements are calibrated to simultaneously capture the macroscopic creep deformation of the material and predict $\Gamma^*_{yy} \approx 6\%$. Model predictions calibrated to this thermo-mechanical history then provide more insight into local changes in stress and strain fields, and the experimental observations made in [105]. The polycrystalline model adopted here is the 39-grain

aggregate, used in Chapter 4, comprised of grains with irregular shapes (Fig. 5.12.a). This 39-grain aggregate is not treated as a RVE of the material, but only serves to probe the general response of polycrystals with anisotropic grains in the presence of grain-boundary sliding during creep. Four meshes with different interface element lengths, l_c, and number of continuum C3D8/C3D6 elements - i) 2.6 μm/10460 elements, ii) 1.8 μm/16417 elements, iii) 1.0 μm/35843 elements and iv) 0.75 μm/59538 elements - were investigated as part of the mesh convergence study. Mesh convergence was assumed when the difference between the macroscopic creep strain, predicted at the end of a creep test for a finite amount of sliding, with further mesh refinement was < 3%. Mesh i) was found to give a suitable degree of accuracy. The creep strain accumulation and fraction of deformation due to sliding are also measured in two smaller volumes within the 39-grain aggregate consisting of 7 and 15 grains. This allows the examination of deformation response in grains, which are not directly affected by the macroscopic boundary conditions. These smaller volumes are constructed either by i) enclosing the volume of grains by a contour along the surrounding boundaries (Fig. 5.12.b) or ii) connecting the centroids of outer grains of given regions (Fig. 5.12.c).

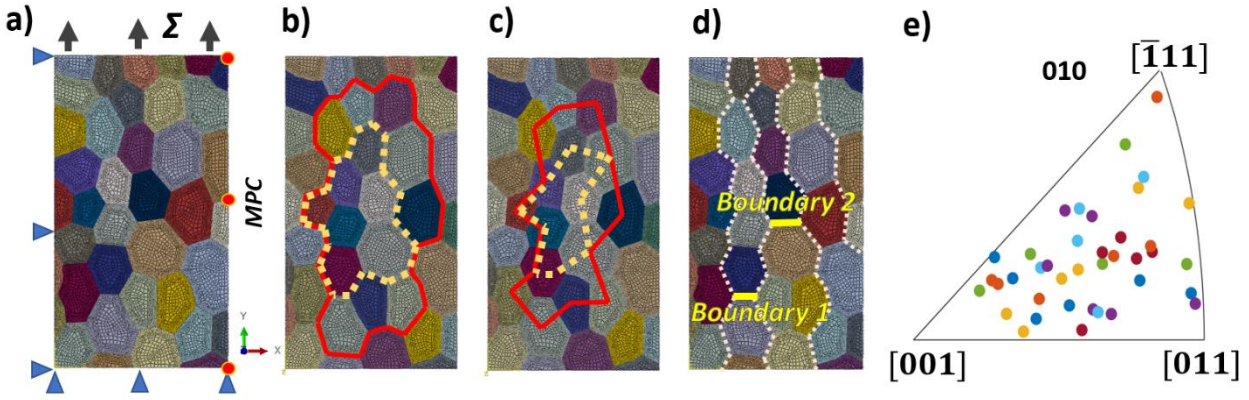


Figure 5.12. a) The 39-grain polycrystalline aggregate with employed boundary conditions. The smaller volumes of 7 grains (dashed line) and 15 grains (solid line), enclosed by b) contour along the surrounding boundaries and c) contour, connecting the centroids of outer grains. d) Two boundaries, along which normal tractions are examined in Section 5.4.2. The dashed lines in d) form columns of grains, examined in Section 5.4.1. e) IPF (010-direction) showing the crystallographic orientations for the 39-grain array (Set 1).

A macroscopic uniaxial stress of 220 MPa is applied along the top surface of the aggregate under quasi-3D plane strain. The left-hand side of the geometry is constrained in the x-direction; the right-hand side remains straight through a MPC. Contrary to Section 5.3, PBC are not imposed here since the nodes on alternate boundaries of the aggregate in Fig. 5.12 do not match. The elastic interface stiffnesses and the value of the penalty function *P* are of the same order of magnitude as in Section 5.3. The calibration procedure from Chapter 3 is employed to determine the micromechanical model parameters, describing the initial state and evolution of the dislocation structure (Table 5.1). The calibration during short-term plasticity and creep is carried-out in the absence of sliding along interfaces. Solution-treated (ST) Type 316 [105] is examined here, in which phase transformations will cause evolution of the contributions to the internal resistance from precipitates (τ_p) and solute atoms (τ_s). Rapid kinetics of precipitate formation and growth, and relatively constant distribution of intra- and intergranular $M_{23}C_6$ precipitates are reported in this heat of Type 316 by [26,105] over the creep exposures considered in this section (< 300 hours), consistent with results on another ST heat [183,184]. Hence, the average spacing and size of intra- and intergranular precipitates is assumed constant with $L_p = 500\ nm, r_p^m = 55\ nm;\ \lambda_p = 90\ nm, d_p = 75\ nm$ after [26,105], respectively. The calibrated creep response in the absence of sliding is shown in Fig. 5.13.a). The short-term plasticity response is omitted for brevity.

Table 5.1. Material parameters for the CPFE model and interface elements, employed in the 39-grain aggregate study, Type 316 at 625°C. Values of C_{ij}, ν, G_0, b and α_d are those from Tables 3.2 and 4.2.

Parameter	Value	Parameter	Value
D_C	4.5 x 10^{-14} m^2/s **	N_0	3.0 x 10^{13} $1/m^2$
$\dot{\gamma}_0$	1.0 1/s	j	1.75 x 10^{15} $1/m^2$
α_0	1.0	P	1 x 10^9 N/mm
ΔL_r	$8b$	W_C	32.0
τ_p	31 MPa	τ_s	39 MPa
K_n	10^6 MPa/mm	K_t	10^6 MPa/mm
σ_0	220 MPa	$\dot{\delta}_{0t}$	$1.0 \times 10^{-26} \sim 1.0 \times 10^{-7}$ mm/s

5.4.1. Variation of creep strain and influence by grain-boundary sliding

Once calibrated to experimental data, the framework is employed to study the variation in creep strain due to grain-boundary sliding by progressively increasing the relative sliding rate, $\dot{\delta}_{0t}$. The crystallographic orientation set from Fig. 5.12.e) which gives a weak texture is assumed for the grains, in order to treat the material as a globally-isotropic body. Based on the observations from Sections 5.1.2 and 5.3, the sliding rates considered in this section are relevant to the behaviour of Type 316 over practical loading conditions (i.e. $\phi_0 > 0.4$). The fraction of deformation due to sliding (Γ_{yy}^*) in the 39-grain aggregate was computed for model predictions at each value of $\dot{\delta}_{0t}$. It is found that a reference sliding rate of $\dot{\delta}_{0t} = 4.5 \times 10^{-10}\ mm/s$ predicts the experimentally-recorded value of $\Gamma_{yy}^* \approx 6\%$, determined in [105]. This particular value of $\dot{\delta}_{0t}$ corresponds to $\phi_0 = 6.43$, obtained with respect to the reference value of macroscopic strain rate in the absence of sliding, $\dot{E}_{yy,lock}$. The changes in creep response at 625°C with increasing values of $\dot{\delta}_{0t}$ are shown in Fig. 5.13.a). To provide a context for these results, it is useful to examine model predictions over comparable values of ϕ_0 for i) the 7-grain array presented in Section 5.3 and ii) the creep response of the 39-grain aggregate at 550°C in the presence of sliding, employing the set of model parameters from Chapter 4. Note that the simulated creep curves of the 39-grain aggregate for finite values of ϕ_0 at 550°C are not presented here for the sake of brevity. For the 7-grain aggregate of configuration H-S-H, the steady-state creep rate is enhanced by factors of 1.07 and 1.44 at ϕ_0 = 6.43 and 0.4, respectively. Predictions of the 39-grain array response at 550°C give values of 1.07 and 1.32, respectively. Thus, at a given ϕ_0, the heterogeneous stress field in the 39-grain aggregate due to sliding has a similar, but reduced effect compared to the 7-grain cell.

A different trend in response of the 39-grain aggregate at 625°C is observed in Fig. 5.13.a). Within the examined range of ϕ_0, the steady-state creep rate of the aggregate at 625°C decreases with increasing value of $\dot{\delta}_{0t}$. Contrary to the findings from the preceding paragraph and Section 5.3, the creep rate of the larger irregular array at 625°C decreases by a factor of 0.86 at $\phi_0 = 1.4$. However, model predictions from Section 5.3 demonstrate that grain-boundary sliding can relax local constraints on grains. Incompatibilities between anisotropic grains are accommodated as a result of sliding. This leads to a reduction in the variation of local stress and inelastic strain within the aggregate, as demonstrated for the 7-grain cell in Section 5.3.1.3. The phenomenon is further illustrated by the 39-grain aggregate macroscopic creep curve at $\dot{\delta}_{0t} = 7 \times 10^{-9}\, mm/s$ ($\phi_0 = 0.4$) in Fig. 5.13.b). At this larger amount of grain-boundary sliding, a greater accumulation of creep strain is noted in the primary regime. This is a result of both the additional strain contribution by grain-boundary sliding and the heterogeneous stress field induced as a result of sliding. However, with further straining, the predicted creep rate in Fig. 5.13.b) decreases gradually due to the partial relaxation of the stress field provided by the accommodating effect of sliding.

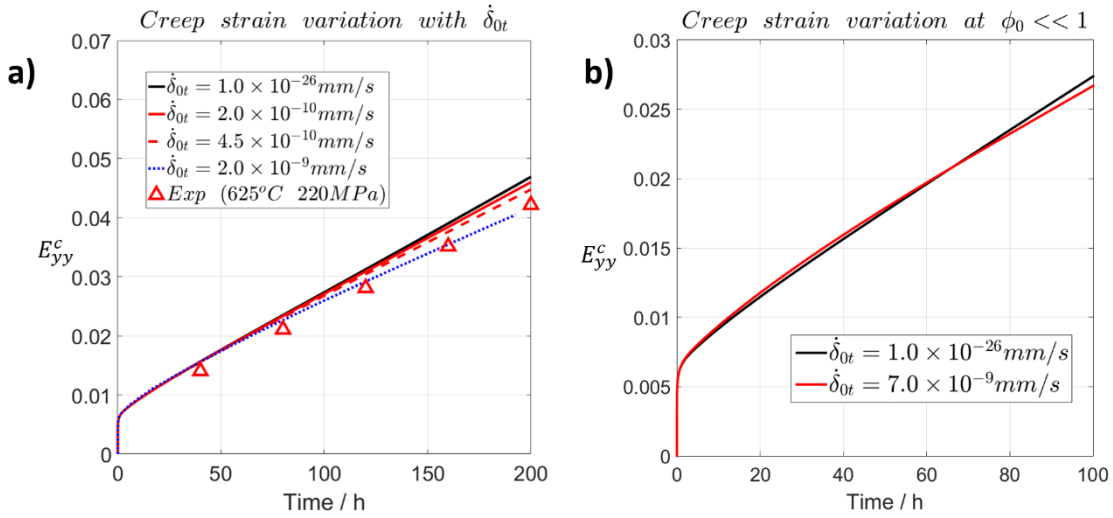


Figure 5.13. a) Creep curves at 220 MPa and 625°C with $\dot{\delta}_{0t}$ for the 39-grain aggregate of crystallographic orientations set from Fig. 5.12.e) and experimental data from [23,105]. b) Macroscopic creep curves without sliding and towards the free sliding limit at $\dot{\delta}_{0t} = 7 \times 10^{-9}\ mm/s$.

Accommodation of incompatibilities between grains as a result of grain-boundary sliding also reduces the constraint on lattice rotations within grains. Figs. 5.14.a) and b) show the initial and final crystallographic orientations of two selected grains in the 39-grain aggregate after creep exposure of 200 hours at 550°C and 625°C in the presence and absence of sliding. The reduction in lattice rotations in the presence of sliding is pronounced at 625°C (Fig. 5.14.b). Over this time interval, the amount of lattice rotation in the absence and presence of sliding at 550°C is virtually the same. This result suggests that, at the lower temperature, grain-boundary sliding allows for limited accommodation of the inhomogeneities between grains (see Fig. 5.14.c). This is supported by the predicted response of the 39-grain aggregate at 550°C with an increase in creep rate at $\phi_0 < 1$, contrary to the results at 625°C. Changes in the lattice rotations could play an important role on the creep response in the presence of sliding. This is briefly discussed in Section 5.6.

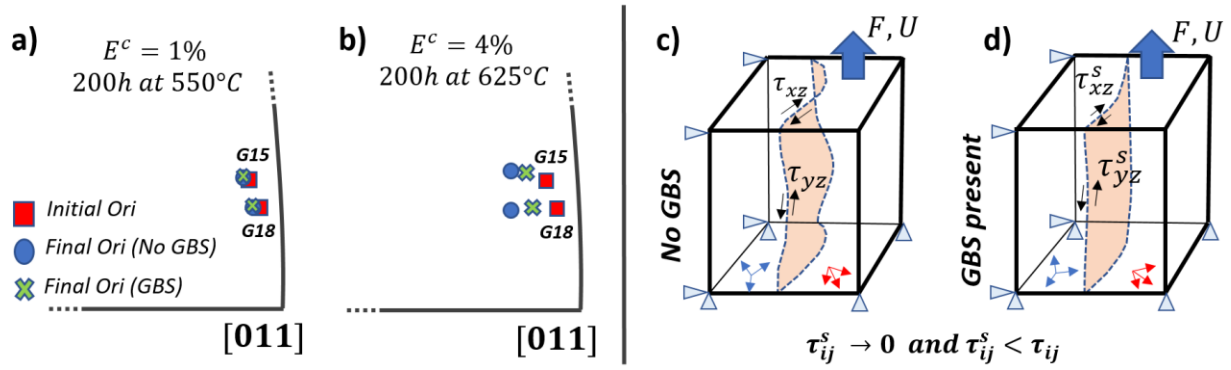


Figure 5.14. Close-up of IPF in sample 010-direction showing initial and final crystallographic orientations for grains 15 and 18 after creep at a) 550°C and b) 625°C with and without boundary sliding (GBS). Reduction of lattice rotations is more pronounced at 625°C. The potential accommodation mechanism of local inhomogeneities c) without GBS due to d) boundary shear stress relaxation in the presence of GBS.

Additional simulations of the 39-grain aggregate were conducted to verify that the results from Fig. 5.13 are real and not a consequence of numerical accuracy. This includes analysis of the 39-grain array in which grains of the same crystallographic orientation are arranged in the H-S-H-S-H configuration from Fig. 5.12.d) (equivalent to Set iii, Fig. 5.4.d). The 39-grain H-S-H-S-H

configuration accumulated 1.51% macroscopic creep strain after 100 hours at 220 MPa in the absence of sliding. At $\phi_0 = 0.4$, the accumulated creep strain after 100 hours was higher at 1.62%, but a decrease in minimum creep rate by a factor of 0.96 was found. The findings from the additional simulations support the findings from Fig. 5.13. The creep response of the 39-grain aggregate for $\phi_0 = 6.43$ was examined for another 9 sets of crystallographic orientations in order to assess the observed behaviour over a larger number of samples. The change in creep rate within the two representative volumes from Figs. 5.12.b-c), obtained by the first term of the integral in Eq. 5.14, was also examined in the presence of sliding. The distinct decrease of creep rate at $\phi_0 = 6.43$ from Fig. 5.13.a) was predicted for the 9 different sets of 39 grains and the two representative volumes. The results are not presented for brevity. These observations suggests that in realistic polycrystals, comprised of anisotropic grains, the effect of grain-boundary sliding on macroscopic creep deformation is more subtle, compared to the effect in the geometries of Section 5.3. Furthermore, the results from Fig. 5.13 demonstrate that the increase of creep rate in Type 316 due to grain-boundary sliding will be weak over the range of ϕ_0 for practical applications. The following section quantifies the changes in local stress profile along grain boundaries due to sliding and identifies aspects of the variation in boundary stress, which are of importance to damage formation during creep.

5.4.2. Inhomogeneity of stress field and influence by grain-boundary sliding

The heterogeneous stress field within grains in the presence of sliding and its variation with respect to local crystallographic orientations is examined here. The stress distributions within the smaller volumes from Figs. 5.12.b-c) are assessed to provide insight into field variations in regions away from the global boundary conditions. Examples of heterogeneous steady-state σ_{yy} fields within the aggregate are presented in Fig. 5.15. The predicted stress distribution as a result of both sliding

and mismatch due to grain misorientations resembles that from Section 5.3. Stress concentrations near the triple lines and discontinuity of stress along transverse boundaries are evident with increasing $\dot{\delta}_{0t}$. Similar to the findings in Section 5.3, the imposed local constraint prevents the opening of triple junctions. This is illustrated in Fig. 5.15.d) at a triple junction for the highest sliding rate considered here, where stress concentrations are observed along the boundary transverse to the applied load. This agrees with findings from Section 5.3.2 where it was found that the local stress state depends on the constraint at the triple junction. These stress concentrations along transverse boundaries near triple junctions can be associated with potential nucleation sites for wedge cracks, observed by Morris and Harries [105]. This is discussed in Section 5.6.

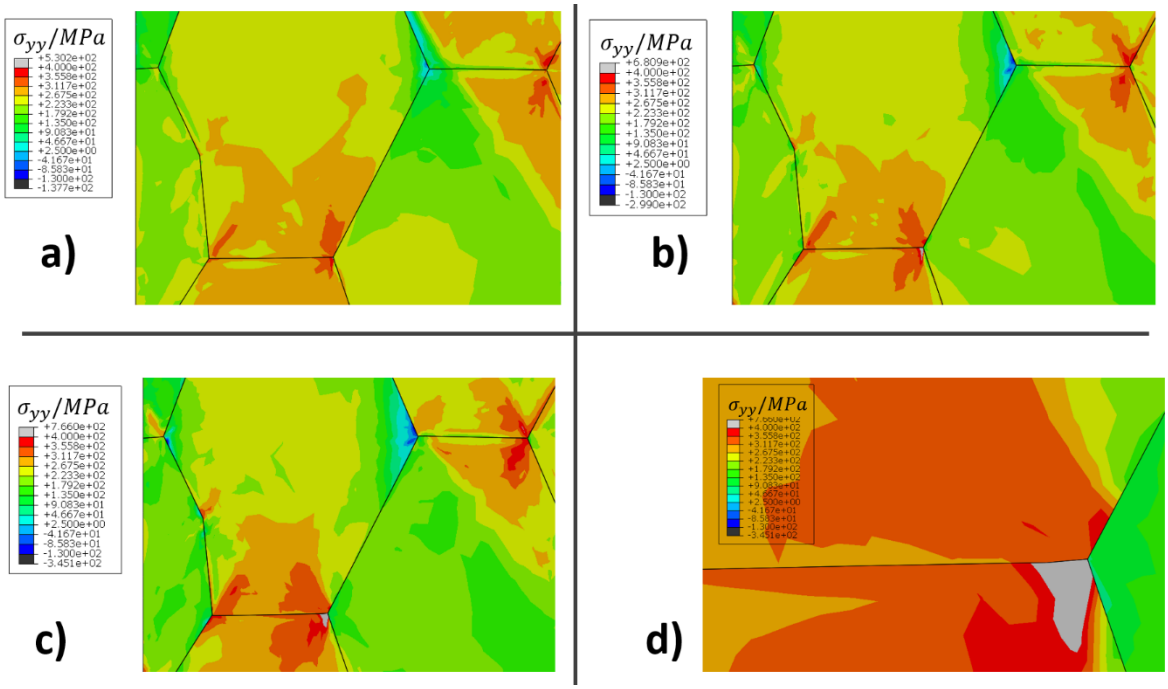


Figure 5.15. Contour plot of σ_{yy} after creep for 100 hours – a) no sliding, b) $\dot{\delta}_{0t} = 2.0 \times 10^{-9}\ mm/s$ and c) $\dot{\delta}_{0t} = 7.0 \times 10^{-9}\ mm/s$ at 625°C and 220 MPa within the Type 1 representative volume. In d), a close-up view of a triple line location at free sliding from c) is presented.

The normal stress distribution during creep at 625°C along two boundaries, approx. transverse to the load axis (Fig. 5.12.d), within the Type 1 representative volume is examined. The

stress profile along boundaries with this orientation is of importance, since intergranular cavitation is pertinent to such boundaries [121]. The stress along the selected boundaries in the absence and presence of sliding in the aggregate is shown in Fig. 5.16. A local increase in σ_{yy} of ~200-300 MPa at a distance of 0.7 μm from the triple line is predicted at $\phi_0 = 0.4$. However, for the scenario examined experimentally in [105] ($\phi_0 = 6.43, \dot{\delta}_{0t} = 4.5 \times 10^{-10}\ mm/s$), the local increase of σ_{yy} in the vicinity of triple junctions is lower (30-40 MPa). The average σ_{yy} along the boundaries increases by 3% for $\phi_0 = 6.43$ and ~20% for $\phi_0 = 0.4$ ($\dot{\delta}_{0t} = 7 \times 10^{-9}\ mm/s$).

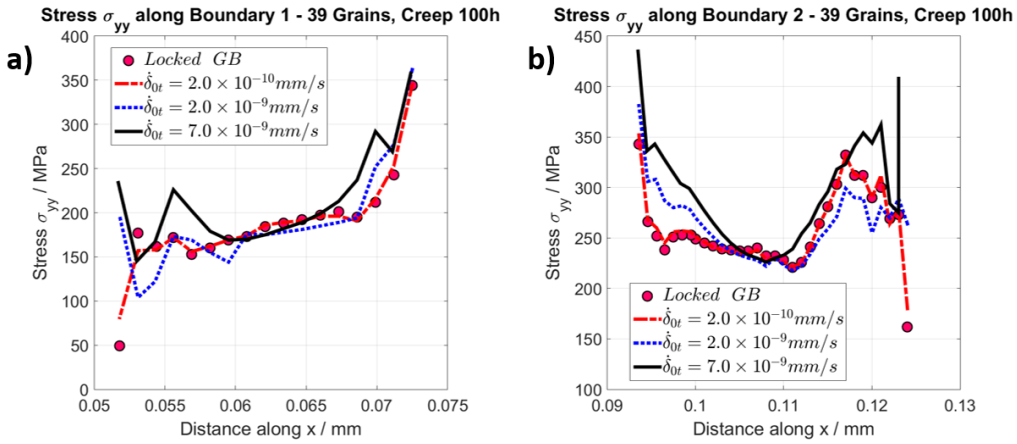


Figure 5.16. Line plots of σ_{yy} with distance along x-coordinate for two transverse boundaries after creep at 625°C. The stress distributions for different amounts of sliding along a) Boundary 1 and b) Boundary 2.

Similar findings were made in the 39-grain aggregate at 550°C. The stress concentrations for a given value of ϕ_0 from Fig. 5.16 appear higher than those predicted for the hexagonal cells. This stems from the greater crystallographic mismatch and irregular grain shapes, leading to a "wedging effect", in the 39-grain aggregate. Furthermore, the normal tractions along Boundary 2 are higher than those along Boundary 1. The insights provided by the results on smaller aggregates (Section 5.3) suggest that this difference is due to the different crystallographic orientations of the

grains that border the boundaries. In the remainder of this section, the influence of crystallographic orientations of neighbouring grains on normal traction across the boundary is examined.

The steady-state normal stress distribution along Boundaries 1 and 2, predicted for the 10 different crystallographic orientation sets of 39 grains examined in Section 5.4.1, are plotted in Fig. 5.17. A difference of ~180 MPa arises between the average stress along a boundary for different crystallographic orientations on either side of the boundary, e.g. average normal stresses of 180 and 367 MPa along Boundary 1 are obtained for orientation sets 7 and 8, respectively.

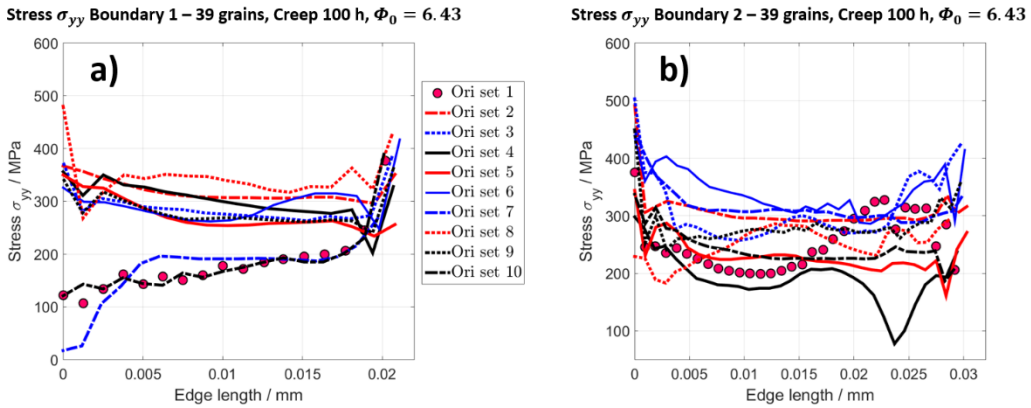


Figure 5.17. Line plots of σ_{yy} along length of a) Boundary 1 and b) Boundary 2 after creep at 625°C and applied load of 220 MPa predicted for the 10 different crystallographic orientation sets examined.

The variation of normal stress across boundaries between grains of different crystallographic orientations from this section agrees qualitatively with the trend from Section 5.3. Predictions in Section 5.3 demonstrate that boundaries enclosed by plastically-harder grains, with orientations away from the [001]-direction on the IPF in Fig. 5.12.e), carry higher normal stresses. The opposite trend is found for boundaries bordered by grains of crystallographic orientations closer to the [001]-direction. This agrees with findings from [191,192] for other FCC materials under elastic-plastic deformation. In an attempt to correlate the predicted variation of stress along boundaries in the 39-grain aggregate with the relative crystallographic orientations of

neighbouring grains, σ_{yy} stress fields and crystallographic orientations are examined within grains above and below Boundary 1 (grains 30, 38 in Fig. 5.18.a). Grains with crystallographic orientations away from the [001]-direction on the IPF in Fig. 5.18.b) tend to carry higher stresses, e.g. grain 30 in orientation sets 8 and 9, demonstrated in the σ_{yy} plots (Fig. 5.18.c). Higher inelastic strains were accumulated in grains with orientations closer to the [001]-direction, e.g. grains 30 and 38 in orientation set 4. N.B. Contour plots of inelastic strain fields are not shown for brevity. Examination of Fig. 5.18 confirm that the higher normal tractions along Boundary 1 are associated with neighbouring grains of relatively harder orientations, e.g. sets 8 and 9. The same trend was noted for the variation of stress along Boundary 2.

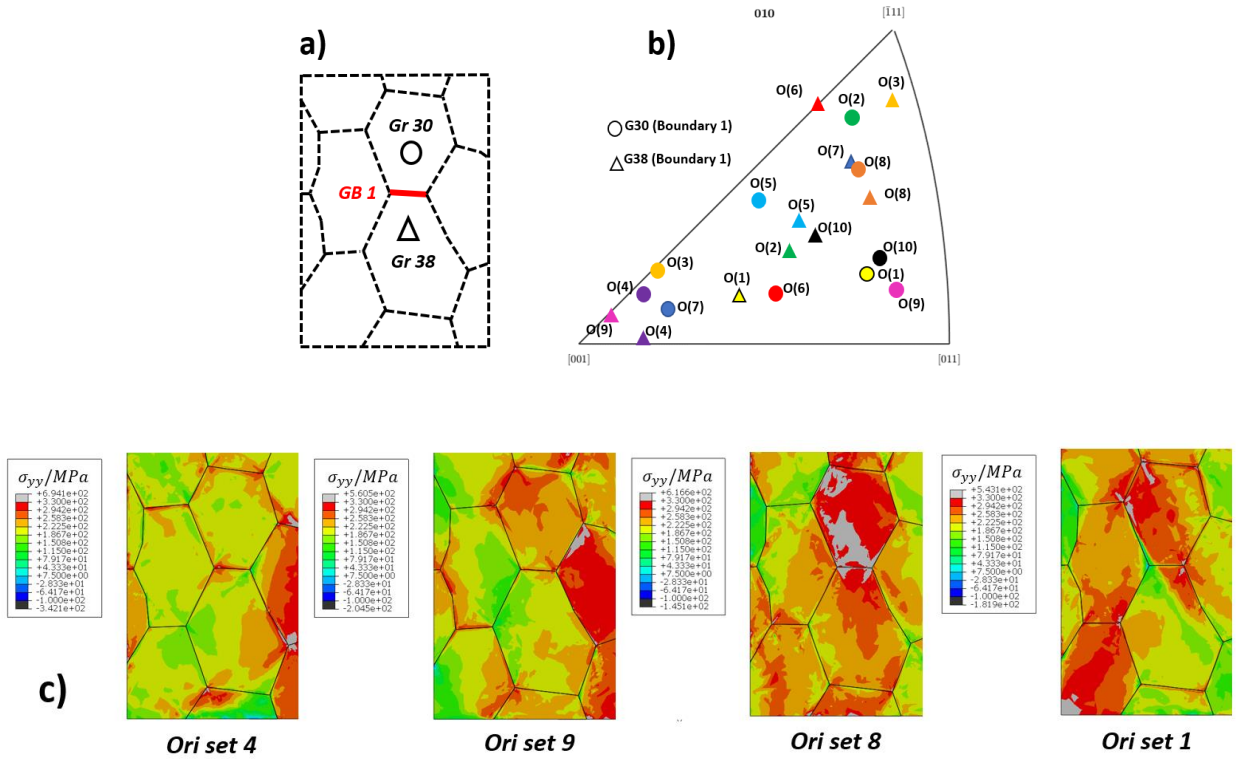


Figure 5.18. a) Location of Boundary 1 in the 39-grain aggregate and grains either side, namely grains 30 (o) and 38 (Δ). In b), the IPF shows the relative crystallographic orientations of grains 30 and 38 for each orientation set (N.B. Grains of the same set are presented in the same colour). In c), contour plots of the steady-state σ_{yy} stress field are shown for three selected orientation sets indicating the higher stresses transmitted through grains of relatively harder orientations, away from the [001]-direction in b).

Some of the presented results may appear to be in disagreement with this trend. An example is the relatively lower normal stress along Boundary 1 for set 10 (Fig. 5.17.a) which is enclosed by relatively harder orientations, according to Fig. 5.18.b). Closer evaluation of this orientation set revealed that the grains on the left and right-hand side of Boundary 1 are of harder crystallographic orientations with respect to grains 30 and 38, thus, transmitting higher stress. These results confirm the observed trend of higher stress along boundaries, enclosed by grains of harder crystallographic orientations. The findings illustrate that the stress across a boundary depends on the grain crystallographic orientations either side and within the local environment. Comparison is also made between the predicted stress distribution along Boundaries 1 and 2 for the 10 crystallographic orientation sets in the cases of no sliding and $\phi_0 = 6.43$. The local increase of σ_{yy} along these boundaries within ~1 μm from the triple lines is in the range 10-60 MPa with an increase in mean normal stress of ~3% along the boundaries. Some of the implications of these findings are discussed in Section 5.6. In Section 5.5, the relationship between the presence of intergranular particles and the sliding rate is discussed. This aims to assess whether the determined sliding rates by the FE model are consistent with those obtained by micromechanical models in the literature.

5.5. ACCOMMODATION PROCESS OF SLIDING AT INTERGRANULAR PARTICLES

Second-phase particles are found in Type 316 [25,114,196]. They control the creep response of both grains and grain boundaries [23,25,26]. Sliding along boundaries can generate high stresses at obstacles such as discrete particles [127], and local deformation mechanisms are required to accommodate the sliding process. Raj and Ashby [178,197] found that the accommodation process for grain-boundary sliding around hard particles, when grains deform by dislocation-controlled creep, is by diffusion along the particle/matrix interface. The balance between the lattice and interface diffusivities controls the process. A micromechanical model is derived in [197] for the

relative sliding rate along a boundary with a population of particles. The model from [197] is employed to assess the effect of particle size, d_p, on the reference sliding rate $\dot{\delta}_{0t}$ in Type 316 stainless steel at 625°C, determined within the interface element framework in Section 5.4. Morris and Harries [25] found that $M_{23}C_6$ precipitates are the dominant intergranular particles at this temperature. The particles can coarsen during prolonged creep exposures and it proves useful to assume that the volume of intergranular precipitates per unit boundary area remains constant (i.e. $f_{VA} = d_p^3/\lambda_p^2 = const.$, where λ_p is particle spacing). This allows $\dot{\delta}_{0t}$ to be expressed by the model from [197] as a function of the physical variables that characterise the boundary as

$$\dot{\delta}_{0t} = \frac{1.6\Omega D_L}{kTf_{VA}}\left(1+\frac{5\delta_b D_i}{d_p D_L}\right)\sigma_0 = \alpha^p\left(1+\frac{\beta^p}{d_p}\right)\sigma_0 \tag{5.16}$$

where D_L is the lattice diffusivity, D_i is the particle/matrix interface diffusivity, δ_b is the boundary thickness and Ω is the atomic volume. Eq. 5.16 suggests that the relative sliding rate in the material decreases with increasing particle size, as larger particles require diffusional transport over greater distances to accommodate sliding. The quantities α^p and β^p can be determined from independent measurements of the fundamental quantities in Eq. 5.16. The measured parameters for Type 316, shown in Table 5.2, give $\alpha^p = 1.86 \times 10^{-16}\, mm/s.MPa$ and $\beta^p = 46.5\, mm$. The interface diffusivity is assumed to be the grain-boundary diffusivity. For an intergranular precipitate size of 75 nm as measured in [25], a value of $\dot{\delta}_{0t} = 2.5 \times 10^{-8}\, mm/s$ is obtained. This value is much larger than the value of $\dot{\delta}_{0t} = 4.5 \times 10^{-10}\, mm/s$, determined in Section 5.4 to give a fraction of total deformation from sliding of $\Gamma_{yy}^* \approx 6\%$ for the material tested in [105]. The discrepancy stems from the fact that the particle/matrix interface diffusivity D_i is difficult to measure and is assumed to be the grain-boundary diffusivity here. In practice, D_i is expected to be significantly less than the grain-boundary diffusivity [198], supporting the trend observed here. Application of Eq. 5.16

to EX Type 316H at 550°C, taking into account the reported particle sizes in [111], yields a reference sliding rate of $\dot{\delta}_{0t} = 7.6 \times 10^{-14}\, mm/s$. Based on the simulations results at 550°C from this chapter, the amount of sliding at this temperature is limited ($\phi_0 \sim 200$). Hence, grain-boundary sliding is not included in any remaining simulations at 550°C. Eq. 5.16 suggests that with increasing values of D_i, i.e. increasing β^p with all other quantities kept constant, the reference sliding rate increases. When precipitates coarsen with time, $\dot{\delta}_{0t}$ decreases and the resistance of the boundaries to sliding increases. Observations from this section demonstrate that the reference sliding rate along boundaries is strongly-dependent on the morphology of second-phase particles. In turn, the sliding along boundaries can alter the evolution of local stress state along the boundary, which can have implications on intergranular cavitation. This is discussed further in Chapter 6.

Table 5.2. Material parameters characterising the grain boundaries in Type 316 stainless steel at 625°C for $\sigma_0 = 220\, MPa$. N.B. The interface diffusivity, D_i, is assumed the same as the grain-boundary diffusivity.

Parameter	Value	Parameter	Value
Ω	1.21 x 10^{-21} mm^3 *	$D_i = D_b$	1.152 x 10^{-7} mm^2/s §
f_{VA}	5.2 × 10^{-5} mm **	δ_b	5.0 x 10^{-7} mm *
D_L	6.197 x 10^{-15} mm^2/s §		

* Data from [90]. ** Data from [25]. § Data interpolated from [199].

5.6. DISCUSSION

The framework developed in this chapter was employed to study the effects of grain-boundary sliding on the creep rate of hexagonal grain arrays and larger polycrystalline aggregates with grains of irregular shapes. Of importance is the behaviour of the realistic larger aggregate in the presence of sliding. In contrast to the trend of increasing creep rate in the 39-grain geometry with increasing relative sliding rate predicted at 550°C, a decrease in creep rate is observed with increasing amount of sliding at 625°C over the practical range of $\dot{\delta}_{0t}$ explored. This is contrary to the predicted creep response in the presence of sliding for the hexagonal grain arrays in Sections 5.2 and 5.3. The

observed behaviour is a result of the additional degrees of freedom in the 39-grain geometry, which allow for the accommodation of inhomogeneities between grains with natural boundary conditions. This partially relaxes the heterogeneous stress field due to sliding and reduces the amount of lattice rotation, required to satisfy the internal boundary condition and accommodate slip. In addition, the relaxed constraint on lattice rotations required to accommodate inelastic deformation assists the change in creep response. Although not presented here, detailed examination of the change in crystallographic orientations of all grains in the 39-grain aggregate, up to the inelastic strains considered, does not reveal a clear pattern of lattice rotation towards either plastically-harder or softer configurations. Nevertheless, model predictions suggest that initial crystallographic orientations, which evolve towards softer orientations during deformation, experience lower amounts of lattice rotation in the presence of sliding, resulting in harder configurations compared to those in the absence of sliding. The observation that the amount of grain lattice rotation is lower in the presence of, as compared to the absence of sliding, agrees qualitatively with findings from [128] that sliding can supress texture evolution and grain elongation. In spite of the fact that changes in local stress and lattice rotations due to sliding are subtle, these can affect the global deformation response due to the highly-nonlinear constitutive models employed. Experimental studies in which the rate of sliding at the boundaries is systematically changed are required to verify this behaviour. Such experiments are complicated to devise since changes in grain-boundary properties only, without affecting the grain microstructure, would be difficult to achieve.

The grain shapes within the 39-grain geometry resemble the grain shapes in realistic microstructures. However, due to the quasi-3D nature of this geometry, the out-of-plane component of interface sliding, present in full-3D geometries, is missing and its effects on the deformation behaviour and stress redistribution in the aggregate are not considered here. Grain-

boundary sliding in power-law creeping full-3D aggregates has been examined in [200,201]. These studies suggest that the intensity of heterogeneous stress field and increase in creep rate due to sliding, predicted for power-law creeping 2D aggregates, will increase in magnitude in the 3D case. This could have implications on findings from this chapter for aggregates with grains deforming according to the CPFE model. The CPFE-interface element framework could be readily extended to study grain-boundary sliding in full-3D aggregates of anisotropic grains to further examine this. This is outside the scope of this thesis and is identified as a direction for future work.

Model predictions from Section 5.4 suggest that normal tractions along transverse and inclined boundaries will vary from facet to facet in polycrystalline materials, with or without grain-boundary sliding and in the absence of damage. Insights into the normal stress distribution along transverse boundaries to the applied load are provided in this chapter. These insights are of importance since coalescence of intergranular creep cavities and formation of microcracks usually occurs along these facets [202]. In Section 5.4, such boundaries are found to carry higher normal stresses when the neighbouring grains have plastically-harder crystallographic orientations, i.e. away from the [001]-direction on the IPF. Lower stresses are transmitted along facets between plastically-softer configurations. This is in agreement with [191,192]. A combination of experimental techniques, e.g. digital image correlation (DIC) and electron backscatter diffraction (EBSD), could prove useful in confirming these trends in Type 316. Note that this variation of stress along different facets could also be responsible for the non-uniform development of intergranular creep damage, observed in experiments [146]. This is examined in Chapter 7.

Predictions from Section 5.4 for the 39-grain aggregate suggest that, for the highest sliding rates considered ($\phi_0 = 0.4$), an increase of ~20% in the average normal traction along transverse facets is expected. In the case of $\phi_0 = 6.43$, replicating the experiments from [105] with $\Gamma_{yy}^{*} \approx 6\%$, the

predicted increase is minor (~3%). In this case, a local increase of σ_{yy} near the triple grain junction in the range 10-60 MPa is predicted for an applied stress of 220 MPa. The predicted increase of stress in the vicinity of triple grain junctions, where wedge cracking was observed experimentally, suggests that the formation of wedge cracks is probably a result of increased local cavitation activity and conglomeration of voids. This agrees with the hypothesis in [96], rather than the decohesion mechanism proposed in [105]. Another important finding from this chapter is the relative sliding along boundaries, transverse to the principal load axis. The rate of sliding along transverse facets was predicted ~1-3 orders of magnitude lower than the rate on inclined boundaries. As will be discussed in the following chapter, intergranular cavitation is sensitive to the deformation response of the boundary. A limited amount of grain-boundary sliding between anisotropic grains will not fully relax the shear traction along facets. This could accelerate the cavitation process as hypothesised in [203]. Furthermore, Argon et al. [123] estimate that stress concentrations at intergranular particles could reach ~20 times the mean traction along a boundary. The implications of second-phase particles on intergranular failure are discussed in Chapter 6.

Findings from this chapter suggest that sliding and local tractions along boundaries in polycrystalline Type 316 stainless steel depend on the i) boundary orientation to the loading axis, ii) relative crystallographic orientation of the bordering grains, and iii) particle morphology and local accommodation mechanism of sliding. The developed modelling framework in this chapter does not consider the intergranular damage behaviour of the material and its sensitivity to the deformation response during creep. In the following chapter, experimental observations of creep cavitation in Type 316 are reviewed. Appropriate models, describing cavity nucleation and growth in the material, are identified and modified. The cavitation models from Chapter 6 are then

implemented within this CPFE-interface element framework in Chapter 7 to assess the cavitation response of the alloy and how this is influenced by microstructural variations.

5.7. SUMMARY

The present chapter introduces a computational method to model the inelastic deformation of grains and grain boundaries in polycrystalline aggregates. The boundaries are modelled using interface elements, which obey an elastic-creep traction-separation law, capturing the interface normal and tangential response. The framework is employed in this chapter to study the internal stress variation and changes in creep response in the presence of grain-boundary sliding in Type 316 stainless steel. Triple grain junctions at boundary intersections are modelled explicitly in order to constrain the potential formation of voids due to relative sliding on adjacent boundaries. The modelling framework is validated for idealised geometries, where grains deform by isotropic plasticity models, against results from the literature. The CPFE model from Chapter 4 is then used within the framework to describe the grain response in realistic polycrystals of irregular grain shapes. The framework provides insights into the effects of grain-boundary sliding in Type 316 stainless steel under creep. Experimental data from the literature on fraction of deformation due to sliding are used to calibrate the global deformation response of the material. Modelling of grain-boundary sliding in hexagonal arrays of grains was also conducted, results from which help explain some of the observed trends in behaviour of the realistic aggregate. The anisotropic deformation of the grains and the mismatch in crystallographic orientation between them is found to control the extent of sliding and stress profile along boundaries, particularly at triple grain junctions. Boundaries, transverse to the applied load, tend to carry higher normal stresses in cases where the

neighbouring grains consist of plastically-harder crystallographic orientations and vice versa. The major conclusions from this chapter are:

1. A decrease in creep rate with increasing $\dot{\delta}_{0t}$ in Type 316 at 625°C is found. Accommodation of inhomogeneities between grains with natural boundary conditions due to sliding leads to partial relaxation of local constraint and a reduced amount of lattice rotation required to satisfy the internal boundary conditions. The effect is less pronounced at 550°C.
2. The effect of sliding on the creep deformation rate in realistic polycrystals of Type 316 stainless steel is found subtle.
3. In Type 316 steel under the conditions examined here, an increase in normal stress near the triple junctions on transverse interfaces of ~25 MPa is predicted for $\phi_0 = 6.43$ ($\Gamma_{yy}^* \approx 6\%$) with an average increase of 6.6 MPa along the transverse facets.
4. Boundaries bounded by plastically-harder grains, with crystallographic orientations away from the [001]-direction, tend to carry higher stress. The opposite is observed for plastically-softer grains closer to the [001]-direction, which accumulate higher inelastic strains.
5. Sliding is found along transverse interfaces as a result of grain anisotropy either side of the facet. Sliding on normal interfaces is 1-3 orders of magnitude slower than along inclined interfaces and could modify the local traction distribution along boundaries.
6. The two main effects of grain-boundary sliding are i) a heterogeneous stress field due to relaxation of shear stresses along sliding boundaries and ii) contribution to macroscopic strain due to sliding. The attenuation of heterogeneous stress fields and reduction in lattice rotations in the presence of sliding, as compared to the no sliding case, is the third main effect of GBS in real polycrystalline materials.

CHAPTER 6

INTERGRANULAR CREEP FAILURE IN TYPE 316 STAINLESS STEEL – EXPERIMENTAL OBSERVATIONS AND MODELS

6.1. MOTIVATION FOR BETTER UNDERSTANDING OF CAVITY NUCLEATION AND INTERGRANULAR CREEP FAILURE

As discussed in Chapter 2, under typical operating conditions of high-temperature power plants, intergranular creep cavitation is the common failure mode in polycrystalline Type 316 stainless steels [95,97]. The process of cavity growth is well understood [100–102]. However, the detailed mechanisms of cavity nucleation are still open to discussion. Experimental studies demonstrate that the creep ductility is sensitive to the nucleation of cavities along the grain boundaries, as well as the evolution of second-phase particles [114,145,196,204]. Furthermore, intergranular creep fracture is a process of sequential failure along different grain boundaries, controlled by the deformation of the surrounding grains [95,205]. This suggests that creep failure is intimately linked to the deformation process. A number of damage assessment approaches in industry are based on measures of inelastic deformation, e.g. ductility exhaustion models [13]. These practical approaches do not explicitly account for any microstructural features, which influence the process of cavity formation and onset of failure, leading to a significant degree of conservatism in life assessment. The development of robust physically-informed models for creep deformation and damage is required to provide further understanding of the process of intergranular creep failure, as well as its sensitivity to microstructural features. This could provide guidelines for the

improvement of existing models in assessment approaches, as well as the development of a unified cavity nucleation theory.

The focus of Chapters 3-5 was to enhance existing micromechanical deformation models and develop a robust multi-scale modelling framework to capture both global and local creep deformation of grains and grain boundaries in Type 316 stainless steel. The aim of this chapter is to review the intergranular failure process in the material. The effects of second-phase particles, impurity content and prior loading history on creep failure are discussed in Sections 6.2 and 6.3. Section 6.4 reviews the major creep cavity nucleation theories. The discussion is centred on creep damage in austenitic stainless steels, and is informed by reviewing modelling studies and experimental data. Several existing models for cavity nucleation and growth are identified as appropriate to describe the intergranular creep failure processes under the thermo-mechanical conditions of interest. In Section 6.5, important features of certain micromechanical processes are considered in order to enhance the existing mechanistic models for cavity nucleation. Application and probing of the described cavity nucleation and growth models within the multi-scale polycrystalline modelling framework, developed in Chapter 5, is identified as a suitable approach to simulate and provide more understanding of the intergranular damage process in Type 316.

6.2. REVIEW OF FRACTURE BEHAVIOUR OF TYPE 316 STAINLESS STEEL

6.2.1. Creep fracture response in solution-treated Type 316 stainless steel

Dean [98] finds that the creep ductility of solution-treated (ST) Type 316H stainless steel is sensitive to the observed failure mode, particularly when interpreted as a function of stress. The observations in [98] suggest that the deformation process strongly affects creep failure in the material. Morris and Harries [23,25,26] examined in detail the variation of deformation and

damage behaviour of ST Type 316. The study found an intrinsic variation of creep ductility (Fig. 6.1.a). At a given temperature, the ductility initially decreases with failure time, followed by an increase before reaching a peak. At longer exposure times, the ductility falls rapidly. As confirmed in [206], the variation was associated with the nucleation, growth and coarsening of intergranular second-phase particles [23]. Details of this phase transformation process are given in Fig. 6.1.b).

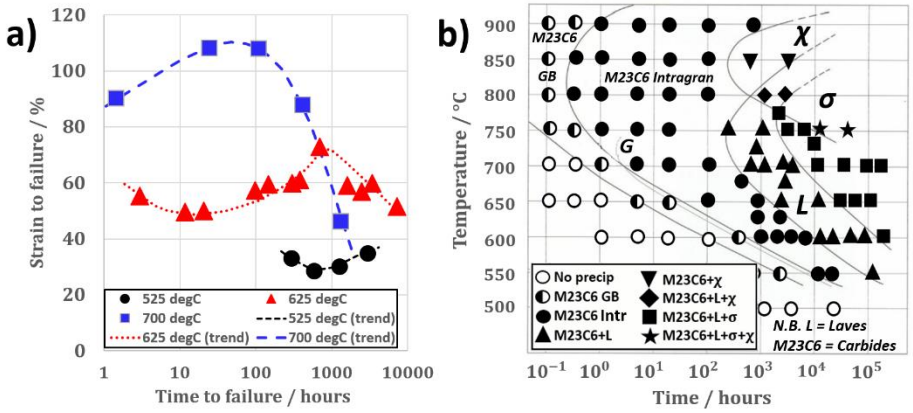


Figure 6.1. a) Ductility with rupture time at 525°C, 625°C and 700°C for Type 316 stainless steel [25]. b) Time-temperature-precipitation (TTP) diagram for Type 316H under thermal ageing [207].

This suggests that the creep failure mechanisms are dependent on the kinetics and morphology of second-phase particles [208]. This thesis is limited to ex-service material where intergranular creep cavitation is the common failure mechanism [95,97,111,209]. Consistent with observations from this section, intergranular cavities are usually found at second-phase particles in ex-service material. This will be reviewed in more detail in the following sections. Investigation of the failure response of solution-treated material is beyond the scope of this thesis.

6.2.2. Creep fracture in ex-service Type 316 stainless steel

Experimental studies on ex-service material after operation in plant for >65000 hours at temperatures 500-625°C and stresses in the range 10-300 MPa reveal a common creep fracture mode – intergranular cavitation at second-phase particles [95,97,111,209] (Fig. 6.2).

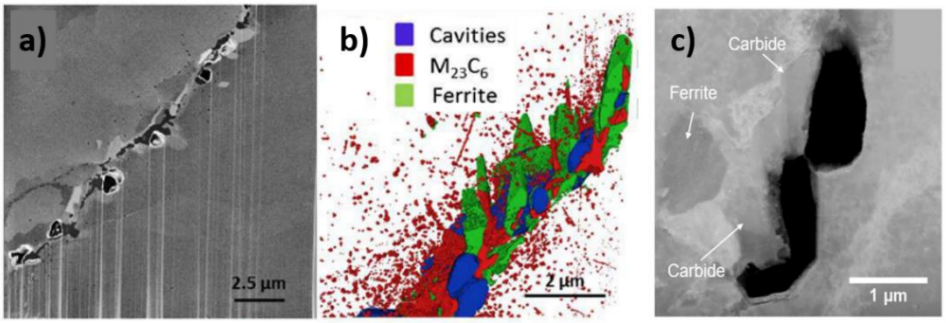


Figure 6.2. a) Cavities at intergranular carbide and ferrite particles in EX Type 316H and b) 3D visualisation of the region [95]. c) Cavities at carbides found at all locations (courtesy of Siqi He, University of Bristol).

Chen et al. [196] suggest that creep cavity formation in Type 316H stainless steel is a result of stress concentrations at obstacles along grain boundaries due to localized inelastic deformation. Ex-service Type 316H contains pre-existing populations of second-phase particles, mostly inter- and intragranular $M_{23}C_6$ carbides. Their evolution in ex-service material is minimal since the kinetics of coarsening are slow enough to be neglected [210]. Creep cavities in the material were found mostly at intergranular $M_{23}C_6$ carbides with an average particle diameter of ~400 nm (min. 100 nm to max. 1500 nm). Observations of cavity morphology across ex-service material suggest that cavities are of approx. spherical shape with diameters between 200 and 1500 nm [61,95,97,111,114,204,209,211]. Note that Bouchard et al. [212] measured the minimum cavity size to be approx. 14 nm. However, Chen et al. [111] highlight the limitation of experimental techniques to observe newly-nucleated cavities due to their resolution. The fractional size distribution of cavities has been investigated during creep at 550°C and 320 MPa [204] (Fig. 6.3), demonstrating that cavity nucleation in the material is continuous. It is difficult to determine where the nucleation process commences since a population of cavities have grown substantially in this sample, extracted from an ex-service component. Lenticular cavities with average diameters between 1-3 µm were also noted at ferrite particles in Type 316H [211]. The role of ferrite is negligible since the spacing of this phase (~10 µm) is too large to lead to interlinkage of cavities.

Under certain conditions cavities are found at the intermetallic σ-phase [207]. The σ-phase has not been observed in Type 316/316H stainless steel at temperatures <600°C and creep exposures of <100000 hours [26,95,97,111,196,209]. Furthermore, the NIMS report on Type 316H [207] shows that σ-phase does not form after 100000 hours at 550°C. The focus of the creep damage part of this thesis is on short-term creep response of ex-service Type 316H at <600°C. Based on the findings from this section, σ-phase will be ignored as a nucleation site in this study. Further aspects of the grain-boundary morphology, related to cavitation, are discussed in the following sections.

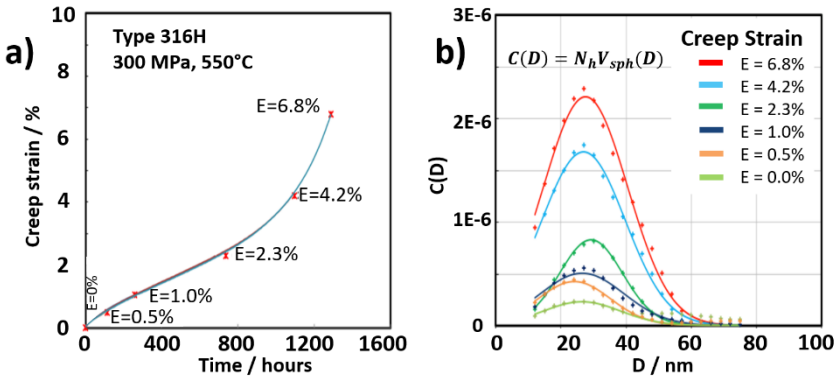


Figure 6.3. a) Creep curve at 550°C, 320 MPa (8% pre-strain); interruption points have been labelled with % of creep strain, *E*. In b), fractional size distribution of cavities, C(D), is shown. Adopted from [204].

6.3. REVIEW OF THE EFFECTS OF PRIOR LOADING HISTORY, PARTICLE MORPHOLOGY AND PRESENCE OF IMPURITIES

6.3.1. Effect of prior history on creep failure in Type 316 stainless steel

Wilshere and Willis [115] observed that the creep strength and ductility decrease with increasing amount of cold working in Type 316 stainless steel. The behaviour is explained by the hardening of the lattice through dislocation multiplication. Respectively, the grain deformation is unable to accommodate the damage processes along the boundaries. Auzoux [213] studied relaxation cracking in Type 316H weldments in the temperature range 500-600°C. The author correlated the

creep failure with the higher stresses transmitted through the HAZ which accelerated intergranular cavity nucleation and growth at intergranular $M_{23}C_6$ carbides in this region. Furthermore, a study on another FCC material with a population of intergranular particles [202] found a positive correlation between higher cavity densities along grain boundaries and high local stress in the vicinity of the boundary. The evolution of local stress and strain fields in the lattice appear to indirectly control the cavitation response along the grain interfaces. This suggests a relation between the dislocation activity in the lattice and intergranular cavitation. This aspect will be discussed in Sections 6.4.2, 6.5.1 and 6.5.3 in the context of cavity nucleation models.

6.3.2. Precipitate morphology and grain-boundary character

The general trends in kinetics of second-phase particles in Type 316 stainless steels are well-understood, e.g. [25,26,140,206,208,214–216] where the particle size and spacing evolution are reported in detail. An example is illustrated in Fig. 6.1.b). With respect to cavity nucleation, it is important to consider the intergranular particle shapes and the presence of impurities.

It is often assumed that grain-boundary particles are of spherical shapes. However, detailed observations in [95,211,217] reveal that intergranular particles in Type 316 are of highly-irregular shapes with multiple faces. Studies by Jonas et al. [218] and Hong et al. [219] demonstrate that the formation of intergranular $M_{23}C_6$ carbides is also highly-dependent on the misorientation of grain boundaries. Acute, triangular carbide particles were observed at random boundaries and more platelet-like particles were found at symmetric boundaries [219] (see Fig. 6.4.a-b). Kim et al. [220,221] found that planar carbides with serrated grain boundaries offered higher cavitation resistance under creep. These findings suggest that the cavity nucleation process will be sensitive to the detailed shape of intergranular particles. As will be discussed in Section 6.4, successful models for cavity nucleation should take into account this microstructural feature.

6.3.3. Observations on addition of impurity elements

It is demonstrated in [222] that additions of boron and cerium in austenitic steels suppress the appearance of tertiary creep [223] due to the resulting fine distribution of precipitates. Phosphorus has been found to finely disperse $M_{23}C_6$ carbides [224]. However, as mentioned in Section 2.6.3, large concentrations of phosphorus lead to segregation of P at the $M_{23}C_6$-austenite interface in Type 316H [114] (Fig. 6.4.c). This decreases the interface surface energy, lowering the nucleation energy barrier for cavitation, as confirmed by theoretical predictions in [121]. The implications of this on mechanistic cavity nucleation models are briefly discussed in Section 6.4.3.3.

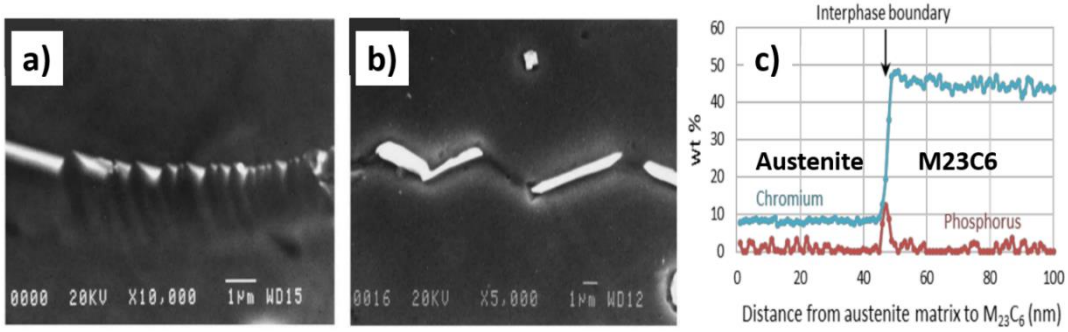


Figure 6.4. SEM images of Type 316 showing a) triangular carbides (straight GBs) after conventional heat treatment (HT) and b) planar carbides (serrated GBs) after modified HT [220]. c) EDS profile from austenite to $M_{23}C_6$ showing phosphorous segregation at the interface, ex-service 316H stainless steel [114].

6.4. REVIEW OF EXISTING MODELS FOR CAVITY NUCLEATION

6.4.1. Informing the development of nucleation theories

The process of cavity nucleation during creep of metallic materials is still not well-understood. Several general families of cavity nucleation theories exist in the literature, summarised by Kassner and Hayes [17] and illustrated in Fig. 6.5, as follows:

1. Nucleation by grain-boundary sliding – where voids form at triple grain junction locations or at tensile ledges along the boundaries;

2. Nucleation by vacancy condensation at locations of high stress concentration (e.g. particles);
3. Nucleation due to a Zener-Stroh mechanism (delamination) at intergranular obstacles.

No general agreement between these cavity nucleation theories has been established [17]. The experimentally-recorded on-average cavity nucleation rates are proportional to the inelastic strain rate [10]. It is suggested in [119] that the proportionality of the nucleation rate with strain rate is associated with grain-boundary sliding, in agreement with the hypotheses in [203,225]. Dyson [10] rules out grain-boundary sliding as a cavity nucleation mechanism since the presence of boundary particles in engineering alloys would suppress the interface sliding process. Instead, it is suggested that localized grain deformation near grain-boundary particles induces stress concentrations which cause local decohesion and cavity formation [118,122,226]. However, creep cavities were found in precipitate-free metals, such as lower purity Al (99.99%) [227], OFHC Cu polycrystals [228] and Cu bicrystals [229]. Void formation was suggested to be as a result of slip band intersections along boundaries. Raj [230] examined intergranular creep failure of copper bicrystals containing significant amounts of oxide particles along grain boundaries. Cavities were associated with hard oxide particles instead of slip band intersections. Other studies support the hypothesis that stress causes condensation of vacancies leading to cavity formation, e.g. Gandhi and Raj [231] and Raj and Ashby [9]. Observations in [231] also suggest that in both bicrystals and polycrystalline aggregates of Type 316 stainless steel, a threshold stress for cavity nucleation exists, below which cavities of observable size are not evident. Two major cavity nucleation models, functions of either strain-rate or stress, stem from the general theories discussed above. The models will be reviewed in turn and the discrepancies between them will be commented.

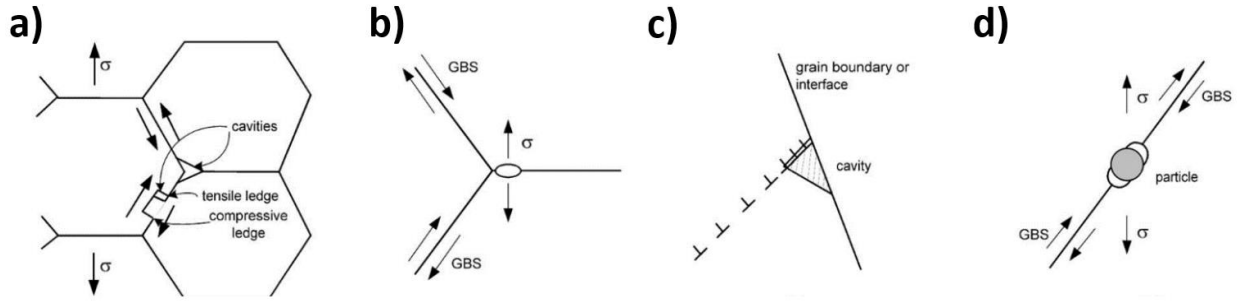


Figure 6.5. Cavity nucleation mechanisms: a) cavitation at ledges, b) vacancy condensation, c) Zener-Stroh mechanism and d) formation of a cavity at a particle via combination of (a-c), adopted from [17].

6.4.2. Strain-based cavity nucleation theories

6.4.2.1. Phenomenological strain-based (Dyson-type) nucleation theory

When employed within a continuum plasticity framework as a function of macroscopic inelastic strain rate $\dot{E}^{ine}$, the strain-based (called here 'Dyson-type') model gives a nucleation rate

$$\dot{N}_h = \alpha' \dot{E}^{ine} \tag{6.1}$$

which reflects the correlation of the on-average variation in cavity density with inelastic strain, established by a series of measurements in [10]. The nucleation constant α' depends on the material and loading conditions. Its value can be estimated from experimental measurements of the nucleation sites per unit boundary (N_m), grain size (d_g), harmonic average of the cavity diameters (d_h) and the axial fracture strain in the specimen (E_f), according to $\alpha' = \left(d_g N_m / \pi d_h E_f \right)$. Predictions of the cavity nucleation rate in various FCC polycrystalline materials (e.g. Fig. 6.7.a), including Type 316 stainless steel [232], via the Dyson-type phenomenological model are in good agreement with experimental data. This indicates a strong link between the lattice deformation process and cavity formation along the grain boundaries, consistent with Section 6.3.1. However, the model of Eq. 6.1 does not provide details of the underlying physics of cavity nucleation.

6.4.2.2. Nucleation theories based on accumulation of local stress and delamination as a result of deformation processes

It is demonstrated in [10,94,233] and Section 6.3.1 that prior plasticity increases the probability of intergranular cavitation during creep. Cavity spacing is often found to be similar to the slip band spacing [228,234]. Dyson et al. [202] identified that cavity nucleation in Nimonic 80A (FCC) is associated with slip bands impinging on intergranular particles causing cavities to nucleate. The authors suggest that nucleation occurred via a Zener-Stroh decohesion mechanism. Early in creep life, cavity distributions in [202] showed peaks at boundaries, approx. parallel to the loading axis, similar to observations from [217,226] (Fig. 6.6). Later in creep life, cavity growth was observed along boundaries transverse to the loading axis, while cavities along parallel boundaries did not readily grow, agreeing with [235]. In addition, the authors in [202] reason that higher cavity number densities are limited to boundaries enclosed by plastically-softer grains, where local slip activity in the vicinity of grain boundaries is greater. Only preferentially-orientated boundaries for diffusive growth (i.e. approx. normal to principal load or enclosed by plastically-harder grains, which carry higher stresses) are prone to cavity coalescence. Unnikrishnan et al. [236] also demonstrated that microcracks in Type 316H form between grains with higher orientation mismatch, associated with local plastic straining.

Chen and Argon [96] reason that nucleation of cavities is a result of transient elastic stress concentrations due to grain-boundary sliding. Furthermore, sliding along inclined boundaries enhances the normal tractions on transverse facets [185] which would increase both nucleation and growth [96,225]. The general notion is that transverse grain boundaries do not slide and therefore are unable to nucleate cavities as a result of a sliding process [9,100,121,237]. Findings from Chapter 5 demonstrate that transverse boundaries between anisotropic grains readily slide and

carry shear tractions. Furthermore, inclined boundaries in FCC materials tend to have higher number densities of cavities (Fig. 6.6) [217,226], whereas larger cavities are found along transverse boundaries to the principal loading axis, i.e. the latter are prone to cavity growth [226]. Since grain-boundary sliding is dominant along inclined interfaces, the latter finding suggests that shear tractions assist the cavity nucleation process. Slater et al. [217] examined the dependence of cavitation on grain-boundary orientation with respect to the loading axis in ex-service Type 316H. More cavities were found on boundaries orientated at approx. 60° to the principal load direction [217], agreeing qualitatively with [95]. Their findings suggest that nucleation will be most potent at grain boundaries orientated at ~60° to the principal load. Along such boundaries, the normal and shear stresses acting on particles would have the largest combined contribution.

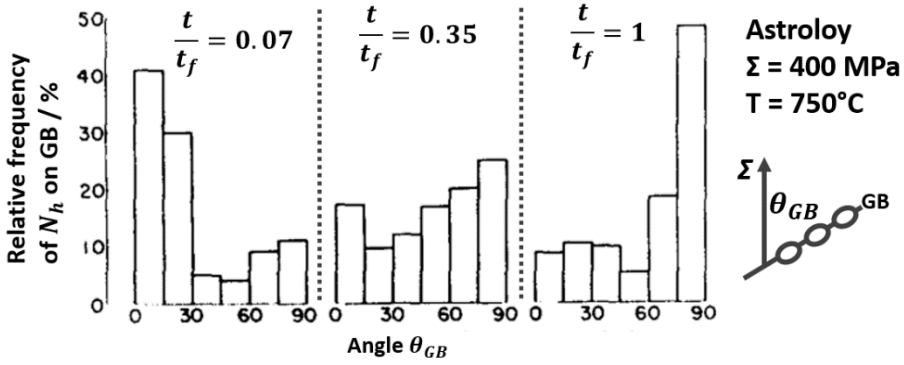


Figure 6.6. Relative frequency of number of cavities along grain boundaries with different angles with respect to the loading axis in FCC Astroloy [226].

In a series of papers, He and Sandstrom [119,120,238,239] examined cavity nucleation in austenitic stainless steels. A nucleation model was derived [119] under the assumption that the energy contributions from the applied stress and grain-boundary dislocations, impeded at sub-grain boundaries, provide sufficient energy for the creation of new cavity surfaces [119]. Nucleation at particles is also considered by assuming that a particle threshold size exists above which sufficient stress to form a cavity surface is concentrated at particles due to sliding. Having identified sub-

grain boundaries and particles as nucleation sites, a 1-D Dyson-type model was developed [119,238] as a function of the intergranular particle spacing (λ_p) and subgrain size (d_{sub}):

$$\dot{N}_h = \frac{0.9C_s}{d_{sub}}\left(\frac{1}{\lambda_p^2}+\frac{1}{d_{sub}^2}\right)\dot{E}^c \tag{6.2}$$

where C_s is a constant related to the microstructure and the amount of grain-boundary sliding as a proportion of the total creep deformation. The assumptions in [119] correctly predict the threshold stress, required to overcome the energy barrier for cavity formation, as well as the on-average variation of cavity number density with creep strain [238]. The nucleation model from [119] suggests a relationship between the creep deformation process of the grains, the grain-boundary morphology and the nucleation rate. However, due to its continuum nature, it fails to explain the distribution of cavities with respect to grain-boundary orientation and its effect on the subsequent events leading to complete failure (see Section 6.6). However, it is worth pointing out that the model in [119] supports the view that a successful cavity nucleation model should capture the microstructural features along the boundary and local stresses in the vicinity of particles.

6.4.3. Mechanistic stress-based nucleation theories

6.4.3.1. Classical nucleation theory

Contrary to the strain-based nucleation theories from Section 6.4.2, a mechanistic theory for cavity nucleation by Raj and Ashby [9] is based on the assumption that vacancy condensation leads to formation of creep voids. The stress driving the vacancy condensation process, T_{nuc}, provides the chemical potential for the reaction ($\Delta\mu_0 = -T_{nuc}\Omega$; Ω is the atomic volume) [121]. In [9], the free energy of a formed cavity is expressed as the sum of a surface term, given by the expended energy of the formed cavity surface, and a volume term, given by the work done by the stress, as

$\Delta G = 3\gamma_s \rho^2 f_v(\psi') - T_{nuc}\rho^3 f_v(\psi')$. Here, γ_s is the lattice surface energy per unit area, ρ is the cavity radius and f_v is the volumetric factor of the cavity/particle geometry with a dihedral angle ψ' : $f_v = 4\pi/3\,(2 - 3\cos\psi' + \cos^3\psi')$. When ΔG is maximised $(\partial G/\partial\rho = 0)$, the energy barrier for creation of a critical cavity nucleus is obtained as $\Delta G^* = 4\gamma_s^3 f_v(\psi')/T_{nuc}^2$. The product of the vacancy absorption rate of the nucleus, β^*, the area number density of critical nuclei, $c_o^* = (c_{max} - c)\, exp(-\Delta G^*/kT)$, and a factor Z^* [121], which accounts for dissolution of supercritical nuclei, gives the nucleation rate of critical nuclei $\dot{c}_h = Z^*\beta^* c_0^*$. Note that c_{max} is the concentration of potential nucleation sites, c is the concentration of critical nuclei, k is the Boltzmann constant and T is temperature. The vacancy absorption rate is a function of the vacancy diffusivity, D_{vac}, vacancy equilibrium concentration c_0, the critical radius of the cavity, $\rho^* = (2\gamma_s/T_{nuc})$, and a perimeter shape factor f_p [9], according to

$$\beta^* = \left(\frac{f_p(\psi')\rho^*\delta_b}{\Omega^{2/3}}\right)\left(c_0 \exp\left(\frac{T_{nuc}\Omega}{kT}\right)\right)\left(\frac{4D_{vac}}{\Omega^{2/3}}\right)\frac{1}{4} \tag{6.3}$$

This gives the nucleation rate of critical voids due to vacancy condensation as

$$\dot{c}_h = \frac{f_p(\psi')\delta_b D_b T_{nuc}}{2\Omega^{1/3}\left[3\pi kT\gamma_s f_v(\psi')\right]^{1/2}}\left(c_{\max} - c\right)\exp\left(-\frac{4\gamma_s^3 f_v(\psi')}{T_{nuc}^2 kT}\right) \tag{6.4}$$

where $\delta_b D_b$ is the grain-boundary diffusivity [121]. Note that T_{nuc} here is a scalar. In engineering alloys with a population of intergranular particles, c_{max} and c are determined by multiplying the number density of total (N_p) and already-cavitated particles (N_h) by the number of nuclei which can be formed on the particle surface, $\left(r_p T_{nuc}/\gamma_s\right)^2$, respectively. When the classical nucleation theory is employed within a continuum plasticity framework, the predicted nucleation rate is proportional to $\exp(-1/T_{nuc}^2)$ (Fig. 6.7.b). The nucleation rate is therefore extremely sensitive to

the applied stress. From a practical perspective, it essentially predicts a threshold stress above which the rate of nucleation of spherical cavities ($\psi' \sim 70°$) is rapid and below which it is so slow that it can be ignored [121]. This disagrees with the continuous evolution of cavity density with inelastic strain observed experimentally and depicted in Fig. 6.7.a. There is still a lack of understanding of the reasons for this discrepancy [121,122] and whether the cavity nucleation mechanism at the micro-scale is stress or strain-rate controlled. The potential links between nucleation theories based on stress and strain-rate will be discussed in more detail in the following sections. The aim of the remainder of this chapter is to interpret important aspects of potential cavity nucleation mechanisms, as well as the process of cavity growth. Insights will then be used to identify features, which need to be considered within micromechanical theories of cavity nucleation and growth. Suitable modelling approaches, in which the cavitation theories can be incorporated to capture the cavitation process in polycrystalline materials, will be identified.

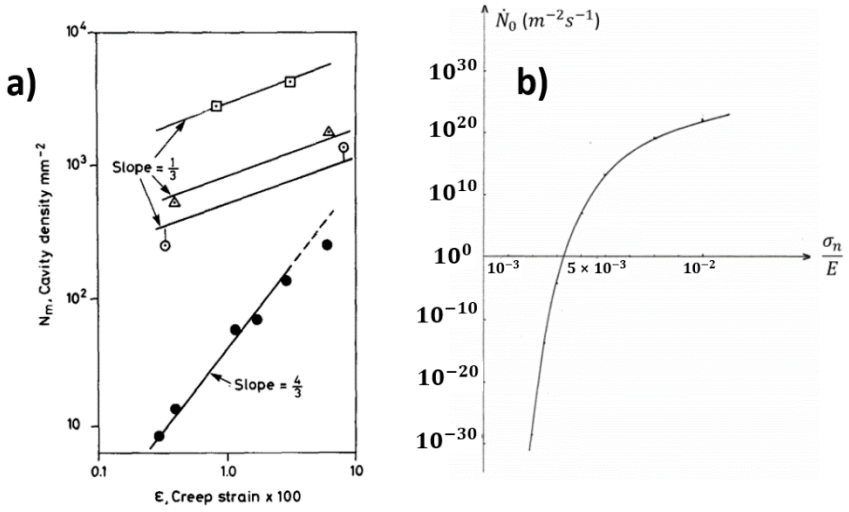


Figure 6.7. a) Cavity density in Nimonic 80A (FCC) with strain for solution-treated (solid circles) and pre-strained material to 10% (□), 3% (Δ) and 2% (○) [94], illustrating the linear variation of cavity density with inelastic strain (Dyson-type). b) Cavity nucleation rate as a function of the remote tensile stress for Type 316 stainless steel via Eq. 6.4, showing exponential variation with stress [232]. N.B. $N_m = N_h; \dot{N}_0 = \dot{N}_h$.

6.4.3.2. Classical nucleation theory and its deficiencies

The discrepancy between the linear dependence of cavity nucleation rate on inelastic strain rate and predictions via classical nucleation theory is noted in the literature [10,121]. It is evident that the mechanistic model in its original form (Eq. 6.4) is unable to describe accurately the nucleation process. Riedel [237] finds a threshold nucleation stress, predicted by Eq. 6.4 [9], of the order of 1000 MPa for spherical cavity shapes. This is much greater than the experimentally-recorded threshold stresses (10-40 MPa for engineering alloys [17,121]). The prediction is dependent on the assumed shape of the newly-nucleated void, described by the dihedral angle of the cavity/particle geometry, ψ'. This aspect is discussed in Section 6.4.3.4. In [123,237], grain-boundary sliding is identified as a mechanism which can augment the local particle stresses to levels approximating the predicted threshold value [9]. However, the particle stresses during elastic transients could relax due to diffusive or dislocation creep mechanisms [121,123,240]. This is considered in Section 6.5.3. Further criticism of the stress-based classical nucleation theory by Binder and Stauffer [241] is that the surface energy, a mesoscopic property, is applied at the atomistic scale.

6.4.3.3. Improving the predictions via classical nucleation theory

Reasonable predictions of the nucleation threshold stress are made under the assumption that newly-nucleated cavities assume narrow profiles (Fig. 6.8) with low values of the volumetric shape factor $f_v(\psi')$ [231], compared to the commonly assumed profiles in the literature with $\psi' > 50°$ [237]. Intergranular particle geometries in Type 316H (ex-service, 500-600°C) are often of multi-faceted profiles with acute angles at the particle tip, as illustrated in Fig. 6.2 and demonstrated experimentally in [95,111,217]. Compared to the case when particles are spherical, the volumetric shape factor of newly-nucleated cavities could be lower at such faceted particle geometries. Hence, the assumption that upon nucleation a cavity could assume a narrow shape along the faceted profile

of a particle does not appear unrealistic. Detailed experiments are required to assess the cavity-particle configurations during the early stages of nucleation to verify this hypothesis.

Raj [242] suggests a modification to the stress-based classical nucleation theory, namely, an incubation time, t_i. This is defined as the period during which randomly-dispersed vacancies travel the minimum distances to condensate. Stress concentrations build up at nucleation sites for $t < t_i$ and it is argued in [242] that the nucleation process commences after the incubation period. However, this assumption does not address the issue of instantaneous nucleation of cavities. Arguments in [243] also suggest that an incubation time for cavity nucleation is meaningless since the model of Eq. 6.4 already captures the probability of vacancies along the boundary coming together to form a critical void. The author of this thesis supports this view.

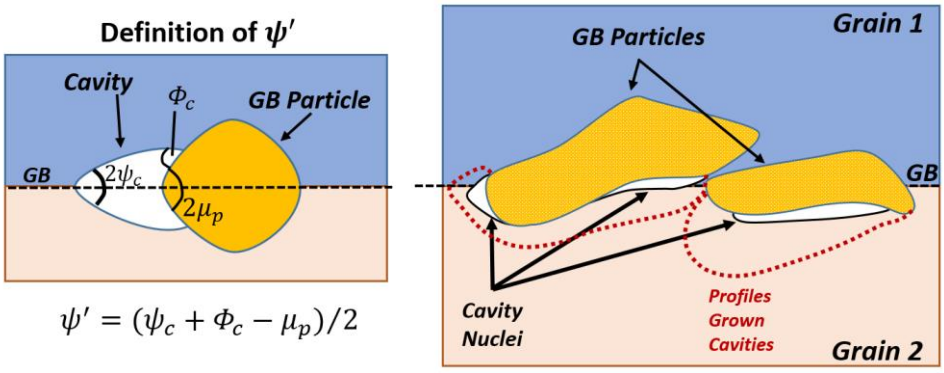


Figure 6.8. Schematic of ψ' and possible cavity nuclei with narrow profiles at the particles from Fig. 6.3.

Trinkaus [244] and Yoo and Chen [245] derived a modified expression for the critical nucleation stress, taking into account the effect of impurity segregation at grain-boundary particles. Predicted values for nucleation stress were closer to experimentally-recorded ones. This finding, together with the experimental observation from Section 6.3.3, confirm the sensitivity of cavity nucleation to the presence of impurities. This suggests that the effect should be considered in any robust cavity nucleation theory. Theoretical approaches to capture this aspect from [121,245] relate

the change in surface energy along an interface to the area coverage of impurity and host atoms. However, application and calibration of such models poses difficulties due to uncertainty in experimental assessment of the impurity coverage and its direct effect on surface energy.

Svoboda and Sklenicka [246] reasoned that when a cavity is nucleated at the particle/matrix interface, thermodynamic equilibrium of the configuration can be reached through a change in the shape of the inclusion. Via this modified approach, the authors found that the activation energy for the nucleation process is similar to that for lattice diffusion, Q_L. Although the latter approach seems to illustrate a link between classical nucleation theory and lattice deformation, the assumption that a change in geometry of intermetallic particles occurs is speculative. Intermetallic particles are somewhat insensitive to shape change over moderate temperatures since their lattice diffusivities are much lower than those of the adjacent grain lattice and boundary [247,248].

6.4.3.4. Classical nucleation theory and continuous cavity nucleation

By assuming a distribution of pre-existent cavities at some particles, Cocks [249] demonstrates that the growth of the initial cavities increases the stress on the remaining non-cavitated particles as the void fraction increases (Fig. 6.9). Only when the stress acting on the remaining uncavitated particles has increased substantially, nucleation at the next set of particles with a higher nucleation threshold is possible. This results in a continuous nucleation process. The hypothesis is supported by findings in Type 316H steel in Section 6.4.2.2. Cavities along a given grain boundary were found only at some of the observed $M_{23}C_6$ particles of irregular shapes [217], suggesting that the particle population has a distribution of nucleation thresholds or “strengths” at the micro-scale.

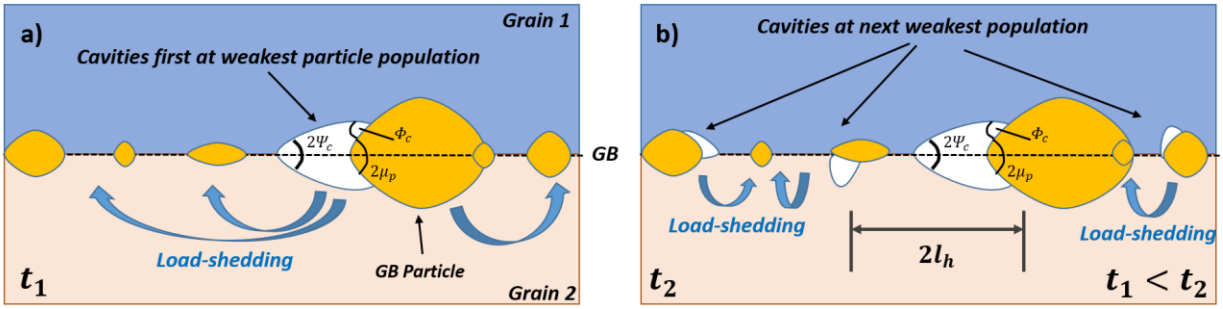


Figure 6.9. Schematic of continuous nucleation at different GB cavity/particle configurations. Load redistributes from cavitated particles (lower nucleation barriers) to those with higher nucleation barriers.

Several studies in the literature have attempted to enhance the mechanistic nucleation models by accounting for a distribution of particles, e.g. [121,250–252]. Of interest here is the study by Wang et al. [250] on ODS MA 754 alloy. The authors compared i) the variation of stress at GB particles of different size (estimated after [123]) for different log-normal size distributions and ii) the stress required to produce a nucleation rate of 1.0 $m^{-2}s^{-1}$ via the stress-based classical nucleation theory of Eq. 6.4. The cumulative distribution of particles prone to cavity formation was then expressed as a function of the applied stress. It was found that by assuming a log-normal size distribution of the oxide dispersoids in the material, where cavities were usually found, the experimentally-recorded nucleation threshold stress was predicted [250].

It is worth pointing out that local plastic flow near the boundary can affect the diffusive transport of material out of the cavity, modifying the local stress state and accelerating growth rate (see Section 6.5.4). Localised plastic flow can shorten the diffusive distance along the boundary over which matter is transported by diffusion. According to Needleman and Rice [102], this coupling between plastic flow and diffusion is represented by a characteristic diffusive length, $\Lambda = \left(\delta_b D_b \Omega \sigma^{\infty} / kT\dot{\varepsilon}^{\infty}\right)^{1/3}$, where σ^{∞} and $\dot{\varepsilon}^{\infty}$ are the stress and associated strain rate in the grains either side of the boundary. The length-scale parameter Λ estimates the characteristic region over

which diffusion will control the local deformation process along the boundary. The significance of this characteristic length is that when 2Λ is greater than the intergranular cavity ($2r_h$) or particle size (d_p), diffusive transport dominates over plastic flow (i.e. moderate σ^{∞} and T). This minimises the contribution to cavity growth from plasticity and alleviates associated stress concentrations [102]. Hence, although the model in [250] captures the threshold for nucleation in the ODS alloy, where $d_p > 2\Lambda$, its application to Type 316 stainless steel ($d_p < 2\Lambda$) is questionable due to the nature of the model from [123]. This is considered in Sections 6.5.2 and 6.5.3.

Findings from this and the preceding sections suggest that modifications of the stress-based nucleation theory are needed. These must capture stress concentrations at particles, associated with features of the deformation process in the vicinity of boundaries, and the shapes of the newly-nucleated cavity/particle configurations. These aspects are discussed in Sections 6.5.2-6.5.3.

6.5. PROPOSED MODIFICATIONS OF EXISTING NUCLEATION MODELS. CAVITY GROWTH MODELS

In the following sections, novel modifications of the existing general theories for cavity nucleation as part of this study are proposed. An approach to employ the strain-based Dyson-type empirical nucleation model at the microscale is introduced. The section then proposes two modifications to the mechanistic classical nucleation theory, by considering the dependence of the cavity formation process on particle morphology and local stress, discussed in the preceding sections. Models describing diffusive cavity growth are also presented. The damage models are formulated in the context of their implementation within polycrystalline modelling frameworks, which is discussed in Section 6.6.

6.5.1. Proposed local Dyson-type nucleation model

The findings from Section 6.4.2.2 demonstrate that formation of cavities is likely to be as a results of local delamination at particle interfaces as a result of localised slip activity. This is expected to be particularly pronounced at boundaries between grains of plastically-softer crystallographic orientations. A simplistic approach to relate the nucleation process to the localized slip activity in the vicinity of a grain boundary is to express the Dyson-type nucleation model of Eq. 6.1 as a function of the maximum inelastic resolved shear strain rate, $\dot{\gamma}_{max}$, near a boundary according to

$$\dot{N}_h = \alpha' \dot{\gamma}_{\max} \tag{6.5}$$

Eq. 6.5 describes the nucleation process by local delamination, whereby the slip activity is the likelihood of a Zener-Stroh mechanism taking place and the nucleation constant serves as a scaling parameter for the failure induced. Note that, according to Eq. 6.2, the nucleation constant α' can be estimated in terms of local microstructural features, such as particle spacing. Employing Eq. 6.5 within a polycrystalline crystal plasticity framework would assist in interpreting cavity nucleation as a function of crystallographic orientation of the grains, enclosing the boundaries, and the relative local inelastic strain accumulation. Chapter 7 will assess the suitability of this phenomenological model in describing the intergranular failure process and damage morphology.

6.5.2. Proposed modification of classical nucleation theory – Distribution of particle strengths

As discussed in Section 6.4.3.4, the concept of employing a statistical distribution of particles with different nucleation thresholds within the mechanistic nucleation theory appears important in describing the nucleation process. Based on the findings from Sections 6.3.2 and 6.4.3.4, the dihedral angle ψ' which describes the cavity/particle geometry upon nucleation is identified in this

study as an important microstructural feature, associated with the nucleation energy barrier, agreeing with [121,122,230]. This suggests that a distribution of ψ' for the existing population of particles along a boundary could be incorporated within the mechanistic theory of Eq. 6.4. Here, it is assumed that a log-normal distribution of volumetric shape functions, $f_v(\psi')$, exists at a given material point along the boundary. The number density of GB particles on which cavities form with volumetric shape factors between f_v and f_v +δf_v is

$$N_p(f_v) = \lambda_p^{-1/2}\left(CDF(f_v+\delta f_v) - CDF(f_v)\right) \tag{6.6}$$

where λ_p is the average spacing of intergranular particles, and

$$CDF(f_v) = \frac{1}{2}\left(1+erf\left(\frac{\ln(f_v)-\ln(\mu)}{\ln(\tilde{\sigma})\sqrt{2}}\right)\right) \tag{6.7}$$

where μ and $\tilde{\sigma}$ are the mean and standard deviation of the log-normal distribution. The total nucleation rate of critical nuclei is then obtained by integration over the nucleation rates for each population of particles in the distribution according to

$$\dot{c}_h = \int_0^{f_{v,\max}} \frac{5.012\, f_v^{0.226}\delta_b D_b T_{nuc}}{2\Omega^{1/3}\left[3\pi kT\gamma_s f_v(\psi')\right]^{1/2}}\left(c_{\max}(f_v) - c(f_v)\right)\exp\left(-\frac{4\gamma_s^3 f_v(\psi')}{T_{nuc}^2 kT}\right)df_v \tag{6.8}$$

Note that c_{max} is a function of $N_p(f_v)$ and will vary for different values of f_v. For simplicity, it is assumed here that only one stable cavity can form on a particle, which is often observed in experimental studies, e.g. [111]. Hence, the number density of cavitated particles, N_h (or simply number density of cavities in Fig. 6.9) is $N_h = c_h\left(r_p T_{nuc}/\gamma_s\right)^{-2}$. The modified version of the classical nucleation theory will be employed and evaluated in detail in Chapter 7.

6.5.3. Proposed modification of classical nucleation theory – Maximum stress at particles and residual stress due to prismatic loops

6.5.3.1. Maximum stress at intergranular particles

Local stresses along grain boundaries can increase in the vicinity of intergranular particles. Direct measurement of this local stress increase is difficult [237]. Several studies [123,237,242,250] have attempted to predict the stress concentrations arising from localised deformation. Argon et al. [123] analysed the maximum local stress at particles due to relaxation of shear stresses when the accommodation around the particle is by plasticity and diffusional flow [197]. Burton and Beere [253] and Riedel [121] analysed the other limiting case of normal stress relaxation in the particle-free region of the boundary. Closed form solutions for maximum particle stress are given in Argon et al. [123] and Riedel [121] which predict stress concentrations of the order of 22 times the average traction along the boundary when particles are larger than the diffusive length of the material, Λ (see Section 6.4.3.4). At higher temperatures and for smaller particles, diffusion modifies the stress distribution [123]. Under such conditions, when $2\Lambda \gg 2r_p$, the maximum local traction at the particle interface is approximated in [121,123] by $\tau_i^p = T_i \Big/ \left(d_p/\lambda_p\right)^2$, where T_i is the average traction carried by the boundary, d_p and λ_p are the particle diameter and spacing, and subscript *i* is either *n* for the normal or *t* for the shear component of the traction (see Fig. 6.10). In polycrystalline materials, grain boundaries will carry both shear and normal tractions. Findings from Section 6.4.2.2 further suggest that the stress driving the vacancy condensation process in Eq. 6.4 (T_{nuc}) is in fact a resultant traction, T_e, which is a function of the shear and normal boundary tractions. Note that the solution for τ_i^p is similar for both the shear and normal traction limiting cases in [121,123]. Hence, in the vicinity of particles on a grain boundary, the maximum possible

local stress τ^* under the condition $2\Lambda \gg 2r_p$ would need to take into account both contributions from shear and normal traction, according to

$$\tau^* = T_e \Big/ \left(d_p/\lambda_p\right)^2 \tag{6.9}$$

where T_e is a resultant traction along the boundary. Note that this quantity is a scalar, since T_e is also a scalar. The approach to define the coupling between T_n and T_t to determine T_e is presented in Chapter 7. As will be shown in Chapter 7, the diffusive lengths in Type 316 stainless steel over the temperature and stress range of interest are larger than particle sizes in the material (see Section 7.3.1 for estimation of Λ in Type 316/316H over the temperature range of interest). Hence, Eq. 6.9 could be employed within the multi-scale modelling framework, which computes the average tractions along grain boundaries in the presence and absence of sliding, to estimate the maximum possible stresses at particles.

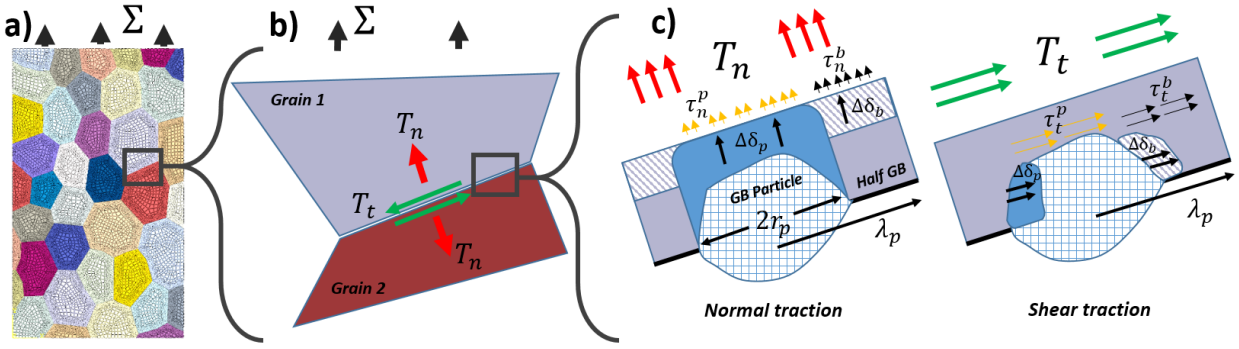


Figure 6.10. a) Macroscopic load applied in the polycrystal. In b), grain boundaries carry average shear and normal tractions. In c), the local tractions at the particle (τ_i^p) and boundary regions (τ_i^b) are in equilibrium with the average traction T_i (i = n,t). Normal or shear displacement incompatibilities arise along the particle interface, since the interface diffusivity is lower than the grain-boundary diffusivity. Slower accommodation of incompatibilities at particles, in blue in c), causes an increase in stress at that region.

It should also be noted that a timescale, t_{red}, associated with the increase of particle stress due to diffusive accommodation along particle-free regions, exists as discussed in [123,253]. The

timescale is associated with the period over which normal or shear displacement incompatibilities arise along the particle interface, since the interface diffusivity is lower than the grain-boundary diffusivity (see Chapter 5). This is shown in Fig. 6.10.c). For $t_{red} \to 0$, the maximum stress at particles will be given by Eq. 6.9, whereas for $t_{red} \to \infty$, the particles will carry the average boundary traction. The estimates for t_{red}, associated with the redistribution of normal and shear stresses from the particle-free region to the particles, are given in [123,253] and take the form of

$$t_{red} = \frac{kTd_p\lambda_p^2 \log(T_i/\tau_i^b)}{\delta_b D_b \Omega E} \tag{6.10}$$

where τ_i^b is the traction along the particle-free region and *E* is the elastic modulus of the matrix. All other terms remain as defined before. Note that the value of $\log(T_i/\tau_i^b)$ is of the order of ~10 for T_i in the range of interest to this study and $\tau_i^b \to 0$. In Chapter 7, the aspects of this redistribution time and the coupling between the normal (T_n) and shear (T_t) tractions in relation to the local stress state in the vicinity of the boundary will be assessed.

6.5.3.2. Residual stress due to prismatic loops at intergranular particles

The variation of cavity nucleation rate with inelastic strain rate supports the relation between cavity nucleation and dislocation activity in the vicinity of the grain boundary. As discussed in Section 6.4.2.2, it is believed that lattice dislocation structures, such as dislocation pile-ups, at intergranular particles or ledges are responsible for cavity formation by increasing the local stress exerted on such obstacles [10,254,255]. This poses the requirement for any mechanistic model of cavity nucleation to take into account the residual stress at potential nucleation sites due to local dislocation features. As discussed in Section 2.5, dislocations bypass precipitates via an Orowan process in Type 316. This causes the formation and storage of geometrically-necessary prismatic

loops around particles to accommodate local inhomogeneity [256]. Following the approach from Section 2.5 (see [6]) to determine the evolution of residual microscopic stress in the lattice, $\dot{\bar{\tau}}_m^r$, the residual stresses at intergranular particles due to the presence of lattice prismatic loops in the vicinity of boundaries $\bar{\tau}_p^{GB}$ can be approximated. The simplistic analysis, presented here, aims to highlight a feature of the dislocation loop structure near the boundary, which could result in elevation of local stresses at intergranular particles. Detailed derivation of such a model is cumbersome and is outside the scope of this thesis. Experimental [257] and computational studies [160] demonstrate that higher dislocation densities are likely to accumulate in the vicinity of grain boundaries, particularly at room temperature. However, measurements of the dislocation density in the vicinity of grain boundaries and the grain bulk in Type 316 [258] show a difference between the two regions of less than ~15% in the temperature range >400°C. Based on this, it could be assumed in a simplistic manner that the density of loops, N_{li}^A and N_{li}^B, and microscopic residual stresses in the lattice, $\bar{\tau}_{m,A}^r$ and $\bar{\tau}_{m,B}^r$, are similar in the bulk and boundary regions (regions A and B in Fig. 6.11.a). Considering the force equilibrium in Region B in the unloaded state ($\bar{\tau}_{m,B}^r(1-f_a^{GB}) + \bar{\tau}_p^{GB} f_a^{GB} = 0$) allows the residual stress at GB particles due to the presence of lattice prismatic loops to be associated with inelastic deformation near the boundary, according to

$$\dot{\bar{\tau}}_p^{GB} = -0.7\alpha_d G \frac{(1-f_a^{GB})}{f_a^{GB}} \left(2\pi \left(r_p^m\right)^2 \dot{N}_{li}^{\max} \left(3 f_v^p\right)^{-1}\right) \left(f_v^p\right)^{3/2} \tag{6.11}$$

where f_a^{GB} is the area fraction of GB particles. Note that $\bar{\tau}_p^{GB}$ here is a scalar as it accounts for the on-average density of dislocation loops on all four slip systems. The CPFE framework employed in Chapters 4 and 5, predicts the evolution of $\dot{N}_{li}$ during creep within the lattice. Application of the approximate model from Eq. 6.11 within the framework would also allow estimation of residual stress at intergranular particles as a result of local plastic straining. The local residual stress at the

intergranular particles, $\bar{\tau}_p^{GB}$, provides a contribution to the stress at intergranular particles, defined by Eq. 6.9. From the perspective of the mechanistic nucleation theory of Eq. 6.8, the stress driving vacancy condensation (T_{nuc}) is determined by coupling of the residual stress on particles due to prismatic loops with the maximum stress on a particle due to the applied load, analysed in Section 6.5.3.1. This is presented schematically in Fig. 6.11.b) and will be examined in Chapter 7. Note that the prismatic dislocation loops, assumed here to generate a contribution to T_{nuc}, are an idealization of the possible dislocation features in the vicinity of grain boundary particles. As will be discussed in Chapter 7, taking account of the local stresses generated by this idealised dislocation feature highlights the importance of considering the effects of dislocation structures on cavity nucleation. In reality, other dislocation features (e.g. dislocation pile-ups) may exist in the vicinity of intergranular particles.

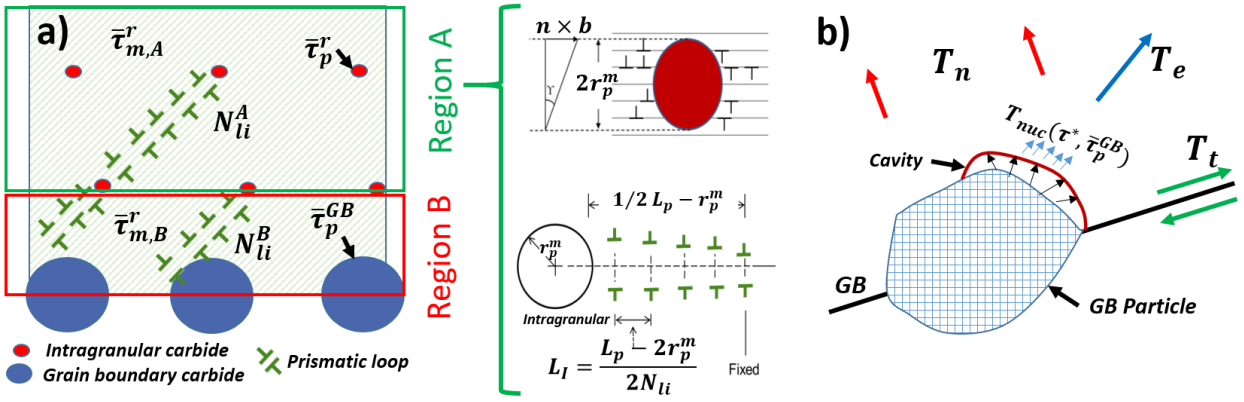


Figure 6.11. a) In Region A (grain bulk), shear strain and thermal recovery result in an evolution of prismatic dislocation loop density, N^A_{li}, in the lattice. The presence of loops gives rise to microscopic residual stresses at intragranular particles ($\bar{\tau}^r_p$) and matrix ($\bar{\tau}^r_m$). The residual stress at GB particles, $\bar{\tau}^{GB}_p$, due to the presence of prismatic loops in the vicinity of the boundary (Region B) is estimated by assuming $\bar{\tau}^r_{m,A} = \bar{\tau}^r_{m,B}$. In b), schematic of the contributions to T_{nuc} from Sections 6.5.2-6.5.3 is shown.

6.5.4. Diffusive cavity growth model and evolution of damage

Coupling between diffusion- and plasticity-controlled growth of cavities is possible under certain deformation scenarios, e.g. at high stresses or at large particles [102,259]. It will be demonstrated in Chapter 7 that in Type 316 under the thermo-mechanical conditions of interest, the local diffusive distances in the material are greater than both particle and cavity sizes. Hence, the contribution to the growth rate of cavities by plasticity would be minimal [102]. During diffusive growth of cavities, surface and grain-boundary diffusion are responsible for the transfer of matter along the cavity surface to the grain boundary [121]. For the practical case, where the surface diffusivity is greater than the boundary diffusivity, the volumetric growth rate of cavities due to vacancy influx and plating of atoms along grain-boundary regions is expressed in [100] as

$$\dot{V} = \frac{2\pi\delta_b D_b \Omega}{kT \ln\left(1/f_h\right)} T_n \tag{6.12}$$

where f_h is the cavity area fraction on the boundary ($f_h = r_h^2/l_h^2$; r_h is the cavity radius and $l_h = N_h^{-1/2}/2$ is the half-spacing) and T_n is the average normal traction at a material point along the boundary. The inelastic opening rate of the boundary $\dot{\delta}_n^{cr}$ due to cavity growth is expressed as

$$\dot{\delta}_n^{cr} = \frac{2\delta_b D_b \Omega}{kT \ln\left(1/f_h\right) l_h^2} T_n = \frac{8\delta_b D_b \Omega}{kT \ln\left(1/f_h\right)} N_h T_n \tag{6.13}$$

since, from geometry, $\dot{V} = \pi l_h^2 \dot{\delta}_n^{cr} = \pi \dot{\delta}_n^{cr}/4N_h$. Following the approach from [100], the cavity area fraction evolution law as a function of the boundary inelastic opening rate is expressed as

$$\dot{f}_h = \dot{\delta}_n^{cr} \sqrt{N_h} \Big/ \left(h(\psi') \sqrt{f_h} \right) \tag{6.14}$$

where $h(\psi')$ is a function of the cavity shape [9], taking a value of ~0.6 for spherical cavities, often observed during the growth stage. Coalescence of cavities occurs when the area fraction

reaches a limiting value, f_h^c, often taken as 0.25 [100,239]. The models from Eqs. 6.13 and 6.14 will be employed in Chapter 7 to describe the cavity growth process and the evolution of cavity area fraction, respectively. The following section considers some important aspects of the implementation of these models within polycrystalline modelling frameworks.

6.6. CONSIDERATIONS ON APPLICATION OF DAMAGE MODELS IN MULTI-SCALE MODELLING FRAMEWORKS

6.6.1. Constrained cavity growth

As discussed in [17,100,103,106,260,261], assuming that failure on all facets occurs simultaneously underestimates the creep strength of the material. In polycrystalline materials some grain boundaries are more prone to cavitate than others and failed facets can end up being encapsulated by undamaged material [100]. This is ascribed to the following phenomena:

- Grain boundaries carry different stresses due to the orientation of the boundaries with respect to the principal load and the relative crystallographic orientation of adjacent grains;
- Failure in the polycrystal is not controlled by coalescence of cavities along facets, but rather the events leading to the interlinkage of failed facets.

Thus, failure on widely-spaced facets, which is often observed in practice [95], can be controlled by the deformation of the surrounding undamaged region of grains posing a constraint on cavity growth rate, termed constrained cavity growth [106]. This assumption was used in [100] within a continuum plasticity formalism to express the stress exerted on the constrained cavitating boundary, which is now lower than the remotely-applied stress. Cocks and Ashby [100] reason that the constraint virtually disappears when the spacing of cavitated facets (*2L*) equals the facet

size (d). Then the opening rate along grain boundaries is readily accommodated by the deformation of the surrounding material. For $2L>d$, the constrained cavity growth rate can be obtained by using a reduced stress within the unconstrained diffusive growth model of Eq. 6.13 [121,205]. The approach is employed in [120,121] and general agreement with experimental results on cavity growth rates and creep strength is established in cases with and without coupling to continuous cavity nucleation. It is worth pointing out, however, that natural constraints from the deformation of the surrounding grains will be exerted on a cavitating grain boundary in the polycrystalline CPFE framework, demonstrated in Chapter 5. Therefore, application of the unconstrained diffusive growth model (Eq. 6.13) within this polycrystalline model would naturally take into account the variation of normal stresses along boundaries. Dyson [106,262] further comments on the redistribution of stress from failed boundaries to uncavitated regions, which also accelerates local creep rates. Some implications of the stress redistribution process between grains during intergranular creep failure on life estimation of polycrystals are discussed in Section 6.6.3.

6.6.2. Continuous nucleation and growth of cavities

Numerous studies [112,119–121,213,231] have concluded that creep failure in Type 316 stainless steel occurs by continuous nucleation and diffusive growth of cavities along grain interfaces. These findings confirm that cavity nucleation in Type 316 austenitic stainless steel is the rate-controlling mechanism for creep damage. This is illustrated in Fig. 6.12, where the correct failure response of Type 316 is captured only when cavity nucleation is considered in the model. Another example is the study by He and Sandstrom [239], where agreement is established between experimental creep strength data for austenitic steels and predictions by a combined diffusive constrained cavity growth model [121,263] and the nucleation model from Eq. 6.2 [120,239]. The discussed findings here suggest that a combination of these processes can describe the cavitation response of the

material. Therefore, successful implementation of the damage models from Section 6.5 would require the evolution of f_h as a function of nucleation and growth to be captured simultaneously.

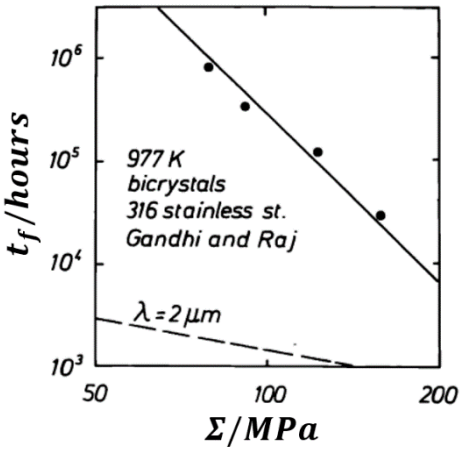


Figure 6.12. Creep strength of Type 316 stainless steel bicrystals, 700°C. Continuum plasticity model prediction from [121] by coupled Dyson-type nucleation law, $\alpha' = 3 \times 10^{12}\ m^{-2}$, and diffusive cavity growth (solid line) and prediction assuming diffusive cavity growth only (dashed line). N.B. Exp. data (•).

6.6.3. Multi-scale polycrystalline modelling of intergranular creep failure

Burnett et al. [95] comment on the changing length scale of damage during tertiary creep. The authors suggest that the damage processes change from cavity growth and coalescence at the grain scale to crack interlinkage at the macroscale. The argument in [95] indicates that although the process of cavity growth is understood, the events leading to intergranular failure are more complex and their consideration is necessary in any modelling approach. Several studies [125,174] have modelled intergranular failure of polycrystalline, power-law creeping aggregates of hexagonal grains. Cavity growth and interlinkage of failed facets was found to be controlled by the stress redistribution process between grains. It was observed that when creep constraint on cavity growth is active, the cavitation on inclined boundaries relaxes the stresses along the latter and redistributes them to the transverse facets, accelerating local growth. The framework from [174] was extended in [194] through the introduction of a cavity nucleation model as a function of

the effective creep strain rate in the vicinity of grain boundaries. By considering local inelastic strain fields, rather than using the macroscopic inelastic strain rate as in [10,120], the study found variations in nucleation rates along different facets. However, the increased nucleation activity locally in [194] stemmed from inhomogeneous strain fields due to the presence of a pre-existent microcrack. In realistic polycrystalline materials, the grain crystallographic orientation (i.e. plastically harder/softer) will affect the failure propagation pattern along intergranular facets. Elastic-plastic anisotropy of the grains will result in heterogeneous stress and strain fields between grains in the absence of damage. This suggests that the variation of nucleation activity would be more representative in polycrystalline aggregates, where grains deform by crystal plasticity models. Furthermore, irregular crystal shapes, which resemble closely realistic grain structures, were found in [193] to also affect the intergranular failure process.

The observations from Section 6.6 suggest that multi-scale polycrystalline modelling of anisotropic grain deformation and damage development along grain boundaries would be a suitable approach to provide more understanding into the interactions between cavitating facets and the deformation of adjacent grains in realistic materials. Such modelling approaches will allow the sensitivity of the i) macroscopic failure response and ii) damage morphology during creep to different local nucleation models to be evaluated. Therefore, the focus of Chapter 7 is to employ the developed polycrystalline model for anisotropic grains with irregular shapes and grain boundaries from Chapter 5 to study intergranular creep damage by probing the local Dyson-type and modified classical nucleation models, defined in this chapter, coupled with diffusive growth. The proposed modified strain- and stress-based nucleation models, as well as cavity growth models, will be employed within the traction-separation laws from Chapter 5, describing the boundary response. This is described in Chapter 7.

6.8. SUMMARY

The intergranular cavity growth process is well-understood. Under loading histories, typical of plant operating conditions, the process is controlled by the rate of grain-boundary diffusion of material away from the growing cavity. However, the detailed physics of cavity nucleation are unclear. Nucleation sites in Type 316/316H are predominantly intergranular $M_{23}C_6$ carbides. The nucleation process is affected by prior deformation, particle morphology, impurity concentrations and evolution of the dislocation structure. Empirical models, used in industry, and existing phenomenological models for nucleation assume a linear variation of on-average nucleation rate with global inelastic strain rate. Such models agree with experimental data, but they do not provide information of the physical process and its sensitivity to the above-mentioned aspects. The existing classical nucleation theory predicts high nucleation threshold stresses and a highly-non-linear dependence of the nucleation rate on the macroscopic stress, both of which disagree with experimental observations.

Coupling between cavitation models and crystal plasticity models within multi-scale polycrystalline modelling schemes is identified in this chapter as a suitable approach to explore the interactions between the intergranular damage process and the deformation of the material. Cavitation models can describe the inelastic response of grain-boundary regions, whereas crystal plasticity models capture the creep deformation of anisotropic grains. Observations from the literature have indicated that the cavity nucleation activity is dependent on the grain-boundary spatial orientation and the crystallographic orientation of adjacent grains. Modelling frameworks of this type capture the tractions and displacements along boundaries, and the local deformation response of the grains. Both features can be used to inform intergranular damage models.

In this chapter, key aspects of the grain-boundary microstructural morphology and local deformation processes in the vicinity of the boundary are identified as essential to be included within the classical nucleation theory. The continuous nucleation process is represented by a modification of the theory to account for a distribution of intergranular particles with different "strengths", motivated by physical observations in Type 316. A log-normal distribution of newly-nucleated cavity/particle volumetric shape factors, f_v, is considered for which the overall nucleation rate is obtained by integrating the individual rates across the populations. Stress concentrating features at intergranular particles are also considered and used to inform the mechanistic theory. A model for the maximum local stress at intergranular particles is introduced. Another approximate model captures the build-up of residual stresses at intergranular particles due to the accumulation of dislocation structures – prismatic loops across the lattice in the vicinity of the boundary - resulting from localized inelastic deformation. Both of these aspects can lead to high stresses at potential nucleation sites, i.e. particles. It should be noted that within the polycrystalline modelling approach of Chapter 5, average boundary tractions and residual stresses, arising from the deformation process, will vary between grains of different crystallographic orientations. The sensitivity of nucleation to localized slip activity and crystallographic orientation of grains can also be explored phenomenologically. This can be done by employing the Dyson-type model along a boundary region as a function of the resolved shear strain rate in the vicinity of the boundary. Comparison between predictions via coupled crystal plasticity, cavity diffusive growth and cavity nucleation, employing the modified classical nucleation theory and local Dyson-type nucleation model, will be made in the following chapter. The objective of Chapter 7 is to improve the further understanding of the intergranular cavitation process during creep in polycrystalline Type 316H stainless steel. The sensitivity of the process to the local features

considered needs to be assessed. This aims to provide guidelines for the development of a unified cavity nucleation model and identify key aspects of the process on which future experimental work should focus. The key intergranular cavitation models from this chapter are summarized below:

a) Inelastic displacement rate of grain boundary due to diffusive growth

$$\dot{\delta}_n^{cr} = \frac{8\delta_b D_b \Omega}{kT \ln\left(1/f_h\right)} N_h T_n$$

b) Cavity area fraction and its evolution due to growth

$$f_h = r_h^2 / l_h^2 = 4 r_h^2 N_h, \;\; \dot{f}_h = \dot{\delta}_n^{cr} \sqrt{N_h} \Big/ h(\psi') \sqrt{f_h}$$

c) Local Dyson-type nucleation model as a function of resolved shear strain rate

$$\dot{N}_h = \alpha' \dot{\gamma}_{\max}$$

d) Classical nucleation theory with a distribution of volumetric shape factors, f_v

$$\dot{c}_h = \int_0^{f_{v,\max}} \frac{5.012 f_v^{0.226} \delta_b D_b T_{nuc}}{2\Omega^{1/3} \left[3\pi kT \gamma_s f_v(\psi')\right]^{1/2}} \left(c_{\max}\left(f_v\right) - c\left(f_v\right)\right) \exp\left(-\frac{4\gamma_s^3 f_v(\psi')}{T_{nuc}^2 kT}\right) df_v$$

e) Possible nucleation sites for a population of cavity/particle geometries of given f_v

$$c_{\max}(f_v) = N_p(f_v)\left(r_p T_{nuc} / \gamma_s\right)^2$$

f) Particle number density with cavities of volumetric shape factors between f_v and $f_v + \delta f_v$

$$N_p(f_v) = \lambda_p^{-1/2}\left(CDF(f_v + \delta f_v) - CDF(f_v)\right)$$

g) Cumulative distribution function for the assumed log-normal distribution of f_v

$$CDF(f_v) = \frac{1}{2}\left(1 + erf\left(\frac{\ln(f_v) - \mu}{\tilde{\sigma}\sqrt{2}}\right)\right)$$

h) Total number density of cavities (assuming one critical nucleus per particle)

$$N_h = c_h \left(r_p T_{nuc} / \gamma_s \right)^{-2}$$

i) Maximum stress at particles due to applied load and relaxation from particle-free regions

$$\tau^* = T_e(T_n, T_t) \Big/ \left(d_p / \lambda_p \right)^2$$

j) Residual stress at intergranular particles due to prismatic loops

$$\dot{\bar{\tau}}_p^{GB} = -0.7 \alpha_d G \frac{(1 - f_a^{GB})}{f_a^{GB}} \left(\frac{2\pi \left(r_p^m \right)^2}{3 f_v^p} \dot{N}_{li}^{\max} \right) \left(f_v^p \right)^{3/2}$$

CHAPTER 7

MODELLING INTERGRANULAR CREEP FAILURE IN TYPE 316H STAINLESS STEEL

7.1. MOTIVATION

Intergranular creep cavitation is a common failure mechanism in austenitic stainless steel components under high-temperature power plant conditions. The cavity nucleation process controls the intergranular creep failure. As described in Chapter 6, the existing mechanistic models for cavity nucleation are deficient in describing the cavity formation process. In order to predict accurately the global creep failure response, further insights into the physical phenomenon of cavity nucleation and improved models of the process are needed. Based on the discussion of experimental observations, modified versions of the strain-based (called here Dyson-type) and stress-based (classical nucleation theory) models for cavity nucleation were introduced in Chapter 6. These take into account a number of local features of the nucleation process in FCC materials. The applicability of these modified models to describe the cavity formation process during creep is assessed in the present chapter, taking austenitic Type 316H stainless steel as an example. Furthermore, existing cavity nucleation and growth models are often applied within continuum modelling frameworks. Such continuum approaches do not capture the localization effects, the associated stress redistribution process between grains and grain boundaries, and the distribution of cavities with respect to orientation of grain boundaries in polycrystalline materials. Hence, such approaches are not suitable to assess in detail the deficiencies of cavity formation models. Use of multi-scale modelling frameworks is required to assess in detail the sensitivity of polycrystalline

failure to different nucleation models by employing the latter at the microscale. The focus of this chapter is to extend the multi-scale CPFE-interface element framework of Chapter 5 in capturing intergranular creep damage by probing the modified cavity nucleation and growth models from Chapter 6. The local strain-based Dyson-type model and modified stress-based classical nucleation theory are coupled to diffusive growth models, and implemented within the interface element FE framework in Section 7.2. The constraint at triple grain junctions in the polycrystal from Chapter 5 is modified to account for the potential volumetric opening due to damage along adjacent interface elements. The applicability of the local strain- and stress-based nucleation models from Chapter 6 in predicting i) macroscopic failure, ii) the continuous nucleation process, and iii) cavity distributions and damage morphology within the microstructure is assessed. Model predictions of local and global intergranular creep failure in simple bicrystals and polycrystalline geometries presented in Sections 7.3 and 7.4, respectively, provide further understanding of the sensitivity of intergranular failure to microstructural features, such as particle morphology and local stress state. Guidelines for future modelling and experimental activities are provided in Section 7.5 to support the development of more robust cavity nucleation models.

7.2. MODELLING APPROACH

7.2.1. Summary of proposed models for cavity nucleation and growth

The purpose of this section is to briefly summarise the cavity growth and proposed cavity nucleation models, modified in this study in Chapter 6. This serves to clarify the approach to their implementation into the modelling framework in the present chapter.

The proposed strain-based Dyson-type nucleation model is given by

$$\dot{N}_h = \alpha' \dot{\gamma}_{\max} \tag{7.1}$$

The nucleation rate for the classical nucleation theory, considering a distribution of particle strengths (cavity/particle geometries at nucleation, described by $f_v(\psi')$), is given by

$$\dot{N}_h = \left(r_p T_{nuc} / \gamma_s\right)^{-2} \int_0^{f_{v,\max}} \frac{5.012 f_v^{0.226} \delta_b D_b T_{nuc}}{2\Omega^{1/3}\left[3\pi k T \gamma_s f_v(\psi')\right]^{1/2}} \left(c_{\max}(f_v) - c(f_v)\right) \exp\left(-\frac{4\gamma_s^3 f_v(\psi')}{T_{nuc}^2 kT}\right) df_v \tag{7.2}$$

where T_{nuc} is the stress driving the vacancy condensation process, $c_{\max}(f_v) = N_p(f_v)\left(r_p T_{nuc} / \gamma_s\right)^2$ and $c(f_v) = N_h(f_v)\left(r_p T_{nuc} / \gamma_s\right)^2$. The distribution of particle strengths is determined from

$$N_p(f_v) = \lambda_p^{-1/2}\left(CDF(f_v + \delta f_v) - CDF(f_v)\right) \tag{7.3}$$

where $CDF(f_v) = 1/2\left(1 + erf\left((\ln(f_v/\mu))/\ln(\tilde{\sigma})\sqrt{2}\right)\right)$. Here, T_{nuc} is a function of the maximum particle stress τ^* due to the applied load and the residual stress $\bar{\tau}_p^{GB}$ at intergranular particles due to the presence of prismatic dislocation loops near the particles. These are given by

$$\tau^* = T_e \Big/ \left(d_p / \lambda_p\right)^2 \tag{7.4}$$

and

$$\dot{\bar{\tau}}_p^{GB} = -0.7\alpha_d G(1 - f_a^{GB})\left(2\pi\left(r_p^m\right)^2 \dot{N}_{li}^{\max}\left(3 f_v^{\,p}\right)^{-1}\right)\left(f_v^{\,p}\right)^{3/2} / f_a^{GB} \tag{7.5}$$

where f_a^{GB} is the area fraction of particles. The inelastic opening rate of the boundary $\dot{\delta}_n^{cr}$ due to cavity growth is expressed as

$$\dot{\delta}_n^{cr} = \frac{8\delta_b D_b \Omega}{kT \ln\left(1/f_h\right)} N_h T_n \tag{7.6}$$

When nucleation is considered in addition to growth, the cavity area fraction evolution law as a function of the inelastic opening rate and the nucleation rate is expressed as

$$\dot{f}_h = \dot{\delta}_n^{cr} \sqrt{N_h} \Big/ \left(h(\psi') \sqrt{f_h} \right) + \dot{f}_h^n \tag{7.7}$$

where $\dot{f}_h^n = 4 r_h^2 \dot{N}_h$. The following sections describe the computational implementation of these models, the coupling between T_n and T_t in T_e, and the combination of τ^* and $\bar{\tau}_p^{GB}$ in T_{nuc}.

7.2.2. Theoretical framework

The computational framework employed in this chapter extends that from Chapter 5. Eq. 5.1 gives the solution to the boundary value problem for a body, discretized into finite elements. Solutions are obtained by using the commercial software ABAQUS. The constitutive response of the grains, and determination of stress and the material Jacobian matrix are represented by the physically-based CPFE model, employed in Chapter 4. The surface-type formulation of the interface element from [186], implemented in ABAQUS as a UEL routine, is described in Appendix B. The traction-separation-rate laws of Eqs. 5.3-5.4 represent the elastic-creep response of grain-boundary regions. In this chapter, intergranular damage is of interest and these traction-separation-rate laws are extended. The cavity nucleation and growth models from Section 7.2.1 are implemented within the traction-separation-rate laws. The normal interface separation rate due to opening $\dot{\delta}_n^{cr}$ is given by Eq. 7.6. The reduction of load-carrying capacity of the boundary due to evolution of the cavity area fraction, $\dot{f}_h$ (Eq. 7.7), is considered. The normal and tangential separation rates are given by

$$\dot{\delta}_n = \dot{\delta}_n^e + \dot{\delta}_n^{cr} = \frac{\dot{T}_n}{K_n (1 - f_h)} + \frac{8 \delta_b D_b \Omega}{kT \ln\left(1/f_h\right)} N_h T_n \tag{7.8}$$

$$\dot{\delta}_{tk} = \dot{\delta}_{tk}^e + \dot{\delta}_{tk}^{cr} = \frac{\dot{T}_{tk}}{K_t (1 - f_h)} + \dot{\delta}_{0t} \frac{T_{tk}}{\sigma_0 (1 - f_h)} \tag{7.9}$$

where, at a given integration point along the interface, f_h is the cavity area fraction, $\delta_b D_b$ is the grain-boundary diffusivity, N_h is the number density of cavities, and $\dot{\delta}_i^e$ and $\dot{\delta}_i^{cr}$ represent elastic

and viscous components, respectively. All other terms remain as described in Chapter 5. The tangential and normal stiffnesses selected are sufficiently high with similar values to those from Chapter 5, such that the elastic separation along the boundary is limited. Within the traction-separation rate laws (Eqs. 7.8-7.9), Eq. 7.6 is implemented as the normal inelastic separation rate in Eq. 7.8. The cavity area fraction (Eq. 7.7) increases as a function of the i) inelastic opening $\dot{\delta}_n^{cr}$ (Eq. 7.6), and ii) cavity nucleation as a result of increase in N_h, described either by the Dyson-type nucleation model (Eq. 7.1) or the modified stress-based classical nucleation theory (Eq. 7.2). In turn, evolution of f_h in Eq. 7.7 modifies the normal and shear separation rates in Eqs. 7.8-7.9. Cavity coalescence and failure at an integration point occur when f_h reaches a critical value of $f_h^c = 0.25$ [100]. At this value, the interface tractions reduce to zero. The nucleation rates given by Eqs. 7.1-7.2 modify the separation-rate laws through the evolution of Eq. 7.7. In turn, Eqs. 7.1-7.2 and 7.4-7.5 depend on the current tractions in the traction-separation laws, as well as the current resolved shear strain rate in the matrix for Eq. 7.1. The integration procedure for obtaining solutions and updating f_h, T_n and T_{tk} at the end of each increment is briefly described in Appendix B. The implementation of the damage laws into the modelling framework is presented in detail in the next section and in Appendix D as a flow chart.

7.2.3. Implementation of local cavity nucleation models

The modelling approach to cavity nucleation, adopted here, aims to explore the ability of existing cavity nucleation models, modified in a logical manner in Section 6.5, to predict some general features of the intergranular creep failure process. The objective in this study is not to develop a unified cavity nucleation model. The aim is to identify possible missing features in the existing nucleation theories by applying them at the microscale within the polycrystalline modelling framework for creep deformation. Firstly, the local Dyson-type model of Eq. 7.1 is employed as a

function of the maximum resolved shear strain-rate in the lattice, $\dot{\gamma}_{max}$, in the vicinity of a material point along the interface. The modelling framework extracts the maximum value of $\dot{\gamma}^{(\alpha)}$, computed by the CPFE model at increment *i*, at the two continuum-element integration points either side of an interface integration point (see Fig. 7.1.a). The higher value of the two is used to compute the current nucleation rate at this interface integration point. Explicit integration is used to determine the cavity number density at the end of each increment, according to $N_h^{i+1} = N_h^i + \dot{N}_h^i \Delta t$, where $\dot{N}_h^i$ is the nucleation rate at the *i*-th increment and Δt is the time step.

Two modifications were introduced to the stress-based classical nucleation theory in Section 6.5. The first one is associated with an assumed log-normal distribution of volumetric shape factors $f_v(\psi')$ (or alternatively, dihedral angles ψ') of the nucleated cavity/particle geometries along the interface, described by Eq. 7.3. Within the modelling framework employed here, the cavity number density or number density of cavitated particles at an interface integration point at the end of the *i*-th increment is determined by explicit integration of Eq. 7.2 as

$$N_h^{i+1} = N_h^i + \Delta t\left(r_p T_{nuc} / \gamma_s\right)^{-2} \int_0^{f_{\max}} \dot{c}_h^{f_v}(\Phi_n, T_{nuc}, f_v, c_{\max}(f_v), c(f_v))df_v \qquad (7.10)$$

where Φ_n represents all material properties in Eq. 7.2 and $\dot{c}_h^{f_v}$ is the individual nucleation rate of critical nuclei for a given population of cavity/particle geometries with volumetric shape factors between $f_v(\psi')$ and $f_v(\psi' + \Delta\psi')$ (see Fig. 7.1.b). The integral in Eq. 7.10 is solved numerically by integrating individual nucleation rates across the distribution of dihedral angles $\psi' \in \left[0^\circ, 70^\circ\right]$. An interval of $\Delta\psi' = 0.25°$ was selected as smaller integration steps did not affect the result. The second modification of the stress-based nucleation theory takes into account the local stress field at intergranular particles. Eq. 7.4 can estimate the maximum particle stress due to redistribution of

stress from particle-free grain-boundary regions as a result of diffusive processes. A timescale, t_{red}, is associated with this increase in particle stress given by Eq. 6.10 in Section 6.5.3.1. The limiting cases of particles carrying the average resultant boundary traction ($T_e; t_{red} \to \infty$) and maximum particle stress ($T_e/\left(d_p/\lambda_p\right)^2; t_{red} \to 0$) will be examined in Section 7.3.2 and 7.3.3, respectively. This provides insights on differences in nucleation response with the timescale for stress transfer. Local stress arising from the presence of prismatic dislocation loops in the vicinity of intergranular particles was also considered (Eq. 7.5). Prismatic loops are considered in Section 6.5 as an idealised dislocation feature in the vicinity of particles, since they are already captured in the deformation model of Chapter 4. Note that the accumulation of such local dislocation features and the associated local stress fields will modify the equilibrium between the stresses carried by the particles and the surrounding matrix. This can affect the stress redistribution process described above and will be strongly-dependent on the nature of the local dislocation features. In order to account for the potential elevation of stress at particles due to such local features, a simple superposition between the maximum particle stress (Eq. 7.4) and the residual stress due to prismatic loops in the vicinity of intergranular particles ($\bar{\tau}_p^{GB}$, Eq. 7.5) is assumed. Based on this simple approach, the value of T_{nuc} at grain-boundary particles at a given integration point is:

$$T_{nuc} = \tau^* + \bar{\tau}_p^{GB} = T_e \left(d_p/\lambda_p\right)^{-2} + \max(\bar{\tau}_p^{GB}) \tag{7.11}$$

where d_p and λ_p are the particle diameter and spacing. This is illustrated in Fig. 7.1. The maximum value of $\bar{\tau}_p^{GB}$ is determined by Eq. 7.5, which is a function of the density of prismatic loops in the lattice, N_{li}^{max}. The value of N_{li}^{max} is extracted from the CPFE model as illustrated in Fig. 7.1.c), following the same approach to extract $\dot{\gamma}_{max}$. It is recognised that the assumption of superposition between $\tau^*$and $\bar{\tau}_p^{GB}$ is not rigorous, since force equilibrium would require a negative

stress on the particle-free region if the prismatic loops are to increase the stress at particle regions. In reality, other dislocation features may exist in the vicinity of particles and modify further this local balance. Detailed information on such features in Type 316/316H is not available at present. Nevertheless, the simple superposition assumption is adopted here. This aims to introduce a modelling approach, which allows the effects of local dislocation structures on the nucleation response to be captured. Note also that T_e in Eq. 7.11 is the resultant boundary traction, as discussed in Section 6.5. T_e is determined here by coupling of the normal (T_n) and shear (T_{tk}) tractions, according to

$$T_e = \sqrt{\langle T_n / \alpha_n \rangle^2 + \left(\hat{T}_{tk} / \alpha_t \right)^2} \tag{7.12}$$

where α_n and α_t determine the contribution from the tractions to the resultant traction. In reality, the values of α_n and α_t would be a function of the faceted particle geometry, but for the purpose of this study these parameters are selected arbitrarily. In addition, only tensile normal tractions add a contribution to the resultant traction in Eq. 7.12. Compressive normal tractions will lead to cavity sintering [121], which is not considered in this study. Section 7.4 demonstrates that a unique set of (α_n, α_t) captures the expected distribution of cavity number density in FCC materials. The determined set suggests that the orientation of the resultant boundary traction to the boundary plane, $\kappa = \tan^{-1}\left((T_n / \alpha_n) / (T_t / \alpha_t) \right)$ in Fig. 7.1.d), is associated with important features of the local, intragranular stress field in the vicinity of the boundary. Note that the constraint at triple grain junctions from Chapter 5 in the presence of grain-boundary sliding does not consider volume change due to opening on adjacent boundaries. This is considered in the following section.

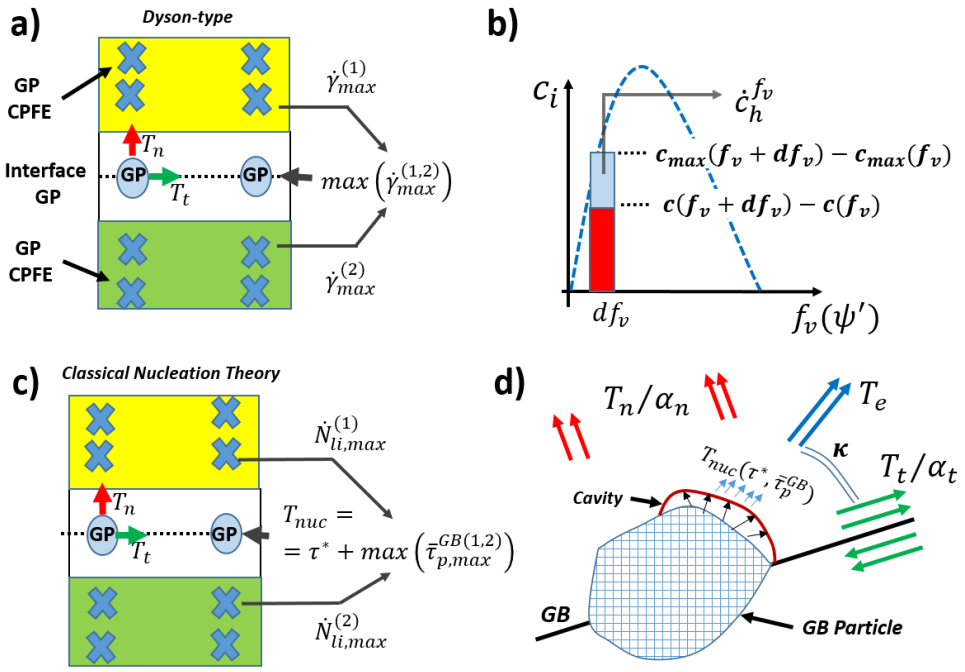


Figure 7.1. Implementation approach for a) local Dyson-type model, b) distribution of cavity/particle geometries with different ψ' and c) determining T_{nuc}. d) Coupling between shear and normal tractions.

7.2.4. Triple grain junctions and inelastic opening of adjacent boundaries

In Section 5.2.2, artificial opening of the triple point as a result of sliding along adjacent boundaries was restricted in thin-sliced, quasi-3D grain aggregates. This was achieved by the introduction of a triple line element, formulated to restrict the change in area ($\dot{L}_{Line}^{s} = \mathbf{A}\dot{\mathbf{U}} = 0$). The developed constraint, however, does not account for inelastic opening due to damage along adjacent boundaries. In the present chapter the deformation and damage response of full-3D bicrystals (Fig. 7.2.a) and quasi-3D, thin-sliced polycrystalline aggregates (Fig. 7.2.b) is examined. Triple lines do not form in the bicrystal, but they do in the polycrystalline geometry. The approach from Section 5.2.2 is extended in this section by considering the volume change of the triple line due to opening along boundaries. Consider the geometry of the front face of the triple line in Fig. 7.2.c), where the boundary has a thickness *h*. The instantaneous rate of area change of the region *N* in Fig. 7.2.c) due to opening along an individual boundary, taking h_{12} as example, is expressed as

$$\dot{A}_{12}^{n} = 1/2\, c_{12}\dot{h}_{12}^{n} + 1/2\, \dot{c}_{12} h_{12} = 1/2\left(h_{23}\sin(\gamma_{\Delta})\left(\dot{u}_i^{n2} - \dot{u}_i^{n1}\right)\right) + 1/2\left(h_{12}\sin(\gamma_{\Delta})\left(\dot{u}_i^{n3} - \dot{u}_i^{n2}\right)\right) \qquad (7.13)$$

where c_{12} is the height of the triangle with respect to h_{12} and $\dot{u}_i^n$ is the nodal displacement rate in a direction, perpendicular to the mid-surface of the adjacent boundary (i.e. direction of opening in the co-ordinate system of the interface element). Assume that the total rate of area change of region *N* is the average of the rates of change due to opening along the boundaries in Fig. 7.2.d):

$$\dot{A}_{\Delta,Front}^{n} \approx 1/3(\dot{A}_{21}^{n} + \dot{A}_{32}^{n} + \dot{A}_{31}^{n} - \sum_{3} e_k) \qquad (7.14)$$

where e_k is the error due to potential overlap of incremental area changes in Fig. 7.2.d, arising from different boundaries. The error introduced will be limited in situations when opening is confined to only one of the three boundaries enclosing the triple line. This is indeed the common scenario in Section 7.4. The error in Eq. 7.14 will not affect the global solution and the approach is adopted here due to its simplicity and ease of implementation. As in Section 5.2.2, Eq. 7.14 can be applied to a triple line of arbitrary orientation, consisting of triangles with nodes (1-3) and (4-6). Dividing through h_{13} gives the rate quantity, independent of boundary thickness,

$$\dot{L}_{Line}^{n} = \frac{1}{2}\frac{\dot{A}_{\Delta}^{n}}{h_{13}} + \frac{1}{2}\frac{\dot{A}_{\Delta}^{n'}}{h'_{13}} = \frac{1}{12}\begin{bmatrix} 3\sin(\beta_{\Delta})(\dot{u}_i^{n2} - \dot{u}_i^{n1}) + 2\sin(\alpha_{\Delta})(\dot{u}_i^{n3} - \dot{u}_i^{n2}) + \\ +\left(\sin(\alpha_{\Delta})\sin(\beta_{\Delta})/\sin(\gamma_{\Delta})\right)(\dot{u}_i^{n3} - \dot{u}_i^{n1}) + 3\sin(\beta_{\Delta}')(\dot{u}_i^{n5} - \dot{u}_i^{n4}) + \\ +2\sin(\alpha_{\Delta}')(\dot{u}_i^{n6} - \dot{u}_i^{n5}) + \left(\sin(\alpha_{\Delta}')\sin(\beta_{\Delta}')/\sin(\gamma_{\Delta}')\right)(\dot{u}_i^{n6} - \dot{u}_i^{n4}) \end{bmatrix} \qquad (7.15)$$

where primed quantities are associated with the rear face, formed by nodes (4-6). Interface elements of zero thickness are employed and change in length of the triple line element is allowed.

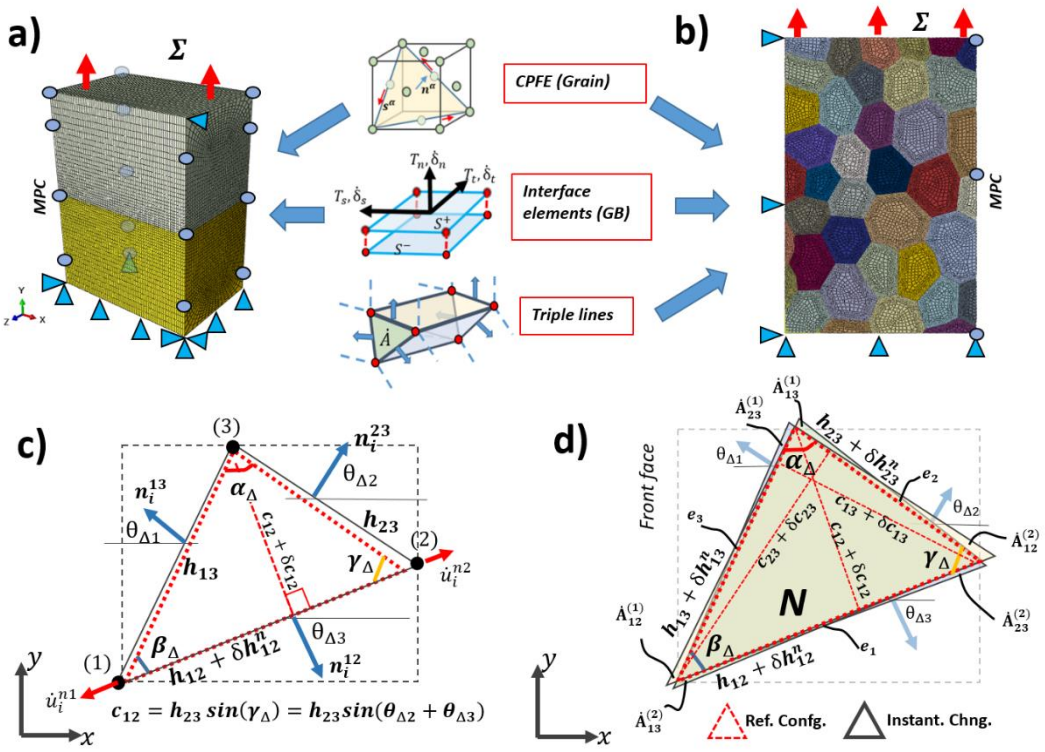


Figure 7.2. Boundary conditions in the a) bicrystal and b) polycrystalline geometries. The instantaneous area change due to normal separation along a single interface element, enclosing the triple line, is illustrated in c) with respect to a reference configuration. The case for opening along all three sides is given in d).

The rate quantity $\dot{L}^n_{Line}$ is a function of the triple line nodal displacements rates in the global co-ordinate system, $\dot{\mathbf{U}}$, as $\dot{L}^n_{Line} = \mathbf{B_n}\dot{\mathbf{U}}$. This is consistent with the form of $\dot{L}^s_{Line}$ due to sliding from Section 5.2.2. The matrix $\mathbf{B_n}$ is given in Appendix C. The constraint in the presence of opening along boundaries, adopted here, requires that the area change due to opening is accommodated by area change due to sliding or opening along adjacent boundaries. The constraint can be expressed as $\dot{L}^t_{Line} = \dot{L}^n_{Line} - \dot{L}^s_{Line} = (\mathbf{B_n} - \mathbf{A})\dot{\mathbf{U}} = \mathbf{M}^{\mathbf{t}}_{\mathbf{Line}}\dot{\mathbf{U}} = 0$. The incremental form of the solution to the FE boundary value problem of Eq. 5.12 at the end of each increment then becomes

$$\frac{\partial \bar{\Psi}}{\partial \mathbf{U}} = \frac{\partial \Psi}{\partial \mathbf{U}} + \sum_{\Delta} \frac{\partial (\mathbf{M}^{\mathbf{t}}_{\mathbf{Line}})^T \dot{L}^t_{Line}}{\partial \mathbf{U}} = \int_V \mathbf{B}^T \frac{\partial \boldsymbol{\sigma}}{\partial \boldsymbol{\varepsilon}} \mathbf{B} dV + \int_{\Gamma_c} \mathbf{B}^T_{\mathbf{c}} \frac{\partial \mathbf{T}_{\mathbf{c}}}{\partial \boldsymbol{\delta}} \mathbf{B}_{\mathbf{c}} d\Gamma + \sum_{\Delta} (\mathbf{M}^{\mathbf{t}}_{\mathbf{Line}})^T \mathbf{M}^{\mathbf{t}}_{\mathbf{Line}} \qquad (7.16)$$

The constraint becomes inactive when all adjacent interface elements begin to open. In Section 7.4.2, the constraint at triple junctions in the presence of damage will be demonstrated.

7.2.5. Modelling approach

The modelling framework from Sections 7.2.1-7.2.4 is used in Section 7.3 to study intergranular creep failure of bicrystals of Type 316 stainless steel. The bicrystal is a simple geometry for which the two modified nucleation models of Eqs. 7.1 and 7.2, coupled to diffusive growth, can be probed along an isolated grain boundary, and calibrated to particular material state and temperature. The local damage response is calibrated to the creep strength response of Type 316 bicrystals at 700°C [231] and ex-service Type 316H at 550°C. The calibrated local damage models are then applied in Section 7.4 within the 39-grain geometry from Fig. 7.2.b) of ex-service Type 316H stainless steel at 550°C. Experimental data for the macroscopic primary, secondary and tertiary creep stages at this temperature are available in the stress range 250-320 MPa. The data are used to assess the suitability of the calibrated nucleation models in capturing the trends in macroscopic failure response, as well as the distribution of cavities with respect to grain-boundary orientation to the applied load. Successful nucleation models would need to capture the trends in macroscopic failure response of both bi- and polycrystalline geometries. In addition, the trend in cavity morphology in FCC materials described in Chapter 6, i.e. higher cavity densities along inclined boundaries (~45-60° to load axis) and dominant failure along transverse boundaries (~90° to load axis), needs to be captured in the polycrystalline model. In the present chapter, the polycrystalline aggregate is not treated as a RVE of the material. The study only provides insights into the intergranular damage process in polycrystals of anisotropic grains with irregular shapes in relation to local stress state, particle morphology and idealised dislocation features near grain boundaries. This allows

identification of possible missing features in the mechanistic model, and provision of guidelines for modelling and experimental studies to support the development of robust nucleation models.

7.3. MODELLING OF BICRYSTALS OF TYPE 316 AND TYPE 316H

In the present section, the developed framework is employed to simulate intergranular creep failure response of the bicrystal of Fig. 7.2.a) of solution-treated Type 316 at 700°C and ex-service Type 316H stainless steels at 550°C. Their composition can be found in [23] and Table 3.1, respectively. Initially, focus is on the response at 700°C since macroscopic creep strength (t_f vs Σ) data at this temperature for Type 316 in the range 60-160 MPa are available in [231]. A portion of the sample from [231] with dimensions 15×20×10 μm is examined. Constant stress is applied on the top face of the cell. Due to ease of implementation, a simple class of boundary conditions (BC) are used throughout Section 7.3, whereby the cell faces remain straight (Fig. 7.2.a). The simplification is acknowledged and, for consistency, the simulations from Section 7.3 were repeated with appropriate periodic boundary conditions (PBC), after Aurora et al. [188]. It was found that macroscopic t_f of the bicrystal with the simpler BC and consistent PBC vary by a factor of ~1.7. This is acceptable due to the scatter in experimental response of the material. The results are not shown for brevity. As discussed in Section 7.2.5, calibration of the bicrystal damage models is based on macroscopic t_f. Hence, for the purpose of this study, the imposed BC to the bicrystal do not significantly alter the result of interest. However, Section 7.5 discusses the importance of PBC when the detailed failure morphology along the boundary is of interest (e.g. comparison between model prediction and experimentally measured distribution of cavity density along the boundary). Continuum C3D8 elements for the grains, deforming according to the CPFE model from Appendix A, and 8-noded linear interface elements along the grain boundaries from Appendix B are

employed. Five different bicrystal meshes with 1, 20, 80, 216 and 480 interface elements along the boundary were used for a mesh convergence study. The mesh with 80 interface elements was selected, since predictions for macroscopic failure time, and distribution of N_h and f_h remain unchanged with further refinement. The crystallographic orientations of the grains either side of the boundary are arbitrarily selected as orientations "H" and "S" from Fig. 5.4. Note that short-term plasticity and creep deformation data for the bicrystals at 700°C and 550°C are not available. For simplicity, their deformation response is calibrated to polycrystalline material deformation data; the predicted creep curves are not presented for the sake of brevity. Based on observations from Section 6.2.2, only $M_{23}C_6$ intergranular carbides are treated as cavity nucleation sites in this study. Information about the inter- and intragranular carbide morphology is obtained from experimental studies on solution-treated (ST) Type 316 [25,231] and ex-service Type 316H [95,97,111,196]. As discussed in [25,26], the kinetics of precipitate formation and growth are rapid in ST Type 316 at 700°C. The precipitate size and spacing of inter- and intragranular $M_{23}C_6$ carbides in both ST and EX material is assumed constant. The carbide morphology is assumed identical along all boundaries within both bicrystals and polycrystals for a given temperature and material. The model parameters for the CPFE and interface elements are given in Table 7.1.

Table 7.1. Material parameters for the CPFE and interface models, employed in the bicrystal and 39-grain cell. Values of C_{ij}, ν, $\dot{\gamma}_0$, G_0, α_0, b, Ω and α_d are those from Tables 4.2 and 5.2.

Parameter	Value - ST 700°C	Value - EX 550°C	Parameter	Value - ST 700°C	Value - EX 550°C
D_C	2.3×10^{-13} m^2/s *	6.47×10^{-15} m^2/s *	N_0	2.5×10^{13} 1/m^2	
$\delta_b D_b$	5.33×10^{-23} m^3/s **	1.52×10^{-24} m^3/s **	j_s	1×10^{15} (2×10^{15}) 1/m^2	2×10^{15} (6×10^{15}) 1/m^2
$\dot{\delta}_{0t}$	1.0×10^{-26} mm/s		j	5×10^{15} (1×10^{16}) 1/m^2	1×10^{16} (3×10^{16}) 1/m^2
ΔL_r	$4b$	$8b$	W_C	80 (40)	12 (5)
τ_p	15 MPa	21 MPa	τ_s	3 MPa	37 MPa
σ_0	60-160 MPa	230-320 MPa	d_p	1.0 μm ***	400 nm [i]
γ_s	2.0 J/m^2 [ii]		λ_p	2.0 μm ***	680 nm [i]

*Data from [90]. ** Data extrapolated from [199]. *** Values from [231]. [i] Averaged from [95,97,111,196]. [ii] Value from [122]. Values in brackets for bicrystals.

In the following sections, the failure response of the bicrystal is simulated for cases where intergranular cavitation is a function of diffusive cavity growth coupled to i) local Dyson-type model, and stress-based classical nucleation theory with ii) a distribution of particle strengths and iii) a distribution of particle strengths and maximum stress at particles, described in Section 6.5.

7.3.1. Local Dyson-type nucleation model and diffusive growth

In this section, the local Dyson-type cavity nucleation model of Eq. 7.1 is employed, following the approach from Fig. 7.1.a), and coupled to the diffusive growth model of Eq. 7.6 to simulate the failure response of the bicrystal. Initially, focus is on Type 316 stainless steel at 700°C. No pre-existent cavities are assumed along the boundary and the initial density of cavities is $N_h^0 = 0$ with the nucleation model capturing the evolution of cavity density. The sensitivity of time to failure on the nucleation constant α' was assessed for an initial cavity area fraction of $f_h^0 = 10^{-15}$ ($f_h^0 \rightarrow 0$) and failure fraction $f_h^c = 0.25$ in Fig. 7.3.a). Note that the failure response was insensitive to the selected initial cavity area fraction for $f_h^0 < 10^{-2}$. This in agreement with analytical solutions from [264]. Hence, values of $N_h^0 = 0$, $f_h^0 = 10^{-15}$ and $f_h^c = 0.25$ are used in all subsequent sections. In the absence of nucleation, where $N_h^0 = 4.1 \times 10^5\ mm^{-2}$ was assumed, failure is driven by diffusive growth. The trend in creep strength varies linearly with stress, which disagrees with the experimental response. This demonstrates that cavity nucleation needs to be considered in order to capture the non-linear trend in experimental data. Predicted failure times for different α' in the Dyson-type model are presented in Fig. 7.3.a) for $N_h^0 = 0$, and agreement with experimental data is found for a value of $\alpha' = 8.9 \times 10^6\ mm^{-2}$. An example of the mesh convergence study is also given in Fig. 7.3.a) for this value of α'. Note that the interface element framework for the Dyson-type model, as well as for diffusive growth only, was validated against analytical results from [100,121] for an isolated boundary enclosed by grains, deforming by power-

law creep. The validation procedure is not presented here. Note that cavities could also grow in a non-linear manner, controlled by creep of the surrounding matrix. When the diffusive length Λ in the material is greater than both particle (d_p) and cavity sizes ($2r_h$), the contribution to cavity growth rate due to plasticity is minimal. Following from the discussion in Section 6.4.3.4, the mean characteristic diffusive lengths Λ in Type 316 are 40.0 – 4.2 μm (60-160MPa, 700°C) and 1.9 – 0.9 μm (250-320MPa, 550°C). These are larger than values for d_p from Table 7.1 and $2r_h$ predicted by the model here. Throughout this chapter, only diffusive cavity growth is considered.

The nucleation model from Eq. 7.1 is dependent on the deformation response of adjacent grains. In Fig. 7.3.b), the predicted failure response of 5 bicrystals with grains of different crystallographic orientations is simulated for $\alpha' = 8.9 \times 10^6\ mm^{-2}$. Results demonstrate that failure shifts to longer times for samples with plastically-harder grains (e.g. Ori set 5/6). This is associated with changes in the nucleation rate. As discussed in Chapter 5, plastically-harder grains with orientations away from the [001]-direction creep at lower strain rates for the same stress. This retards the nucleation rate for a given value of α' in Fig. 7.3.b).

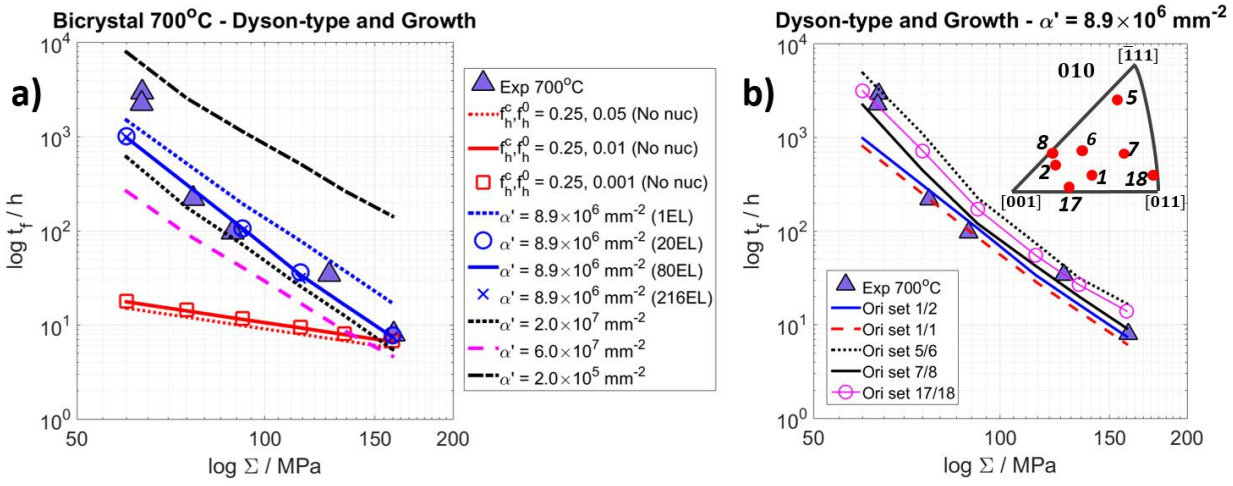


Figure 7.3. a) Predicted creep strength of Type 316 bicrystal at 700°C in absence of nucleation ($N_h = 4.1 \times 10^5\ mm^{-2}$) and Dyson-type model for different α'. b) Predicted creep strength via Dyson-type model with $\alpha' = 8.9 \times 10^6\ mm^{-2}$ for bicrystals of different crystallographic orientations, indicated on the IPF.

The observation is confirmed by evaluation of the average cavity number densities along the boundary after 20 hours of creep at 114 MPa for Ori set 1/2 (softer) and 5/6 (harder). Values of 71×10^4 mm^{-2} and 43×10^4 mm^{-2} were predicted, respectively. As will be demonstrated in Section 7.4, the predicted damage morphology in the polycrystalline aggregate is dependent on the crystallographic orientation of the grains and the assumed nucleation model.

Failure of ex-service Type 316H at 550°C is of interest to this study, but bicrystal data at this temperature are not available at present. This poses difficulties to calibrate the damage models examined here for Type 316H at 550°C. According to Huang [122] and Arnaud [232], the nucleation constant α' for Type 316/316H stainless steels is relatively constant in the range 525-700°C. Hence, the intergranular failure response of a bicrystal of ex-service Type 316H at 550°C, deforming by the CPFE model with parameters given in Table 7.1, is simulated by the calibrated Dyson-type model with $\alpha' = 8.9 \times 10^6\ mm^{-2}$. The predictions of t_f over the stress range 230-320 MPa at 550°C are shown in Fig. 7.4. It is found that the predicted trend by the Dyson-type model for a bicrystal of ex-service Type 316H at 550°C in Fig. 7.4 lies below the polycrystalline experimental creep strength data for ex-service Type 316H at 550°C. This resembles the difference between bi- and polycrystalline data at 700°C, which suggests that the predicted trend by the Dyson-type model at 550°C is reasonable. Since bicrystal creep strength data for Type 316H at 550°C are not available, the predicted response with $\alpha' = 8.9 \times 10^6\ mm^{-2}$ is used in the following sections as reference data to calibrate the modified stress-based nucleation model at this temperature. The calibrated Dyson-type model from this section is then employed in Section 7.4.1 to simulate macroscopic creep failure of polycrystalline ex-service Type 316H at 550°C.

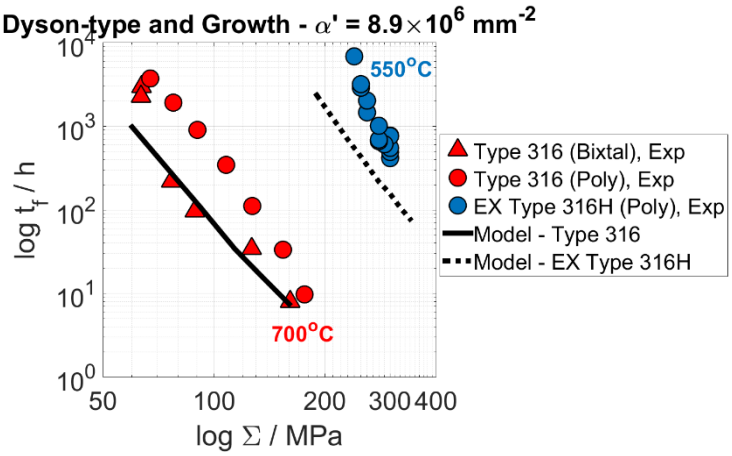


Figure 7.4. Creep strength of Type 316 bicrystals (700°C) and ex-service Type 316H (550°C) – Dyson-type model prediction for $\alpha' = 8.9 \times 10^6 mm^{-2}$ and comparison to experimental data.

7.3.2. Classical nucleation theory with distribution of particle strengths and diffusive growth

In this section, the modified classical nucleation theory of Eq. 7.2, considering a log-normal distribution of nucleated cavity/particle geometries with different volumetric shape factors $f_v(\psi')$ (or dihedral angles ψ') is coupled to the diffusive growth model. Firstly, the failure response of the bicrystal sample of Type 316 at 700°C is examined. In this section, the limiting case of $t_{red} \to \infty$ from Section 7.2.3 is examined, i.e. no relaxation of stress along the particle-free boundary regions. The stress driving the vacancy condensation process is assumed for simplicity to be only the average normal boundary traction, i.e. $T_{nuc} = T_n$. The limiting case of $t_{red} \to 0$ when the maximum particle stress drives vacancy condensation is examined in Section 7.3.3. Before evaluating the failure response for different distributions of $f_v(\psi')$, it is worth demonstrating the predicted trend in creep strength when the original form of the classical nucleation theory from Eq. 6.4 is employed. In this case, all cavity/particle geometries are assumed the same at a given material point (no distribution). The predicted failure response for dihedral angles of ψ' = 5° and

8° for Type 316 at 700°C is shown in Fig. 7.5.a) with all other parameters given in Table 7.1. The trend in creep strength predicted for $\psi' = 5°$ lies closer to experimental data, but does not capture the variation of t_f with macroscopic applied stress Σ. For 90 < Σ < 140 MPa, failure times are approx. an order of magnitude shorter compared to the experimental data, whereas at Σ < 75 MPa failure time rapidly increases with virtually no failure. This illustrates the deficiency of the original form of this nucleation model. Almost instantaneous nucleation of cavities is predicted with applied stress above a certain threshold, in agreement with observations from the literature, e.g. [121]. Next, the response of the bicrystal sample is simulated by coupling the diffusive growth model to the modified classical nucleation theory of Eq. 7.2 for different distributions of $f_v(\psi')$. Examples of the predicted variation in creep strength of the same Type 316 bicrystal at 700°C are illustrated in Fig. 7.5.a) for four distributions of f_v, represented by $\log(\mu(f_v))$ and $\log(\tilde{\sigma}(f_v))$, where μ and $\tilde{\sigma}$ are the mean and standard deviation of the distribution. It is found that a distribution of $\log(\mu(f_v)) = -9$ and $\log(\tilde{\sigma}(f_v)) = 0.6$ captures the trend in experimental creep strength data at this temperature, as shown in Fig. 7.5.a), with the parameters from Table 7.1. N.B. The number densities of nucleation sites (i.e. particles) with different $f_v(\psi')$ for the examined distributions are illustrated in Fig. 7.6. The sharp drop in failure time for Σ > 90 MPa from Fig. 7.5.a), when the original classical nucleation theory of Eq. 6.4 is employed, is not present when a distribution of cavity/particle geometries, or equivalently cavity nucleation thresholds, is considered. To explain this, the difference in predicted variation of average cavity number density N_h by the original (Eq. 6.4) and modified (Eq. 7.2) classical nucleation theory along the boundary of the Type 316 bicrystal at 700°C is examined in Fig. 7.5.b).

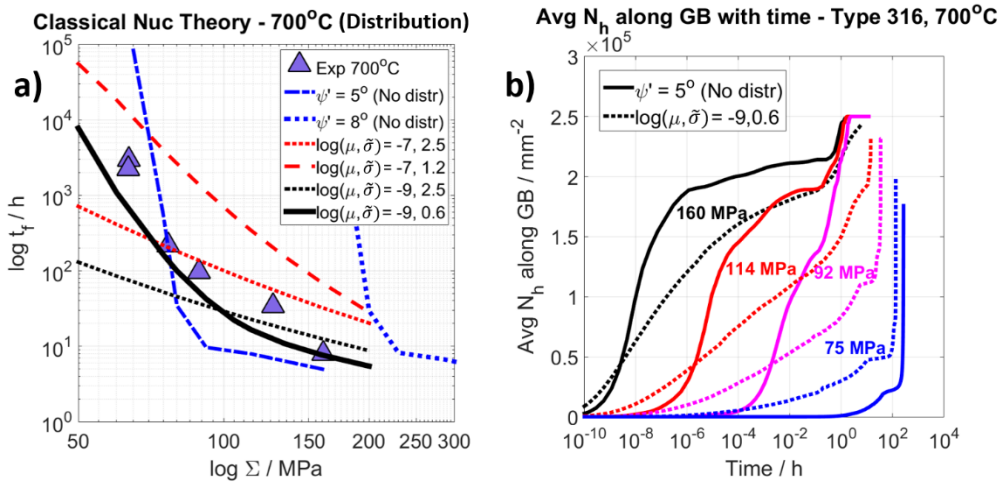


Figure 7.5. a) Predicted creep strength of Type 316 bicrystal at 700°C by classical nucleation theory for different distributions of $f_v(\psi')$ and without a distribution (ψ'=const.). b) Average cavity number density along boundary with and without a distribution for a fit to macroscopic creep strength data.

The original form of the nucleation model predicts virtually no nucleation for $\Sigma < 92$ MPa, whereas approx. 80-100% of all possible nucleation sites (i.e. particles) are depleted for $\Sigma > 92$ MPa in less than 1 hour. This explains the sharp increase in t_f from Fig. 7.5.a) for $\psi' = 5°$. On the contrary, the variation of N_h with time is smoother when a distribution of $f_v(\psi')$ with $\log(\mu(f_v), \tilde{\sigma}(f_v)) = (-9, 0.6)$ is assumed. For the assumed distribution of $f_v(\psi')$, approx. 80% of all possible nucleation sites are depleted at $t < 1$ hour at 160 MPa, but a continuous increase in cavity number density is found between 1 and 300 hours for $\Sigma < 160$ MPa. The findings from Fig. 7.5.b) demonstrate that the stress-based nucleation theory captures the continuous nucleation process when cavity formation at different populations of nucleation sites at a given material point is considered. Now, assume that the distribution of $f_v(\psi')$ is a physical characteristic of the grain boundary in Type 316/316H bicrystals. Then, the calibrated modified nucleation model from Fig. 7.5.a) with $\log(\mu(f_v), \tilde{\sigma}(f_v)) = (-9, 0.6)$ can be employed to simulate the failure response of ex-service Type 316H bicrystals at 550°C and compared to that predicted by the Dyson-model of Section 7.3.1 in the range $\Sigma = 230$-320 MPa. Predictions are given in Fig. 7.6.a). The results show

that, compared to the Dyson-type model results, failure times at 550°C are shorter by two orders of magnitude for $\log(\mu(f_v),\tilde{\sigma}(f_v))$ = (-9, 0.6). In Fig. 7.6.a), we find that for the set of parameters for ex-service Type 316H from Table 7.1, a distribution of $\log(\mu(f_v),\tilde{\sigma}(f_v))$ = (-5, 1.4), illustrated in Fig. 7.6.b), predicts the same trend in creep strength at 550°C as the reference response from Section 7.3.1. The evolution of average N_h along the boundary predicted by the modified classical nucleation theory for $\log(\mu(f_v),\tilde{\sigma}(f_v))$ = (-5, 1.4) at 550°C is also in agreement with that given by the Dyson-model from Section 7.3.1 (see Fig. 7.7).

Several aspects of the findings from Fig. 7.6 need to be considered. Firstly, the determined distribution of f_v with $\log(\mu(f_v))$ = -5 has a mean ψ' of 15°, which gives a lenticular profile of the nucleated cavity/particle geometry, compared to ψ' = 6° for $\log(\mu(f_v))$ = -9. As discussed in Chapter 6, the higher dihedral angle is more realistic. It is therefore assumed that $\log(\mu(f_v),\tilde{\sigma}(f_v))$ =(-5,1.4) characterises the physical distribution of nucleated cavity/particle geometries along this bicrystal boundary. This assumption would require that the latter distribution also captures the trend in creep strength in Type 316 at 700°C. Employing the distribution $\log(\mu(f_v),\tilde{\sigma}(f_v))$ =(-5, 1.4) at 700°C with the parameters from Table 7.1 overpredicts failure times by ~2 orders of magnitude. A change in the adopted parameters is required to capture the trend in response at 700°C. From the physical parameters in Table 7.1, the surface energy (γ_s) and grain-boundary diffusivity could be affected by the microstructural state of the boundary [198]. Note that γ_s has a greater effect on the nucleation rate in Eq. 7.2. We modify the value of γ_s and find that the experimental trend in creep strength of Type 316 at 700°C in Fig. 7.6.a) for $\log(\mu(f_v),\tilde{\sigma}(f_v))$ = (-5, 1.4) is captured when γ_s is set to 0.8 J/m^2. It is likely that γ_s is reduced by the presence of impurities along particle/matrix interfaces [113,245]. Results from [121] suggest that such drastic

reductions in γ_s (~60%) due to temperature change or presence of impurities is unlikely. Further work is needed to investigate the effects of impurity segregation on nucleation.

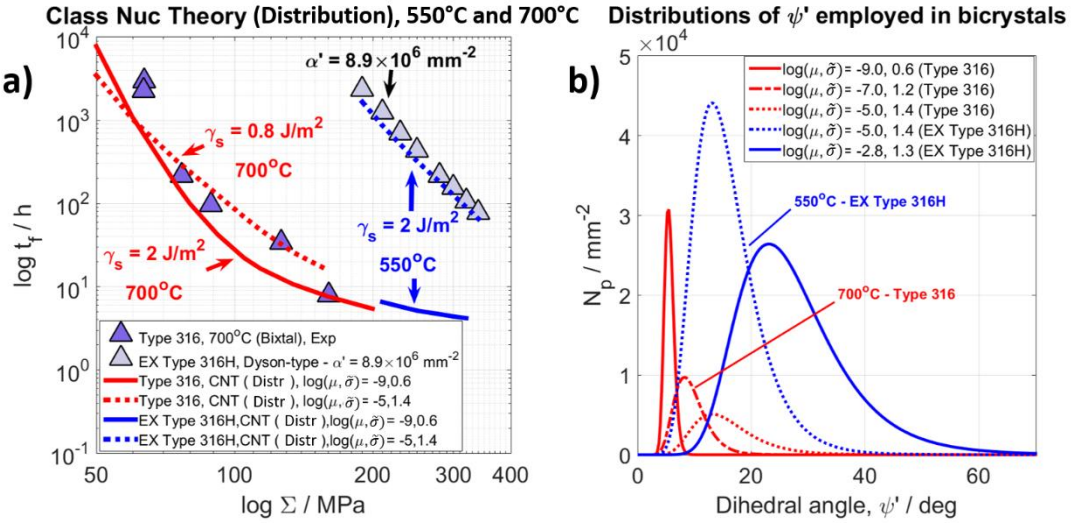


Figure 7.6. a) Predicted creep strength of Type 316 (700°C) and ex-service Type 316H (550°C) by classical nucleation theory for two distributions of $f_v(\psi')$ and different γ_s. Employed distributions are shown in b).

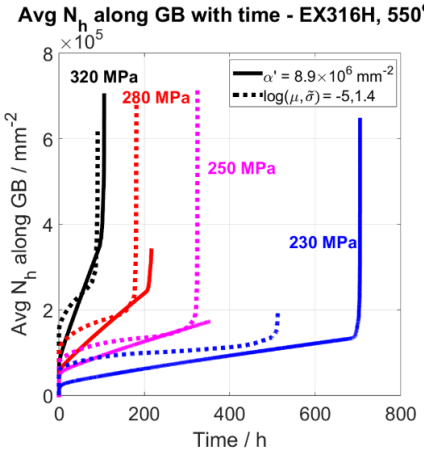


Figure 7.7. Predicted average N_h along boundary by Dyson-type model ($\alpha' = 8.9 \times 10^6\, mm^{-2}$) and modified classical nucleation theory ($\log(\mu(f_v), \tilde{\sigma}(f_v)) = -5,1.4$), ex-service Type 316H at 550°C.

Secondly, the dihedral angle ψ' depends on the energy balance between the grain boundary and particle/matrix interface. This energy balance could potentially change with temperature, e.g. when there are differences in dislocation structure or particle morphology (e.g. σ-phase at 700°C) along the grain boundary at 550°C and 700°C. Hence, it could be possible that different

distributions of $f_v(\psi')$ characterise the grain boundary across the temperature range. Detailed information about such differences in Type 316/316H is not available at present. This and the lack of consideration of the change in γ_s due to the presence of impurities are limitations of the mechanistic nucleation model, discussed in Section 7.5. In the remainder of this chapter, only creep failure of ex-service Type 316H at 550°C is examined. Hence, the distribution of $\log(\mu(f_v), \tilde{\sigma}(f_v))$ =(-5,1.4) is probed in Section 7.3.3 where the vacancy condensation process is driven by the maximum particle stress and residual stress due to prismatic loops (Section 6.5.3.2).

7.3.3. Classical nucleation theory with a distribution of particle strengths and maximum stress at particles and diffusive growth

Application of the modified classical nucleation theory of Eq. 7.2 with a distribution of cavity/particle geometries with different ψ' demonstrated the ability of the model to capture the failure response of bicrystals of ex-service Type 316H at 550°C. However, the stress driving the vacancy condensation process in Section 7.3.2 was assumed to be the average normal traction T_n (i.e. $t_{red} \to \infty$). In this section, the limiting case of rapid relaxation of stress in the matrix region and increase in particle stress is examined ($t_{red} \to 0$). The maximum particle stress due to the applied load and residual stress due to the presence of prismatic loops contribute to T_{nuc}. As discussed in Section 7.2.3, simple superposition of the two is adopted in Eq. 7.11. Three limiting cases for the coupling of normal and shear tractions (Eq. 7.12) along the bicrystal grain boundary are examined: i) $\alpha_n = 1, \alpha_t = \infty$ (normal only), ii) $\alpha_n = \infty, \alpha_t = 1$ (shear only) and iii) $\alpha_n = 1, \alpha_t = 1$ (simple coupling). Examination of these cases aims to provide initial insight into the coupling effect on the intergranular failure response. The coupling between T_n and T_t will be examined in detail in Section 7.4.2.

The failure response of bicrystals of ex-service Type 316H at 550°C is simulated in the stress range 250-320 MPa. Firstly, the modified classical nucleation theory of Eq. 7.2 is coupled to growth and T_{nuc} is given by Eq. 7.11 for $\alpha_n = 1, \alpha_t = \infty$. The distribution from Section 7.3.2 with $\log(\mu(f_v), \tilde{\sigma}(f_v))$ = (-5, 1.4) is employed. Failure times for this set of $\log(\mu(f_v), \tilde{\sigma}(f_v))$ and (α_n, α_t) are shorter by more than an order of magnitude, as compared to the Dyson-type model predictions at 550°C. In order to capture the trend in reference creep strength response at 550°C when T_{nuc} is given by Eq. 7.11, a different distribution of f_v is needed. In Fig. 7.8.a), we find that for $(\alpha_n = 1, \alpha_t = \infty)$, values of $\log(\mu(f_v), \tilde{\sigma}(f_v))$ = (-2.8, 1.3) yield an agreement with the Dyson-type model prediction. The reason for adjusting the mean of the distribution to a higher dihedral angle is because, compared to the results from Section 7.3.2, T_{nuc} is raised here by a factor $(d_p / \lambda_p)^{-2}$. This is illustrated in Fig. 7.8.b) where $T_n / (d_p / \lambda_p)^2$ is of the order of 900 MPa for an applied macroscopic stress of Σ = 300 MPa. Note that for $(\alpha_n = 1, \alpha_t = \infty)$ and values of $\log(\mu(f_v), \tilde{\sigma}(f_v))$ =(-2.8, 1.3), the variation of average N_h along the boundary with time is identical to that from Fig. 7.7. Comparison between the limiting cases for $T_{nuc} \approx T_n / (d_p / \lambda_p)^2$ (this section) and $T_{nuc} = T_n$ (Section 7.3.2) suggests that the maximum stress at particles will steadily increase when $0 < t_{red} < \infty$. This would give rise to another non-linear process, which will gradually accelerate the nucleation activity along the boundary. Employing Eq. 6.10, t_{red} for γ-Fe at 550°C is estimated here to be ~100 s, which is short compared to the creep life of the samples. Hence, in the remainder of this study, only the limiting case of $t_{red} \to 0$ is considered. Next, the failure response for $(\alpha_n = \infty, \alpha_t = 1)$ is simulated by employing the distribution determined for the case $(\alpha_n = 1, \alpha_t = \infty)$. In this case, nucleation was minimal along the boundary and failure was not

observed. This is because the maximum particle stress with contributions only from T_t is ~60 MPa at Σ = 300 MPa, which is not high enough to nucleate cavities for the assumed distribution. For the same reason, the failure response for $(\alpha_n = 1, \alpha_t = 1)$ is identical to that for $(\alpha_n = 1, \alpha_t = \infty)$, since the nucleation stress T_{nuc} in Eq. 7.11 will be dominated by the high value of $T_n / (d_p / \lambda_p)^2$. It is also worth pointing out that the contribution to T_{nuc} from the residual stress at particles $\bar{\tau}_p^{GB}$ is minimal: <10 MPa (Fig. 7.8.b). The low value of $\bar{\tau}_p^{GB}$ predicted stems from the approximations made concerning the estimation of $\bar{\tau}_p^{GB}$ (Eq. 7.5) and its contribution to T_{nuc} in Eq. 7.11. In essence, the accumulation of $\bar{\tau}_p^{GB}$ at intergranular particles in Eq. 7.5 is associated with the creep deformation model in the bulk of the grain and not the detailed evolution of the actual dislocation features at the grain boundary. These aspects are discussed in Sections 7.4 and 7.5.

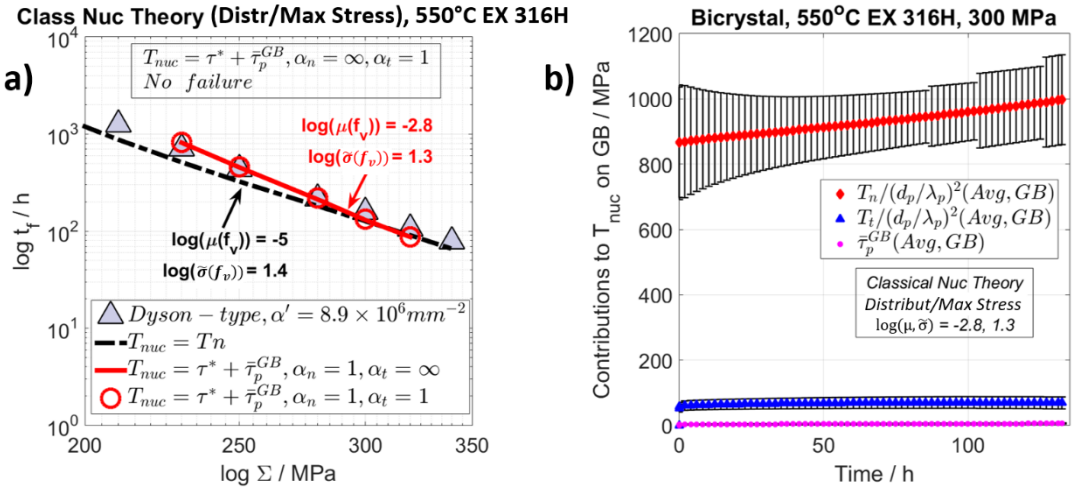


Figure 7.8. a) Predicted creep strength of ex-service Type 316H (550°C) by classical nucleation theory for two distributions of $f_v(\psi')$ with $T_{nuc} = T_n$ and $T_{nuc} = \tau^* + \bar{\tau}_p^{GB}$ (Eq. 7.11) for three limiting couplings of α_n, α_t. b) Contributions to T_{nuc} from average boundary tractions in bicrystal for Σ = 300 MPa.

The Dyson-type model with $\alpha' = 8.9 \times 10^6\ mm^{-2}$ and modified classical nucleation theory with $\log(\mu(f_v), \tilde{\sigma}(f_v))$ =(-2.8,1.3) are calibrated to the predicted reference failure response of an isolated grain boundary. In Section 7.4, the models are probed to simulate the failure response

of polycrystalline EX Type 316H at 550°C. Note that in the remainder of this chapter, T_{nuc} in Eq. 7.2 is determined by Eqs. 7.11-7.12 and different couplings of (α_n, α_t) will be examined.

7.4. INTERGRANULAR CREEP FAILURE IN POLYCRYSTALLINE TYPE 316H

In this section, intergranular creep failure in polycrystalline ex-service Type 316H stainless steel at 550°C is simulated. The polycrystalline array of 39 irregularly-shaped grains from Fig. 7.2.b) is examined. The CPFE model is calibrated to macroscopic short-term plasticity and creep data in the range 280-320 MPa in the absence of damage. The employed model parameters are given in Table 7.1. The response of 10 sets of 39 crystallographic grain orientations is examined. Only the results for one orientation set, shown on the IPF in Fig. 5.12.d), are presented for the sake of brevity since the trends in response are similar in all 10 sets. The aggregate is loaded in uniaxial tension along its top face and the boundary conditions from Fig. 7.2.b) are adopted. Four meshes of different degrees of refinement with interface element lengths i) l_c = 2.6 μm, ii) 1.8 μm, iii) 1.0 μm and iv) 0.75 μm were examined as part of the mesh convergence study. Convergence was assumed when differences between the macroscopic creep strain and t_f at the end of the simulations with further refinement were <5%. The mesh with l_c = 2.6 μm was selected with an example of the mesh convergence study shown in Fig. 7.9. Findings from Chapter 5 show that intergranular particles obstruct significantly grain-boundary sliding in Type 316 and the fraction of deformation due to sliding is <10% with an increase in normal traction on transverse boundaries of ~3%. In this chapter, sliding is not considered ($\dot{\delta}_{0t} \to 0$) with the aim of isolating the effect of intergranular cavitation on creep deformation. Nevertheless, grain-boundary sliding is identified in Section 7.5 as a phenomenon, which needs to be considered in future studies on intergranular cavitation. Here, the Dyson-type model and classical nucleation theory with a distribution of

particle strengths and maximum stress at particles, calibrated in Sections 7.3.1 and 7.3.3, respectively, are coupled to diffusive growth and probed along grain-boundary regions of the 39-grain geometry. The ability of the two nucleation models to capture i) macroscopic creep deformation, ii) variation of cavity density with orientation of grain boundaries with respect to load axis, and iii) failure response in both bi- and polycrystals, is evaluated. The damage morphology with respect to the crystallographic orientations of grains, and relation between nucleation and local stress state in the vicinity of boundaries are also examined.

7.4.1. Local Dyson-type nucleation model and diffusive growth

The polycrystalline failure response of ex-service Type 316H at 550°C is simulated in this section where cavitation along boundaries is represented by the calibrated Dyson-type model with $\alpha' = 8.9 \times 10^6\ mm^{-2}$, coupled to diffusive growth. The macroscopic creep curves in the range Σ = 280-320 MPa in the presence and absence of damage are compared to experimental data in Fig. 7.9. Macroscopic creep strain is computed by Eq. 4.1. The predicted failure times of t_f = 42, 35 and 25 h at 280, 300 and 320 MPa for the polycrystal, where t_f is taken as the end of the tertiary regime, are shorter by ~22 times compared to the experimental response.

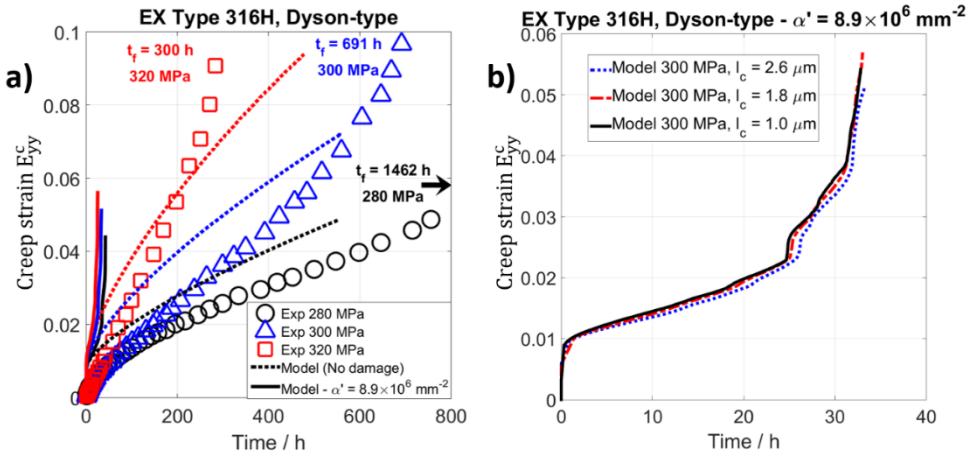


Figure 7.9. a) Predicted macroscopic creep curves in the absence and presence of intergranular damage, EX Type 316H at 550°C and b) example of mesh convergence, Dyson-type model ($\alpha' = 8.9 \times 10^6\ mm^{-2}$).

The shorter failure times predicted are the result of rapid nucleation activity along boundaries in the early stages of creep, since secondary creep regimes are relatively short and the tertiary creep regime occurs at an early stage. This is illustrated by the time variation of cavity number density (N_h) and damage fraction (f_h/f_h^c), averaged along all individual 115 grain boundaries. The results are plotted as a function of boundary orientation to the load axis, θ_{GB}, in Figs. 7.10.a) and b). The polycrystalline average value of N_h across all boundaries at 1 hour and 30 hours for Σ = 300 MPa are 1.8×10^5 mm^{-2} and 7×10^5 mm^{-2}, respectively. These values are larger by 1-2 orders of magnitude compared to the average N_h values in the bicrystal (Section 7.3.1) at 1 hour (6700 mm^{-2}) and 30 hours (2×10^5 mm^{-2}) for Σ=300 MPa. The rapid nucleation, predicted by the calibrated Dyson-type model in the early stages of creep, allows cavity coalescence and failure along boundaries to occur earlier in the polycrystal, compared to experimental data. The reason is that the local inelastic strain rate in the vicinity of boundaries is faster in the polycrystalline aggregate, compared to the bicrystal for a given macroscopic applied stress. This phenomenon is due to localization of strain to accommodate incompatibilities between anisotropic grains in the polycrystal.

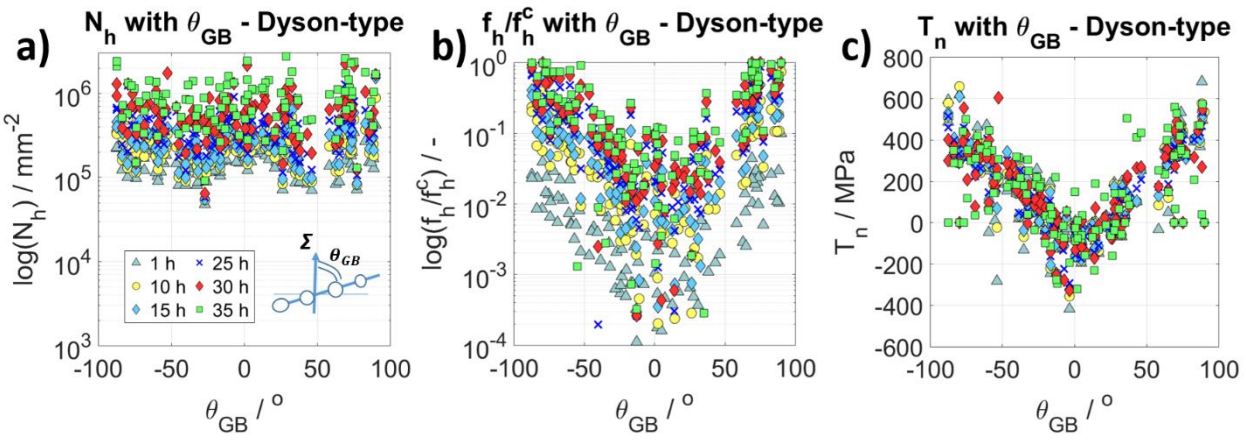


Figure. 7.10. Average a) N_h, b) f_h/f_h^c and c) T_n at different *t* along individual boundaries as a function of boundary orientation to load axis (θ_{GB}), Dyson-type model ($\alpha' = 8.9 \times 10^6\ mm^{-2}$) at Σ=300 MPa.

Another important finding from Fig. 7.10 is that N_h is not a function of θ_{GB} when the Dyson-type model is employed. This does not resemble the general trend in FCC materials from Chapter 6, e.g. [202,217,226], where higher cavity densities are found on boundaries with $\theta_{GB} \approx$ 45-60° as compared to boundaries, transverse to the load axis. The nucleation response is dependent on the local shear strain rate in the vicinity of the boundary ($\dot{\gamma}_{max}$), which in turn depends on the crystallographic orientation of neighboring grains ($\dot{\gamma}_{max}$ varies by a factor of 6 between individual grain boundaries here). This explains the limited variation of N_h with θ_{GB} in Fig. 7.10.a). Boundaries, transverse to the load axis, tend to fail (i.e. $f_h \ / \ f_h^c = 1$) as illustrated in Fig. 7.10.b). These boundaries carry higher normal average tractions, as illustrated in Fig. 7.10.c), and diffusive growth on these boundaries is dominant, leading to cavity coalescence. This is in agreement with the observed distribution of failed facets from [25,105,112,265]. The field variation of N_h and f_h/f_h^c in the polycrystal at failure is examined in Fig. 7.11. When the Dyson-type model is employed, higher cavity densities are found along grain boundaries enclosed by plastically-softer grains with crystallographic orientations closer to the [001]-direction on the IPF, e.g. boundaries 19, 36, 38 in Fig. 7.11. Formation of microcracks is dominant along transverse boundaries, e.g. boundaries 7, 18, 37. At some locations, interlinkage of transverse and inclined facets is observed. This is because the cavity density on the latter is sufficiently high for cavity coalescence to occur at lower values of normal traction along the boundary, T_n. Note that higher normal tractions are found along normal boundaries to the applied load between grains of harder crystallographic orientation (away from [001]-direction). When the Dyson-type model is employed, the cavity number density is lower on such boundaries, but failure, driven by cavity growth due to the higher values of T_n on such boundaries, is observed. This is the case for boundaries 55 and 80.

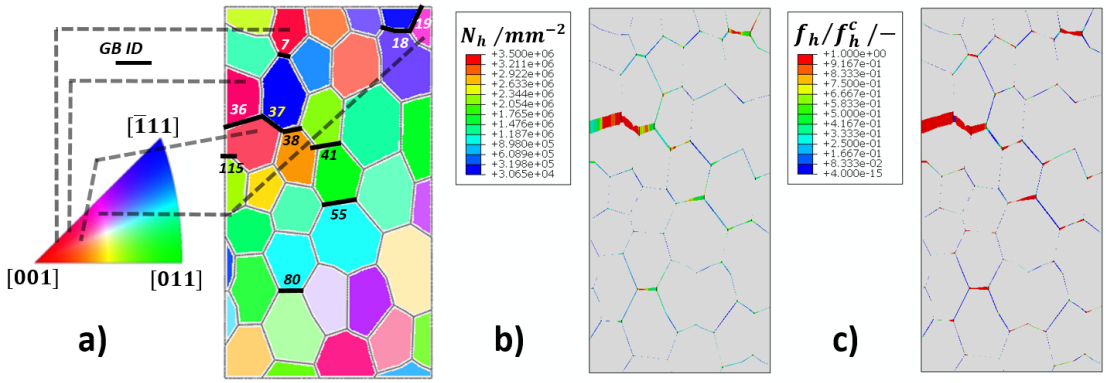


Figure 7.11. a) Crystallographic orientations of grains, enclosing failed boundaries, are illustrated on the IPF (010-direction). Contour plots of b) N_h and c) f_h/f_h^c along boundaries at failure (Dyson-type).

The polycrystalline failure times predicted by the Dyson-type model are shorter than those in bicrystals from Section 7.3.1 for the same value of α'. This disagrees with the trend in experimental creep strength data for Type 316 bi- and polycrystals from Fig. 7.4, where polycrystalline failure times are longer by a factor of 5-10. The model is therefore not applicable to describe intergranular cavitation in both types of aggregates. This is discussed in Section 7.5, where an approach to reach better agreement between bi- and polycrystalline model predictions of t_f is given. The Dyson-type model (Eq. 7.1) is deficient, since the distribution of N_h in the polycrystal is independent of θ_{GB}, and it does not provide further understanding of the nucleation process. The focus of the remaining sections is on the modified classical nucleation theory.

7.4.2. Classical nucleation theory a distribution of particle strengths and maximum stress at particles and diffusive growth

7.4.2.1. Case 1 – Maximum particle stress with $\alpha_n = 1, \alpha_t = \infty$ and $\bar{\tau}_p^{GB}$

The failure response of the 39-grain aggregate is examined here by coupling diffusive growth to the modified classical nucleation theory with T_{nuc} given by Eqs. 7.11-7.12. The case $(\alpha_n = 1, \alpha_t = \infty)$ is evaluated with the distribution of $\log(\mu(f_v), \tilde{\sigma}(f_v)) = (-2.8, 1.3)$ from Section

7.3.3. The macroscopic creep response for Σ = 280-320 MPa in the presence and absence of damage is compared to experimental data in Fig. 7.12. The predicted failure times of 30, 38 and 52 h at Σ = 320, 300 and 280 MPa are ~20 times shorter compared to the experimental response. Similar to findings from Section 7.4.1, this stems from rapid nucleation activity during initial stages of creep. This is supported by the variation of averaged N_h and f_h/f_h^c along the boundaries as a function of θ_{GB} at 300 MPa, examined in Fig. 7.13.a) and b). We find polycrystalline averages of N_h across all boundaries at 1 hour and 30 hours of 8.6×10^4 mm^{-2} and 1.94×10^6 mm^{-2}, respectively. These values are larger by a factor of 10 than the average N_h in the bicrystal from Section 7.3.3 at 1 hour (1.3×10^4 mm^{-2}) and 30 hours (1.9×10^5 mm^{-2}) for Σ = 300 MPa.

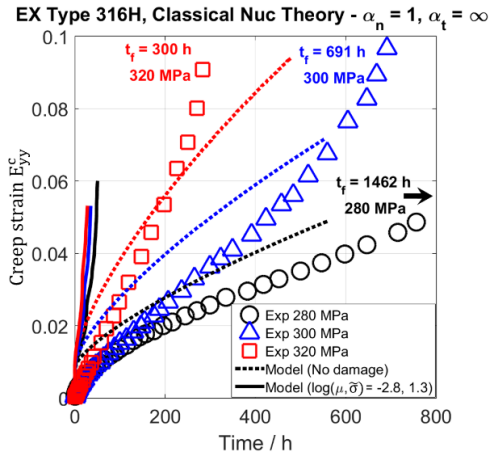


Figure 7.12. Predicted macroscopic creep curves in the absence and presence of intergranular damage, EX Type 316H, 550°C, modified classical nucleation theory with $\alpha_n, \alpha_t = (1.0, \infty)$ and $\log(\mu, \tilde{\sigma}) = -2.8, 1.3$.

The reason is that local concentrations of stress along grain boundaries arise in the polycrystalline aggregate. These stress concentrations increase the tractions carried by individual boundaries, contrary to the isolated boundary in the bicrystal for the same applied stress. At 300 MPa and $\alpha_n, \alpha_t = (1, \infty)$, the average value of $\tau^* = T_n / (d_p / \lambda_p)^2 \sim$ 900 MPa along the bicrystal boundary in Fig. 7.8.b). Along boundaries, normal to the loading direction in the polycrystal with

$\theta_{GB} = \pm 75 \sim 90°$, these values see maxima of up to ~1600 MPa (i.e. $T_n \sim 520 MPa$) in Fig. 7.13.c). The nucleation model of Eq. 7.2 is a function of local stress at particles. As a result, the average cavity number density along individual boundaries in Fig. 7.13.b) follows closely the distribution of τ^* with θ_{GB} from Fig. 7.13.c). The profile of N_h shows higher cavity densities along normal boundaries to the applied load. This disagrees with the expected trend of higher cavity densities on inclined boundaries in FCC materials [202,217,226]. Since cavity densities and average normal boundary tractions are higher on normal boundaries to the applied load, failure is limited to these boundaries (Fig. 7.13.a). Similar to the observations from Section 7.3.3, the magnitude of average $\bar{\tau}_p^{GB}$ along individual boundaries in Fig. 7.13.d) is found lower than τ^* by approx. two orders of magnitude and can be practically ignored. This is further discussed in Section 7.4.2.3.

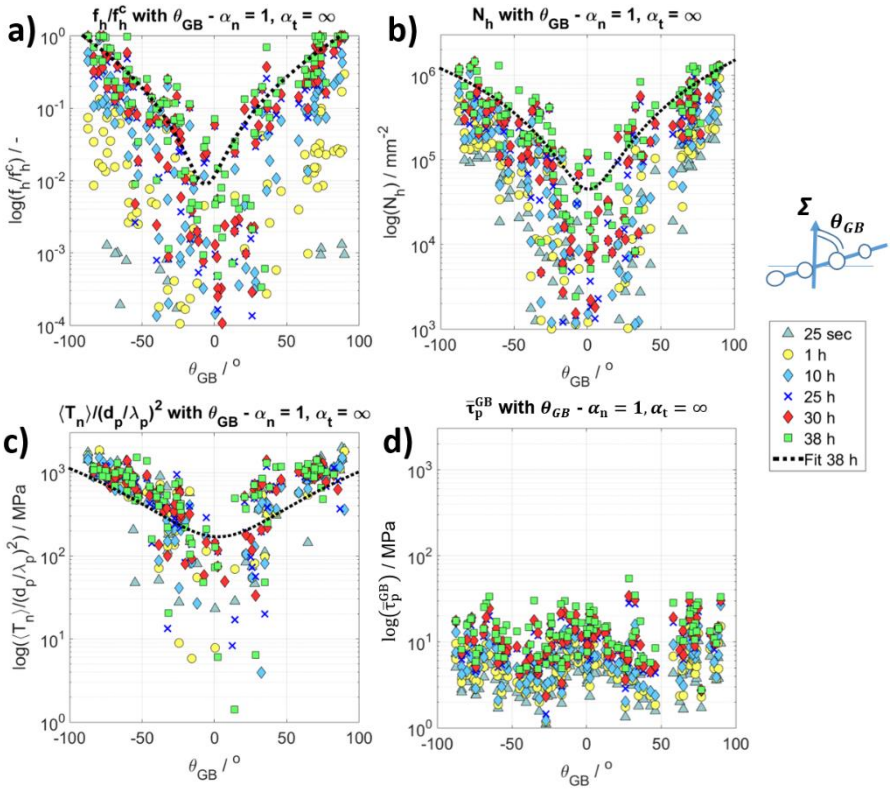


Figure 7.13. Average a) f_h/f_h^c b) N_h, c) $\tau^* = \langle T_n \rangle/\left(d_p/\lambda_p\right)^2$ and d) $\bar{\tau}_p^{GB}$ along boundaries as a function of θ_{GB}, modified classical nucleation theory with $\alpha_n, \alpha_t = (1.0, \infty)$, $\log(\mu, \tilde{\sigma}) = -2.8, 1.3$ at Σ=300 MPa.

The failure morphology for $\alpha_n, \alpha_t = (1.0, \infty)$ is illustrated in Fig. 7.14, where the field variation of N_h and f_h/f_h^c along the boundaries is examined at failure. Contrary to Section 7.4.1, the results from Fig. 7.14 reveal that, when the stress-based nucleation model of Eq. 7.2 is employed, higher cavity densities are found along boundaries enclosed by plastically-harder grains (away from [001]-direction in IPF) which carry higher stresses, e.g. boundaries 18, 41, 80. This is in qualitative agreement with the location of creep cavities along grain boundaries in Type 316L with respect to crystallographic orientations of adjacent grains, reported in [146]. Diffusive growth is again dominant along transverse boundaries, enclosed by harder grains. However, the results from this section reveal that the distribution of N_h with respect to the boundary orientation to the applied load is erroneous when $(\alpha_n = 1, \alpha_t = \infty)$. Hence, it is necessary to assess other assumptions of the coupling between normal and shear tractions at intergranular particles.

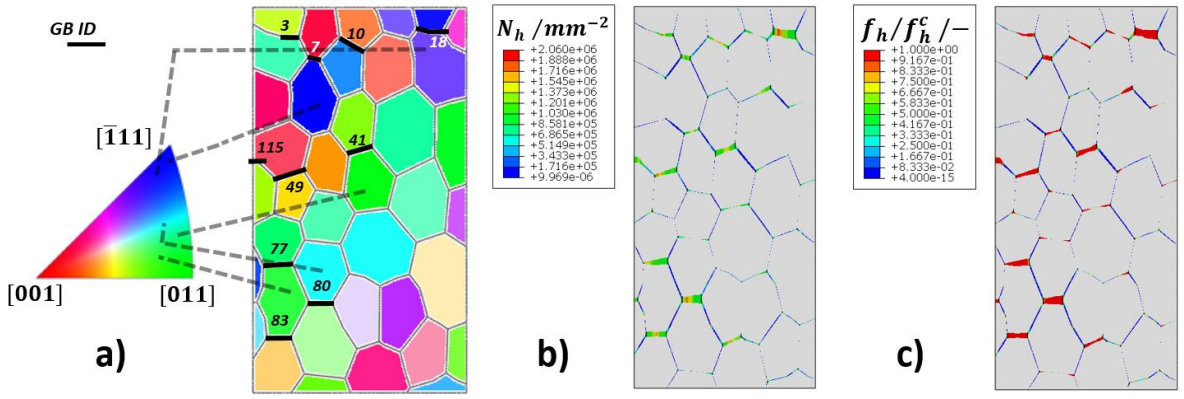


Figure 7.14. a) Crystallographic orientations of grains, enclosing failed boundaries, are illustrated on the IPF (010-direction). Contour plots of b) N_h and c) f_h/f_h^c along boundaries at failure ($\alpha_n, \alpha_t = 1, \infty$).

7.4.2.2. Case 2 – Maximum particle stress with $\alpha_n = \infty, \alpha_t = 1$ and $\bar{\tau}_p^{GB}$

Here, the failure response of the aggregate in the range 280-320 MPa is simulated for the case $(\alpha_n = \infty, \alpha_t = 1)$ when the maximum particle stress is a function of shear tractions only - $\tau^* = T_t / (d_p / \lambda_p)^2$. We find that when the distribution of f_v with $\log(\mu(f_v), \tilde{\sigma}(f_v)) = (-2.8, 1.3)$

from Section 7.3.3 is employed, cavity nucleation along grain boundaries is limited and the macroscopic response is the same as that in the absence of damage. The limited cavitation stems from the magnitude of $T_t/(d_p/\lambda_p)^2$ along boundaries, shown in Fig. 7.15.a). This magnitude is lower by ~2.5 times compared to $T_n/(d_p/\lambda_p)^2$, determined in the previous section. Therefore, when $(\alpha_n=\infty,\alpha_t=1)$ and $\log(\mu(f_v),\tilde{\sigma}(f_v))=(-2.8,1.3)$, the shear tractions along boundaries are not sufficiently high to generate cavity densities which could lead to cavity coalescence and affect the global failure response. This is consistent with observations for the bicrystal from Section 7.3.3. To illustrate an important point, let us assume that the vacancy condensation process is indeed driven by shear tractions only ($\alpha_n=\infty,\alpha_t=1$). A suitable distribution of $f_v(\psi')$ with a lower nucleation barrier (i.e. lower $\mu(f_v)$) for the assumed lower T_{nuc} can be determined to yield an agreement between predicted macroscopic creep response and experimental data. We find that a distribution of $\log(\mu(f_v),\tilde{\sigma}(f_v))$ = (-5.0, 1.4) approximates the experimental data in Fig. 7.15.b).

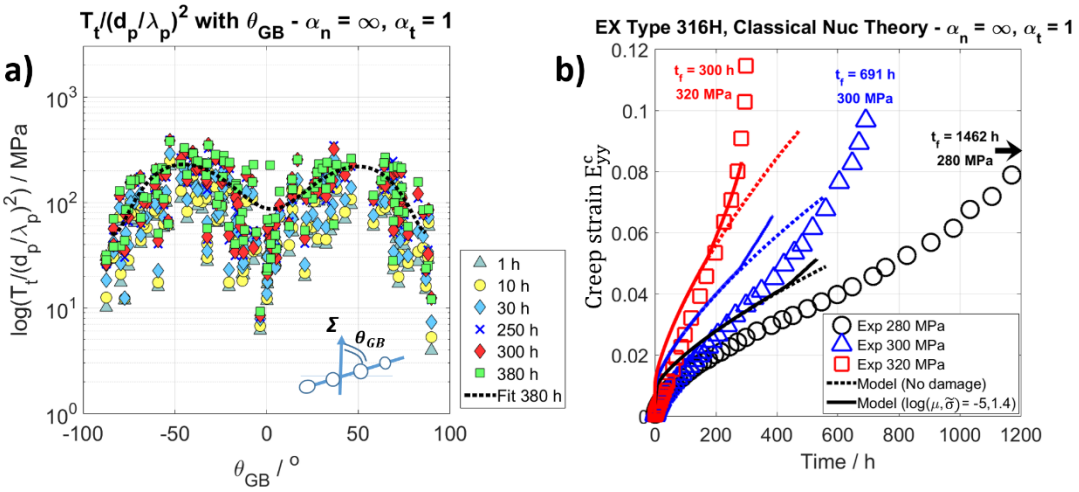


Figure 7.15. a) Average $\tau^* = T_t/(d_p/\lambda_p)^2$ along boundaries with θ_{GB} and b) creep curves in the absence and presence of damage, EX Type 316H at 550°C; $\alpha_n,\alpha_t = (\infty,1)$ and $\log(\mu,\tilde{\sigma})=-5,1.4$.

Examination of predicted distributions of averaged N_h and f_h/f_h^c along individual boundaries in Figs. 7.16.a)-b) reveals that higher cavity densities and damage are accumulated along boundaries inclined at ~45-60° to the applied load. Virtually no cavities nucleate or coalesce on transverse boundaries (N_h <10000 mm^{-2} at $\theta_{gb} = \pm 75 \sim 90°$). The distribution of N_h resembles the profile of $\tau^* = T_t / (d_p / \lambda_p)^2$ from Fig. 7.15.a), where shear tractions are lower on transverse boundaries. The profile of N_h in Fig. 7.16.a) is qualitatively similar to that in FCC materials [202,217,226], but boundaries normal to the applied load remain intact. This disagrees with observations in different grades of Type 316, e.g. [25,112,265]. The distribution of $f_v(\psi')$ with $\log(\mu(f_v), \tilde{\sigma}(f_v))$ =(-5.0,1.4) is also probed in the bicrystal model. It is found that it overpredicts the creep strength at 550°C by a factor of 6 for $(\alpha_n = \infty, \alpha_t = 1)$. This and the preceding sections illustrate that the limiting cases of the coupling between (α_n, α_t) are unable to capture the damage morphology in the material. The following section determines a suitable form of the coupling.

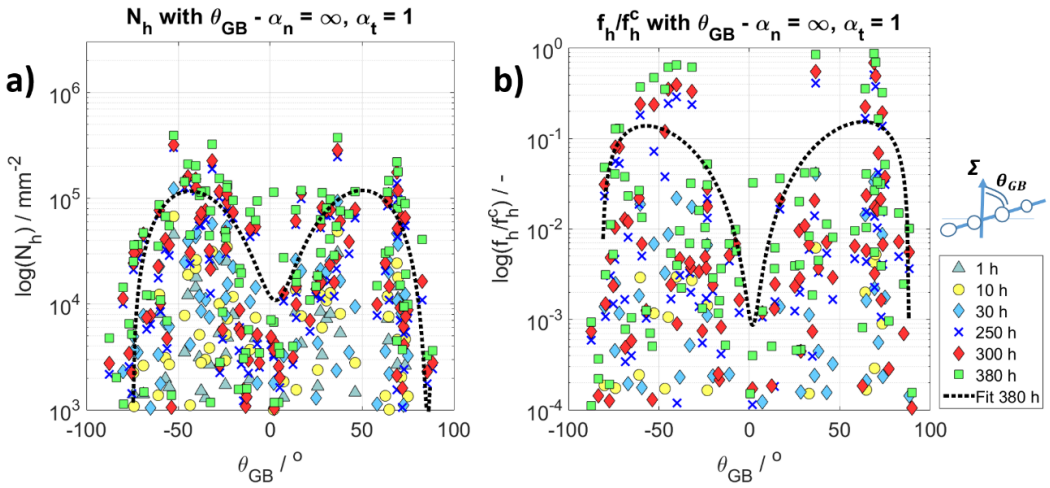


Figure 7.16. Average a) N_h and b) f_h/f_h^c along boundaries as a function of θ_{GB}, modified classical nucleation theory with $\alpha_n, \alpha_t = (\infty, 1)$ and $\log(\mu, \tilde{\sigma}) = (-5, 1.4)$ at Σ=300 MPa.

7.4.2.3. Case 3 – Maximum particle stress with $\alpha_n \neq \infty, \alpha_t \neq \infty$ and $\bar{\tau}_p^{GB}$

In the present section, the failure response of the aggregate is examined using the modified classical nucleation theory for the case $(\alpha_n, \alpha_t) \neq \infty$. The simplest mode of coupling is the case of $\alpha_n, \alpha_t = (1,1)$. The failure response for this set of (α_n, α_t) is identical to the case of $\alpha_n, \alpha_t = (1, \infty)$ from Section 7.4.2.1. This is because the predicted normal tractions along boundaries are ~2 times larger than the shear tractions (see Figs. 7.13.c and 7.15.a) and $T_{nuc} \approx \langle T_n \rangle \Big/ \left(d_p/\lambda_p\right)^2$ for this set of α_n, α_t. Based on the findings from the preceding sections, combinations of parameters in the arbitrary ranges $\alpha_n = 1-2$ and $\alpha_t = 0.25-1$ were examined in this section. This is in an attempt to determine a coupling between tractions, which predicts the highest cavity number densities along inclined boundaries ($\theta_{GB} = \pm 45 \sim 60°$) with lower cavity number densities along transverse boundaries to the applied load ($\theta_{GB} = \pm 75 \sim 90°$). Note that, at present, experimental data for the actual distribution of N_h along boundaries with θ_{GB} in Type 316H are not available. Hence, an arbitrary distribution is assumed, informed qualitatively by results from [202,217,226]. As identified in the preceding section, modification of (α_n, α_t) also requires that the assumed distribution of $f_v(\psi')$ is modified, if the trend in macroscopic creep response is to be captured. The exact fit to experimental data is not of interest here. Difference in failure time within a factor of two is acceptable, due to the scatter in experimental failure data for Type 316H [266]. It is found that, given the assumptions above, the set of parameters $\alpha_n, \alpha_t = (1.5, 0.3)$ and $\log(\mu(f_v), \tilde{\sigma}(f_v))$ = (-2.0, 1.3) captures the general trend in macroscopic creep response of polycrystalline ex-service Type 316H at 550°C in the range 280-320 MPa, as shown in Fig. 7.17. The modelling framework predicts failure times of 283 h, 460 h and 732 h at 320, 300 and 280 MPa, respectively, as compared to experimental failure times of 300 h, 691 h and 1462 h at these stresses.

The predicted distribution of averaged N_h and f_h/f_h^c along individual boundaries is examined in Figs. 7.18.a)-b) at 300 MPa. At 460 h, average cavity number densities of ~4×10^5 mm^{-2} are found along boundaries with $\theta_{GB} = \pm45\sim60°$. These values are higher than cavity number densities of ~2.1×10^5 mm^{-2} along boundaries with $\theta_{GB} = \pm75\sim90°$. The results in Fig. 7.18.b) show that f_h/f_h^c is higher along facets, normal to the load axis with $\theta_{GB} = \pm75\sim90°$.

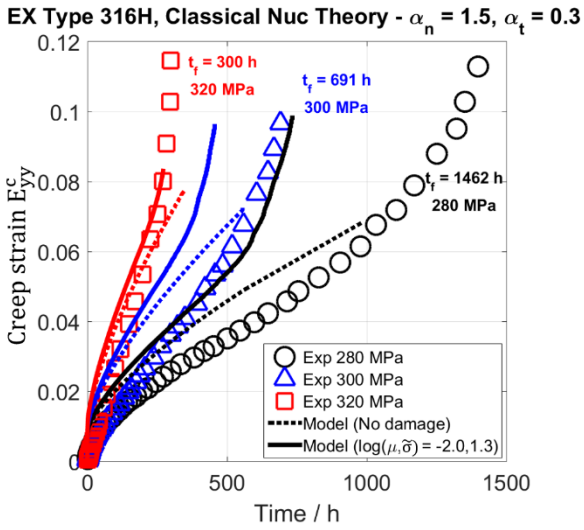


Figure 7.17. Predicted macroscopic creep curves in the absence and presence of damage, EX Type 316H at 550°C, modified classical nucleation theory with $\alpha_n, \alpha_t = (1.5,0.3)$ and $\log(\mu,\tilde{\sigma}) = -2.0,1.3$.

The predicted cavity density profile follows closely the variation of maximum particle stress τ^* with θ_{GB} for the set $\alpha_n, \alpha_t = (1.5, 0.3)$ from Fig. 7.18.c). Note that the cavity number density increases at a lower rate with time, compared to the variation from Fig. 7.13.b) ($\log(\mu(f_v),\tilde{\sigma}(f_v))$ = (-2.8, 1.3) and $\alpha_n = 1, \alpha_t = \infty$). This is because the assumed distribution of $f_v(\psi')$ and coupling between local tractions here result in a lower nucleation rate along grain boundaries. Hence, the continuous nucleation process is more gradual. In Fig. 7.18.d), the averaged accumulated residual stress from prismatic loops, $\overline{\tau}_p^{GB}$, again provides a minor contribution of <10% to T_{nuc}. This finding is in agreement with observations from Section 7.3.3. As discussed,

the simplistic assumption was made in the derivation of Eq. 7.5 that the density of prismatic loops in the vicinity of the boundary is the same as that in the grain bulk. Hence, $\bar{\tau}_p^{GB}$ is determined from equilibrium with the residual matrix stress ($\bar{\tau}_m^r$) due to the presence of loops. Since the stress carried by the matrix is not expected to relax during deformation of the grains, the predicted value of $\bar{\tau}_p^{GB}$ remains low. The importance of this observation is discussed in detail in Section 7.5.

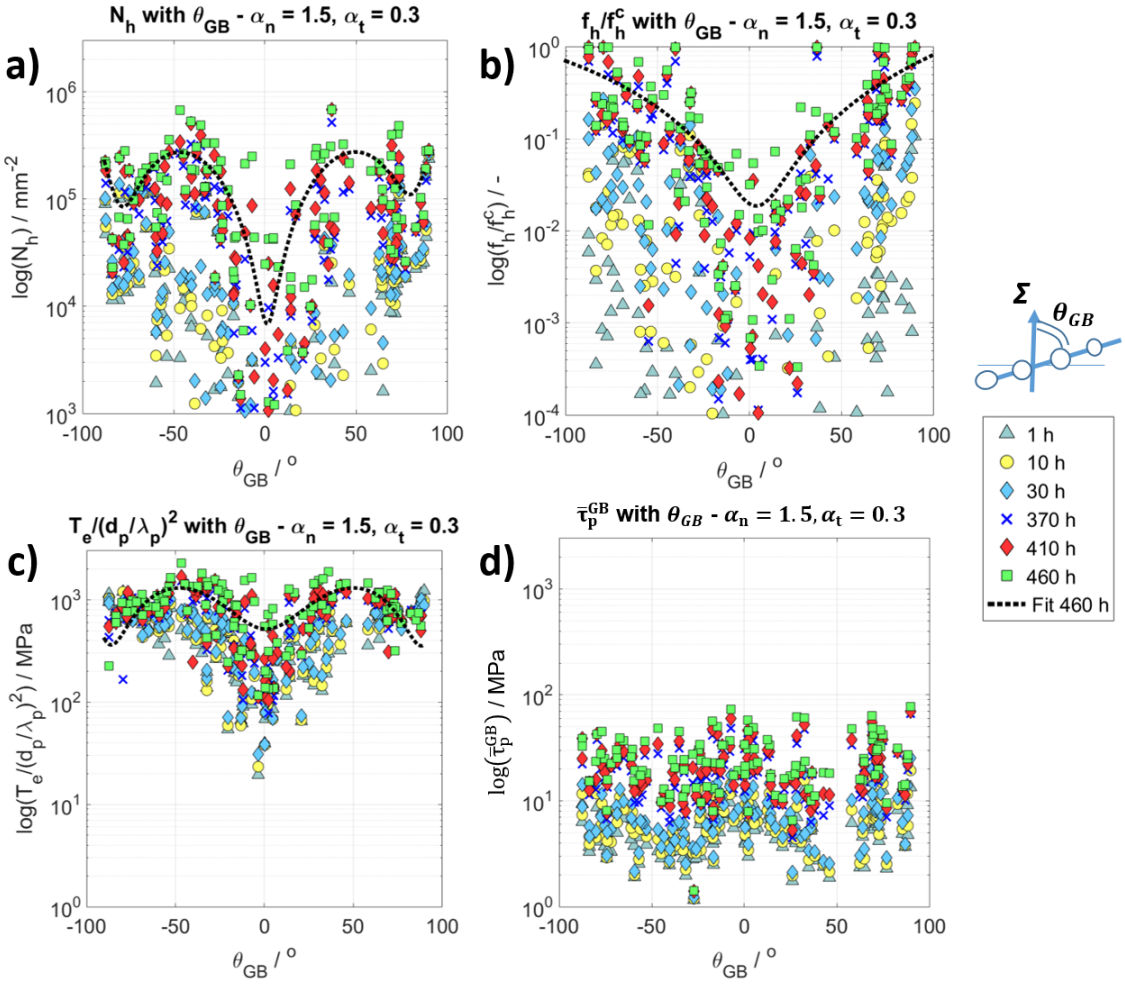


Figure 7.18. Average a) N_h, b) f_h/f_h^c, c) $\tau^* = T_e/(d_p/\lambda_p)^2$ and d) $\bar{\tau}_p^{GB}$ along boundaries as a function of θ_{GB}, modified classical nucleation theory with $\alpha_n, \alpha_t = (1.5, 0.3)$ and $\log(\mu, \tilde{\sigma}) = (-2, 1.3)$ at Σ=300 MPa.

In agreement with findings from Section 7.4.2.1, higher cavity densities and failure are found along grain boundaries between grains with harder crystallographic orientations, away from

the [001]-direction on the IPF in Fig. 7.19. The failure profile from Fig. 7.19 for $\alpha_n, \alpha_t = (1.5, 0.3)$ is a mixture of the predicted profiles for $\alpha_n, \alpha_t = (1, \infty)$ and $\alpha_n, \alpha_t = (\infty, 1)$. Cavity coalescence by diffusive growth is dominant on facets normal to the load direction, e.g. boundaries 18, 83 in Fig. 7.19. Some inclined facets, e.g. boundaries 23 and 43, where sufficiently high number densities of cavities have accumulated, also fail and lead to interlinkage of inclined and normal facets. Note that the facet interlinkage process is a precursor for microcrack formation in Type 316H [236].

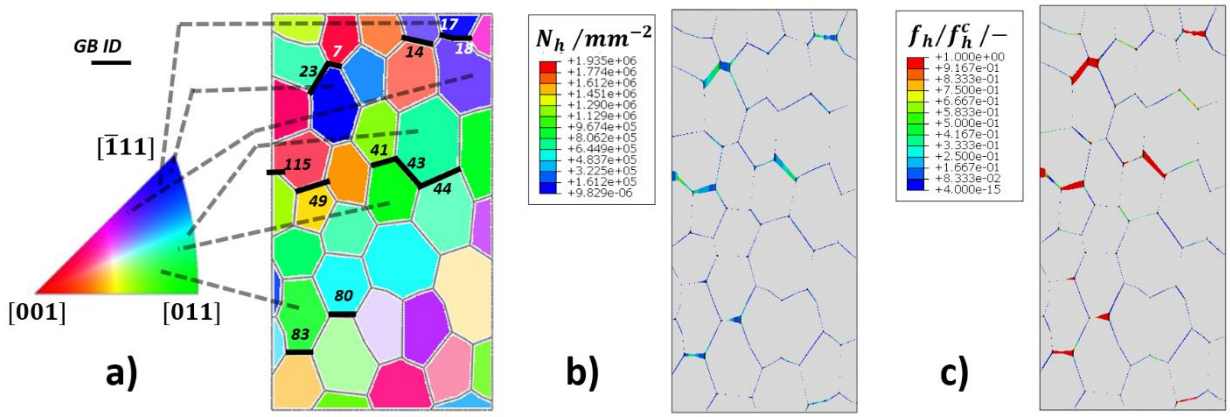


Figure 7.19. a) Crystallographic orientations of grains, enclosing failed boundaries, are illustrated on the IPF (010-direction). Contour plots of b) N_h and c) f_h/f_h^c along boundaries at failure ($\alpha_n, \alpha_t = 1.5, 0.3$).

To further illustrate this, the evolution of average damage fraction f_h/f_h^c, cavity number density N_h and normal boundary traction T_n with time along selected grain boundaries is examined in Fig. 7.20 at 300 MPa for $\alpha_n, \alpha_t = (1.5, 0.3)$. In Fig. 7.20.b), N_h along normal boundaries to the load direction (boundaries 7,18,83 with $\theta_{GB} = \pm 75 \sim 90°$) do not increase rapidly at t > 100 h and cavity coalescence is driven by diffusive growth due to the high normal tractions on these boundaries (Fig. 7.20.c). Along boundaries 23 and 43 ($\theta_{GB} = \pm 45 \sim 60°$), the normal traction is lower, but the nucleation rate is higher. The development of damage along boundaries 23 and 43 in Fig. 7.20.a) is correlated with the evolution and higher values of N_h along these boundaries in Fig. 7.20.b). This allows coalescence at the lower values of T_n on these inclined boundaries. Note

that at failure, the stress carried by the failed boundaries reduced to zero. In Fig. 7.20.c), the tractions from failed boundaries 7, 18, 23 and 49 is redistributed to boundaries in the polycrystal, which are intact, e.g. boundaries 14, 17, 41 and 44. In turn, nucleation and diffusive growth accelerates on the latter boundaries, as seen on Figs. 7.20.a-b).

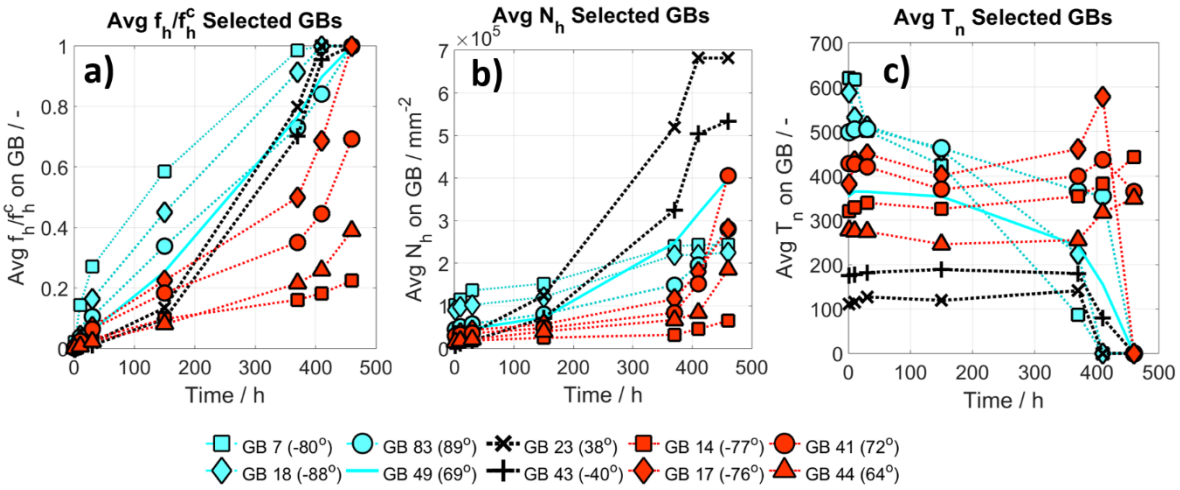


Figure 7.20. Average a) f_h/f_h^c, b) N_h and c) T_n on selected boundaries with time, modified classical nucleation theory with $\alpha_n, \alpha_t = (1.5, 0.3)$ and $\log(\mu, \tilde{\sigma}) = -2, 1.3$ at Σ=300 MPa. N.B. θ_{GB} in brackets.

The progressive failure and stress redistribution process causes an increase in stress within non-damaged grain regions. The stress redistribution process is illustrated in Fig. 7.21.a-c), where the variation of axial stress in the grains at Σ=300 MPa and $\alpha_n, \alpha_t = (1.5, 0.3)$ is plotted at different times. It is found that the increase in stress causes faster creep rates in non-damaged regions of the aggregate. Here, we find that the accelerated creep rate in the grains due to this stress redistribution process constitutes ~96% of the increasing macroscopic creep rate during tertiary creep.

In Figs. 7.21.d-e), examples of deformed configurations at triple lines for failed inclined and transverse boundaries are shown. Artificial voids between interface elements on intersecting boundaries are not formed. Any inelastic opening due to damage is accommodated primarily by deformation of the surrounding matrix and less so by sliding along adjacent boundaries, since only

the limited elastic component of tangential separation is allowed ($\dot{\delta}_{0t} \rightarrow 0$). Model predictions demonstrate that, when the surrounding matrix accommodates inelastic opening along the boundary in the absence of grain-boundary sliding, failure along a boundary causes redistribution of local stresses to the intersections with adjacent boundaries. As a result, tractions along adjacent boundaries in the vicinity of triple junctions increase and failure along the latter also takes place (Fig. 7.21.e). It is found that removal of the constraint in these scenarios does not change the local solution. However, it is important to assess the effects of the triple line constraint in future studies where grain-boundary sliding is pronounced, as this could modify the local damage field.

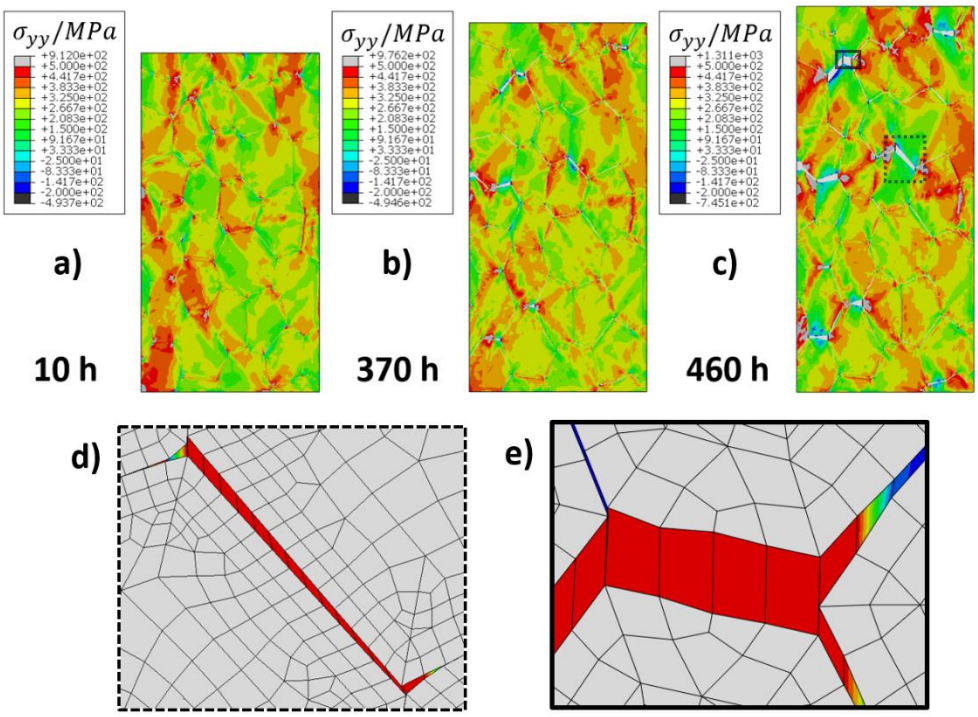


Figure 7.21. Contour plot of axial stress σ_{yy} at a) 10 h, b) 370 h and c) 460 h (at failure); $\alpha_n, \alpha_t = (1.5, 0.3)$ and $\log(\mu, \tilde{\sigma}) = (-2, 1.3)$ at Σ=300 MPa. In d) and e), examples of deformed configuration at selected triple lines at failed inclined and transverse boundaries are presented.

The constraint at the triple junction is implemented here for consistency of the computational method. In Chapter 5, the opening of the boundaries due to damage was prevented

and the constraint was only defined in terms of the sliding displacement components. The local solution in this case is highly-constrained. As discussed, in realistic materials, local diffusive processes can relax the associated stress concentrations. An additional local mechanism is considered in this chapter, associated with opening of the boundary due to diffusive growth and the constraint is modified. In realistic materials, the associated diffusive plating on the boundary due to growth will modify further the local diffusive accommodation mechanisms at the triple junctions, discussed in Section 5.3.3. This is not considered further in this thesis and is identified as future work for this study.

Note that the distribution of $f_v(\psi')$ and set of (α_n, α_t) are arbitrarily selected in this section. It is important to examine the creep strength of the bicrystal from Section 7.3.3 at 550°C with the set $\alpha_n = 1.5, \alpha_t = 0.3;\ \log(\mu(f_v), \tilde{\sigma}(f_v)) = (-2.0, 1.3)$. With this set of parameters, the predicted failure times for the ex-service Type 316H bicrystal are 1070 h, 683 h and 423 h at 280, 300 and 320 MPa, respectively. As shown in Fig. 7.22.a), these failure times are longer by a factor of 1.5, compared to failure times for the polycrystalline material in Fig. 7.17, and by a factor of 5, compared to the reference bicrystal $t_f - \Sigma$ response at 550°C for $\alpha' = 8.9 \times 10^6 mm^{-2}$. A distribution of $f_v(\psi')$ with $\log(\mu(f_v), \tilde{\sigma}(f_v)) = (-3.6, 1.3)$ (Fig. 7.22.b) is needed to capture the reference creep strength response of the bicrystal for the assumed coupling of $\alpha_n, \alpha_t = (1.5, 0.3)$ in Fig. 7.22.a).

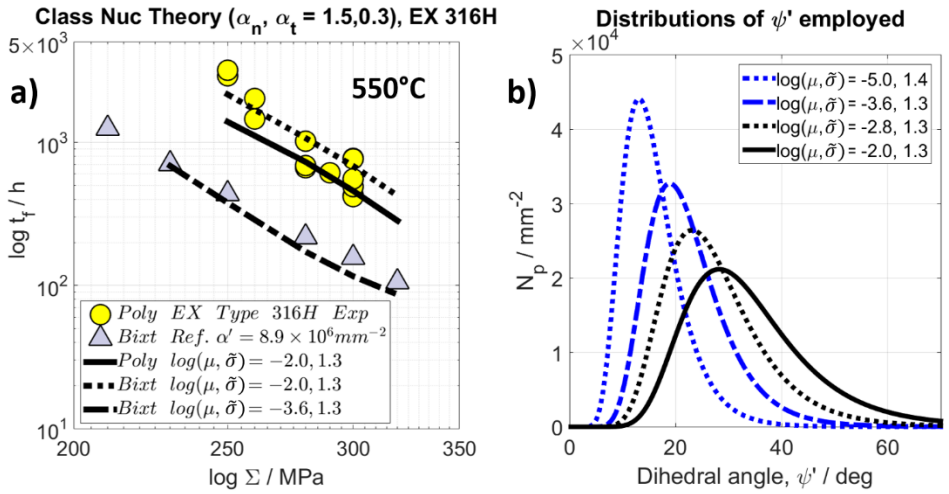


Figure 7.22. a) Predicted creep strength of bi- and polycrystalline EX Type 316H (550°C), classical nucleation theory for $\alpha_n, \alpha_t = (1.5, 0.3)$ and employed distributions of $f_v(\psi')$, shown in b).

This indicates that physical phenomena are missing from the nucleation model of Eq. 7.2, since the failure response of both bi- and polycrystalline samples is not captured simultaneously with the assumed distribution of $f_v(\psi')$ and coupling of (α_n, α_t). This is discussed in Section 7.5. Aspects of the determined coupling between boundary tractions, associated with the local stress state in the vicinity of the boundary, are discussed in the following section.

7.4.2.4. Resultant traction and local stress state in the vicinity of grain boundaries

Modelling the polycrystalline creep failure response via the multi-scale modelling framework in Section 7.4.2 allows the interpretation of local stress, driving the vacancy condensation process ($T_{nuc} \approx \tau^*, \bar{\tau}_p^{GB} << \tau^*$), in terms of the stress state in the grain near the grain boundary. According to Section 7.2.3, the angle between the resultant traction at particles T_e and the boundary plane is $\kappa = \tan^{-1}\left((T_n / \alpha_n)/(T_t / \alpha_t)\right)$. The angle κ is extracted for selected boundaries, with average cavity densities >10^5 mm^{-2} at t/t_f = 0.75, from the polycrystalline simulation results for i) $\alpha_n = 1, \alpha_t = \infty$, ii) $\alpha_n = \infty, \alpha_t = 1$ and iii) $\alpha_n = 1.5, \alpha_t = 0.3$ in Fig. 7.23. The angle β_I between the boundary plane

and the direction of local maximum principal stress (σ_I), averaged for the selected boundaries, is extracted from a row of continuum elements, either side of a boundary, and compared to κ.

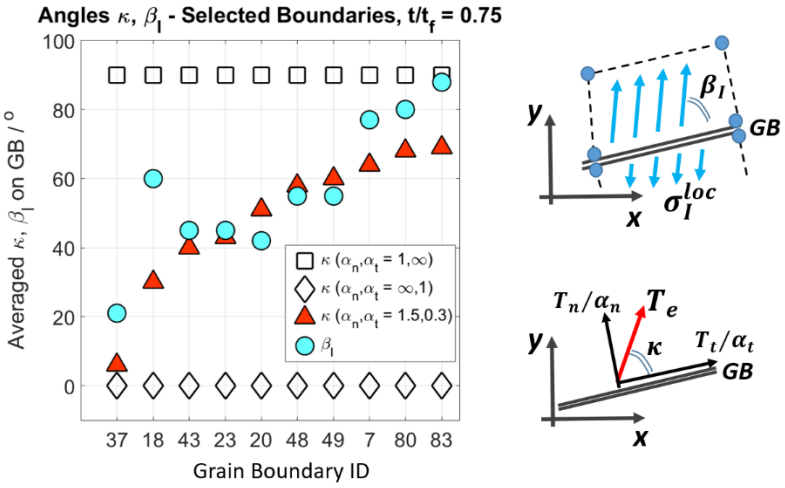


Figure 7.23. Directions of maximum resultant traction at particles (κ) and of maximum principal stress (β_I) to the boundary plane of selected facets for different coupling of α_n, α_t.

In cases i) and ii), the angle κ takes values of 90° and 0° to the boundary plane, respectively. In iii), the angle κ varies between the examined boundaries. It is found that for α_n, α_t = (1.5, 0.3), the direction of the resultant traction at particles (κ) nearly coincides with the orientation of the local maximum principal stress in the lattice with respect to the boundary (β_I), as shown in Fig. 7.23. The same observation is made in the bicrystal sample for $(\alpha_n = 1.5, \alpha_t = 0.3)$, where $\kappa \approx 73°$ and $\beta_I \approx 80°$. The importance of this finding is discussed in Section 7.5.1.

7.5. DISCUSSION

7.5.1. Suitability of examined cavity nucleation models

The Dyson-type model of Eq. 7.1 was employed along grain boundaries as a function of the maximum resolved shear strain rate near a boundary. The model was calibrated to bicrystal Type 316 stainless steel creep strength data at 700°C with $\alpha' = 8.9 \times 10^6\ mm^{-2}$ for the nucleation

constant and used to predict failure in ex-service (EX) Type 316H bicrystals at 550°C. The calibrated model was then used to simulate the intergranular creep failure in polycrystalline EX Type 316H. The predicted distribution of cavity number density (N_h) in the polycrystal was independent of boundary orientation to the load axis. This does not resemble the trend in FCC materials, which develop higher N_h on inclined boundaries [202]. The predicted macroscopic t_f for the polycrystal were shorter by a factor of 22, compared to experimental data. The discrepancy stems from the calibration of the bicrystal deformation response to experimental polycrystalline creep data. The stress and strain fields are uniform within the bicrystal grains, whereas localization of stress and strain in the polycrystal results in faster nucleation rates for the same macroscopic creep rate. Hence, calibration of bi- and polycrystalline deformation responses to the same set of creep data will result in discrepancy between polycrystalline predictions of t_f and experimental data, if α' is calibrated from the bicrystal response. The bicrystal CPFE model should employ parameters, calibrated from a polycrystalline-model fit to polycrystalline data. According to Table 7.1, this would cause the bicrystal to creep faster. A lower value of α' would be calibrated from the bicrystal response, bringing polycrystalline model predictions closer to experimental data. Values of $\alpha' < 8.9 \times 10^6\ mm^{-2}$ for Type 316 are closer to experimentally-recorded values of $6 \times 10^5\ mm^{-2}$ [232], and $2 \times 10^5\ mm^{-2}$ estimated by Eq. 6.2 [119]. Nevertheless, the Dyson-type model does not explain the physical process of cavity nucleation, nor does it predict the distribution of cavities with respect to boundary orientations to the load axis. Hence, this empirical model cannot provide insights into the sensitivity of failure to microstructural features.

The modified classical nucleation theory could provide insights on the sensitivity of cavity nucleation to local stress fields and morphology of nucleation sites. In Sections 7.3.2 and 7.3.3, it was demonstrated that the creep strength of bicrystals of Type 316 at 700°C and ex-service Type

316H at 550°C is captured when a log-normal distributions of cavity/particle geometries of different dihedral angles is assumed at a material point along the boundary. The incorporation of a distribution of nucleation sites allows the continuous nucleation process along an isolated boundary to be captured by this stress-based mechanistic nucleation model. The stress T_{nuc} driving the vacancy condensation process is determined by contributions from normal and shear tractions at intergranular particles, coupled by the parameters α_n and α_t. Various sets of (α_n, α_t) were probed in bi- and polycrystalline samples of ex-service Type 316H at 550°C. A unique set of $\alpha_n, \alpha_t = (1.5, 0.3)$ was found to predict an arbitrary distribution of N_h along grain boundaries in the polycrystal. This resembles the experimentally observed trends in FCC materials, with higher values of N_h along inclined facets at 45-60° and dominant cavity coalescence along transverse facets at 90° to the applied load. This is not the case in the limits $\alpha_n, \alpha_t = (1, \infty)$ and $\alpha_n, \alpha_t = (\infty, 1)$, where both nucleation and failure are concentrated to only transverse or only inclined boundaries, respectively. An important finding is that the orientation of the resultant traction at intergranular particles with respect to the boundary for $\alpha_n, \alpha_t = (1.5, 0.3)$ coincides with the direction of maximum principal stress in the vicinity of the boundary. This suggests that the maximum principal stress near the boundaries determines the coupling of local tractions at nucleation sites and controls the nucleation process. The link between cavity nucleation and maximum principal stress is in qualitative agreement with observations by Cane and Middleton [267] in low-alloy steels at 565°C. A residual stress $\bar{\tau}_p^{GB}$ due to the presence of prismatic dislocation loops near intergranular particles was assumed to add another contribution to T_{nuc}. The contribution from $\bar{\tau}_p^{GB}$ to T_{nuc} was minimal where predicted average values of $\bar{\tau}_p^{GB}$ along boundaries were of the order of $0.08T_{nuc}$. This aspect is discussed in Section 7.5.2.

Predicted boundary tractions and local particle stresses are larger than the global applied stress. Higher stresses along boundaries and particles allow distributions of nucleated cavity/particle geometries with mean dihedral angles of 15-30° to be employed. The predicted nucleated cavity profiles with $\psi' > 15°$ are closer to the lenticular profiles of newly-nucleated cavities hypothesised in [237]. Experimental observations of cavity geometries in the early stages of nucleation in Type 316 are needed to confirm this hypothesis. Note that the distribution with $\log(\mu(f_v), \tilde{\sigma}(f_v))$ = (-2,1.3) employed in the polycrystal at 550°C for $\alpha_n, \alpha_t = (1.5, 0.3)$, yielding an agreement with macroscopic creep failure data, is different from the distribution found to predict the bicrystal failure response for the same α_n, α_t. Furthermore, the distribution of $f_v(\psi')$ which captures the trend in creep strength of the bicrystal at 550°C in Section 7.3.2 is able to capture the response at 700°C only when the surface energy γ_s is reduced from 2.0 J/m^2 to 0.8 J/m^2. These discrepancies highlight missing features in the model, discussed in Section 7.5.2.

The boundary conditions (BC) of the bicrystal cell from Section 7.3 enforce the cell faces to remain straight. The predictions of macroscopic $t_f - \Sigma$ using this simple BC were compared to the case when PBC are imposed. A difference in t_f by a factor of ~1.7 for the same set of damage parameters was found. Note that the crystals either side of the grain boundary are anisotropic. When the sides of the cell remain straight, the crystals do not deform compatibly and the internal constraint within the grains causes variation of local stress and strain at the boundary (e.g. Fig. 7.8). On the other hand, the internal constraint is weaker when PBC are employed. The variation of local stress along the boundary is reduced and the cell deformation response is more creep-compliant. Although not presented, it is found that, for the same set of nucleation model parameters, the predicted nucleation rates by the Dyson-type model (Eq. 7.1) are higher and failure is faster when PBC are employed. Conversely, the nucleation rates predicted by the stress-based nucleation

model (Eq. 7.2) are lower and failure times are longer with adopted PBC. When PBC are employed, the calibrated nucleation model parameters in Section 7.3 need to be changed by less than a factor of 2 in order to capture the trend in creep strength data of the bicrystal (e.g. $\log(\mu, \tilde{\sigma})$ = (-2.8,1.3) (no PBC) changes to $\log(\mu, \tilde{\sigma})$ = (-3.1,1.3) (PBC), and $\alpha' = 8 \times 10^6 mm^{-2}$ (no PBC) changes to $\alpha' = 4.5 \times 10^6 mm^{-2}$ (PBC)). This supports the argument that the adoption of PBC will have limited effect on the global response of the bicrystal. However, due to the reduced variation in local stress and strain when PBC are employed, the distribution of N_h and f_c along the boundary is spatially periodic and, therefore, more realistic. In future studies, when modelling and experimental results for cavity morphology along bicrystal boundaries are compared, PBC should be imposed to the bicrystal cell. Further discussion is outside the scope of this thesis.

7.5.2. Missing features in mechanistic nucleation model and approach

Individual grain boundaries have different misorientations, which are a function of the crystallographic orientation of grains on either side of the boundary. The surface energy, boundary diffusivity [198] and particle shapes [221] will vary along boundaries of different misorientations. The variation of properties and particle morphology (i.e. distribution of $f_v(\psi')$, where ψ' is interpreted as a function of the grain-boundary and particle/matrix interface energies [9]) due to different boundary misorientations will affect the nucleation response on individual boundaries. This is confirmed by Slater et al. [217] and Pommier et al. [146] who found that boundaries with misorientations of 25-55° are prone to cavity formation in Type 316. Furthermore, the presence of impurities (e.g. phosphorus) or other phases (e.g. σ) will modify the surface energy and diffusivity along the boundaries [121,122]. These local features are not considered in the modified classical nucleation model. Note that the effect of boundary misorientations would be more pronounced in bicrystal geometries, since macroscopic failure in the bicrystal is dominated by the response of the

boundary. This is contrary to the polycrystalline behaviour, where failure is dependent on the stress redistribution process between failed and uncavitated regions, as discussed in Section 7.4.2.3. Hence, interpreting the distribution of $f_v(\psi')$ as a function of boundary misorientations could explain the difference in determined $\log(\mu(f_v), \tilde{\sigma}(f_v))$ for bi- and polycrystalline samples.

The residual stress due to prismatic loops in the vicinity of intergranular particles $\bar{\tau}_p^{GB}$ is estimated here from equilibrium considerations with the residual stress due to loops in the matrix, $\bar{\tau}_m^r$, obtained by the grain deformation model. The stress $\bar{\tau}_m^r$ is not fully relaxed during creep since the lattice continues to carry stresses, which drive the deformation. Therefore, the value of $\bar{\tau}_p^{GB}$ is not expected to be large, which is evident from the model predictions in Sections 7.3-7.4. Note that the prismatic loops, considered to affect the nucleation response, are already captured in the deformation model and are an idealisation of possible dislocation features near grain boundaries. At present, detailed information about the dislocation features at intergranular particles in Type 316/316H is not available and experimental studies are needed to identify their nature and evolution during creep. This would allow better models in the form of Eq. 7.5 to be derived in order to estimate the local stresses at possible cavity nucleation sites as a function of localised deformation features (e.g. slip activity, geometrically-necessary dislocations, prismatic loops, pile-ups). Implementation of such models at grain boundaries requires careful consideration of equilibrium between the residual stress due to dislocation features, the applied load and stress redistribution processes between particle and matrix regions. In addition, the energy of dislocations in the vicinity of particles, providing an additional energy term to the exponential in the nucleation theory of Eq. 7.2, needs to be considered, as discussed by He and Sandstrom [119] and Lim [268].

Another aspect of the creep cavitation process, which is not considered in the present model, is cavity sintering [269]. Compressive normal tractions along some boundaries will result in cavity

sintering or reduction of cavity number density, which will alter some of the predicted cavity distributions in the polycrystalline aggregate in Section 7.4. Grain-boundary sliding is also not considered in this chapter with the aim to isolate solely the effect of damage on deformation response. In Chapter 5, it was found that the stress along transverse boundaries increases by <3% in Type 316 for the limited amount of sliding in this material. This suggests that cavity nucleation and growth along transverse facets, predicted in Section 7.4, will be accelerated and the coupling between α_n and α_t will be altered when grain boundaries slide relative to each other.

The discussion identified a number of features of the cavity nucleation process, which need to be considered in mechanistic nucleation models. Capturing these features could provide insights into the dependence of nucleation rate on inelastic strain rate and the physical processes of cavity formation. The modelling framework developed in this study can serve as a tool to incorporate these features and explore their effect on creep damage. Based on the modelling work from this chapter, aspects of the nucleation process, which need to be examined experimentally in order to support the future development of mechanistic nucleation models, are given in Chapter 8.

7.6. SUMMARY

In this chapter, two models for creep cavity nucleation, introduced in Chapter 6 and coupled to diffusive growth, were employed locally along grain boundaries within a multi-scale CPFE-interface element framework. The ability of these nucleation models to capture the trends in macroscopic failure response of bicrystals and polycrystalline samples of Type 316H stainless steel, as well as the damage morphology with respect to grain-boundary orientation to the applied load in the latter geometry, was evaluated. The empirical Dyson-type nucleation model as a function of resolved shear strain rate was calibrated to the trend in creep strength of bicrystals of

Type 316 stainless steel at 700°C. Then, the bicrystal failure response was extrapolated within the temperature range 525-700°C. Employing the calibrated Dyson-type model for the polycrystalline geometry did not capture the expected distribution of higher cavity densities on inclined boundaries to the applied load. Due to its empirical nature, the Dyson-type model does not provide further understanding of the physical process of cavity nucleation and emphasis was put on the mechanistic classical nucleation theory. The modified classical nucleation theory, considering a log-normal distribution of cavity/particle geometries (distribution of $f_v(\psi')$), captures the trend in bicrystal creep strength of the material. Contrary to the instantaneous nucleation of cavities at all possible sites, predicted by the original form of the classical nucleation theory, continuous nucleation is predicted along an isolated boundary when a distribution of $f_v(\psi')$ is incorporated in the model. When the modified classical nucleation theory is used to describe the nucleation process, higher cavity densities are found along boundaries enclosed by grains of plastically-harder crystallographic orientations, carrying higher stresses. This is in qualitative agreement with experimental observations in Type 316. Furthermore, when the maximum stress at intergranular particles is assumed to drive the vacancy condensation process, the newly-nucleated cavities assume lenticular shapes, closer to the geometry of cavities during the early stages of nucleation and growth, hypothesised in the literature. The local maximum stress at particles is represented by a resultant traction, determined by coupling of the shear and normal tractions along a boundary by the parameters α_n and α_t. A set of (α_n, α_t) is found, which predicts an arbitrarily assumed damage morphology in the polycrystal with higher cavity number densities along inclined boundaries and dominant coalescence on boundaries, normal to the applied load. The direction of the resultant maximum traction at particles with respect to the boundary plane coincides with the direction of local maximum principal stress in the vicinity of boundaries. This suggests that the

vacancy condensation process for nucleation is associated with the maximum principal stress, which determines the coupling between normal and shear tractions. Although the modified classical nucleation theory describes the general trend in intergranular creep failure in Type 316, different distributions of $f_v(\psi')$ were found to capture the trend in failure responses in bi- and polycrystalline aggregates. This discrepancy indicates missing features in the modified classical nucleation theory. Further work is required to incorporate the effects of boundary misorientations, impurities, and faceted cavity and particle shapes on the nucleation process. The increase in local stress and additional strain energy at intergranular particles due to presence of local dislocation features needs to be incorporated within the nucleation model. Based on findings from this chapter, key aspects of the nucleation process, which need to be examined experimentally in order to inform future development of a unified mechanistic nucleation model, are given in Chapter 8.

CHAPTER 8

CONCLUSIONS AND FUTURE WORK

8.1. OVERALL CONCLUSIONS

The present study improves the understanding of the high-temperature response of Type 316H stainless steel through the development of mechanistic models capturing the essential physics of creep deformation and damage. This provides guidelines for improvement of deformation models and damage assessment approaches, employed in industry. The predictive capabilities of an existing micromechanical model for inelastic deformation within a self-consistent model (SCM) were enhanced to capture cyclic deformation and stress relaxation. Modelling results via the enhanced framework provide further insights into the evolution of deformation of Type 316H under creep-cyclic loading histories, representative of high-temperature plant components, with respect to the evolution of microstructure and internal residual stress state. Modelling results serve to develop interpolation frameworks for the variation of inelastic material behaviour, which can be used to inform assessment procedures in industry to more accurately account for the accumulation of inelastic strain and damage. The developed SCM is a suitable framework to describe the macroscopic deformation response of the material, but it does not capture local concentrations of stress and strain, which are of importance to the accumulation of intergranular damage. To address this, a crystal plasticity finite element (CPFE) model was developed. It employs the same micromechanical model and predicts the same macroscopic response as the SCM. However, the CPFE framework captures localization effects and is identified as a model which can be extended to capture the deformation and failure response of grain boundaries. A combined CPFE-interface element framework is developed and initially employed to evaluate the

effects of grain-boundary sliding on the deformation response. Model predictions suggest that the effects of grain-boundary sliding on the macroscopic response of the material of interest are limited. Important features of the local stress and strain fields in the vicinity of boundaries are described by the CPFE-interface element framework, making it an ideal candidate to explore the sensitivity of the deformation response on intergranular cavity nucleation and growth. Intergranular cavitation in Type 316H is controlled by cavity nucleation, which is not fully understood. In order to provide further insights into the physics of the nucleation process, as well as guidelines for development of robust nucleation theories, the existing nucleation models in the literature were modified in this study. The modifications were based on considering a range of experimental observations of cavity nucleation in Type 316/316H, and employing the models locally within the developed multi-scale CPFE-interface element framework. The examined Dyson-type model as a function of local inelastic strain rate is deficient. This is because the model does not capture correctly the distribution of cavities in the microstructure and does not explain the physical nature of the nucleation process. By contrast, the modified classical nucleation theory employs a log-normal distribution of cavity/particle geometries of different dihedral angles and considers the on-average local stress state at intergranular particles. This model is able to capture both the macroscopic failure response, and trends in distribution of cavities and failure in the microstructure. This modified mechanistic model provides insights into the sensitivity of the nucleation response to local stress state and intergranular particle morphology. However, a number of missing features are identified in the model, associated with boundary misorientations and dislocation features in the vicinity of intergranular particles. These features need to be incorporated in future mechanistic intergranular cavitation models. Finally, although focus here is on grades of Type 316 stainless steels, the findings and developed methodologies are applicable to a range of engineering alloys.

8.2. FUTURE WORK

8.2.1. Enhancement of micromechanical deformation models

A number of components in high-temperature power plants operate at temperatures of 500-600°C and stresses <100 MPa. Under these thermo-mechanical operating conditions, the dislocation climb mobility over intragranular second-phase particles becomes dominant over dislocation thermal glide in Type 316 [90]. The coupling between dislocation glide and climb and the shift in characteristic plasticity mechanism with reduction in stress is not considered in the present study. It is important to incorporate the effects of dislocation climb over particles within the existing micromechanical deformation model. This will allow the framework to describe cyclic-creep interactions in Type 316H at this very-low-stress/high-temperature regime. Note that mechanistic models for dislocation climb activity over intragranular particles, driven by dislocation core diffusion, can be found in [6] and approaches to coupling the thermal glide and climb mechanisms are discussed in [270]. Diffusion-driven creep deformation is also of importance at this very-low-stress regime and should be incorporated within the models, if the modelling framework is employed to describe the deformation response at these operating conditions.

Another important feature of the deformation process, which is not considered in this study, is dislocation cell formation during cyclic loading. Experimental observations in aged Type 316/316H suggested that dislocation cell formation is not pronounced at <625°C. Hence, the assumed model for dynamic recovery from Chapter 3 only considers the statistical process of dislocation dipole annihilation during cyclic plasticity. Application of the modelling framework to describe deformation of solution-treated Type 316/316H at temperatures >625°C or of pure metals, such as copper (Cu), where cell formation during cyclic loading could be pronounced, would

require the incorporation of cell formation effects. Dislocation cell formation results in mobile dislocation entrapment in cell-like structures within the grains, generating internal residual stresses between cells themselves. The cells provide additional obstacles to other mobile dislocations. Note that the evolution of dislocation-junction obstacle density considering i) the accumulated microscopic residual stress between cell structures of high dislocation density and ii) the reduction of dislocation density in subgrains between cells have been considered in models in the literature, e.g. [271,272]. These models are compatible with the assumed state variables in the present study.

8.2.2. Modelling of intergranular cavitation processes

The effects of grain-boundary sliding on the predicted intergranular creep failure response from Chapter 7 need to be evaluated. The limited amount of grain-boundary sliding in Type 316 stainless steel ($\phi_0 = 1{\sim}6$) will increase the normal tractions along some boundaries in the polycrystalline aggregate. This will modify the predicted trend in failure response from Chapter 7. In addition, the grain geometries from Chapters 5 and 7 consisted of quasi-3D grains of irregular shapes under plane strain boundary conditions. The response of full-3D polycrystalline aggregates of tessellated grains during both grain-boundary sliding and intergranular damage needs to be examined in order to develop additional insights into these phenomena under more realistic boundary conditions.

The modified classical nucleation theory, employed at the microscale within the modelling framework of Chapter 7, provides important insights into the physical aspects of the intergranular cavity formation process during creep of Type 316H. However, missing features in the model were identified. These are associated with

- Potential changes in surface energy (γ_s), grain-boundary diffusivity ($\delta_B D_B$) and volumetric shape factors ($f_v(\psi')$) due to different degrees of grain boundary misorientations.

- Variation in surface energy and grain-boundary diffusivity in the presence of impurities such as phosphorous (P) and different phases along grain boundaries.
- Residual stresses at intergranular particles due to local dislocation features (e.g. prismatic loops, pile-ups, etc.) in the vicinity of grain boundaries. These local dislocation features could also provide additional energy contributions to the vacancy condensation process.

Consideration should be made on another possible effect of local dislocation features in the vicinity of intergranular particles on cavity nucleation. In cases when prismatic dislocation loops are punched-out from the intergranular precipitates, plate-like vacancy loops could form on the particle/matrix interface. Such features will modify the energy balance at the particle/matrix interface and may serve as stable cavity nuclei. This hypothesis needs to be explored further. Note that in the present study, where an engineering material with a large number density of intergranular precipitates is examined, only these particles were assumed as potential cavity nucleation sites. If the developed framework is applied to pure metals (e.g. Cu), alternative possible nucleation sites and local mechanisms, driving cavity formation, should be considered.

8.2.3. Informing development of cavity nucleation models via experiments

Any further development of robust cavity nucleation models would require detailed experimental evaluation of intergranular failure in both bicrystals and polycrystalline samples. Key features to be examined in order to inform the development of nucleation models are:

- Evaluation of creep strain accumulation in bi- and polycrystalline samples, prior to the tertiary creep stage, and quantification of the relative amount of grain-boundary sliding.
- Quantification of morphology (type, size, spacing and geometry) of intergranular particles along grain boundaries in bi- and polycrystalline samples.

- Evaluation of newly-nucleated cavities along isolated grain boundaries in interrupted tests. Where cavities nucleate at intergranular particles, the shape of the newly-formed cavity/particle geometry, and location of cavities on the particle interface with respect to the boundary plane and load axis should be examined. Alternatively, the shape of nucleated cavities on precipitate-free boundaries need to be evaluated in pure metals.
- Quantification of number densities of dislocation features (prismatic loops, pile-ups, etc.) in the vicinity of boundaries or intergranular particles. Evaluation of the detailed morphology of such dislocation features in the vicinity of the particle/matrix interface is of importance.
- Number density and size distribution of cavities along isolated boundaries in bicrystals.
- Number density and size distribution of cavities in polycrystalline aggregates as a function of grain boundary orientation to the load axis.
- Qualitative assessment of frequency of cavitated boundaries with respect to crystallographic orientations of grains either side of the boundary (e.g. plastically-harder grains) and degree of boundary misorientations.
- Presence of impurities and their amount along examined grain boundaries.

Experimental studies of ex-service Type 316H, as described above, would provide valuable information for the development of robust cavity nucleation models. However, pure metals would also need to be examined since a clearer picture of the damage process can be obtained from these simpler material systems. Evaluation of the identified directions for future work in this chapter will provide a significant extension to the research, conducted as part of this thesis.

REFERENCES

[1]. Dean DW, Johns JG. Structural Integrity Issues in High Temperature Nuclear Plant : Experience From Operation of the UK Advanced Gas Cooled Reactor Fleet. *Trans. SMiRT-23 Manchester, United Kingdom*. 2015.
[2]. Spindler MW. Observations regarding creep in 316H (EDF Energy), HT Forum. 2011.
[3]. AGR Materials Data Handbook, R66, EDF Energy. 2011.
[4]. Chen B, Smith DJ, Flewitt PEJ, Spindler MW. Constitutive equations that describe creep stress relaxation for 316H stainless steel at 550 deg C. *Mater. High Temp.* 2011;28:155–64.
[5]. Ainsworth RA. R5 procedures for assessing structural integrity of components under creep and creep–fatigue conditions. *Int. Mater. Rev.* 2006;51:107–26.
[6]. Hu J. A theoretical study of creep deformation mechanisms of Type 316H stainless steel at high temperature. DPhil Thesis, University of Oxford; 2015.
[7]. Hu J, Cocks ACF. A multi-scale self-consistent model describing the lattice deformation in austenitic stainless steels. *Int. J. Solids Struct.* Elsevier Ltd; 2016;78–79:21–37.
[8]. Hu J, Cocks ACF. Correlation Between Microstructure Evolution and Creep Properties of Polycrystalline Austenitic Stainless Steel. *Trans. SMiRT-23 Manchester, United Kingdom*. 2015.
[9]. Raj R, Ashby MF. Intergranular fracture at elevated temperature. *Acta Metall.* 1975;23:653–66.
[10]. Dyson BF. Continuous cavity nucleation and creep ductility. *Scr. Metall.* 1983;17:31–7.
[11]. R5, Assessment Procedure for the High Temperature Responses of Structures, Issue 3, EDF Energy. 1990.
[12]. Wen J-F, Tu S-T, Xuan F-Z, Zhang X-W, Gao X-L. Effects of Stress Level and Stress State on Creep Ductility: Evaluation of Different Models. *J. Mater. Sci. Technol.* Elsevier Ltd; 2016;32:695–704.
[13]. Spindler MW, Payten W. Advanced Ductility Exhaustion Methods for the Calculation of Creep Damage During Creep-Fatigue Cycling. *J. ASTM Int.* 2011;8.
[14]. Cronin T, Spindler MW. The effect of creep dwells on the saturated cyclic stress-strain properties of 316 austenitic stainless steel, Internal Report - EDF Energy. 2016.
[15]. Hyde TH, Hyde CJ, Sun W. Applied Creep Mechanics. McGraw-Hill; 2013.
[16]. Bernasconi G, Piatti G. Creep of Engineering Materials and Structures. Applied Science Purblishers Ltd; 1978.
[17]. Kassner ME, Hayes TA. Creep cavitation in metals. *Int. J. Plast.* 2003;19:1715–48.
[18]. Wang Y. Design, Development and Experiments to Investigate the Effect of Elastic Follow-up on Creep Stress Relaxation in Austenitic Steels, PhD Thesis. University of Bristol; 2015.
[19]. Kassner ME. Fundamentals of Creep in Metals and Alloys. 3rd ed. Butterworth-Heinemann; 2015.
[20]. Ashby MF. Mechanisms of Deformation and Fracture. *Adv. Appl. Mech.* 1983;23:117–77.
[21]. Andrade EN da C. The validity of the t1/3 law of flow of metals. *Philos. Mag.* 1962;7:2003–14.
[22]. Fookes A, Li S, Smith DJ, Spindler M. Stress relaxation during dwells for creep and fatigue cycling of Type 316H stainless steel at 550 deg C. *2nd Int. ECCC Conf. Creep Fract. High Temp. Components-Design Life Assesment*. 2009;1–10.
[23]. Morris DG, Harries DR. Creep and rupture in Type 316 stainless steel at temperatures between 525 and 900°C Part I: Creep rate. *Met. Sci.* 1978;12:525–31.
[24]. Mamun AA. Origin of creep-fatigue back stress and its effect on deformation and damage, PhD Thesis. The Open University; 2016.
[25]. Morris DG, Harries DR. Creep and rupture in Type 316 stainless steel at temperatures between 525 and 900°C Part II: Rupture and ductility. *Met. Sci.* 1978;12:532–41.
[26]. Morris DG, Harries DR. Creep and rupture in Type 316 stainless steel at temperatures between 525 and 900°C Part III: Precipitation behaviour. *Met. Sci.* 1978;12:542–9.
[27]. Hull D, Bacon DJ. Introduction to Dislocations. 5th ed. Elsevier; 2011.
[28]. Kocks UF, Argon AS, Ashby MF. Thermodynamics and Kinetics of Slip. *Prog. Mater. Sci.* 1975;19:1–291.
[29]. Morris DG, Harries DR. Recovery of a creep-deformed Type 316 stainless steel. *J. Mater. Sci.* 1979;14:2625–36.
[30]. Lagneborg R. A modified creep-recovery model and its evaluation. *Met. Sci. J.* 1972;6:127–33.
[31]. McLean M, Ghosh R. High Temperature Deformation in Engineering Alloys - Modelling for Strain or Load Control. *Acta Metall.* 1992;40:3075–83.
[32]. Chaboche JL, Rousselier G. On the Plastic and Viscoplastic Constitutive Equations - Part I: Rules developed with internal variable concept. *J Press Vessel Technol.* 1983;150:153–8.

[33]. Chaboche JL. A review of some plasticity and viscoplasticity constitutive theories. *Int. J. Plast.* 2008;24:1642–93.
[34]. Basoalto H, Dyson BF. Predicting stress relaxation and LCF using a microstructure-based constitutive model. Report, British Energy plc Contract Ref No. 40072908. 2003.
[35]. Miller AK. An inelastic constitutive model for monotonic, cyclic and creep deformation: Part I - Equations development and analytical procedures. *J Eng Mater-T.* 1976;96:97–105.
[36]. Kocks UF. Laws for Work-Hardening and and Low-Temperature Creep. *J. Eng. Mater. Technol.* 1976;76–86.
[37]. Mecking H, Kocks UF. A Mechanism for Static and Dynamic Recovery. Strength Met. Alloy. Pergamon Press Ltd; 1979.
[38]. Estrin Y, Kubin LP. Local strain hardening and nonuniformity of plastic deformation. *Acta Metall.* 1986;34:2455–64.
[39]. Balke H, Estrin Y. Micromechanical modelling of shear banding in single crystals. *Int. J. Plast.* 1994;10:133–47.
[40]. Foreman AJE, Makin MJ. Dislocation movement through random arrays of obstacles. *Philos. Mag.* 1966;14:911–24.
[41]. Kocks UF, Mecking H. Physics and phenomenology of strain hardening: The FCC case. *Prog. Mater. Sci.* 2003;48:171–273.
[42]. Wang H, Clausen B, Tomé CN, Wu PD. Studying the effect of stress relaxation and creep on lattice strain evolution of stainless steel under tension. *Acta Mater.* 2013;61:1179–88.
[43]. Roters F, Eisenlohr P, Hantcherli L, Tjahjanto DD, Bieler TR, Raabe D. Overview of constitutive laws, kinematics, homogenization and multiscale methods in crystal plasticity finite-element modeling: Theory, experiments, applications. *Acta Mater.* 2010;58:1152–211.
[44]. Asaro RJ, Needleman A. Texture development and strain hardening in rate dependent polycrystals. *Acta Metall.* 1985;33:923–53.
[45]. Asaro RJ. Micromechanics of Crystals and Polycrystals. Adv. Appl. Mech. 1983.
[46]. Schmid E, Boas W. Plasticity of crystals: with special reference to metals. Springer US; 1968.
[47]. Argon AS. Strengthening Mechanisms in Crystal Plasticity. Oxford University Press; 2008.
[48]. Manik T, Holmedal B. Review of the Taylor ambiguity and the relationship between rate-independent and rate-dependent full-constraints Taylor models. *Int. J. Plast.* 2014;55:152–81.
[49]. Anand L, Kothari M. A computational procedure for rate-independent crystal plasticity. *J. Mech. Phys. Solids*. 1996;44:525–58.
[50]. Hu JN, Cocks ACF. Effect of creep on the Bauschinger effect in a polycrystalline austenitic stainless steel. *Scr. Mater.* 2017;128:100–4.
[51]. Addleman RL, Webster GA. A simple model of uniaxial creep recovery and stress relaxation based on residual-stress redistribution. *J. Strain Anal. Eng. Des.* 1973;8:99–107.
[52]. Wang YQ, Spindler MW, Truman CE, Smith DJ. Critical analysis of the prediction of stress relaxation from forward creep of Type 316H austenitic stainless steel. *Mater. Des.* Elsevier Ltd; 2016;95:656–68.
[53]. Feltham P. Creep and stress relaxation in alpha-brass at low temperatures. *Philos. Mag.* 1961;6:259–70.
[54]. Coleman SL. Stress Relaxation of Ex-Heysham 1 Superheater Header Type 316H Stainless Steel, Report - Nuclear Electric Ltd. 1996.
[55]. Martin U, Mühle U, Oettel H. Stress Relaxation in Superalloys Due to Microstructural Changes. *Mech. Time-Dependent Mater.* 1998;2:1–12.
[56]. Cocks ACF. Final report on constitutive modelling and stress relaxation of 316 stainless steel. Internal Report - Nuclear Electric Ltd. 1996.
[57]. Rohde RW, Swearengen JC. Metal deformation modelling – stress relaxation of aluminium. *ASTM STP 676*. 1979. p. 21–34.
[58]. Hart EW, Solomon HD. Load relaxation studies of polycrystalline high purity aluminium. *Acta Mater.* 1973;21:295–307.
[59]. Hormozi R, Biglari F, Nikbin KM. Experimental study of Type 316 stainless steel failure under LCF/TMF loading conditions. *Int. J. Fatigue*. 2015;75:153–69.
[60]. Morris DG. Creep in Type 316 Stainless steel. *Acta Metall.* 1978;26:1143–51.
[61]. Chen B, Hu JN, Flewitt PEJ, Smith DJ, Cocks ACF, Zhang SY. Quantifying internal stress and internal resistance associated with thermal ageing and creep in a polycrystalline material. *Acta Mater.* 2014;67:207–19.
[62]. Chen B, Hu JN, Wang YQ, Kabra S, Cocks ACF, Smith DJ, Flewitt PEJ. Internal strains between grains during creep deformation of an austenitic stainless steel. *J. Mater. Sci.* 2015;50.
[63]. Hyde CJ, Sun W, Leen SB. Cyclic thermo-mechanical material modelling and testing of 316 stainless steel. *Int. J. Press. Vessel. Pip.* Elsevier Ltd; 2010;87:365–72.
[64]. Chaboche JL, Rousselier G. On the Plastic and Viscoplastic Constitutive Equations - Part II : Application of internal variable concepts to the 316 Stainless steel. *J Press Vessel Technol.* 1983;105:159–64.
[65]. Gong YP, Hyde CJ, Sun W, Hyde TH. Determination of material properties in the Chaboche unified viscoplasticity model.

Proc. Inst. Mech. Eng. Part L J. Mater. Des. Appl. 2010;224:19–29.
[66]. Dunne FPE, Hayhurst DR. Continuum damage based constitutive equations for copper under high temperature creep and cyclic plasticity. *Proc.R.Soc.Lond.A*. 1992;437:545–66.
[67]. Joseph TD, McLennon D, Spindler MW, Truman CE, Smith DJ. The effect of prior cyclic loading variables on the creep behaviour of ex-service type 316H stainless steel. *Mater. High Temp.* 2013;30:156–60.
[68]. Mamun AA, Moat RJ, Kelleher J, Bouchard PJ. Generation of intergranular strains during high temperature creep fatigue loading of 316H stainless steel. *Mater. High Temp.* 2014;31:378–82.
[69]. Mamun AA, Moat RJ, Kelleher J, Bouchard PJ. Origin of the Bauschinger effect in a polycrystalline material. *Mater. Sci. Eng. A.* 2017;707:576–84.
[70]. Turkmen HS, Dawson PR, Miller MP. The evolution of crystalline stresses of a polycrystalline metal during cyclic loading. *Int. J. Plast.* 2002;18:941–69.
[71]. Nes E, Marthinsen K, Brechet Y. On the mechanisms of dynamic recovery. *Scr. Mater.* 2002;47:607–11.
[72]. Aplin PF, Angelo DD. Dislocation-creep mechanisms in Type 316 steel. In: Wilshere B, Evans RW, editors. *Creep Fract. Eng. Mater. Struct.* Institute of Metals, London; 1990. p. 537–45.
[73]. Gerland M, Violan P. Cyclic Hardening and Dislocation Structures in Type 316 Stainless Steel at 600°C. *Mater. Sci. Eng.* 1986;84:23–33.
[74]. Kestenbach H-J, Krauss W, Silviera TL da. Creep of 316 Stainless Steel under High Stresses. *Acta Metall.* 1978;26:661.
[75]. Mathew MD, Sundararaman M, Mannan SL. Dislocation Substructure and Precipitation in Type 316 Stainless Steel Deformed in Creep. *Mater. Trans.* 1997;38:37–42.
[76]. Neves S, Santos F, Anacleto W, Paulo L. Creep Parameters and Dislocation Substructure in AISI 316 Austenitic Stainless Steel From 600ºC to 800ºC. *Mater. Res.* 2017;20:1–5.
[77]. Kroner E. On the plastic deformation of polycrystals. *Acta Metall.* 1961;9:155–61.
[78]. Budiansky B, Wu TT. Theoretical prediction of plastic strains of polycrystals. *Proc 4th Congr. Appl. Mech*. 1962. p. 1175–85.
[79]. Hill R. Continuum micro-mechanics of elastoplastic polycrystals. *J Mech Phys Solids*. 1965;13:89–101.
[80]. Hutchinson JW. Bounds and Self-Consistent Estimates for Creep of Polycrystalline Materials. *Proc. R. Soc. A Math. Phys. Eng. Sci.* 1976;348:101–27.
[81]. Lebensohn RA, Turner PA, Signorelli JW, Canova GR, Tomé CN. Calculation of intergranular stresses based on a large-strain viscoplastic self-consistent polycrystal model. *Model. Simul. Mater. Sci. Eng.* 1998;6:447–65.
[82]. Wang H, Wu PD, Tomé CN, Huang Y. A finite strain elastic-viscoplastic self-consistent model for polycrystalline materials. *J. Mech. Phys. Solids*. 2010;58:594–612.
[83]. Nemat-Nasser S, Obata M. Rate-Dependent, Finite Elasto-Plastic Deformation of Polycrystals [Internet]. Proc. R. Soc. A Math. Phys. Eng. Sci. 1986. p. 343–75.
[84]. Weng GJ. Self-consistent determination of time-dependent behaviour of metals. *J Appl Mech*. 1981;48:41–6.
[85]. Weng GJ. A unified, self-consistent theory for the plastic-creep deformation of metals. *J Appl Mech*. 1982;49:728–34.
[86]. Hu J, Chen B, Smith DJ, Flewitt PEJ, Cocks ACF. Self-consistent Modelling and the Evaluation of Lattice Deformation in a Polycrystalline Austenitic Stainless Steel. *Mater. Today Proc. 2S*. Elsevier Ltd.; 2015. p. S424–33.
[87]. Hu J, Chen B, Smith DJ, Flewitt PEJ, Cocks ACF. On the evaluation of the Bauschinger effect in an austenitic stainless steel—The role of multi-scale residual stresses. *Int. J. Plast.* Elsevier Ltd; 2016;84:203–23.
[88]. Kroupa P. The interaction between prismatic dislocation loops and straight dislocations. Part I. *Philos. Mag.* 1962;7:783–801.
[89]. Ashby MF. The theory of the critical shear stress and work hardening of dispersion-hardened crystals. Defense Technical Information Center, Harvard Univ Cambridge Mass Div of Eng and Appl Sci; 1966.
[90]. Ashby MF, Frost HJ. Deformation-mechanism maps: the plasticity and creep of metals and ceramics. Oxford Pergamon Press Ltd; 1982.
[91]. Mura T. Micromechanics of defects in solids. Nijhoff M, editor. London: The Hague; 1982.
[92]. Rice JR. On the structure of stress-strain relations for time-dependent plastic deformation in metals. *J. Appl. Mech. Trans. ASME*. 1970;37:728–37.
[93]. Ashby MF, Dyson BF. Creep damage mechanics and micromechanisms. *Natl. Phys. Lab. - Reports DMA*. 1984;77.
[94]. Dyson BF, Mclean D. Creep of Nimonic 80A in torsion and tension. *Met. Sci.* 1977;11:37–45.
[95]. Burnett TL, Geurts R, Jazaeri H, Northover SM, McDonald SA, Haigh SJ, Bouchard PJ, Withers PJ. Multiscale 3D analysis of creep cavities in AISI type 316 stainless steel. *Mater. Sci. Technol.* 2015;31:522–34.
[96]. Chen IW, Argon AS. Creep cavitation in 304 stainless steel. *Acta Metall.* 1981;29:1321–33.
[97]. Jazaeri H, Bouchard PJ, Hutchings MT, Linder P. Study of creep cavitation in a stainless steel weldment using small angle

neutron scattering and Scanning electron microscopy. *Proc. ASME 2014 Press. Vessel. Pip. Conf.* 2014;V06AT06A037 1-6.
[98]. Dean DW. Multi-region Creep damage models - Overview. *Conf. Present. EDF High Temp. Forum - Imp. Coll. London*. 2017. p. 1–12.
[99]. G.Langdon, Miller DA. Creep Fracture Maps for 316 Stainless Steel. *Metall. Trans. A*. 1979;10A:1635–41.
[100]. Cocks ACF, Ashby MF. On creep fracture by void growth. *Prog. Mater. Sci.* 1982;27:189–244.
[101]. Cocks ACF, Ashby MF. Integranular fracture during power-law creep under multiaxial stresses. *Met. Sci.* 1980;395–402.
[102]. Needleman A, Rice JR. Plastic Creep Flow Effects in the Diffusive Cavitation of Grain Boundaries. *Acta Metall.* 1980;28:1315–32.
[103]. Dyson BF. Creep and fracture of metals : mechanisms and mechanics. *Rev. Phys. Appliquée*. 1988;23:605–13.
[104]. Cho HC, Yu J, Park IS. Creep cavitation in a NiCr steel. *Metall. Trans. A*. 1992;23:201–10.
[105]. Morris DG, Harries DR. Wedge crack nucleation in Type 316 stainless steel. *J. Mater. Sci.* 1977;12:1587–97.
[106]. Dyson BF. Constrained cavity growth, its use in quantifying recent creep fracture results. *Can Met Quart*. 1979;18:31–8.
[107]. Stevens RN. Grain-boundary sliding and diffusion creep in polycrystalline solids. *Philos. Mag.* 1971;23:265–83.
[108]. Intrater J, Machlin ES. Grain boundary sliding and intercrystalline cracking. *Acta Metall.* 1959;7:140–3.
[109]. Onck P, Van Der Giessen E. Influence of microstructural variations on steady state creep and facet stresses in 2-D freely sliding polycrystals. *Int. J. Solids Struct.* 1997;34:703–26.
[110]. Swindeman RW, Sikka VK, Klueh R. Residual and trace element effects on the high-temperature creep strength of austenitic stainless steels. *Metall. Trans. A*. 1983;14:581–93.
[111]. Chen B, Flewitt PE., Smith DJ, Jones CP. An improved method to identify grain boundary creep cavitation in 316H austenitic stainless steel. *Ultramicroscopy*. Elsevier; 2011;111:309–13.
[112]. Cui Y, Sauzay M, Caes C, Bonnaillie P, Arnal B, Cabet C, Blat-Yrieix M, Dubiez-Legoff S. Modeling and experimental study of long term creep damage in austenitic stainless steels. *Eng. Fail. Anal.* Elsevier Inc.; 2015;58:452–64.
[113]. Erhart H, Grabke HJ. Equilibrium segregation of phosphorus at grain boundaries of Fe-P , Fe-C-P , Fe-Cr-P , and Fe-Cr-C-P alloys. *Met. Sci.* 1981;15:401–8.
[114]. Martinez-Ubeda AI, Payton OD, Scott TB, Griffiths I, Younes CM. Role of long term ageing on the creep life of Type 316H austenitic stainless steel bifurcation weldments. *Proc. ASME 2016 Press. Vessel. Pip. Conf.* 2016. p. 1–7.
[115]. Wilshire B, Willis M. Mechanisms of Strain Accumulation and Damage Development during Creep of Prestrained 316 Stainless Steels. *Metall. Mater. Trans. A*. 2004;35:563–71.
[116]. Kachanov LM. Introduction to Continuum Damage Mechanics. Springer BV; 1968.
[117]. Svensson L-E, Dunlop GL. Growth mechanism of intergranular creep cavities in α-brass. *Met. Sci.* 2010;16:57–64.
[118]. Needham NG, Gladman T. Nucleation and growth of creep cavities in a type 347 steel. *Met. Sci.* 1980;14:64–72.
[119]. He J, Sandstrom R. Formation of creep cavities in austenitic stainless steels. *J. Mater. Sci.* 2016;51:6674–85.
[120]. He J, Sandstrom R. Creep cavity growth models for austenitic stainless steels. *Mater. Sci. Eng. A*. Elsevier; 2016;674:328–34.
[121]. Riedel H. Fracture at High Temperatures. Springer-Verlag Berlin; 1987.
[122]. Huang PL. Simulation micromécanique et étude expérimentale de l'endommagement par fluage des aciers austénitiques inoxydables, PhD Thesis. Universite Pierre et Marie Curie; 2018.
[123]. Argon AS, Chen IW, Lau CW. Intergranular cavitation in creep: Theory and Experiments. In: Pelloux RM, Stollof N, editors. *Creep-Fatigue-Environmental Interact.* 1980. p. 46.
[124]. Crossman FW, Ashby MF. The non-uniform flow of polycrystals by grain-boundary sliding accommodated by power-law creep. *Acta Metall.* 1975;23:425–40.
[125]. Tvergaard V. Effect of grain boundary sliding on creep constrained diffusive cavitation. *J. Mech. Phys. Solids*. 1985;33:447–69.
[126]. Ghahremani F. Effect of grain boundary sliding on anelasticity of polycrystals. *Int. J. Solids Struct*. Pergamon Press Ltd.; 1980;16:825–45.
[127]. Ashby MF. Boundary defects and atomistic aspects of boundary sliding and diffusional creep. *Surf. Sci.* 1972;31:498–542.
[128]. Bower AF, Wininger E. A two-dimensional finite element method for simulating the constitutive response and microstructure of polycrystals during high temperature plastic deformation. *J. Mech. Phys. Solids*. 2004;52:1289–317.
[129]. Kikuchi S, Ilschner B. Effects of a small prestrain at high temperature on the creep behaviour of AISI 304 stainless steel. *Scr. Mater.* 1986;20:159–62.
[130]. Ajaja O, Ardell AJ. The effect of prior cold work on the creep characteristics of AISI Type 304 austenitic stainless steel, Report. 1978.
[131]. Fookes A, Li SX, Smith DJ. Influence of prior cyclic hardening on high temperature deformation and crack growth in Type 316L(N) stainless steel. *Mater. High Temp.* 1999;15:187–93.

[132]. Petkov M, Hu J, Cocks ACF. Self-consistent modelling of cyclic loading and relaxation in austenitic 316H stainless steel. *Philos. Mag.* 2018;99:789–834.
[133]. Petkov M, Chevalier M, Dean D, Cocks ACF. Creep-cyclic deformation in high temperature power plant structural materials: Informing assessment procedures in industry via multi-scale physical modelling. *Trans. SMiRT-25 Charlotte, USA*. 2019.
[134]. Petkov MP, Chevalier M, Dean D, Cocks ACF. On the creep-fatigue interactions in a polycrystalline structural material under typical high-temperature power plant operating conditions. *Mater. Des.* 2020;to appear.
[135]. Li DF, O'Dowd NP, Davies CM, Zhang SY. Microscale prediction of deformation in an austenitic stainless steel under uniaxial loading. *Eur. J. Mech. A/Solids*. Elsevier Ltd; 2011;30:748–60.
[136]. Bachmann F, Hielscher R, Schaeben H. Grain detection from 2D and 3D EBSD data - Specification of the MTEX algorithm. *Ultramicroscopy*. 2011;11:1720–33.
[137]. Henderson BJ, Snedden JD. Creep recovery of commercially pure copper. *J. Mech Eng Sci*. 1968;10:24–35.
[138]. Kamaya M. A procedure for estimating Young's modulus of textured polycrystalline materials. *Int. J. Solids Struct.* Elsevier Ltd; 2009;46:2642–9.
[139]. Ledbetter HM. Elastic constants of polycrystalline copper at low temperatures. Relationship to single-crystal elastic constants. *Phys. Status Solidi*. 1981;66:477–84.
[140]. Lai J. A study of precipitation in AISI type 316 stainless steel. *Mater. Sci. Eng.* 1983;58:195–209.
[141]. Mehmanparast A, Davies CM, Dean DW, Nikbin K. Effects of plastic pre-straining level on the creep deformation, crack initiation and growth behaviour of 316H stainless steel. *Int. J. Press. Vessel. Pip.* Elsevier Ltd; 2016;141:1–10.
[142]. Spindler MW. The prediction of creep damage in type 347 weld metal. Part I: The determination of material properties from creep and tensile tests. *Int. J. Press. Vessel. Pip.* 2005;82:175–84.
[143]. McLean M. On the threshold stress for dislocation creep in particle strengthened alloys. *Acta Metall.* 1985;33:545–56.
[144]. Petkov M, Hu J, Tarleton E, Cocks ACF. Comparison of self-consistent and crystal plasticity FE approaches for modelling the high-temperature deformation of 316H austenitic stainless steel. *Int. J. Solids Struct.* 2019;171:54–80.
[145]. Chen, B., Spindler, M.W., Smith, D.J., and Flewitt PEJ. A review of the effect of Thermo-Mechanical History on the Reheat Cracking in 316H Austenitic Stainless Steel Weldments. *Int. J. Press. Vessel. Pipings*. 2010;531–42.
[146]. Pommier H, Busso EP, Morgeneyer TF, Pineau A. Intergranular damage during stress relaxation in AISI 316L-type austenitic stainless steels: Effect of carbon, nitrogen and phosphorus contents. *Acta Mater.* Elsevier Ltd; 2016;103:893–908.
[147]. Song D, Ponte Castañeda P. A finite-strain homogenization model for viscoplastic porous single crystals: II – Applications. *J. Mech. Phys. Solids*. 2017;107:580–602.
[148]. Song D, Ponte Castañeda P. A finite-strain homogenization model for viscoplastic porous single crystals: I – Theory. *J. Mech. Phys. Solids*. 2017;107:560–79.
[149]. Lebensohn RA, Tomé CN, Castañeda PP. Self-consistent modelling of the mechanical behaviour of viscoplastic polycrystals incorporating intragranular field fluctuations. *Philos. Mag.* 2007;87:4287–322.
[150]. Ponte Castañeda P. Fully optimized second-order variational estimates for the macroscopic response and field statistics in viscoplastic crystalline composites. *Proc. R. Soc. A Math. Phys. Eng. Sci.* 2015;471.
[151]. Liu Y, Ponte Castañeda P. Homogenization estimates for the average behavior and field fluctuations in cubic and hexagonal viscoplastic polycrystals. *J. Mech. Phys. Solids*. 2004;52:1175–211.
[152]. Ponte Castañeda P. Second-order homogenization estimates for nonlinear composites incorporating field fluctuations: II - Applications. *J. Mech. Phys. Solids*. 2002;50:759–82.
[153]. Bornert M, Ponte Castaneda P. Second-order estimates of the self-consistent type for viscoplastic poly crystals. *Proc. R. Soc. A Math. Phys. Eng. Sci.* 1998;454:3035–45.
[154]. Lebensohn RA, Liu Y, Ponte Castañeda P. Macroscopic properties and field fluctuations in model power-law polycrystals: Full-field solutions versus self-consistent estimates. *Proc. R. Soc. A Math. Phys. Eng. Sci.* 2004;460:1381–405.
[155]. Doghri I, Brassart L, Adam L, Gérard JS. A second-moment incremental formulation for the mean-field homogenization of elasto-plastic composites. *Int. J. Plast.* Elsevier Ltd; 2011;27:352–71.
[156]. Peirce D, Asaro RJ, Needleman A. An analysis of nonuniform and localized deformation in ductile single crystals. *Acta Metall.* 1982;30:1087–119.
[157]. Bronkhorst CA, Kalidindi SR, Anand L. Polycrystalline plasticity and the evolution of crystallographic texture in FCC metals. *Phil Trans R. Soc A*. 1992;341.
[158]. Becker R, Butler JF, Hu H, Lalli LA. Analysis of an aluminum single crystal with unstable initial orientation (001) [110] in channel die compression. *Metall. Trans. A*. 1991;22:45–58.
[159]. Li DF, O'Dowd NP. On the evolution of lattice deformation in austenitic stainless steels - The role of work hardening at finite strains. *J. Mech. Phys. Solids*. Elsevier; 2011;59:2421–41.

[160]. Dunne FPE, Rugg D, Walker A. Lengthscale-dependent, elastically anisotropic, physically-based hcp crystal plasticity: Application to cold-dwell fatigue in Ti alloys. *Int. J. Plast.* 2007;23:1061–83.
[161]. Venkatramani G, Ghosh S, Mills M. A size-dependent crystal plasticity finite-element model for creep and load shedding in polycrystalline titanium alloys. *Acta Mater.* 2007;55:3971–86.
[162]. Srivastava A, Needleman A. Effect of crystal orientation on porosity evolution in a creeping single crystal. *Mech. Mater.* 2015;90:10–29.
[163]. Liu WH, Zhang XM, Tang JG, Du YX. Simulation of void growth and coalescence behavior with 3D crystal plasticity theory. *Comput. Mater. Sci.* 2007;40:130–9.
[164]. Wei YJ, Anand L. Grain-boundary sliding and separation in polycrystalline metals: Application to nanocrystalline fcc metals. *J. Mech. Phys. Solids*. 2004;52:2587–616.
[165]. Simonovski I, Cizelj L. Cohesive zone modeling of intergranular cracking in polycrystalline aggregates. *Nucl. Eng. Des.* Elsevier B.V.; 2015;283:139–47.
[166]. Fleck NA, Muller GM, Ashby MF, Hutchinson JW. Strain gradient plasticity: Theory and experiment. *Acta Metall. Mater.* 1994;42:475–87.
[167]. Quey R, Dawson PR, Barbe F. Large-scale 3D random polycrystals for the finite element method: Generation, meshing and remeshing. *Comput. Methods Appl. Mech. Eng.* Elsevier B.V.; 2011;200:1729–45.
[168]. Lebensohn RA, Liu Y, Castañeda PP. On the accuracy of the self-consistent approximation for polycrystals: Comparison with full-field numerical simulations. *Acta Mater.* 2004;52:5347–61.
[169]. Gill SPA, Cocks ACF. A variational approach to two dimensional grain growth—II. Numerical results. *Acta Mater.* 1996;44:4777–89.
[170]. Chen B, Hu JN, Flewitt PEJ, Cocks ACF, Ainsworth RA, Smith DJ, Dean DW, Scenini F. Effect of thermal ageing on creep and oxidation behaviour of Type 316H stainless steel. *Mater. High Temp.* 2015;32:592–606.
[171]. Simonovski I, Cizelj L. Representative Volume Element Size of a Polycrystalline Aggregate with Embedded Short Crack. *Intern. Conf. Nucl. Energy New Eur. 2007*. 2007;1–8.
[172]. Mirkhalaf SM, Andrade Pires FM, Simoes R. Determination of the size of the Representative Volume Element (RVE) for the simulation of heterogeneous polymers at finite strains. *Finite Elem. Anal. Des.* Elsevier; 2016;119:30–44.
[173]. Cailletaud G, Diard O, Feyel F, Forest S. Computational Crystal Plasticity : From Single Crystal to Homogenized Polycrystals. *Tech. Mech. Uni Magdebg.* 2003;130–45.
[174]. Van Der Giessen E, Tvergaard V. A Creep-Rupture Model Accounting for Cavitation at Sliding Grain-Boundaries. *Int. J. Fract.* 1991;48:153–78.
[175]. Ghahremani F. Effect of grain boundary sliding on steady creep of polycrystals. *Int. J. Solids Struct.* Pergamon Press Ltd.; 1980;16:847–62.
[176]. Hu J, Chen B, Smith D, Flewitt PEJ, Cocks ACF. Self-consistent model in the Local residual stress evaluation of 316H Stainless Steel. *13th Int. Conf. Fract. June 16–21*. 2013. p. 1–10.
[177]. Brunner H, Grant NJ. Deformation resulting from grain boundary sliding. *Trans. AIME*. 1959;215.
[178]. Raj R, Ashby MF. Grain boundary sliding and the effects of particles on its rate. *Metall. Trans.* 1972;1937–42.
[179]. Gates RS. Grain boundary sliding in Type 316 austenitic steel. Part II. The creep strain and stress dependencies. *Mater. Sci. Eng.* 1977;27:115–25.
[180]. Hsia KJ, Parks DM, Argon AS. Effects of grain boundary sliding on creep-constrained boundary cavitation and creep deformation. *Mech. Mater.* 1991;11:43–62.
[181]. van der Giessen E, Tvergaard V. Interaction of cavitating grain boundary facets in creeping polycrystals. *Mech. Mater.* 1994;17:47–69.
[182]. Garofalo F, Richmond O, Domis WF, Gemmingen F Von. Strain-time, rate-stress and rate-temperature relations during large deformations in creep. *Proc. Inst. Mech. Eng. Conf Proc*. 1963;178:1–31.
[183]. Gates RS. Grain Boundary Sliding in Type 316 Austenitic Steel. Part III: The temperature dependence. *Mater. Sci. Eng.* 1977;27:127–32.
[184]. Gates RS, Horton CAP. Grain boundary sliding in Type 316 austenitic steels. Part I: The grain size dependence. *Mater. Sci. Eng.* 1977;27:105–14.
[185]. Petkov MP, Elmukashfi E, Tarleton E, Cocks ACF. Modelling grain-boundary sliding during creep of Type 316 stainless steel within a crystal plasticity finite element modelling framework. *To Appear*. 2020;
[186]. Elmukashfi E, Cocks ACF. A theoretical and computational framework for studying creep crack growth. *Int. J. Fract.* Springer Netherlands; 2017;
[187]. Ortiz M, Pandolfi A. Finite-deformation irreversible cohesive elements for three-dimensional crack-propagation analysis. *Int. J. Numer. Methods Eng.* 1999;44:1267–82.

[188]. Arora H, Tarleton E, Li-Mayer J, Charalambides MN, Lewis D. Modelling the damage and deformation process in a plastic bonded explosive microstructure under tension using the finite element method. *Comput. Mater. Sci.* Elsevier B.V.; 2015;110:91–101.
[189]. Xia Z, Zhang Y, Ellyin F. A unified periodical boundary conditions for representative volume elements of composites and applications. *Int. J. Solids Struct.* 2003;40:1907–21.
[190]. Reid CN, Owen WS. Deformation geometry for materials scientists. Elsevier B.V.; 1973.
[191]. Chen T, Tan L, Lu Z, Xu H. The effect of grain orientation on nanoindentation behavior of model austenitic alloy Fe-20Cr-25Ni. *Acta Mater.* Elsevier Ltd; 2017;138:83–91.
[192]. Lin B, Zhao LG, Tong J. A crystal plasticity study of cyclic constitutive behaviour, crack-tip deformation and crack-growth path for a polycrystalline nickel-based superalloy. *Eng. Fract. Mech.* Elsevier Ltd; 2011;78:2174–92.
[193]. Van Der Giessen E, Tvergaard V. Effect of random variations in microstructure on the development of final creep failure in polycrystalline aggregates. *Model. Simul Mater Sci Eng*. 1994;2:721–38.
[194]. Van Der Giessen E, Tvergaard V. Development of final creep failure in polycrystalline aggregates. *Acta Metall. Mater.* 1994;42:959–73.
[195]. Shawish S El, Cizelj L, Simonovski I. Modeling grain boundaries in polycrystals using cohesive elements: Qualitative and quantitative analysis. *Nucl. Eng. Des.* 2013;261:371–81.
[196]. Chen B, Flewitt PEJ, Smith DJ. Microstructural sensitivity of 316H austenitic stainless steel: Residual stress relaxation and grain boundary fracture. *Mater. Sci. Eng. A*. Elsevier B.V.; 2010;527:7387–99.
[197]. Raj R, Ashby MF. On grain boundary sliding and diffusional creep. *Metall. Trans.* 1971;2:1113–27.
[198]. Sutton AP, Balluffi RW. Interfaces in Crystalline Materials. Brook R, Cheetham A, Heuer A, Hirsch P, Marks TJ, Silcox J, et al., editors. Clarendon Press Oxford; 1995.
[199]. Perkins RA, Padgett RA, Tunali NK. Tracer diffusion of 59Fe and 51Cr in Fe-17 wt pct Cr-12 wt pct Ni Austenitic Alloy. *Metall. Trans.* 1973;4:1665–9.
[200]. Anderson PM, Rice JR. Constrained creep cavitation of grain boundary facets. *Acta Metall.* 1985;33:409–22.
[201]. Rodin GJ, Dib MW. Effective properties of creeping solids undergoing grain boundary sliding. Int. J. Fract. 7. 1989.
[202]. Dyson BF, Loveday MS, Rodgers MJ. Grain Boundary Cavitation Under Various States of Applied Stress. *Proc. R. Soc. A Math. Phys. Sci.* 1976;349:245–59.
[203]. Chen IW. Cavity growth on a sliding grain boundary. *Metall. Trans. A.* 1983;14:2289–93.
[204]. Jazaeri H, Bouchard P, Hutchings M, Spindler M, Mamun A, Heenan R. An Investigation into Creep Cavity Development in 316H Stainless Steel. *Metals (Basel).* 2019;9:318.
[205]. Rice JR. Constraints on the diffusive cavitation of isolated grain boundary facets in creeping polycrystals. *Acta Metall.* 1981;29:675–81.
[206]. Lai JKL, Chastell DJ, Flewitt PEJ. Precipitate phases in type 316 austenitic stainless steel resulting from long-term high temperature service. *Mater. Sci. Eng.* 1981;49:19–29.
[207]. NIMS. Metallographic atlas of long-term crept materials - SUS 316H TB, Report. National Institute for Materials Science, Japan. 2003.
[208]. Lai JKL, Horton CAP. Some Effects of Thermal Aging and Grain Size on the Creep Behaviour of a Cast of AISI Type 316 Stainless Steel. *Mater. Sci. Eng.* 1982;54:285–9.
[209]. Jazaeri H, Bouchard PJ, Hutchings MT, Mamun AA, Heenan RK. Study of cavities in a creep crack growth test specimen. *Procedia Struct. Integr.* Elsevier B.V.; 2016;2:942–9.
[210]. Lai JKL. CEGB Report TRPD; L/2383/N82. 1983.
[211]. Warren AD, Griffiths IJ, Harniman RL, Flewitt PEJ, Scott TB. The role of ferrite in Type 316H austenitic stainless steels on the susceptibility to creep cavitation. *Mater. Sci. Eng. A.* 2015;635:59–69.
[212]. Bouchard PJ, Withers PJ, McDonald SA, Heenan RK. Quantification of creep cavitation damage around a crack in a stainless steel pressure vessel. *Acta Mater.* 2004;52:23–34.
[213]. Auzoux Q. Fissuration en relaxation des aciers inoxydables austénitiques - Influence de l'écrouissage sur l'endommagement intergranulaire, PhD Thesis. Ecole Nationale Superieure des Mines de Paris; 2004.
[214]. Lai JK, Wickens A. Microstructural changes and variations in creep ductility of 3 casts of type 316 stainless steel. *Acta Metall.* 1979;27:217–30.
[215]. Sourmail T. Precipitation in creep resistant austenitic stainless steels. *Mater. Sci. Technol.* 2001;17:1–14.
[216]. Weiss B, Stickler R. Phase instabilities during high temperature exposure of 316 austenitic stainless steel. *Metall. Trans.* 1972;3:851–66.
[217]. Slater TJA, Bradley RS, Bertali G, Geurts R, Northover SM, Burke MG, Haigh SJ, Burnett TL, Withers PJ. Multiscale correlative tomography: An investigation of creep cavitation in 316 stainless steel. *Sci. Rep.* Springer US; 2017;7:1–10.

[218]. Jones R, Randle V, Owen G. Carbide precipitation and grain boundary plane selection in overaged type 316 austenitic stainless steel. *Mater. Sci. Eng. A*. 2008;496:256–61.
[219]. Hong HU, Rho BS, Nam SW. Correlation of the M23C6 precipitation morphology with grain boundary characteristics in austenitic stainless steel. *Mater. Sci. Eng. A*. 2001;318:285–92.
[220]. Kim KJ, Hong HU, Min KS, Nam SW. Correlation between the carbide morphology and cavity nucleation in an austenitic stainless steels under creep-fatigue. *Mater. Sci. Eng. A*. 2004;387–389:531–5.
[221]. Kim KJ, Hong HU, Nam SW. Investigation on the formation of serrated grain boundaries with grain boundary characteristics in an AISI 316 stainless steel. *J. Nucl. Mater.* Elsevier B.V.; 2009;393:249–53.
[222]. White CL, Padgett RA, Swindeman RW, Division C, Ridge O, Ridge O. Sulfur and Phosphorus segregation to creep cavities and grain boundaries in 304 SS. *Scr. Metall.* 1981;15:777–82.
[223]. Marshall P. Austenitic stainless steels - Microstructure and Mechanical Properties. Elsevier Appl Sci Publ; 1984.
[224]. Kegg GR. PhD Thesis. Imperial College London; 1971.
[225]. Ayensu A, Langdon TG. The inter-relationship between grain boundary sliding and cavitation during creep of polycrystalline copper. *Metall. Mater. Trans. A*. 1996;27:901–7.
[226]. Shiozawa K, Weertman JR. Studies of Nucleation Mechanisms and the Role of Residual-Stresses in the Grain-Boundary Cavitation of a Super-Alloy. *Acta Metall.* 1983;31:993–1004.
[227]. Yavari P, Langdon TG. Cavitation in high purity aluminium during fatigue at elevated temperatures. *J. Mater. Sci. Lett.* 1983;2:522–4.
[228]. Watanabe T, Davies PW. Grain boundary sliding and intergranular fracture behaviour of copper bicrystals. *Philos. Mag. A Phys. Condens. Matter, Struct. Defects Mech. Prop.* 1978;37:649–81.
[229]. Afshar S, Biscondi M. Intergranular cavitation observed during OFHC copper bicrystal creep. *Scr. Metall.* 1986;20:707–11.
[230]. Raj R. Intergranular fracture in bicrystals. *Acta Metall.* 1978;26:341–9.
[231]. Gandhi C, Raj R. Integranular Fracture in bicrystals - II. *Acta Metall.* 1982;30:305–20.
[232]. Arnaud JC. Etude de l'endommagement par fluage des aciers inoxydables austenitiques entre 550 degre C et 650 degre C, PhD Thesis. Ecole Nationale Superieure de Mines de Saint-Ettienne; 1987.
[233]. Dyson BF, Henn DE. The effect of room temperature pre-strain on grain boundary cavitation in Nimonic 80A. *J. Microsc.* 1973;97:165–70.
[234]. Nieh TG, Nix WD. A comparison of the dimple spacing on intergranular creep fracture surfaces with the slip band spacing for copper. *Scr. Metall.* 1980;14:365–8.
[235]. Yu KS, Nix WD. On the relation between creep cavitation and grain boundary orientation. *Scr. Metall.* 1984;18:173–8.
[236]. Unnikrishnan R, Northover SM, Jazaeri H, Bouchard PJ. Investigating plastic deformation around a reheat-crack in a 316H austenitic stainless steel weldment by misorientation mapping. *Procedia Struct. Integr.* Elsevier B.V.; 2016;2:3501–7.
[237]. Riedel H. Cavity nucleation at particles on sliding grain boundaries. A shear crack model for grain boundary sliding in creeping polycrystals. *Acta Metall.* 1984;32:313–21.
[238]. He J, Sandström R. Modelling grain boundary sliding during creep of austenitic stainless steels. *J. Mater. Sci.* 2016;51:2926–34.
[239]. He J, Sandström R. Brittle rupture of austenitic stainless steels due to creep cavitation. *Procedia Struct. Integr.* Elsevier B.V.; 2016;2:863–70.
[240]. Anderson PM, Shewmon PG. Stress redistribution and cavity nucleation near a diffusively growing grain boundary cavity. *Mech. Mater.* 2000;32:175–91.
[241]. Binder K, Stauffer D. Statistical theory on nucleation, condensation and coagulation. *Adv Phys.* 1976;25:343–96.
[242]. Raj R. Nucleation of cavities at second phase particles in grain boundaries. *Acta Metall.* 1978;26:995–1006.
[243]. Yang MS, Weertman JR, Roth M. In: Wilshere, B., Owen, D.R.J. (Eds.). *Proc. 2nd Int. Conf. Creep Fract. eng. Mater. Struct. Pineridge, Swansea*. 1984. p. 149.
[244]. Trinkaus H. Theory of the nucleation of multicomponent precipitates. *Phys Rev*. 1983;27.
[245]. Yoo MH, Chen IW. Creep cavitation under interfacial segregation. *Acta Mater.* 1984;32:1499–508.
[246]. Svoboda J, Sklenička V. Thermal cavity nucleation at intergranular inclusions in high temperature creep. *Acta Metall. Mater.* 1990;38:1141–9.
[247]. Ashby MF, Centamore RM. The dragging of small oxide particles by migrating grain boundaries in copper. *Acta Metall.* 1968;16:1081–92.
[248]. Xiao X, Liu G, Hu B, Wang J, Ma W. Coarsening behavior for M23C6 carbide in 12 %Cr-reduced activation ferrite/martensite steel: Experimental study combined with DICTRA simulation. *J. Mater. Sci.* 2013;48:5410–9.
[249]. Cocks ACF. The nucleation and growth of voids in a material containing a distribution of grain-boundary particles. *Acta*

Metall. 1985;33:129–37.
[250]. Wang JS, Stephens JJ, Nix WD. A statistical analysis of cavity nucleation at particles in grain boundaries. *Acta Metall.* 1985;33:1009–21.
[251]. Riedel H. Continuous nucleation of grain boundary cavities in creep rupture. *Zeitschrift für Met.* 1985;76:669–75.
[252]. Hui-Ying X, Xiu-San X. A statistical theory of creep fracture. *Acta Phys. Sin. (overseas Ed.* 1997;6:578–88.
[253]. Burton B, Beeré WB. Grain boundary diffusional creep of materials containing particles. *Philos. Mag. A.* 1981;43:37–41.
[254]. Gifkins RD. A Mechanism for the Formation of Intergranular Cracks when Boundary Sliding Occurs. *Acta Metall.* 1956;4:98–9.
[255]. Yoo MH, Trinkaus H. Interaction of slip with grain boundary and its role in cavity nucleation. *Acta Metall.* 1986;2381–90.
[256]. Brown LM, Stobbs WM. The work-hardening of copper-silica - I. A model based on internal stresses, with no plastic relaxation. *Philos. Mag.* 1971;185:1185–99.
[257]. Stoter LP. Thermal ageing effects in AISI type 316 stainless steel. *J. Mater. Sci.* 1981;16:1039–51.
[258]. Janeček M, Tangri K. The influence of temperature and grain size on substructure evolution in stainless steel 316L. J. Mater. Sci. 1995. p. 3820–6.
[259]. Chen IW, Argon AS. Diffusive growth of grain-boundary cavities. *Acta Metall.* 1981;29:1759–68.
[260]. Riedel H. Life prediction methods for constrained grain boundary cavitation. *Int. J. Press. Vessel. Pip.* 1989;39:119–34.
[261]. Don J, Majumdar S. Creep cavitation and grain boundary structure in type 304 stainless steel. *Acta Metall.* 1986;34:961–7.
[262]. Dyson BF. In: Mishra, R.S., Earthman, J.C., Raj, S.V. (Eds.). *Creep Deform. Fundam. Appl. TMS, Warrendale*. 2002. p. 309.
[263]. Riedel H, Rice JR. In: Fracture Mechanics: Twelfth Conference. In: ASTM, editor. *ASTM STP 700, P.C. Paris*. 1980. p. 112–30.
[264]. Raj R, Shih HM, Johnson HH. Correction to: "Intergranular fracture at elevated temperature." *Scr. Metall.* 1977;11:839–42.
[265]. Skelton RP, Gandy D. Creep-fatigue damage accumulation and interaction diagram based on metallographic interpretation of mechanisms. *Mater. High Temp.* 2008;25:27–54.
[266]. Mehmanparast A, Davies CM, Webster GA, Nikbin KM. Creep crack growth rate predictions in 316H steel using stress dependent creep ductility. *Mater. High Temp.* 2014;31:84–94.
[267]. Cane BJ, Middleton CJ. Intergranular creep-cavity formation in low-alloy bainitic steels. *Met. Sci.* 1981;15:295–301.
[268]. Lim LC. Cavity nucleation at high temperatures involving pile-ups of grain boundary dislocations. *Acta Metall.* 1987;35:1663–73.
[269]. Exner HE, Arzt E. No Title. In: Cahn RW, Haasen P, editors. *Phys. Metall.* Third Edn. Elsevier B.V; 1983. p. 1885–912.
[270]. Geers MGD, Cottura M, Appolaire B, Busso EP, Forest S, Villani A. Coupled glide-climb diffusion-enhanced crystal plasticity. *J. Mech. Phys. Solids*. Elsevier; 2014;70:136–53.
[271]. Mughrabi H. Dislocation wall and cell structures and long-range internal stresses in deformed metal crystals. *Acta Metall.* 1983;31:1367–79.
[272]. Nes E, Pettersen T, Marthinsen K. On the mechanisms of work hardening and flow-stress saturation. *Scr. Mater.* 2000;43:55–62.

APPENDIX A. 3D CRYSTAL PLASTICITY FINITE ELEMENT FRAMEWORK

The CPFE model has been implemented as a user material subroutine (UMAT) within ABAQUS. The deformation gradients at the beginning and end of the time increment, $\mathbf{F}_t$ and $\mathbf{F}_{t+\Delta t}$ are provided. The UMAT computes the stress and Jacobian ($\partial\delta\boldsymbol{\sigma}/\partial\delta\boldsymbol{\varepsilon}$) at the end of the increment, and updates state variables. An implicit scheme, using an elastic predictor and plastic corrector terms, following Dunne et al. [160], is employed to compute the stress through a Newton-Raphson scheme. The plastic part of the velocity gradient is $\mathbf{L^p} = \sum_\alpha \dot{\gamma}^{(\alpha)} \left(\mathbf{s}^{(\alpha)} \otimes \mathbf{n}^{(\alpha)}\right)$, where $\dot{\gamma}^{(\alpha)}$is the

shear strain rate for the *α-th* slip system. The stress at the end of the increment is obtained using an elastic predictor Cauchy stress, $\boldsymbol{\sigma}_{\mathbf{trial}} = \boldsymbol{\sigma}_{\mathrm{t}} + \mathbf{C}^{\mathbf{rot}}\Delta\boldsymbol{\varepsilon} + (\mathbf{W}\boldsymbol{\sigma}_{\mathrm{t}} - \boldsymbol{\sigma}_{\mathrm{t}}\mathbf{W})\Delta t$ (where $\mathbf{W}$ is the continuum spin), the elastic strain increment $\Delta\boldsymbol{\varepsilon}^{\mathbf{e}}$ and the plastic strain increment $\Delta\boldsymbol{\varepsilon}^{\mathbf{p}}$ as

$$\boldsymbol{\sigma}_{t+\Delta t} = \mathbf{C}^{\mathbf{rot}}\left(\boldsymbol{\varepsilon}_{\mathbf{t}}^{\mathbf{e}} + \Delta\boldsymbol{\varepsilon}^{\mathbf{e}}\right) = \boldsymbol{\sigma}_{\mathbf{trial}} - \mathbf{C}^{\mathbf{rot}}\Delta\boldsymbol{\varepsilon}^{\mathbf{p}} \qquad (A.1)$$

The matrix $\mathbf{C}^{\mathbf{rot}}$ is the anisotropic stiffness matrix for the crystal with respect to global coordinates. The plastic strain increment is expressed by the plastic velocity gradient as

$$\Delta\boldsymbol{\varepsilon}^{\mathbf{p}} = 1/2\left(\mathbf{L}^{\mathbf{p}} + \mathbf{L}^{\mathbf{p}T}\right)\Delta t = sym(\mathbf{L}^{\mathbf{p}})\Delta t \qquad (A.2)$$

Using the expression for $\mathbf{L}^{\mathbf{p}}$ and Eq. A.1 allows Eq. A.2 to be expressed as

$$\delta\Delta\boldsymbol{\varepsilon}^{\mathbf{p}} = \mathbf{P}\delta\boldsymbol{\sigma}_{t+\Delta t} = \sum_{\alpha} Z\Delta t\mathbf{A}_{\mathbf{m}}^{(\boldsymbol{\alpha})} \otimes \mathbf{A}_{\mathbf{m}}^{(\boldsymbol{\alpha})}\delta\boldsymbol{\sigma}_{t+\Delta t} \qquad (A.3)$$

with $\mathbf{A}_{\mathbf{m}}^{(\boldsymbol{\alpha})}$ defined by $\mathbf{A}_{\mathbf{m}}^{(\boldsymbol{\alpha})} = \mathbf{s}^{(\alpha)} \otimes \mathbf{n}^{(\alpha)}$. The term Z contains the differential of the flow rule employed (e.g. Eq. 2.17) with respect to the resolved shear stress. A residual stress term $\widetilde{\boldsymbol{\Sigma}}$ is used to re-express Eq. A.1 in differential form as $\delta\widetilde{\boldsymbol{\Sigma}} = \delta\boldsymbol{\sigma}_{\mathrm{t}+\Delta\mathrm{t}} - \delta\boldsymbol{\sigma}_{\mathbf{trial}} + \mathbf{C}^{\mathbf{rot}}\delta\Delta\boldsymbol{\varepsilon}^{\mathbf{p}}$. Combining this expression with Eq. A.3, employing a Taylor expansion and setting $\widetilde{\boldsymbol{\Sigma}} \to 0$, one obtains

$$\tilde{\boldsymbol{\Sigma}} + \left(\partial\tilde{\boldsymbol{\Sigma}}/\partial\delta\boldsymbol{\sigma}_{t+\Delta t}\right)\delta\boldsymbol{\sigma}_{t+\Delta t} = \boldsymbol{\sigma}_{t+\Delta t} - \boldsymbol{\sigma}_{\mathbf{trial}} + \mathbf{C}^{\mathbf{rot}}\Delta\boldsymbol{\varepsilon}^{\mathbf{p}} + (\mathbf{I} + \mathbf{C}^{\mathbf{rot}}\mathbf{P})\delta\boldsymbol{\sigma}_{t+\Delta t} = \mathbf{0} \qquad (A.4)$$

where $\mathbf{I}$ is the identity matrix. The increment in stress is obtained from Eq. A.4 as

$$-(\mathbf{I} + \mathbf{C}^{\mathbf{rot}}\mathbf{P})^{-1}\left[\boldsymbol{\sigma}_{t+\Delta t} - \boldsymbol{\sigma}_{\mathbf{trial}} + \mathbf{C}^{\mathbf{rot}}\Delta\boldsymbol{\varepsilon}^{\mathbf{p}}\right] = \delta\boldsymbol{\sigma}_{t+\Delta t} \qquad (A.5)$$

which is used iteratively, until the residual stress decreases to a specified tolerance ($\widetilde{\boldsymbol{\Sigma}}$ < 1x10^{-8} MPa). The Jacobian $\mathbf{J}$ is calculated following [160]; for $\widetilde{\boldsymbol{\Sigma}} \approx 0$ and $\delta\boldsymbol{\sigma}_{\mathbf{trial}} \approx \mathbf{C}^{\mathbf{rot}}\delta\boldsymbol{\varepsilon}$, one obtains

$$\mathbf{J} = \partial\delta\boldsymbol{\sigma}/\partial\delta\boldsymbol{\varepsilon} = (\mathbf{I} + \mathbf{C}^{\mathbf{rot}}\mathbf{P})^{-1}\mathbf{C}^{\mathbf{rot}} \qquad (A.6)$$

All state variables are updated at the end of increment.

APPENDIX B. INTERFACE ELEMENT FORMULATION

Full description of the interface element FE formulation is given in [185] with only a brief summary provided here. The constitutive response of the interface is defined on the mid-surface S_0, between the upper and lower surfaces S^+ and S^- of the elemental body in Fig. B.1.

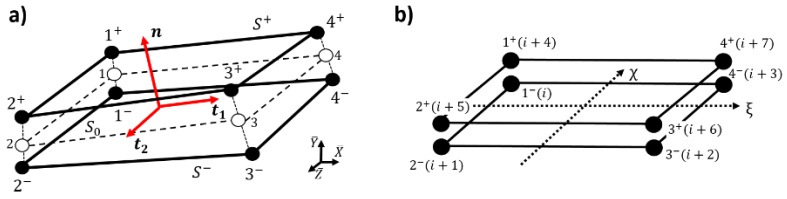


Figure B.1. Definition of interface element in 3D – a) physical and b) parent domain. An 8-noded brick element is used in 3D, defined by a normal ($\bar{n}$) and two sliding directions ($\bar{t}_1, \bar{t}_2$).

Following the approach from [186], the local separations $\boldsymbol{\delta}$ ([3x1] vector) are obtained as $\boldsymbol{\delta} = \mathbf{N}\mathbf{L}_\mathbf{k}\mathbf{R}\mathbf{U} = \mathbf{B}_\mathbf{C}\mathbf{U}$, where $\mathbf{N}$ contains the shape functions along the parent domain, $\mathbf{L_k}$ is the displacement-separation matrix and $\mathbf{U}$ is the nodal displacement vector in global coordinates. The coordinate transformation matrix, $\mathbf{R}$, is constructed from a vector $\mathbf{Q} = \begin{bmatrix}\mathbf{t}_1 & \mathbf{t}_2 & \mathbf{n}\end{bmatrix}^T$. An incremental approach to compute the interface tractions is adopted. At increment *i* and for $\dot{\delta}_n^{cr} = 0$ (sliding only), the traction increments can be expressed from Eqs. 5.3 and 5.4 as

$$\Delta T_n = K_n \Delta\delta_n \;;\; \Delta T_{tk} = \frac{(\Delta\delta_{tk} - B_t T_{tk}^i \Delta t)}{(A_t + B_t \Delta t)}; k = 1,2 \qquad (B.1)$$

where Δt is the time increment, T_{tk}^i are the tangential tractions at the start of increment *i*, $B_t = \dot{\delta}_{0t}/\sigma_0$ and $A_t = 1/K_t$. The change in tractions over the increment is $\Delta\mathbf{T_c} = \mathbf{C_K}\Delta\boldsymbol{\delta} = \mathbf{C_K}\mathbf{B_c}\Delta\mathbf{U}$, where $\Delta\mathbf{T_c}$ is a [3x1] vector. In Chapter 7, the cavity area fraction evolves during creep damage due to diffusive growth, driven by the normal traction, and cavity nucleation. To allow for a more straight-forward implementation of the constitutive response, the number density of cavities is assumed constant during the increment ($N_h^i = const.$) and is updated explicitly after the solution

for f_h and $\mathbf{T_c}$ is obtained. The area fraction increases during the increment as a results of diffusive growth. N.B. This alters the tangential and normal response of the boundary. An increment in cavity area fraction due to diffusive growth during the *i-th* increment is $\Delta f_h = \Delta\dot{\delta}_n^{cr}\sqrt{N_h^i}\Big/\left(h(\psi)\sqrt{f_h^i+\Delta f_h}\right)$. This and Eqs. 7.10-7.11 can be re-written in incremental form as

$$f(\Delta T_{tk}) = \Delta\delta_{tk} - \frac{\Delta T_{tk}}{K_t\left(1-\left(f_h^i+\Delta f_h\right)\right)} - \frac{\dot{\delta}_{0t}T_{tk}^i\Delta t}{\sigma_0\left(1-\left(f_h^i+\Delta f_h\right)\right)} - \frac{\dot{\delta}_{0t}\Delta T_{tk}\Delta t}{\sigma_0\left(1-\left(f_h^i+\Delta f_h\right)\right)} = 0 \qquad (B.2)$$

$$g(\Delta T_n) = \Delta\delta_n - \frac{\Delta T_n}{K_n\left(1-\left(f_h^i+\Delta f_h\right)\right)} - \frac{8\delta_b D_b\Omega T_n^i N_h^i\Delta t}{kT\ln\left(1/\left(f_h^i+\Delta f\right)\right)} - \frac{8\delta_b D_b\Omega\Delta T_n N_h^i\Delta t}{kT\ln\left(1/\left(f_h^i+\Delta f\right)\right)} = 0 \qquad (B.3)$$

$$h(\Delta f_h) = \Delta f_h - \frac{\Delta\delta_n\sqrt{N_h^i}}{h(\psi)\sqrt{f_h^i+\Delta f_h}} - \frac{A_n\Delta T_n}{\left(1-\left(f_h^i+\Delta f_h\right)\right)}\frac{\sqrt{N_h^i}}{h(\psi)\sqrt{f_h^i+\Delta f_h}} = 0 \qquad (B.4)$$

Newton-Raphson method is used to solve Eqs. B.2-B.4, e.g. $\Delta T_n^{i+1} = \Delta T_n^i - g\left(\Delta T_n^i\right)\Big/g'\left(\Delta T_n^i\right)$. The solution procedure begins with an initial guess for ΔT_{tk}^i and ΔT_n^i; then Δf_h^i is determined for this set of traction increments. The expressions for the Jacobian matrix for i) sliding only and ii) combined opening/sliding viscous response along the interface are given by:

$$\mathbf{C}_{\boldsymbol{\kappa}}^{sliding} = \frac{\partial\Delta\mathbf{T_c}}{\partial\Delta\boldsymbol{\delta}} = \begin{bmatrix} \frac{1}{\left(A_t+B_t\Delta t\right)} & 0 & 0 \\ 0 & \frac{1}{\left(A_t+B_t\Delta t\right)} & 0 \\ 0 & 0 & K_n \end{bmatrix} \quad ; \quad \mathbf{C}_{\boldsymbol{\kappa}}^{opening/sliding} = \frac{\partial\Delta\mathbf{T_c}}{\partial\Delta\boldsymbol{\delta}} = \begin{bmatrix} \frac{\partial\Delta T_{t1}}{\partial\Delta\delta_{t1}} & 0 & \frac{\partial\Delta T_{t1}}{\partial\Delta\delta_n} \\ 0 & \frac{\partial\Delta T_{t2}}{\partial\Delta\delta_{t2}} & \frac{\partial\Delta T_{t2}}{\partial\Delta\delta_n} \\ 0 & 0 & \frac{\partial\Delta T_n}{\partial\Delta\delta_n} \end{bmatrix} \qquad (B.5)$$

APPENDIX C. TRIPLE LINE ELEMENTS – SHAPE FUNCTIONS

For the general 2D element, **A** is a [1x9] vector with respect to global coordinate system given by

$$\mathbf{A} = \frac{1}{2}\begin{bmatrix} n^{13}\cos(-\theta_{\Delta 1}) + n^{12}(\sin(\alpha_\Delta)/\sin(\gamma_\Delta))\cos(-\theta_{\Delta 3}) \\ -n^{13}\sin(-\theta_{\Delta 1}) - n^{12}(\sin(\alpha_\Delta)/\sin(\gamma_\Delta))\sin(-\theta_{\Delta 3}) \\ 0 \\ n^{23}(\sin(\beta_\Delta)/\sin(\gamma_\Delta))\cos(\theta_{\Delta 2}) + n^{12}(\sin(\alpha_\Delta)/\sin(\gamma_\Delta))\cos(-\theta_{\Delta 3}) \\ -n^{23}(\sin(\beta_\Delta)/\sin(\gamma_\Delta))\sin(\theta_{\Delta 2}) - n^{12}(\sin(\alpha_\Delta)/\sin(\gamma_\Delta))\sin(-\theta_{\Delta 3}) \\ 0 \\ n^{13}\cos(-\theta_{\Delta 1}) + n^{23}(\sin(\beta_\Delta)/\sin(\gamma_\Delta))\cos(\theta_{\Delta 2}) \\ -n^{13}\sin(-\theta_{\Delta 1}) - n^{23}(\sin(\beta_\Delta)/\sin(\gamma_\Delta))\sin(\theta_{\Delta 2}) \\ 0 \end{bmatrix}^T \qquad (C.1)$$

where $n^{13} = -1$, $n^{23} = +1$, $n^{12} = +1$ and angles $\theta_{\Delta i}$, α_Δ, β_Δ, γ_Δ are obtained from geometry. In the quasi-3D thin-slice geometries, **A** for the triple line element is a [1x18] vector:

$$\mathbf{A} = \frac{1}{4}\begin{bmatrix} n^{13}\cos(-\theta_{\Delta 1}) + n^{12}(\sin(\alpha_\Delta)/\sin(\gamma_\Delta))\cos(-\theta_{\Delta 3}) \\ -n^{13}\sin(-\theta_{\Delta 1}) - n^{12}(\sin(\alpha_\Delta)/\sin(\gamma_\Delta))\sin(-\theta_{\Delta 3}) \\ 0 \\ n^{23}(\sin(\beta_\Delta)/\sin(\gamma_\Delta))\cos(\theta_{\Delta 2}) + n^{12}(\sin(\alpha_\Delta)/\sin(\gamma_\Delta))\cos(-\theta_{\Delta 3}) \\ -n^{23}(\sin(\beta_\Delta)/\sin(\gamma_\Delta))\sin(\theta_{\Delta 2}) - n^{12}(\sin(\alpha_\Delta)/\sin(\gamma_\Delta))\sin(-\theta_{\Delta 3}) \\ 0 \\ n^{13}\cos(-\theta_{\Delta 1}) + n^{23}(\sin(\beta_\Delta)/\sin(\gamma_\Delta))\cos(\theta_{\Delta 2}) \\ -n^{13}\sin(-\theta_{\Delta 1}) - n^{23}(\sin(\beta_\Delta)/\sin(\gamma_\Delta))\sin(\theta_{\Delta 2}) \\ 0 \\ n^{13}\cos(-\theta'_{\Delta 1}) + n^{12}(\sin(\alpha_\Delta')/\sin(\gamma_\Delta'))\cos(-\theta'_{\Delta 3}) \\ -n^{13}\sin(-\theta'_{\Delta 1}) - n^{12}(\sin(\alpha_\Delta')/\sin(\gamma_\Delta'))\sin(-\theta'_{\Delta 3}) \\ 0 \\ n^{23}(\sin(\beta_\Delta')/\sin(\gamma_\Delta'))\cos(\theta'_{\Delta 2}) + n^{12}(\sin(\alpha_\Delta')/\sin(\gamma_\Delta'))\cos(-\theta'_{\Delta 3}) \\ -n^{23}(\sin(\beta_\Delta')/\sin(\gamma_\Delta'))\sin(\theta'_{\Delta 2}) - n^{12}(\sin(\alpha_\Delta')/\sin(\gamma_\Delta'))\sin(-\theta'_{\Delta 3}) \\ 0 \\ n^{13}\cos(-\theta'_{\Delta 1}) + n^{12}(\sin(\alpha_\Delta')/\sin(\gamma_\Delta'))\cos(-\theta'_{\Delta 3}) \\ -n^{13}\sin(-\theta'_{\Delta 1}) - n^{12}(\sin(\alpha_\Delta')/\sin(\gamma_\Delta'))\sin(-\theta'_{\Delta 3}) \\ 0 \end{bmatrix}^T \qquad (C.2)$$

where the primed quantities are associated with the rear face of the triple line element. The matrix $\mathbf{B_n}$ for an arbitrary triple line element with respect to the global coordinate system is

$$\mathbf{B_n} = \frac{1}{12}\begin{bmatrix} -3\sin(\beta_\Delta)\sin(-\theta_{\Delta 3}) - (\sin(\alpha_\Delta)\sin(\beta_\Delta)/\sin(\gamma_\Delta))\sin(-\theta_{\Delta 1}) \\ -3\sin(\beta_\Delta)\cos(-\theta_{\Delta 3}) - (\sin(\alpha_\Delta)\sin(\beta_\Delta)/\sin(\gamma_\Delta))\cos(-\theta_{\Delta 1}) \\ 0 \\ 3\sin(\beta_\Delta)\sin(-\theta_{\Delta 3}) - 2\sin(\alpha_\Delta)\sin(\theta_{\Delta 2}) \\ 3\sin(\beta_\Delta)\cos(-\theta_{\Delta 3}) - 2\sin(\alpha_\Delta)\cos(\theta_{\Delta 2}) \\ 0 \\ 2\sin(\alpha_\Delta)\sin(\theta_{\Delta 2}) + (\sin(\alpha_\Delta)\sin(\beta_\Delta)/\sin(\gamma_\Delta))\sin(-\theta_{\Delta 1}) \\ 2\sin(\alpha_\Delta)\cos(\theta_{\Delta 2}) + (\sin(\alpha_\Delta)\sin(\beta_\Delta)/\sin(\gamma_\Delta))\cos(-\theta_{\Delta 1}) \\ 0 \\ -3\sin(\beta_\Delta')\sin(-\theta'_{\Delta 3}) - (\sin(\alpha_\Delta')\sin(\beta_\Delta')/\sin(\gamma_\Delta'))\sin(-\theta'_{\Delta 1}) \\ -3\sin(\beta_\Delta')\cos(-\theta'_{\Delta 3}) - (\sin(\alpha_\Delta')\sin(\beta_\Delta')/\sin(\gamma_\Delta'))\cos(-\theta'_{\Delta 1}) \\ 0 \\ 3\sin(\beta_\Delta')\sin(-\theta'_{\Delta 3}) - 2\sin(\alpha_\Delta')\sin(\theta'_{\Delta 2}) \\ 3\sin(\beta_\Delta')\cos(-\theta'_{\Delta 3}) - 2\sin(\alpha_\Delta')\cos(\theta'_{\Delta 2}) \\ 0 \\ 2\sin(\alpha_\Delta')\sin(\theta'_{\Delta 2}) + (\sin(\alpha_\Delta')\sin(\beta_\Delta')/\sin(\gamma_\Delta'))\sin(-\theta'_{\Delta 1}) \\ 2\sin(\alpha_\Delta')\cos(\theta'_{\Delta 2}) + (\sin(\alpha_\Delta')\sin(\beta_\Delta')/\sin(\gamma_\Delta'))\cos(-\theta'_{\Delta 1}) \\ 0 \end{bmatrix}^T \qquad (C.3)$$

APPENDIX D. IMPLEMENTATION OF NUCLEATION AND GROWTH MODELS IN INTERFACE ELEMENT FRAMEWORK – FLOW CHARTS

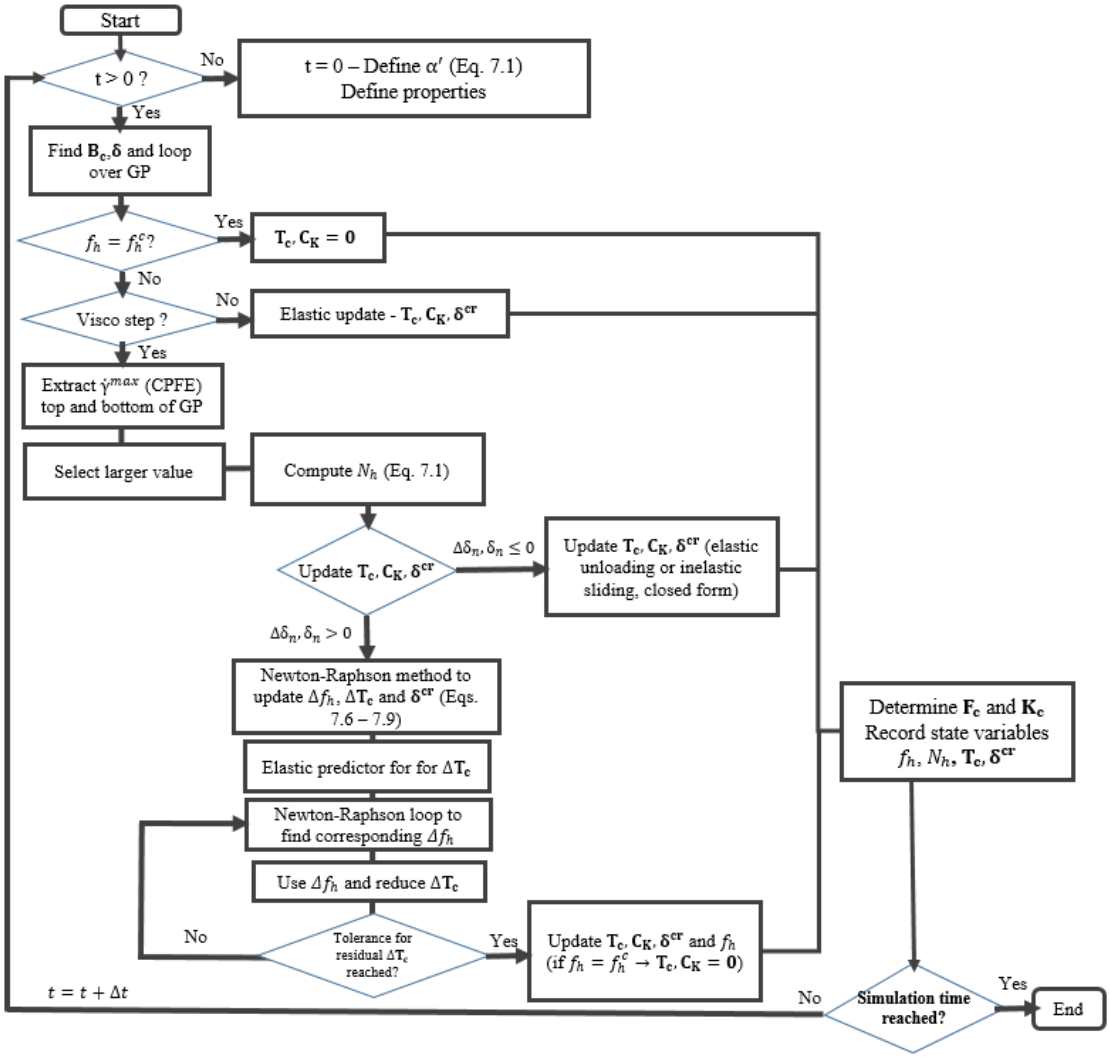


Figure D.1. Flowchart describing the implementation of the Dyson-type nucleation and growth models from Section 7.2 within the interface element framework.

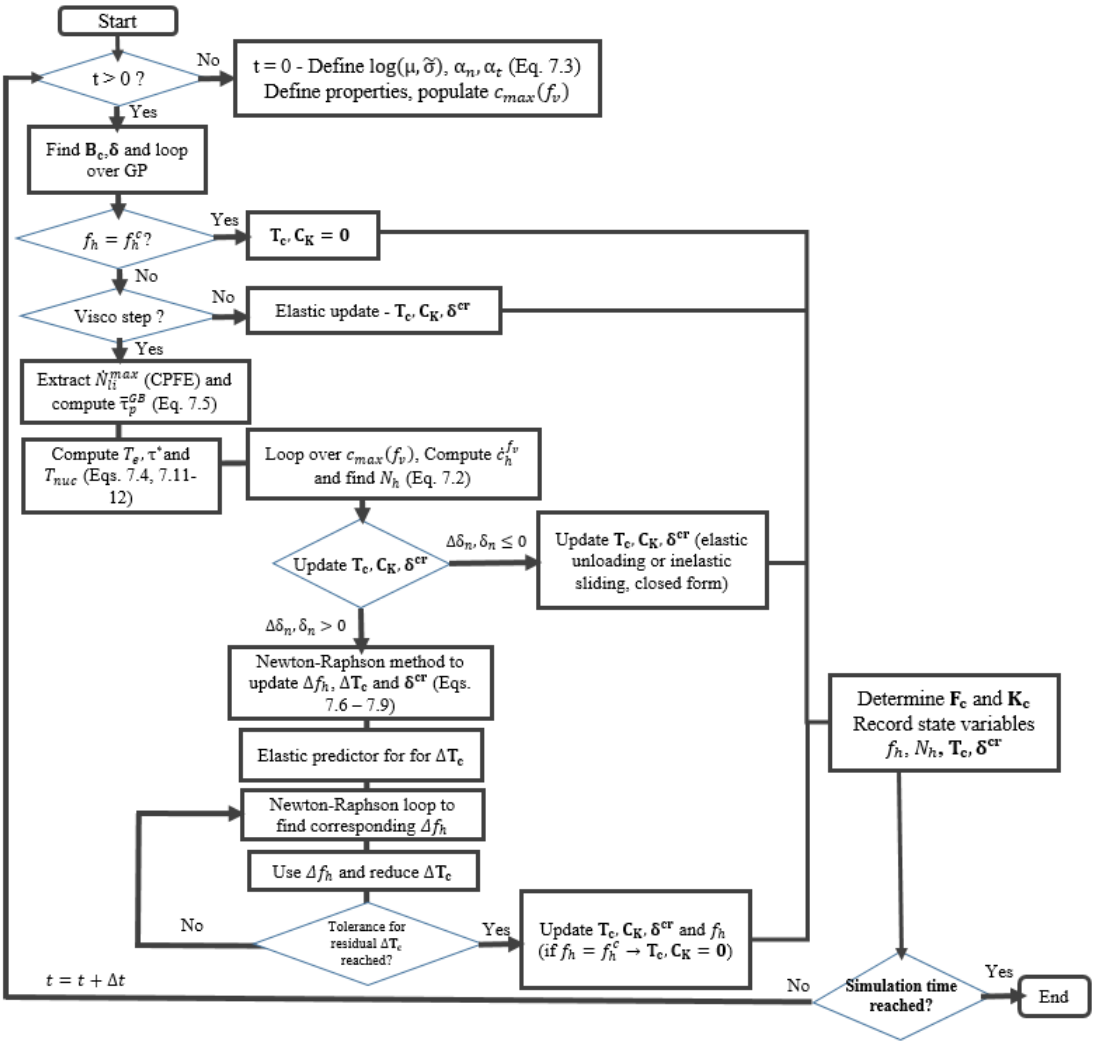


Figure D.2. Flowchart describing the implementation of the modified classical nucleation theory and growth models from Section 7.2 within the interface element framework.